DISS. ETH NO. 24345

Molecular level picture of the interaction between ice and trace gases

A thesis submitted to attain the degree of
DOCTOR OF SCIENCES of ETH ZURICH
(Dr. sc. ETH Zurich)

presented by
ASTRID WALDNER
M.Sc., Ruprecht-Karls-Universität Heidelberg

born on 27.05.1988
citizen of Germany

accepted on the recommendation of
Prof. Dr. Thomas Peter, examiner
Prof. Dr. Markus Ammann, co-examiner
Prof. Dr. Jan B. C. Pettersson, co-examiner

2017

Contents

ABSTRACT – ZUSAMMENFASSUNG

Ice and trace gases are ubiquitous in the environment and can interact with each other, both in the atmosphere and on the ground. These interactions impact geochemical cycles, the environment, and human health. However, as discussed in Chapter 1, a commonly accepted picture of the underlying molecular level processes is missing.
Ambient pressure X-ray electron spectroscopy (APXES) is well suited to investigate ice – trace gas interactions. It enables surface sensitive, chemical selective analysis of ice – trace gases interactions. Unlike most other techniques, the APXES technique X-ray photoelectron spectroscopy (XPS) is a direct, non-destructive method for investigating chemical composition profiles. Using the APXES technique near edge X-ray Absorption fine structure (NEXAFS) spectroscopy enables detection of changes in the hydrogen-bonding network of the uppermost nanometers of the same ice.
Within the frame of this thesis, I analyzed the molecular level interaction between ice and the three trace gases propionaldehyde (C_2H_5COH), formic acid (HCOOH), and hydrogen chloride (HCl). The aim was to investigate the effect of solubility and acidity of a trace gas on ice – trace gas interactions.
In the context of these investigations, the near ambient pressure photoemission endstation (NAPP) at Swiss Light Source (SLS), a synchrotron providing tunable X-rays, was commissioned, as presented in Chapter 2.
In addition, the laboratory based APXES set-up at Lawrence Berkeley National Laboratory was commissioned to enable further measurements independent of as-

signed beamtime for measurements (Chapter 3). The isotherms of the interaction between ice and propionaldehyde, together with the observed temperature trend of the interactions in a temperature range from 230 to 270 K, measured using this set-up, confirm that surface adsorption is the dominant interaction process and that propionaldehyde does not influence the hydrogen-bonding network of the uppermost ice layers. Propionaldehyde has a relatively low Henry constant, thus is relatively insoluble and dissolution into the DI is of minor importance for the interaction ice-propionaldehyde.

The interaction ice-HCOOH, presented in Chapter 4, shows an uptake behavior different from pure surface adsorption. The carboxylic acid, which is rather soluble, penetrates several nanometers into the ice. These observations may be explained by a spreading of the HCOOH within the naturally disordered interface (DI) of the ice surface layers following Henry's law. According to NEXAFS analyses, HCOOH seems to not significantly change the hydrogen-bonding structure in the uppermost ice layers.

In Chapter 5, the interaction between ice and HCl is discussed. HCl, an even stronger acid than HCOOH, is also found to penetrate several nanometers into the ice. In addition, part of the HCl dissociates and changes in the hydrogen-bonding structure in the uppermost ice layers can be observed.

As summarized in Chapter 6, the presented results indicate that revising the simple picture of Langmuir type surface adsorption as molecular level process for ice – trace gas interactions is justified. The interaction between ice and trace gases could be surface adsorption and dissolution into the DI. Depending on the temperature and the effective solubility of the trace gas, dissolution into the DI can play an important role for the interaction in addition to surface adsorption.

NEXAFS analyses revealed that only at relatively high Cl^- concentrations the hydrogen-bonding network of the uppermost ice layers is influenced by the ice – trace gas interactions. However, we are not able to confirm if the DI is thickened, or the high concentration of Cl^- leads to a modification of the hydrogen-bonding network, since a significant amount of H_2O molecules may be tied up in the hydration shell of chloride. For that, further analysis, including theoretical thermodynamical investigations if possible, would be necessary.

To summarize, the presented analyses may contribute to a revised picture of the molecular level process of the ice – trace gas interactions facilitating improved atmosphere and climate models.

Ein wichtiger Bestandteil unsere Umgebung sind Eis und Gase die miteinander wechselwirken. Diese Wechselwirkungen beeinflussen unsere Umwelt, das Klima und auch unsere Gesundheit. Wie in Chapter 1 diskutiert gibt es trotz der Bedeutsamkeit von Eis-Spurengas Wechselwirkungen bis heute kein einheitlich anerkanntes Bild wie genau Eis und Gase miteinander interagieren und was für Folgen die Interaktion hat. Es mangelt insbesondere an Untersuchungen die Wechselwirkung zwischen Eis und Gasen auf molekularer Ebene betrachten. Ambient pressure X-ray electron spectroscopy (APXES) ist eine besonders geeignete Möglichkeit um die Interaktionen von Eis und Spurengasen auf der molekularen Ebene genauer zu untersuchen, die sich durch ihre chemische Empfindlichkeit und ihre Oberflächensensitivität auszeichnet. Mittels synchrotron basiertem APXES können Konzentrationsprofile im Eis bestimmt werden. Auch ist es möglich Änderungen der Struktur der Anordnung der H_2O Moleküle und der Wasserstoffbrückenbindungen in den obersten Eisschichten, die besonders wichtig für Eis-Spurengas Wechselwirkungen sind, zu erkennen.
Im Rahmen dieser Arbeit habe ich die Wechselwirkung dreier verschiedener Spurengase (Propanal, Ameisensäure (HCOOH), und Salzsäure (HCl)) mit Eis auf molekularer Ebene untersucht mit dem Fokus darauf die Verteilung der Spurengases im Eis und den Effekt der Säurestärke auf die Wechselwirkung zu untersuchen, um damit ein genaueres Bild über die grundlegenden Prozesse von Eis-Spurengas Wechselwirkungen zu ermöglichen. In diesem Zusammenhang habe ich den experimentellen Aufbau der near ambient pressure endstation (NAPP), die für den Betrieb am Synchrotron des PSI, die Swiss Light Source (SLS), bereit steht, zur Anwendung von APXES Untersuchungen auf Eis-Gas Interaktionsexperimente weiterentwickelt. Eine detaillierte Erklärung des Aufbaus, sowie erste Experimente sind in Chapter 2 gegeben.
Aufgrund der an Synchrotronen stark limitierten Messzeiten wurde, wie in Chapter 3 beschrieben, ein weiteres Experiment in Berkeley, USA, aufgebaut, das mit einer Labor-Röntgenquelle mit fixer Photonenenergie ausgestattet ist und unabhängig von Synchrotronmesszeiten betrieben werden kann. Erste Untersuchung von Eis-Spurengas Wechselwirkungen mit diesem Aufbau ergaben, dass aufgrund des Temperaturtrends der Aufnahme davon ausgegangen werden kann, dass die Wechselwirkung zwischen Propanal und Eis von Oberflächeadsorption dominiert ist. Propanal beeinflusst die Anordnung der H_2O Moleküle in den obersten Eisschichten nicht.
Untersuchungen der Interaktion zwischen HCOOH und Eis, beschrieben in Chapter 4, ergaben, dass hier eine tiefergehende Wechselwirkung stattfindet. Die Amei-

sensäure dringt in die obersten Eisschichten ein und verteilt sich dort. Die Anordnung der H_2O Moleküle, genauer die mittlere Struktur des Netzwerks der Wasserstoffbrückenbindungen, wird jedoch nicht beeinflusst.
Wie in Chapter 5 diskutiert dringt auch HCl tiefer in das Eis ein. Des Weiteren liegt ein Teil des HCl in seiner dissoziierten Form vor. Auch kann im Fall von relativ hohen HCl Konzentrationen eine Veränderung der Anordnung der H_2O Moleküle und der mittleren Struktur des Netzwerks der Wasserstoffbrückenbindungen in den obersten Eisschichten beobachtet werden.
Diese Untersuchungen bringen uns zu dem Schluss, dass für die Interaktion zwischen Eis und Gasen mehrere Prozesse wichtig sind. Wie in Chapter 6 erläutert, spielen zusätzlich zur Oberflächenadsorption die Lösung der Spurengase in den obersten Eisschichten eine wichtige Rolle.
Die near edge X-ray absorption fine structure (NEXAFS) spektroskopischen Untersuchungen ergaben, dass im Fall der stärksten Säure eine Veränderung der mittleren Anordnung der Wassermoleküle in den obersten Nanometern des Eises auftritt. Ob diese Veränderung durch eine Zunahme der Schichtdicke der obersten 'liquid like' Grenzschicht hervorgerufen wird, oder einfach der überwiegende Teil der Wassermoleküle mit der Hydrierung des dissozierten HCl beschäftigt sind, können wir mit unseren Untersuchungen nicht unterscheiden. Hierfür wären weitere Untersuchungen, wenn möglich verbunden mit theoretischen Studien, nötig.
Insgesamt können die präsentierten Untersuchungen zu einem erweiterten Verständnis der Wechselwirkung zwischen Eis und Spurengasen beitragen und somit die Weiterentwicklung von Atmosphären- und Klimamodellen vereinfachen.

CHAPTER 1

Ice – trace gas interactions

1.1 Why are we interested in ice – trace gas interactions?

1.1.1 Atmospheric and environmental relevance

Interest in ice – trace gas interactions arose in the mid 1980s with the realization that ozone could be destroyed at high altitudes (e.g. Abbatt et al. (1992)). Later studies (early 2000s) of atmospheric ice – trace gas interactions were triggered by interest in the partitioning of gases to cirrus ice particles (e.g. Kärcher (2003)) and findings of reactive trace gas emissions from the polar ice (Jacobi et al. (2004)). Those and subsequent studies revealed that interactions between ice and trace gases are interesting for numerous reasons, as they have, for example, the ability to initiated and influence (photo)chemical processes relevant for ozone concentration, nitrogen oxide budget, and oxidation cycles. Today, it is well known that ice can be seen as a reactive medium that can take up, scavenge, accumulate and release highly diverse compounds to and from other compartments of the environ-

ment (Molina et al. (1996), Borrmann et al. (1997), Dominé and Shepson (2002), Grannas et al. (2007), Voigt et al. (2007)). Ice consequently plays an integral role in transferring gases to and from the atmosphere, biosphere, cryosphere and hydrosphere.
In general, one can classify ice – trace gas interactions of three different kinds. One is the partitioning of gases to the ice, leading to a (temporary) loss from the gas phase. Here the partitioning of HNO_3 to the ice is a prominent example, explained in more detail later. The changed HNO_3 concentration influences the NO_x concentration in the upper troposphere lower stratosphere. This in turn influences the O_3 concentration, resulting in changes to the radiation balance of the atmosphere. In addition, chemical reaction of gases, for example of $ClONO_2$ and HCl, on ice are important ice – trace gas interactions. Furthermore, chemical reactions in ice represent important ice – trace gas interactions. The photolysis of organics in snow, resulting in emission of aldehydes from the cryosphere, thus influencing the oxidation capacity of the atmosphere, is an example.
It is important to know both, to what degree gaseous species partition to and from ice, and by which mechanisms the partitioning takes place. One prominent example is the accurate analysis and interpretation of ice core profiles, which is essential for reliable climate analysis. Chemical reactions and physical exchange processes can significantly modify signals (amount and location) of gases in ice leading to peak widening or shifts of time signals may occur, affecting the chronology of ice cores (De Angelis and Legrand (1994), Pasteur and Mulvaney (2000)).
Despite previous advances, there is no unified, commonly accepted picture, describing and quantifying the interactions between ice and atmospheric compounds, such as (trace) gases (e.g. Bartels-Rausch et al. (2012)).

1.1.2 Are lab-based studies of interest?

There are numerous reasons confirming the need for laboratory based molecular level ice–gas interaction studies.
Common to all gas-ice interactions are the underlying molecular processes. The capacity of the uptake of gases to ice observed during field studies may not necessarily fully agree with the results obtained from laboratory based experiments. Impurities and the interaction between several trace gases present in the environment may modify the uptake of individual compounds to clean ice. However, a profound

understanding of the fundamental molecular level processes occurring during ice–gas interactions can only be obtained from laboratory experiments looking at the molecular picture of the interaction. Studies of the molecular level processes are fundamental to understand and estimate ice–gas interactions.
Field studies and experimental observations reveal many large-scale influences of the small-scale phenomena of the molecular level interaction between ice and gases (e.g. Wettlaufer (1999)).

1.2 What is known about ice? What about trace gases?

1.2.1 Basics about ice

Ice is ubiquitous in the environment. Atmospheric ice occurs in many forms, including snowflakes, ice clouds, and graupel. Ice clouds are especially widespread in the atmosphere. In addition to their effect on the radiation budget, which strongly depends on their actual constitution (Watson and Albritton (2001)), ice clouds influence the chemical composition and oxidation capacity of the atmosphere. For example, the presence of cirrus cloud, widely prevalent in the upper troposphere and tropopause region, can decrease the ozone in the tropical stratosphere by activating chlorine constituents (Solomon et al. (1997)).
In addition to atmospheric ice, there is terrestrial ice located at the earth's surface as firn, glacial ice, polar caps, and snow. Snow can cover up to 50% of landmasses in the Northern Hemisphere (Robinson et al. (1993)). Antarctic and Greenland ice sheets make up 97% of the glaciated area of the world and 99.8% of its volume (Ohmura et al. (1996)). Terrestrial ice is involved in the chemistry of the boundary layer. It can act as a sink for many organic pollutants but also as source of e.g. NO_x, reactive bromine, and small organics.
Ice can be described as a multiphase medium consisting of different compartments. As main compartments, one can differentiate between bulk crystal ice with a quasi-liquid disordered interface (DI), crystal grain boundaries, pores, and liquid pockets (e.g. Bartels-Rausch et al. (2014) and references therein). A scheme of these ice domains together with possible ice – trace gas interactions is shown in Figure 1. The physical and chemical properties may vary strongly between these individual

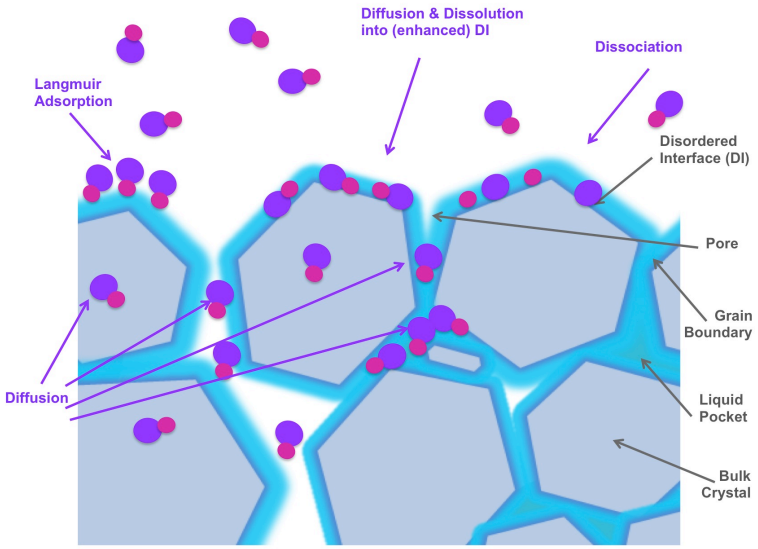

Figure 1.1: Scheme of the multiphase medium ice showing the different compartments important for the interaction ice–trace gas. In addition, chemical reactions in any compartment may occur.

compartments (e.g. Bartels-Rausch et al. (2014) and references therein). For example, the presence of a liquid phase may strongly modify interactions between ice and gases, due to higher diffusion coefficients of trace gases and by higher uptake coefficients of the trace gas, thus higher rate at which trace gases are transferred from the gas phase to the ice. A liquid and/or quasi liquid in ice will exist even in the bulk-solid region of the phase diagram in thermodynamic equilibrium, if by being there, the total free energy of the system is reduced.
Temperature gradients common in the environment induce changes of the ice, leading to a restructuring of the ice, thus changing the distributions and occurrences of the different compartments. Studies show that up to 60% of the total ice mass in snow can be redistributed within 12 hours under environmentally relevant conditions (Schneebeli and Sokratov (2004)).

Nature of the ice surface The surface layer of ice crystals is one of the most important compartments of ice for ice – trace gas interactions. This layer is the direct interface at which exchange with the gas phase takes place (Bartels-Rausch et al. (2014), Dash et al. (1995), Dash et al. (2006)).
The ice surface itself is highly dynamic. Many monolayers of water molecules evap-

orate from and (re)condense onto ice per second at equilibrium conditions. Those mobile water (H_2O) molecules at the ice surface promote (hydrolysis) reactions that do not proceed in the gas phase or in the more rigid ice underneath.
Actually, this is not the only thing making the ice surface interesting for ice – trace gas interactions. Even an assumingly 'static' ice surface has properties that are considered to be different from the bulk crystalline ice.
At environmentally relevant conditions, crystalline bulk ice is mostly composed of tetrahedrally coordinated H_2O molecules. However, the surface of the crystals reveals a modified crystal structure (Nenow and Trayanov (1989), Mellenthin et al. (2008)). This modification occurs due to outer layers' missing bonds and is an inherent interfacial property of crystals. It is the result of a reduction of the total excess surface free energy (Dash et al. (2006) and references therein).
In conclusion, the ice surface layer is quite different from bulk ice. Properties, such as mobility of molecules, diffusivity and structure, are considered to be different from the bulk crystalline ice. Reactive heterogeneous chemistry and unique chemical reactions, having impacts on air quality, climate change, and biological cycles, can occur in/on the interface.
Faraday first described the ice-air interface in 1840 (Faraday (1840)). The DI, also called liquid-like or quasi-liquid layer (QLL), can be understood as a layer of increased molecular disorder of the H_2O molecules compared to the ordered bulk crystal ice. Its importance is a matter of common knowledge. However, a profound and generally accepted description and quantification of this natural DI and its detailed impact on ice – trace gas interaction processes is still lacking. Since Faraday, substantial progress has been made and the DI has been investigated using many techniques. However, findings spread widely.
A reason for the inconsistencies may be the techniques with which the DI has been interrogated. They investigate different properties and the depths that are probed, as well as the depth resolution, are very different. Techniques used for the analysis are some molecular dynamic (MD) simulations, neutron scattering optical refraction and reflection analysis, atomic force microscopy, molecule spectroscopic methods, proton channeling, as well as glancing-angle X-ray diffraction (XRD), and photoemission spectroscopy. MD simulations, as for example used by Shepherd et al (2012), model only the uppermost 2 nm of the ice, defining the lowermost ice layers to be bulk ice. Neutron scattering, as for exampled used by Toubin et al. (2001), can observe changes in the uppermost 2-3 nm of the ice, assuming the DI to be liquid water. Optical measurements, including ellipsometry, can mainly detect changes of the ice surface layer that emerge over several tens of

nm, as for example demonstrated by Elbaum et al. (1993), or McNeill et al. (2006). Atomic force spectroscopy is based on the difference in mechanical properties of bulk ice and the surface layer, which is assumed to be liquid water (e.g. Bluhm and Salmeron (1999), Döppenschmidt and Butt (2000)). Molecule spectroscopic methods as sum frequency generation analyze the effect of symmetry changes on atoms with an actual probe depth of ~15 nm (e.g. Wei et al. (2002), Kahan et al. (2007)). Proton channeling probes depths of several 100 nm with a depth resolution of ~35 nm (Golecki and Jaccard (1978)). XRD, for example used by Dosch et al. (1995) is known to have probe depths of ~5-1000 nm. Photoemission spectroscopy has a probe depth of ~6 nm (Bluhm et al. (2002)).
The observed thickness of the DI vary widely, from less than 1 nm to several tens of nm, sometimes even within repeated measurements. In addition to the technique itself, which analyze different properties and depths as mentioned above, impurities or different ice morphologies may influence the DI (Bartels-Rausch et al. (2014)).
However, it is commonly expected that at temperatures close to the melting point ice surfaces reveal a more pronounced, thicker DI (e.g. Bluhm et al. (2002)).
As with the thickness, the description of the interfacial layer as a liquid is a controversial discussion. Some MD simulations and experimental observations give little support for a liquid interface hypothesis (Bartels-Rausch et al. (2014) and references therein). Some others support the hypothesis. For example, MD simulations by Shepherd et al (2012) showed, that when the DI is thicker than 1 nm, the structure of the H_2O molecules and the solubility of trace gases in the center of the DI are the same as in bulk liquid water. Using laser confocal microscopy, Sazaki et al (2012) observed small moving liquid droplets at the ice surface. This supports the theory of the presence of a liquid phase, but also indicates a laterally inhomogeneous DI.
As pointed out above, the presence of a disordered ice surface layer and its importance for the interaction with gases is non-controversial, but its detailed properties are still debated.

1.2.2 Basics about trace gases

Nitrogen, oxygen, and argon make up about 99.96% of earth's atmosphere. The remaining are trace gases. The existence of those trace gases is significant for atmospheric chemistry. Their presence and influence on atmospheric composition,

air quality, climate as well as human and ecosystem health play a prominent role in today's politics and research. Climate change is a major issue, but also the fate of (organic) contaminants (AMAP (2009)), are important aspects. Montreal Protocol, Kyoto Protocol, IPCC reports, are only few examples of common public debates, reviews and reports about environmental and climate issues involving atmospheric trace gases.

Certainly far more components of the atmosphere are worthy of discussion. I focus on some, which seem particularly interesting in the context of this thesis. I concentrate on the interaction between organic, as well as acidic trace gases and ice. The chosen gases represent gases, interesting due to their exemplary importance for ice-atmosphere interactions, including atmospheric chemistry (Huthwelker et al. (2006), Jedlovszky et al. (2008)). A representative for strong acids (hydrochloric acid (HCl), see Chapter 5), one weaker organic acid (formic acid (HCOOH), Chapter 4), and one aldehyde (Propionaldehyde (CH_3CH_2COH)), Chapter 3) were used for the trace gas-ice interaction experiments.

Short chain aldehydes are prevalent in the atmosphere. They are emitted directly to the atmosphere from combustion. Secondary sources are production through photo-oxidation of volatile organic compounds of anthropogenic and biogenic origin (Lary and Shallcross (2000)). Deposition (dry and wet) and reaction with NO_3 radicals are important removal mechanisms (Finlayson and Pitts (2000)). Another sink is photolysis leading to OH production. The production of OH modulates the level of key oxidants, making aldehydes very important for atmospheric chemistry. The uptake of aldehydes to ice clouds affects the role of aldehydes as radical source. While aldehydes are photolytically active, hydration of propionaldehyde leads to a reduction of absorbance of UVA light, thus aldehydes are less active in the ice phase. In addition, the partitioning between gas and ice influences the rate at which aldehydes are emitted from the snow surface, which is in turn influencing the radical budget. What makes aldehydes particularly interesting for ice – trace gas interaction research is that their concentration in ice, more precisely in the interstitial air of snow, was found to be enhanced due to photo-production (Chen et al. (2007), Yang et al. (2002)). This leads to the fact that aldehydes contribute significantly to the OH budget in the, often shallow, boundary layer of Polar Regions. In summary, partitioning of aldehydes to ice is worthwhile to be investigated since the interaction between ice and aldehydes influence the OH concentration, thus oxidation capacity of the atmosphere playing an important role for atmospheric chemistry.

HCOOH is, together with acetic acid (CH_3COOH), one of the most abundant

organic acids in the atmosphere. HCOOH is a relatively strong (pKa: 3.77) and the simplest carboxylic acid. It is a naturally occurring component of the atmosphere, primarily due to direct emissions and as secondary product from oxidation of biogenic volatile organic compounds. HCOOH has a relatively long photochemical lifetime. Main sinks of organic acids in the atmosphere are uptake to ice and aqueous particles, as well as cloud processing (Millet et al. (2015) and references therein). In summary, partitioning of HCOOH to ice (clouds) represents a sink of HCOOH in the atmosphere, which influences the OH budget (Jacob (1986)), thus oxidative capacity, of the atmosphere.

Halogen atoms are efficient in the degradation of volatile organic compounds (VOC's) in the atmosphere, thus enhancing hydrocarbon oxidation (Monks (2005), Platt and Hönninger (2003)). Even though the concentration of chlorine is typically orders of magnitude lower than that of OH radicals, chlorine is of particular interest since chlorine atoms are about 1000 times more reactive than OH (Monks (2005)). Chlorine containing compounds in the atmosphere can be divided in two different groups: organic and inorganic chlorine. The highly acidic ($pK_S : -7$) HCl, is the most important inorganic chlorine compound. Its main sources in the troposphere are acidification of sea salt particles and volcanic eruptions. In the stratosphere photolysis of CFCs leads to Cl atoms, which are very reactive to hydrocarbons (mainly methane in the stratosphere) with which they react by H abstraction to yield HCl.

HCl dissolves very readily, leading to an efficient removal of HCl from the lower atmosphere. Measurements show that the HCl mixing ratio is less than 0.1 ppbv at elevations above 7 km, and less than 0.04 ppbv at 13.7 km (Vierkorn-Rudolph et al. (1984)). At higher altitudes inorganic chlorine is abundant, most of it in form of HCl or $ClONO_2$. These so called "chlorine reservoirs" do not themselves react with ozone, but they can initiate the formation of chlorine-containing radicals (Cl, ClO, ClO_2), which do. An increase in the concentration of chlorine reservoirs leads to an increase in the concentration of the ozone-destroying radicals. Here, the presence of ice particles are relevant drivers for the heterogeneous reactions of HCl and $ClONO_2$ to Cl_2 and HNO_3. Photolysis of Cl_2 then forms the Cl atom. In summary, the interplay between ice and chlorine containing compounds influences the oxidation capacity and ozone concentration in the atmosphere.

1.3 What is already known about ice – trace gas interactions?

Numerous field and laboratory studies showed that ice hosts unique reactions influencing climate, air quality, and biology (Grannas et al. (2007), Kahan and Donaldson (2010)). One of the most evident observations of chemical processes involved in ice – trace gas interactions is the almost complete ozone depletion in boundary layer air during polar spring for chemistry in/on ice (Barrie et al. (1988)).
In addition, ice is known to play a substantial role for heterogeneous and multiphase chemistry in the atmosphere.
Partitioning of gases to ice is a further interaction between ice and gases important for the environment. Studies investigating the partitioning of gases to ice show partly contradictory results. Sometimes the uptake of gases to ice was found to be driven by fast and limited (Langmuir, described below) surface adsorption (Ullerstam et al. (2005)). Other studies (e.g. Huthwelker et al. (2006), Kerbrat et al. (2010)) revealed an additional pronounced long-term uptake, which in some cases substantially exceeded the initial uptake. Postulated processes, which could lead to an uptake featuring such a second regime, are: formation of hydrates, presence of liquid phase and/or diffusion in bulk ice or other ice compartments. In addition, dissociation, self-reaction, or even unidentified processes may occur, leading to a modification of the ice, thus influencing the interaction between gas and ice.
The following paragraphs and Figure 1 give an overview and description about physical and chemical (exchange) processes that can be important for ice-gas interactions.
Furthermore, temperature, impurities and expectations about the interaction behavior of the specific trace gases used within this PhD study are discussed.

Physical (exchange) processes The main and most important physical partitioning processes between ice and atmosphere are surface adsorption/desorption and diffusion (Abbatt (2003), Huthwelker et al. (2006), Bartels-Rausch et al. (2012)).
The interactions between gases and ice are (mostly) first initiated by adsorption. Adsorption, as well as the counter-process desorption, operate on short time-scales (nanoseconds to milliseconds) and therefore respond quickly to changes in envi-

ronmental conditions. The total capacity for the uptake via adsorption is limited by surface area. The adsorption-desorption equilibrium is often described using the Langmuir isotherm. It predicts a first linear increase of the surface coverage at lowest concentrations, followed by slow saturation of the surface coverage at certain gas-phase concentrations as the adsorbing species molecules compete for a fixed number of fixed adsorption sites. It is assumed to describe the adsorption of many organic and inorganic species to ice reasonably well (Crowley et al. (2010)). In addition, diffusion into the ice may occur. Here, bulk ice crystals, the DI with possibly enhanced thickness, grain boundaries, and/or pockets of air and liquid play a role. A drastic change in the uptake properties, especially the capacity, can for example be assumed in the presence of a different phase. Diffusion into the ice can take place with diffusion rates in the order of $4 \cdot 10^{-10}$ $m^2 s^{-1}$ in strongly disordered and inhomogeneous ice, meaning consisting of various compartments, to $4 \cdot 10^{-15}$ $m^2 s^{-1}$ in single crystal ice structures (Huthwelker et al. (2006), Lu et al. (2009), Bartels-Rausch et al. (2014)).

Chemical (exchange) processes Beyond physical processes, chemical processes are important for ice–gas interactions. Heterogeneous chemistry occurs at the ice surface. In addition, chemicals can be formed or destroyed in ice.
From a molecular perspective formation of hydrogen bonds and dissociation seem to be the initial chemical interaction steps between ice and trace gases (Parent et al. (2002), Parent et al. (2011)).
Temperature, the local environment, as well as the composition of the ice itself may play an important role enabling and influencing chemical processes. One should keep in mind that ice can be a multiphase medium and depending on the type of compartment, its phase and fraction, different chemical processes may occur. Dissociation, the forming of hydrates and complexes, intermolecular interactions as well as local concentrations, depending on freeze-concentration effects, can lead to changes in the physical and chemical properties of the gas and of the (compartments of the) ice. Physical and chemical properties in turn affect solubility, effective acidity and optical properties, thus influence (photo)chemical reactions. Apparent reaction rates can be decreased, remain unchanged, or be enhanced up to a factor of ten in the presence of ice.
However, since chemistry in ice and at ice surfaces is a relatively new area of study, there is still a lack of understanding of the detailed processes. A full representation

of the distinct compartments and the different physiochemical processes important for ice-gas interactions has not been attempted.

Effect of ice temperature The ice temperature may influence the partitioning and the capacity of the uptake of gases to ice. Especially at temperatures higher than 250 K, an uptake of gases to ice with a behavior quite different from Langmuir type adsorption has been reported (Abbatt et al. (2008)). Using MD simulations, Pfalzgraff et al. (2011) showed that diffusion into the ice is enhanced at warmer temperatures. Pratte et al. (2006) and Kong et al. (2014) demonstrated that the uptake coefficient of D_2O does not show a continuous temperature trend. Especially at around 190 K a sudden change was observed. In addition, Kong et al. (2014) postulated that at warmer temperatures an increasingly disordered ice surface layer might also influence the uptake of gases to ice. The uptake coefficient must dramatically increase by approaching higher temperature since liquid water has a far higher uptake coefficient (Miles et al. (2012)).

Effect of impurities Ice – trace gas interactions may be strongly influenced by impurities. For example, the presence of impurities, can lead to changes of the ice surface's hydrogen-bonding network modifying the natural DI discussed in Chapter 1.2.1. Sometimes, even small impurity levels lead to partial melting (Elbaum et al. (1993)) due to the classical colligative effect (melting point depression). Ice is an efficient segregator of impurities, leading to impurities being strongly concentrated in the remaining liquid fraction sometimes residing at the ice surface, during freezing.
In summary, impurities have the ability to alter the ice (properties), such as surface charge densities, and intermolecular interactions, thus affect ice–gas interactions (Bartels-Rausch et al. (2012) and references therein).

Results of previous ice – trace gas investigations relevant to this project Non-acidic organics: Starr et al. (2011) using surface sensitive spectroscopic methods directly probing the interaction between acetone and ice, showed that adsorption of acetone to ice follows a Langmuir type isotherm. Changes in the hydrogen-bonding network of the ice surface layers did not occur. Similar conclusions were obtained from coated wall flow tube (CWFT) studies. CWFT is an indirect measurement

technique, analyzing concentration changes in the gas-phase. Also, 2-Propanol follows Langmuir type adsorption as shown by Newberg and Bluhm (2015). According to results from CWFT and computer simulations (grand canonical Monte Carlo), small Aldehydes also follow Langmuir type adsorption (Hantal et al. (2007), Darvas et al. (2012)). However, Petitjean et al. (2009) found that at temperatures higher than 223 K, the uptake of aldehydes to ice deviates from Langmuir. Hydration of aldehydes may initiate accretion processes (oligomerisation) that may enhance uptake. Using ellipsometry, Kuo (2013), additionally showed that short chain aldehydes can induce and enhance surface disorder.

Acids: For the interaction between ice and acids, it is interesting to inquire if the acidity of a gas influences ice – trace gas interaction, if weak(er) acids show a different interaction behavior from stronger acids. Electro negativity and polarity, as well as electron density distribution may influence the interaction between ice and (acidic) trace gases.

Weak Acids: Spectroscopy of the interaction CH_3COOH–ice indicates a 60% deprotonation of CH_3COOH in ice. The acid penetrates the topmost bilayers of the ice. Only minor perturbations in the hydrogen-bonding network of the ice occur (Křepelová et al. (2012)). Due to the somewhat higher acid dissociation constant of HCOOH, and the additional methyl group (hydrophobic) of CH_3COOH, different ice-HCOOH and ice-CH_3COOH interactions might be expected. Comparing the interaction of HCOOH and CH_3COOH with ice at 250 K using MD simulations, Compoint et al. (2002) found that incorporation of HCOOH is favored compared to CH_3COOH. HCOOH penetrates the ice easily and distributes into the whole DI. Furthermore, they found the uptake process to be irreversible within the time-scale of the simulation (10 nsec). Using a combination of computer simulation (grand canonical Monte Carlo) and CWFT experiments operating over longer time scales Jedlovszky et al. (2008) investigated the uptake of HCOOH to ice at temperatures from 187-221 K. Up to a relative HCOOH pressure of 0.04 (the relative HCOOH pressure, also called saturation ratio, is the HCOOH pressure in the vapor phase normalized by the saturation vapor pressure of the pure liquid HCOOH) Langmuir type surface adsorption was observed in the lower temperature range. For higher temperatures (> 209K), the interaction changed. The amount of adsorbed molecules at a given relative pressure is higher and the amount of molecules in the ice increases almost in linear manner with increasing HCOOH partial pressure.

Strong Acids: Křepelová et al. (2010) studied the uppermost 6 nm of ice interacting with nitric acid (HNO_3) at atmospherically relevant conditions. They showed that HNO_3 can modify the hydrogen-bonding network of the ice surface. The ice

surface can be understood as a mixture of clean ice and nitrate ions coordinated as in a concentrated solution at the same temperature, but higher HNO_3 pressures. Using ellipsometry, Kuo (2013) confirmed this observation. Furthermore, his CWFT studies indicated that the nature of HNO_3 uptake changes from reversible adsorption to a continuous flux of HNO_3 into the ice if the DI is modified or when the system approaches the phase boundary to hydrates or HNO_3 solutions.
For the interaction of relatively high partial pressures of HCl (p(HCl)) with ice, a substantial, irreversible uptake of HCl to ice was observed (Molina et al. (1987), Leu (1988)). The high HCl pressure most probably led to melting of ice since it thermodynamically forced the system to the HCl aqueous solution regime. Infrared experiments additionally showed dissociation of HCl and the formation of solid hydrates (Barone et al. (1999)).
Measurements by McNeill et al. (2006) close to the thermodynamic phase transition, indicate the formation of an induced DI due to the exposure of the ice to the HCl. In case of such an induced DI, a nearly constant flux of HCl into the ice, a long-term trend, was observed.
For lower p(HCl), the solubility in ice seems orders of magnitude smaller (Barone et al. (1999), Gross (1967)). Surface coverages were found to be in the monolayer range (Hynes et al. (2001), Abbatt et al. (1992), Lee et al. (1999)). The most recent study by Zimmermann et al. (2016) looked at the interaction between ice and HCl at temperatures from 190 to 220 K using CWFT. They ascertained that a dissociative Langmuir-model describes the uptake best. However, they found that the uptake of HCl to ice is temperature independent.

1.4 What would be good to know about ice – trace gas interactions?

As emphasized, the interaction between (trace) gases and ice is a subject of scientific interest. It is increasingly recognized that ice acts as multiphase reactors in which (heterogeneous) reactions, photochemical reactions, and physical exchange processes take place. Ice–gas interactions play a role in global warming, atmospheric oxidation capacity, fresh water supply, avalanches, environmental archive as well as air and water pollution.
Numerous studies looked at the interaction between gases and ice. But, only very few of these studies were able to look directly at the interaction of trace gases with

ice, or were performed under environmentally relevant conditions, involving low trace gas partial pressures and ice temperatures ranging from 210 K close to the melting point (273 K). The presented analyses already provide valuable information about ice – trace interactions but so far, a consistent and commonly accepted picture of the interaction ice – trace gas is missing. The observed varying results of capacity and trend of uptakes of trace gases to ice may result from the measurement technique itself, as well as different properties of the ice (compartments, impurities, temperature, and pressure), as with the discrepancies in findings for the DI. For example, (unintended) growing or evaporation of the ice during the experiment may affect the observed ice – trace gas interaction, since it may strongly influence the ice compartments and properties.
However, studies of the molecular-level of ice–gas interaction under environmentally relevant conditions, applying direct analysis of the adsorbed trace gas, their location in/on the ice and the effect of the DI on the interaction between trace gases and ice, as well as their chemical state, are experimentally challenging and have rarely been conducted. From this perspective, the fundamental aspects in the way cryosphere and atmosphere interact represent a relatively unexplored field. This hampers successful development and appropriate inclusion of ice-atmosphere interactions in atmosphere chemistry and climate models. Of major importance to understand ice–gas interactions is a proper knowledge about all compartments of ice, especially the ice surface which plays a particularly important role. Furthermore, more molecular interaction processes such as diffusion and chemical (exchange) processes, should be taken into account.
Interesting questions include: Do ice – trace gas interactions modify the hydrogen-bonding network of the ice-air interfacial layer? If there is an effect of the ice–trace gas interactions on the ice, is it local? How does the interface change? Does the effect of ice–trace gas interactions on the ice depend on impurities in the ice and/or the ice temperature? Where and how do ice and trace gases interact? Does dissociation occur at the ice surface or in the ice, and how does this influence the interaction between ice and trace gas? Which are the relevant processes for ice – trace gas interactions? To what degree do adsorbed species diffuse into the bulk? Is the uptake of trace gases to ice irreversible?
These lead to the summarized questions: How do ice and trace gases interact? What are the consequences of the interactions? Assuming these questions will be answered, a more detailed modeling of atmosphere-ice interactions allowing for more accurate climate modeling might be possible, and the question of how ex-

change processes influence ice core concentration profiles might be answered.

1.5 How did I study ice – trace gas interactions?

The aim of this thesis is to address some of the questions highlighted in the paragraphs above, specifically: *Where are trace gases located in ice? Do they penetrate in the ice or only adsorb to the ice surface? What is the impact of the acidity of the trace gas on the interaction with the ice? Does dissociation take place? Does/can the interaction with (acidic) trace gases lead to a changed ice surface?*

I approached these challenges using the surface sensitive ambient pressure X-ray

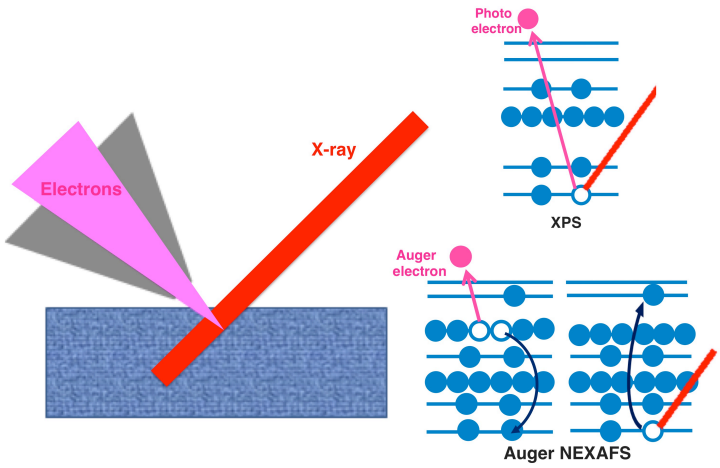

Figure 1.2: Scheme of XPS and partial electron Auger yield NEXAFS analysis.

spectroscopy methods X-ray photoelectron spectroscopy (XPS) and partial electron yield (Auger) near edge absorption fine structure spectroscopy (NEXAFS). A scheme of XPS and NEXAFS probing is displayed in Figure 1.2. As displayed and described below, XPS and electron yield NEXAFS spectroscopy rely on the detection of electrons emitted upon interaction of X-rays with core electrons of elements in the sample. XPS and NEXAFS have become established tools in surface science during the last few decades (e.g. Somorjai and Li (2010)). Synchrotron based XPS and NEXAFS are of importance in environmental science, enabling element and chemical state specific distribution analysis, as well as investigation

of structural properties of various material surfaces. (e.g. Huthwelker et al. (2006), Salmeron and Schlögl (2008), Huse et al. (2009), Křepelová et al. (2012)).
Synchrotron radiation sources have been employed as an independent tool to investigate materials for about half a century. Today's synchrotron sources, such as Swiss Light Source (SLS) and Advanced Light Source (ALS), provide radiation with a small spot size, and great brilliance. The light is conveyed from the synchrotron's storage ring to experimental chambers via beamlines featuring a monochromator and focusing mirrors. When the synchrotron radiation enters the experimental chamber, it has two properties that distinguish it from conventional X-rays created by lab-sources: the monochromatic X-rays can be polarized and the wavelength of the radiation is tunable. The available range of wavelength and brilliance is determined by the chosen beamline and respective wigglers or undulators emitting X-ray radiation.
One challenge of using photoelectron spectroscopy (PE) for environmental analysis purposes is that the technique requires low pressure conditions (10^{-8} mbar), since scattering of the photoelectrons in the gas-phase reduces the photoemission signal dramatically. Due to that fact, traditional PE experiments are performed under ultra high vacuum (UHV) conditions. The vapor pressure of ice under environmentally relevant conditions (i. e. temperatures close to the melting point) is far too high (up to 5 mbar) to ensure an appropriate signal. Therefore, the application of an ambient pressure X-ray electron spectroscopy (APXES) set-up, featuring a differentially pumped electrostatic lens system to transfer electrons from the sample region into the electron analyzer kept under UHV conditions, is indispensable (e.g. Salmeron and Schlögl (2008)).
For the experiments performed in Switzerland (HCOOH and HCl), the near ambient pressure photo emission endstation (NAPP) at SLS was commissioned and used. For a detailed description of NAPP, see the following chapter focusing on development, set-up, and proof-of-principle measurements. The commissioned set-up of the experiments performed in Berkeley is described in chapter 3. There, in addition to synchrotron based experiments a laboratory X-ray source was used.

1.5.1 X-ray photoelectron spectroscopy – XPS

What is XPS – How does it work? Developed in 1957 by Kai Siegbahn (Nordling et al. (1957)), XPS is one of the most surface sensitive probing techniques for sur-

face elemental composition analysis that is also chemically specific (Huefner (1995), Bluhm (2010), Salmeron and Schlögl (2008), Falicov and Somorjai (1985) , Ackermann et al. (2005)). It enables identification of elements, together with the analysis of their chemical states.
XPS is based on the photoelectric effect. Occupied electronic levels are probed by the detection of electrons emitted after the irradiation of a sample with X-rays (see Figure 1.2). The ejected electrons are called photoelectrons.

The kinetic energy (E_{kin}) of a photoelectron is given by the difference between

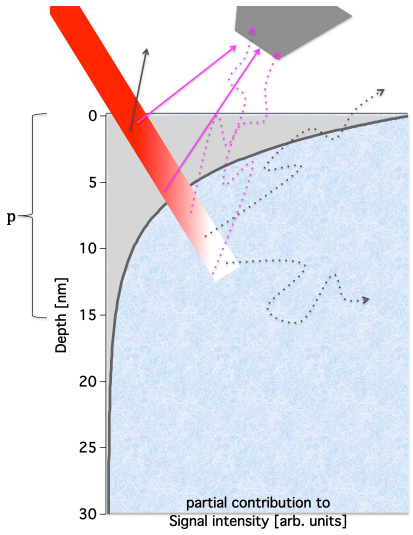

Figure 1.3: Scheme of XPS probing depth. In red the X-ray, in purple detectable photoelectrons (reaching the analyser) and in grey photoelectrons not detectable are displayed. Dashed lines indicate trajectories with inelastic scattering events, wheras solid lines represent elastically scattered photoelectrons. p indicates the probing depth.

the photon energy of the incoming X-ray ($\mathbf{h\nu}$) and the element and chemical state specific binding energy (E_{bind}) of the core electron, and an experimental set-up dependent workfunction (θ_f) => ($E_{kin} = \mathbf{h\nu} - E_{bind} - \theta_f$). The observed E_{kin} of a detected electron can thus be ascribed to a corresponding E_{bind} of a core electron.

In condensed matter, scattering of photoelectrons is taking place. For data analysis, only elastically scattered electron, resulting in a sharp peak feature, are considered. All electrons experiencing inelastic scattering may still leave the sample at reduced E_{kin}, thus only contribute to the background, which is subtracted to obtain the peak area related to the elastically scattered electrons. An exem-

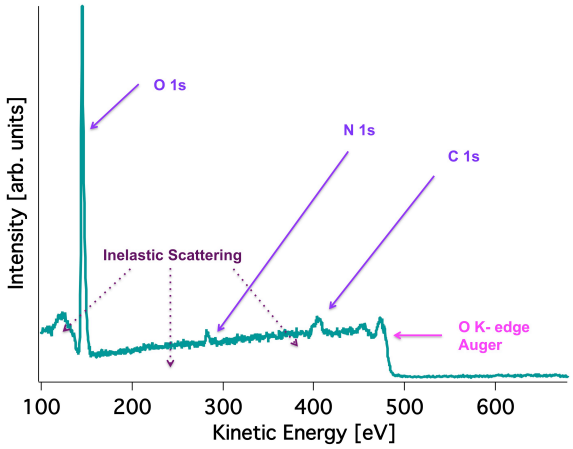

Figure 1.4: Exemplary survey spectrum of ice with carbon and nitrogen contamination measured at SIM X11MA beamline at SLS using a photon energy of 680 eV. One can clearly identify the sharp features of the elastically scattered photoelectrons resulting from core electron excitation (O 1s, N 1s, and C1s). In addition, the oxygen K-edge Auger feature and the background of inelastically scattered photoelectrons is visible.

plary photoemission spectrum is shown in Figure 1.4. One can clearly identify the sharp photoemission core level peaks and background features. Although X-rays penetrate up to many microns deep into the sample, electrons generated at great depths do not contribute to the XPS peaks used for analysis, since the photoelectrons are scattered inelastically.

The inelastic mean free path (IMFP) of a photoelectron, depending on its kinetic energy (E_{kin}) , describes the characteristic distance a photoelectron with a given Ekin can travel through a solid without being inelastically scattered. The dependence of the IMFP of the E_{kin} is complex. It exhibits a minimum at around 100 eV of around 1nm and increases towards lower and higher kinetic energies. An exemplary plot of the ability, thus the relative intensity, of detected electrons leaving a sample from a certain depth, without inelastic scattering is shown in Figure 1.3. Assuming an IMFP of 6 nm and a set-up dependent take-off angle of the photoelectrons reaching the detector of ~30°, we get a probing depth (p) of 15 nm. Hence, 98% of the detected elastically scattered electrons originate from the uppermost 15 nm of the sample. For practical photoelectron spectroscopy applications, the typical photon energy range is from around 200 eV to 10 000 eV, and photoelectron E_{kin} from 100 to several thousands eV. This means that p may be varied from just a few to a few tens of nm. Given the scales at the ice surface, this nicely coincides with the range of thicknesses discussed for the DI. The X-ray

penetrates about 80 times deeper into the ice.
By varying $\mathbf{h\nu}$, thus E_{kin} and the IMFP of the photoelectrons of a given corelevel, p can be varied and integrated concentration depth profiles can be obtained. A further non-destructive analysis method to analyze concentration depth profiles in ice is Rutherford Backscattering (RBS) (Krieger et al. (2002)). However, in contrary to synchrotron based XPS, it is not chemically selective. Thus, analyses of the profiles of molecular HCl and dissociated HCl, as demonstrated in Chapter 5, is not possible using RBS.

What do I look at? XPS enables me to quantify the amount of gases taken-up by the ice as well as analyze its chemical state, thus focusing on the question: *What is the surface coverage of the trace gas on the ice? Does dissociation or other reactions take place?*
Using synchrotron based XPS, implying X-rays with different photon energies, I was able to measure concentration profiles of trace gases in ice samples, giving answer to: *Where are trace gases located in ice? Do they penetrate into the ice or only adsorb to the ice surface?*

An example of a typical XPS analysis is shown in Figure 1.5. A typical Cl 1s XPS

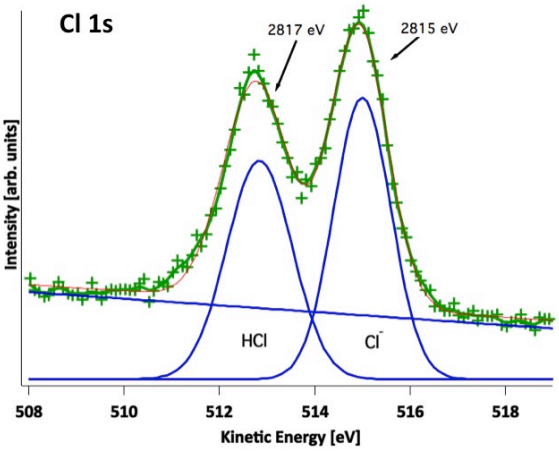

Figure 1.5: Cl1s XPS spectrum of HCl on ice at 253 K measured at a photon energy of 3325 eV, thus a resulting kinetic energy around 515 eV.

spectrum of 10^{-6} mbar HCl interacting with ice is displayed. The spectrum was acquired at $\mathbf{h\nu}$ 3325 eV, using a E_{kin} window from 509-519 eV. It clearly shows 2 peaks. The two peaks can be assigned to molecular HCl and deprontonated Cl−,

with respective E_{bind} of 2817 and 2815 eV. This spectrum reveals that for this HCl partial pressure not only molecular HCl is present on the ice surface, but that dissociation of HCl has occurred (for more details see Chapter 5).

1.5.2 Near edge absorption finestructure spectroscopy – NEXAFS

What is NEXAFS – How does it work? NEXAFS was developed in the mid 1980s. Its aim is to resolve the (chemical) structure of molecule bonds. It directly probes density and orientation of unoccupied electronic states of lowest molecular orbitals, thus structural and chemical properties, and provides element specific information about inter-atomic distances and bonding geometries of materials.
During NEXAFS measurements, the sample is irradiated with monochromatic X-rays. The energy of the X-rays is varied around an ionization edge of a given core level. This absorption step results from the excitation of core electrons to the continuum. Around the ionization threshold, resonant transitions occur. Such transitions arise if the energy of the incoming X-ray exactly matches the energy difference between the initial state and an unoccupied state, typically in the outermost molecular orbitals. The character of these states depends on the chemical environment (e.g. neighbors, bond lengths, and angles), which results in specific patterns of a NEXAFS spectrum. For example, molecules with double and triple bonds show a 1s to π^* transition resonance below the ionization potential.
The intensities of the transitions vary with the orientation of the electric field vector of the incoming X-ray, thus the polarization, relative to the orientation of the molecule. The intensity is highest when the electric field vector lies along the direction of the final states molecular orbital (Haehner (2006)).
The core hole resulting from the excitation of the core electrons, core hole, is filled either via the Auger effect, as displayed in Figure 1.2, or by electron capture resulting in a fluorescence photon that is detected. Using the Auger effect an Auger electron is detected. For heavy elements, fluorescence is the dominant process, whereas in light elements core hole relaxation occurs mostly via Auger electron emission. However, both processes directly measure the existence of a core hole created by X-ray absorption. Since relevant valence to core level binding energy differences for many important elements range around a few hundred eV, Auger electrons have E_{kin} of typically a few hundred eV, leading to an IMFP in the lower nm range. This makes Auger yield NEXAFS a surface sensitive technique. Since

Auger peaks are relatively broad features as visible in Figure 1.4, in Auger yield NEXAFS the electron yield over part or the whole Auger peaks (a E_{kin} range) is measured as a function of the incident $\mathbf{h\nu}$.

What do I look at? I primarily use Auger yield oxygen (O) K-edge NEXAFS measurements to examine changes of the hydrogen-bonding network of the ice surface due to exposure to gases. Additionally, information about interaction configurations of trace gases on/in ice can be derived.
The shallow probing depth of ~6 nm, resulting from electrons have a E_{kin} of around 500 eV for measurements of the O K-edge Auger, enables surface sensitive analysis. However, we get information about greater depths than, for example, MD simulations. In addition, NEXAFS makes no *a priori* assumption about the phase and properties of the DI, but can distinguish between liquid water and ice. These make NEXAFS a powerful technique for ice–trace gas interaction experiments and helps to answer: (Myneni et al. (2002), Bluhm et al. (2002), Nilsson et al. (2010)).
Does/can the interaction with (acidic) trace gases lead to a changed ice surface?

To measure an O K-edge NEXAFS spectrum, the energy of the incoming X-ray is varied around the O K-edge from 525-560 eV and the summed intensity of the emitted Auger electrons close to the ionization edge is analyzed. In Figure 1.6, typical ice and water NEXAFS spectra measured by Bluhm et al. (2002) are shown. Features around 532.5 eV $\mathbf{h\nu}$ (I) can be assigned to residual adsorbed oxygen in nitrate or carboxyls/carbonyl contamination of the ice sample. The pre-edge peak at 535 eV (A) originates from the transition of O1s core level electrons to empty states derived from the $4a_1$ lowest unoccupied molecular orbitals. Due to the dipole selection rule, the intensity of this peak depends on the degree of s or p character of the molecular orbitals.
In ice, oxygen molecules are tetrahedrally coordinated, resulting in mainly s-type orbitals due to symmetry arguments, thus having a low excitation probability. If the symmetry is broken, p character is more probable, leading to an increase in intensity due to the higher excitation probability. For the energy range from 537-545 eV (B), distinct features showing the difference between water and ice NEXAFS can be observed. The NEXAFS spectrum of ice shows a distinct double-peak structure, whereas liquid water exhibits a changed peak ratio. In this region, the pronounced peak at ~542 eV for ice can be assigned to the more strongly H-bonded

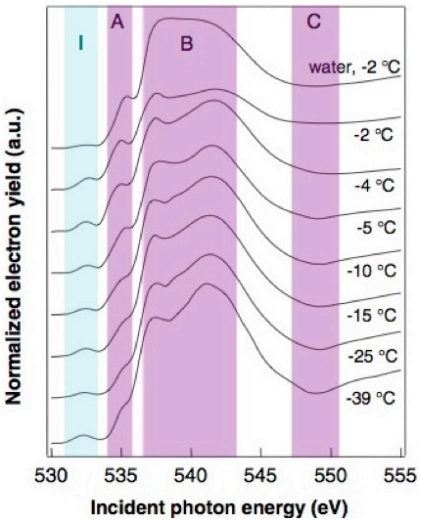

Figure 1.6: Oxygen K-edge Auger yield NEXAFS spectrum of liquid water and ice at different temperatures.
Most pronounced differences can be observed in the pre-edge region (A), as well as regions B and C. (modified from Bluhm et al. (2002))

OH groups. For the tetrahedrally coordinated water molecules in ice, both OH groups are coordinated with neighboring water molecules, thus are more strongly bound. In region C, a dip can be observed for cold ice temperatures, indicating a strongly ordered surface.

Using ambient pressure XPS and NEXAFS, I analyze interactions between ice and trace gases. During my work, I focused on the questions: *Where are trace gases located in ice? (What) makes interactions reversible? Does dissociation take place? Can/Does the interaction with (acidic) trace gases lead to changes of the ice surface? Does the acidity of the trace gas play a role?*
This work aims to answer these questions, contributing to an improved understanding of ice – trace gas interactions important for atmosphere and climate research.

Bibliography

Abbatt, J. P. D., Beyer, K. D., Fucaloro, A. F., McMahon, J. R., Wooldridge, P. J., Zhang, R., Molina, M. J.: Interaction of HCl vapor with water–ice: Implications for the stratosphere. *Journal of Geophysical Research: Atmospheres*, **97(D14)**, 15819-15826, 1992.

Abbatt, J. P.:Interactions of atmospheric trace gases with ice surfaces: Adsorption and reaction. *Chemical reviews*, **103(12)**, 4783-4800, 2003.

Abbatt, J. P. D., Bartels-Rausch, T., Ullerstam, M., Ye, T. J.: Uptake of acetone, ethanol and benzene to snow and ice: effects of surface area and temperature. *Environmental Research Letters*, **3(4)**, 045008, 2008.

Ackermann, M. D., Pedersen, T. M., Hendriksen, B. L. M., Robach, O., Bobaru, S. C., Popa, I., Quiros, C., Kim, H., Hammer, B., Ferrer, S., Frenken, J. W. M.: Structure and reactivity of surface oxides on Pt (110) during catalytic CO oxidation. *Physical review letters*, **95(25)**, 255505, 2005.

Assessment, AMAP AMAP: "Human health in the Arctic." *Oslo, Norway: Arctic Monitoring and Assessment Programme*, **254**, 2009.

Ammann, M., Cox, R. A., Crowley, J. N., Jenkin, M. E., Mellouki, A., Rossi, M. J., Troe, J., Wallington, T. J.: Evaluated kinetic and photochemical data for atmospheric chemistry: Volume VI - heterogeneous reactions with liquid substrates. *Atmos. Chem. Phys*, **13**, 8045–8228, 2013.

Barone, S. B., Zondlo, M. A., Tolbert, M. A.: Investigation of the heterogeneous reactivity of HCl, HBr, and HI on ice surfaces. *The Journal of Physical Chemistry A*, **103(48)**, 9717-9730,

1999.

Barrie, L. A., Bottenheim, J. W., Schnell, R. C., Crutzen, P. J., Rasmussen, R. A.: Ozone destruction and photochemical reactions at polar sunrise in the lower Arctic atmosphere. *Nature*, **334**, 138-141, 1988.

Bartels, T., Eichler, B., Zimmermann, P., Gäggeler, H. W., Ammann, M.: The adsorption of nitrogen oxides on crystalline ice. *Atmospheric Chemistry and Physics*, **2(3)**, 235-247, 2002.

Bartels-Rausch, T., Bergeron, V., Cartwright, J. H., Escribano, R., Finney, J. L., Grothe, H., Gutierrez, P., J., Haapala, J., Kuhs, W. F., Pettersson, J. B. C., Price, S. D., Sainz-Diaz, C. I., Stokes, D. J., Strazzulla, G., Thomson, E., S., Trinks, H., Uras-Aytemiz, N.: Ice structures, patterns, and processes: A view across the icefields. *Reviews of Modern Physics*, **84(2)**, 885, 2012.

Bartels-Rausch, T., Jacobi, H. W., Kahan, T. F., Thomas, J. L., Thomson, E. S., Abbatt, J. P. D., Ammann, M., Blackford, J. R., Bluhm, H., Boxe, C., Domine, F., Frey, M. M., Gladich, I., Guzmán, M. I., Heger, D., Huthwelker, Th., Klán, P., Kuhs, W. F., Kuo, M. H., Maus, S., Moussa, S. G., McNeill, V. F., Newberg, J. T., Pettersson, J. B. C., Roeselová, M., Sodeau, J. R.: A review of air-ice chemical and physical interactions (AICI): liquids, quasi-liquids, and solids in snow, *Atmos. Chem. Phys.*, **14**, 1587–1633, 2014.

Bluhm, H., Salmeron, M.: Growth of nanometer thin ice films from water vapor studied using scanning polarization force microscopy. *The Journal of chemical physics*, **111(15)**, 6947-6954, 1999.

Bluhm, H., Ogletree, D. F., Fadley, C. S., Hussain, Z., Salmeron, M.: The premelting of ice studied with photoelectron spectroscopy. *Journal of Physics: Condensed Matter*, **14(8)**, L227, 2002.

Bluhm, H.: Photoelectron spectroscopy of surfaces under humid conditions. *Journal of Electron Spectroscopy and Related Phenomena*, **177(2)**, 71-84, 2010.

Borrmann, S., Solomon, S., Avallone, L., Toohey, D., Baumgardner, D.: On the occurrence of ClO in cirrus clouds and volcanic aerosol in the tropopause region.*Geophysical research letters*, **24(16)**, 2011-2014, 1997.

Chen, G., Huey, L. G., Crawford, J. H., Olson, J. R., Hutterli, M. A., Sjostedt, S., Tanner, D., Dibb, J., Lefer, B., Blake, N., Davis, D., Stohl, A.: An assessment of the polar HOx photochemical budget based on 2003 Summit Greenland field observations. *Atmospheric Environment*, **41**, 7806-7820, 2007.

Compoint, M., Toubin, C., Picaud, S., Hoang, P. N. M., Girardet, C.: Geometry and dynamics of formic and acetic acids adsorbed on ice. *Chemical physics letters*, **365(1)**, 1-7, 2002.

Crowley, J. N., Ammann, M., Cox, R. A., Hynes, R. G., Jenkin, M. E., Mellouki, A., Rossi, M. J., Troe, J., Wallington, T. J.: Evaluated kinetic and photochemical data for atmospheric chem-

istry: Volume V–heterogeneous reactions on solid substrates. *Atmospheric Chemistry and Physics*, **10(18)**, 9059-9223, 2010.

Darvas, M., Lasne, J., Laffon, C., Parent, P., Picaud, S., Jedlovszky, P.: Adsorption of acetaldehyde on ice as seen from computer simulation and infrared spectroscopy measurements. Langmuir : *the ACS journal of surfaces and colloids*, **28**, 4198-207.

Dash, J. G., Fu, H., Wettlaufer, J. S.:The premelting of ice and its environmental consequences. *Reports on Progress in Physics*, **58(1)**, 115, 1995.

Dash, J. G., Rempel, A. W., Wettlaufer, J. S.: The physics of premelted ice and its geophysical consequences. *Reviews of modern physics*, **78(3)**, 695, 2006.

De Angelis, M., and M. Legrand: Origins and variations of fluoride in Greenland precipitation. *Journal of Geophysical Research* **Atmospheres 99(D1)**, 1157-1172, 1994.

Dominé, F., Shepson, P. B.: Air-snow interactions and atmospheric chemistry. *Science*, **297(5586)**, 1506-1510, 2002.

Dosch, H., Lied, A., Bilgram, J. H.: Glancing-angle X-ray scattering studies of the premelting of ice surfaces. *Surface science*, **327(1-2)**, 145-164, 1995.

Döppenschmidt, A., Butt, H. J.: Measuring the thickness of the liquid-like layer on ice surfaces with atomic force microscopy. *Langmuir*, **16(16)**, 6709-6714,2000.

Elbaum, M., Lipson, S. G., Dash, J. G.: Optical study of surface melting on ice. *Journal of crystal growth*, **129(3)**, 491-505, 1993.

El Zein, A., Bedjanian, Y.: Reactive uptake of HONO to TiO2 surface:“dark” reaction. *The Journal of Physical Chemistry A*, **116(14)**, 3665-3672, 2012.

Falicov, L. M., Somorjai, G. A.: Correlation between catalytic activity and bonding and coordination number of atoms and molecules on transition metal surfaces: Theory and experimental evidence. *Proceedings of the National Academy of Sciences*, **82(8)**, 2207-2211, 1985.

Faraday, M.: Letter to *Phil. Mag*, **17**, 162, 1840.

Finlayson-Pitts, B. J.; Pitts, J. N.: Chemistry of the Upper and Lower Atmosphere: Theory, Experiments, and Applications; *Academic Press: San Diego*, 2000.

Golecki, I., Jaccard, C.: Intrinsic surface disorder in ice near the melting point. *Journal of Physics C: Solid state physics*, **11(20)**, 4229, 1978.

Gross, G. W.: Some effects of trace inorganics on the ice/water system. *Adv. Chem. Ser.*, **73**, 27–97, 1967.

Grannas, A. M., Jones, A. E., Dibb, J., Ammann, M., Anastasio, C., Beine, H. J., Bergin, M., Bottenhem, J, Boxe, C. S., Carver, G., Crawford, J. H., Domine, F., Frey, M. M., Guz-

man, M. I., Heared, D. E., Helmig, D. Hoffmann, M. R., Honrath, R. E., Huey, L. G., Hutterli, M., Jacobi, H. W., Klan, P., Lefer, B., McConnel, J., Plane, J., Sander, R., Savarino, J., Shepson, P. B., Simpson, W. R., Sodeau, J. R., von Glasow, R., Weller, R., Wolff, E. W., Zhu, T., Chen, G.: An overview of snow photochemistry: evidence, mechanisms and impacts. *Atmospheric Chemistry and Physics*, **7(16)**, 4329-4373, 2007.

Haehner, G.: Near edge X-ray absorption fine structure spectroscopy as a tool to probe electronic and structural properties of thin organic films and liquids. *Chemical Society Reviews*, **35(12)**, 1244-1255, 2006.

Hantal, G., Jedlovszky, P., Hoang, P. N. M., Picaud, S.: Calculation of the Adsorption Isotherm of Formaldehyde on Ice by Grand Canonical Monte Carlo Simulation. *Journal of Physical Chemistry C*, **111**, 14170-14178, 2007.

Huefner, J: Photoelectron Spectroscopy. *Chemical Physics Letters*, **315(1)**, 7-11, 1999.

Huse, N., Wen, H., Nordlund, D., Szilagyi, E., Daranciang, D., Miller, T. A., Nilsson, A., Schoenlein, R. N., Lindenberg, A. M.: Probing the hydrogen-bond network of water via time-resolved soft x-ray spectroscopy. *Physical Chemistry Chemical Physics*, **11(20)**, 3951-3957, 2009.

Huthwelker, T., Ammann, M., Peter, T.: The uptake of acidic gases on ice. *Chem. Rev.*, **106**, 1375-1444, 2006.

Hynes, R. G., Mössinger, J. C., Cox, R. A.: The interaction of HCl with water-ice at tropospheric temperatures. *Geophysical research letters*, **28(14)**, 2827-2830, 2001.

Jacob, D. J.: Chemistry of OH in remote clouds and its role in the production of formic acid and peroxymonosulfate. *Journal of Geophysical Research: Atmospheres*, **91(D9)**, 9807-9826, 1986.

Jacob, D. J., Wofsy, S. C.: Photochemistry of biogenic emissions over the Amazon forest. *Journal of Geophysical Research: Atmospheres*, **93(D2)**, 1477-1486, 1988.

Jacobi, H. W., Bales, R. C., Honrath, R. E., Peterson, M. C., Dibb, J. E., Swanson, A. L., Albert, M. R.: Reactive trace gases measured in the interstitial air of surface snow at Summit, Greenland. *Atmospheric Environment*, **38(12)**, 1687-1697, 2004.

Jedlovszky, P., Hantal, G., Neuróhr, K., Picaud, S., Hoang, P. N., Hessberg, P. V., Crowley, J. N.: Adsorption isotherm of formic acid on the surface of ice, as seen from experiments and grand canonical Monte Carlo simulation. *The Journal of Physical Chemistry C*, **112(24)**, 8976-8987, 2008.

Kärcher, B.: Simulating gas-aerosol-cirrus interactions: Process-oriented microphysical model and applications. *Atmospheric Chemistry and Physics*, **3(5)**, 1645-1664, 2003.

Kahan, T. F., Reid, J. P., Donaldson, D. J.: Spectroscopic probes of the quasi-liquid layer on ice. *The Journal of Physical Chemistry A*, **111(43)**, 11006-11012, 2007.

Kahan, T. F., Donaldson, D. J.: Benzene photolysis on ice: Implications for the fate of organic contaminants in the winter. *Environmental science & technology*, **44(10)**, 3819-3824,2010.

Kerbrat, M., Huthwelker, T., Gäggeler, H. W., Ammann, M.: Interaction of nitrous acid with polycrystalline ice: Adsorption on the surface and diffusion into the bulk. *The Journal of Physical Chemistry C*, **114(5)**, 2208-2219, 2010.

Kong, X., Papagiannakopoulos, P., Thomson, E. S., Markovic, N., Pettersson, J. B.: Water accommodation and desorption kinetics on ice. *The Journal of Physical Chemistry A*, **118(22)**, 3973-3979, 2014.

Křepelová, A., Huthwelker, T., Bluhm, H., Ammann, M.: Surface chemical properties of eutectic and frozen NaCl solutions probed by XPS and NEXAFS. *ChemPhysChem*, **11(18)**, 3859-3866, 2010.

Křepelová, A., Bartels-Rausch, T., Brown, M. A., Bluhm, H., Ammann, M.: Adsorption of acetic acid on ice studied by ambient pressure XPS and partial-electron-yield NEXAFS spectroscopy at 230–240 K. *J Phys Chem A*, **117**, 401-409, 2012.

Krieger, U. K., Huthwelker, T., Daniel, C., Weers, U., Peter, T., Lanford, W. A.: Rutherford backscattering to study the near-surface region of volatile liquids and solids. *Science*, **295(5557)**, 1048-1050, 2002.

Kuo, M.-H.: Trace Gas-Induced Brine and Disordered Interfacial Layers on Ice. *PhD Thesis*, Columbia University, 2013.

Lary, D. J., Shallcross, D. E.: Central role of carbonyl compounds in atmospheric chemistry. *Journal of Geophysical Research 2000*, **105**, 19771, 2000.

Lee, S. H., Leard, D. C., Zhang, R., Molina, L. T., Molina, M. J.: The HCl+ ClONO2 reaction rate on various water ice surfaces. *Chemical Physics Letters*, **315(1)**, 7-11, 1999.

Leu, M. T.: Heterogeneous reactions of N2O5 with H2O and HCl on ice surfaces: Implications for Antarctic ozone depletion. *Geophysical research letters*, **15(8)**, 851-854, 1988.

Lu, H., McCartney, S. A., Sadtchenko, V.: H/D exchange kinetics in pure and HCl doped polycrystalline ice at temperatures near its melting point: Structure, chemical transport, and phase transitions at grain boundaries. *The Journal of chemical physics*, **130(5)**, 054501, 2009.

McNeill, V. F., Loerting, T., Geiger, F. M., Trout, B. L., Molina, M. J.: Hydrogen chloride-induced surface disordering on ice. *Proceedings of the National Academy of Sciences*, **103(25)**, 9422-9427, 2006.

Mellenthin, J., Karma, A., Plapp, M.: Phase-field crystal study of grain-boundary premelting. *Physical Review B*, **78(18)**, 184110, 2008.

Miles, R. E., Reid, J. P., Riipinen, I.: Comparison of approaches for measuring the mass accommodation coefficient for the condensation of water and sensitivities to uncertainties in

thermophysical properties. *The Journal of Physical Chemistry A*, **116(44)**, 10810-10825, 2012.

Millet, D. B., Baasandorj, M., Farmer, D. K., Thornton, J. A., Baumann, K., Brophy, P.,S. Chaliyakunnel, J. A., de Gouw, M., Graus, L., Hu, A., Koss, B. H., Lee, F. D., Lopez-Hilfiker, J. A., Neuman, F., Paulot, J., Peischl, I. B., Pollack, T. B., Ryerson, C., Warneke, B. J., Williams, and J. Xu: A large and ubiquitous source of atmospheric formic acid. *Atmospheric Chemistry and Physics*, **15(11)**, 6283-6304, 2015.

Molina, M. J., Tso, T. L., Molina, L. T., Wang, F. C. Y.: Antarctic stratospheric chemistry of chlorine nitrate, hydrogen chloride, and ice: Release of active chlorine. *Science*, **238(4831)**, 1253-1257, 1987.

Molina, M. J., Molina, L. T., Kolb, C. E.: Gas-phase and heterogeneous chemical kinetics of the troposphere and stratosphere. *Annual Review of Physical Chemistry*, **47(1)**, 327-367, 1996.

Monks, P. S.: Gas-phase radical chemistry in the troposphere. *Chemical Society Reviews*, **34(5)**, 376-395, 2005.

Myneni, S., Luo, Y., Cavalleri, M., Ogasawara, H., Pelmenschikov, A., Wernet, P., Vaterlein, P., Heske, C., Hussain, L., Pettersson, L. G. M., Nilsson, A.: Spectroscopic probing of local hydrogen-bonding structures in liquid water. *Journal of Physics: Condensed Matter*, **14(8)**, L213, 2002.

Nenow, D., Trayanov, A.: Surface premelting phenomena. *Surface Science*, **213(2)**, 488-501, 1989.

Newberg, J. T., Bluhm, H.: Adsorption of 2-propanol on ice probed by ambient pressure X-ray photoelectron spectroscopy.*Physical Chemistry Chemical Physics*, **17(36)**, 23554-23558, 2015.

Nordling, C., Sokolowski, E., Siegbahn, K.: Precision method for obtaining absolute values of atomic binding energies. *Physical Review*, **105(5)**, 1676, 1957.

Nilsson, A., Nordlund, D., Waluyo, I., Huang, N., Ogasawara, H., Kaya, S., Bergmann, U., Naeslund, L.-A., Oestroem, H., Wernert, Ph., Andersson, K. J., Schiros, T., Pettersson, L. G. M.: X-ray absorption spectroscopy and X-ray Raman scattering of water and ice; an experimental view. *Journal of Electron Spectroscopy and Related Phenomena*, **177(2)**, 99-129, 2010.

Ohmura, A., Wild, M., Bengtsson, L.: A possible change in mass balance of Greenland and Antarctic ice sheets in the coming century. *Journal of Climate*, **9(9)**, 2124-2135, 1996.

Orem, M. W., Adamson, A. W. (1969): Physical adsorption of vapor on ice: II. n-alkanes. *Journal of Colloid and Interface Science*, **31(2)**, 278-286, 1969.

Parent, P., Laffon, C., Mangeney, C., Bournel, F., Tronc, M.: Structure of the water ice surface studied by x-ray absorption spectroscopy at the O K-edge. *The Journal of chemical physics*, **117(23)**, 10842-10851, 2002.

Parent, P., Lasne, J., Marcotte, G., Laffon, C.: HCl adsorption on ice at low temperature: a combined X-ray absorption, photoemission and infrared study. *Physical Chemistry Chemical Physics*, **13(15)**, 7142-7148, 2011.

Pasteur, E. C., Mulvaney, R.: Migration of methane sulphonate in Antarctic firn and ice. *Journal of geophysical research*, **105(D9)**, 11525-11534, 2000.

Petitjean, M., Mirabel, P., Le Calv, S.: Uptake measurements of acetaldehyde on solid ice surfaces and on solid/liquid supercooled mixtures doped with HNO3 in the temperature range 203-253 K. *The journal of physical chemistry. A*, **113**, 50918, 2009.

Pfalzgraff, W., Neshyba, S., Roeselova, M.: Comparative molecular dynamics study of vapor-exposed basal, prismatic, and pyramidal surfaces of ice. *The Journal of Physical Chemistry A*, **115(23)**, 6184-6193, 2011.

Platt, U., Hönninger, G.: The role of halogen species in the troposphere. *Chemosphere*, **52(2)**, 325-338, 2003.

Pratte, P., van den Bergh, H., Rossi, M. J.: The kinetics of H2O vapor condensation and evaporation on different types of ice in the range 130− 210 K. *The Journal of Physical Chemistry A*, **110(9)**, 3042-3058, 2006.

Robinson, D. A., Dewey, K. F.,Heim Jr, R. R.: Global snow cover monitoring: An update. *Bulletin of the American Meteorological Society*, **74(9)**, 1689-1696, 1993.

Salmeron, M., Schlögl, R.: Ambient pressure photoelectron spectroscopy: A new tool for surface science and nanotechnology. *Surface Science Reports*, **63(4)**, 169-199, 2008.

Sazaki, G., Zepeda, S., Nakatsubo, S., Yokomine, M., Furukawa, Y.: Quasi-liquid layers on ice crystal surfaces are made up of two different phases. *Proceedings of the National Academy of Sciences*, **109(4)**, 1052-1055, 2012.

Schneebeli, M., Sokratov, S. A.: Tomography of temperature gradient metamorphism of snow and associated changes in heat conductivity. *Hydrological Processes*, **18(18)**, 3655-3665, 2004.

Shepherd, T. D., Koc, M. A., Molinero, V.: The quasi-liquid layer of ice under conditions of methane clathrate formation. *The Journal of Physical Chemistry C*, **116(22)**, 12172-12180, 2012.

Solomon, S., Borrmann, S., Garcia, R. R., Portmann, R., Thomason, L., Poole, L. R., Winker, D., McCormick, M. P.: Heterogeneous chlorine chemistry in the tropopause region. *Journal of Geophysical Research: Atmospheres*, **102(D17)**, 21411-21429, 1997.

Somorjai, G. A., Li, Y.: Introduction to surface chemistry and catalysis. *John Wiley & Sons*, **2**, 417-425, 2010.

Starr, D. E., Pan, D., Newberg, J. T., Ammann, M., Wang, E. G., Michaelides, A., Bluhm, H.: Acetone adsorption on ice investigated by X-ray spectroscopy and density functional theory.

Physical Chemistry Chemical Physics, **13(44)**, 19988-19996, 2011.

Toubin, C., Picaud, S., Hoang, P. N. M., Girardet, C., Demirdjian, B., Ferry, D., Suzanne, J.: Dynamics of ice layers deposited on MgO (001): Quasielastic neutron scattering experiments and molecular dynamics simulations. emphThe Journal of Chemical Physics, **114(14)**, 6371-6381, 2001.

Ullerstam, M., Thornberry, T., Abbatt, J. P.: Uptake of gas-phase nitric acid to ice at low partial pressures: evidence for unsaturated surface coverage. *Faraday discussions*, **130**, 211-226, 2005.

Vierkorn-Rudolph, B., Bächmann, K., Schwarz, B., Meixner, F. X.: Vertical profiles of hydrogen chloride in the troposphere. *Journal of atmospheric chemistry*, **2(1)**, 47-63, 1984.

Voigt, C., Kärcher, B., Schlager, H., Schiller, C., Krämer, M., Reus, M. D., Vossing, H., Borrmann, S., Mitev, V.: In-situ observations and modeling of small nitric acid-containing ice crystals. *Atmospheric Chemistry and Physics*, **7(12)**, 3373-3383, 2007.

Watson, R. T., Albritton, D. L.: Climate change 2001: Synthesis report: Third assessment report of the Intergovernmental Panel on Climate Change. *Cambridge University Press.*, 2001.

Wei, X., Miranda, P. B., Zhang, C., Shen, Y. R.: Sum-frequency spectroscopic studies of ice interfaces. *Physical Review B*, **66(8)**, 085401, 2002.

Wettlaufer, J. S.: Ice surfaces: macroscopic effects of microscopic structure. *Philosophical Transactions of the Royal Society of London A: Mathematical, Physical and Engineering Sciences*, **357(1763)**, 3403-3425, 1999.

Yang, J., Honrath, R. E., Peterson, M. C., Dibb, J. E., Sumner, A. L., Shepson, P. B., Frey, M., Jacobi, H.-W., Swanson, A., Blake, N.: Impacts of snowpack emissions on deduced levels of OH and peroxy radicals at Summit, Greenland. *Atmospheric Environment*, **36**, 2523-2534, 2002.

Zimmermann, S., Kippenberger, M., Schuster, G., Crowley, J. N.: Adsorption isotherms for hydrogen chloride (HCl) on ice surfaces between 190 and 220 K. *Physical Chemistry Chemical Physics*, **18(20)**, 13799-13810, 2016.

CHAPTER 2

The near ambient pressure photoemission endstation at SLS

2.1 The environmental photochemistry of oxide surfaces and the nature of frozen salt solutions: A new in situ XPS approach

Published as: Orlando, F., Waldner, A., Bartels-Rausch, T., Birrer, M., Lee, M., Proff, C., Huthwelker, T., Kleibert, A., Bokhoven, J., and Ammann, M.: The environmental photochemistry of oxide surfaces and the nature of frozen salt solutions: A new in situ XPS approach, *Topics in Catalysis*, **8**, 1-14, 2016.

I actively participated in all analyses described below, actively contributed to the commissioning and improvement of the chamber system and the cryo-stage. Furthermore I developed procedures for growing ice and was main responsible for the development of the dosing system

2.1.1 Abstract

Recent years have witnessed fast advancements in near ambient pressure X-ray photoelectron (NAPP) spectroscopy, which is emerging as a powerful tool for the investigation of surfaces in presence of vapors and liquids. In this paper we present a new chamber for the investigation of solid/vapor interfaces relevant to environmental and atmospheric chemistry that fits to the NAPP endstation at the Swiss Light Source. The new chamber allows for performing X-ray photoelectron spectroscopy (XPS) and electron yield near-edge X-ray absorption fine structure spectroscopy (NEXAFS) using soft, tender and hard X-ray in vacuum and in near-ambient pressures up to 20 mbar at environmentally relevant conditions of temperature and relative humidity. In addition, the flow tube design of the chamber enables the dosing of sticky reactive gases with short pressure equilibration time. The accessible photoelectron kinetic energy ranges from 2 to 7000 eV. This range allows the determination of surface and bulk electronic properties of ice and other environmental materials, such as metal oxides and frozen solutions, which are relevant to understanding atmospheric chemistry. The design of this instrument and first results on systems of great interest to the environmental and atmospheric chemistry community are presented. In particular, near-ambient pressure XPS and NEXAFS, coupled to a UV-laser set-up, were used to study the adsorption of water on a TiO_2 powder sample. The results are in line with previously proposed adsorption models of water on TiO_2, and, furthermore, indicate that the concentration of water molecules tends to increase upon UV irradiation. In a second example we illustrate how NEXAFS spectroscopy measurements at the chlorine K-edge can provide new insight on the structures of eutectic and sub-eutectic frozen NaCl solutions at high and low relative humidity, respectively, indicating the formation of solution and solid NaCl phases, respectively. Finally, we demonstrate the assets of this new chamber for the dosing of sticky acidic gases and, in particular, for the investigation of formic acid uptake on ice surfaces.

2.1.2 Introduction

Since its development between 1950 and 1960 by K.Siegbahn, X-ray photoelectron spectroscopy (XPS) has been successfully employed in a number of scientific fields, including heterogeneous catalysis, materials science or semiconductor technology, just to name a few. However, the pressure limitations imposed by the electron

energy analyzer, which must be kept under high vacuum conditions, and by the short inelastic mean free path (IMFP) of the photoelectrons at elevated pressure has traditionally restricted the application of this technique mainly to solid/vacuum interfaces, with some pioneering exceptions [1–3]. This also explains why, despite XPS being one of the most powerful and widely used surface science characterization tools, the potential of this technique has not been fully exploited for practical systems and samples in operating conditions. A crucial step forward in this direction has been made via the development of differentially-pumped electrostatic lenses [4], which has greatly improved the transmission of photoelectrons through the analyzer, thus allowing for XPS measurements performed close to ambient pressure, better known as near ambient pressure photoelectron spectroscopy (NAPP). The fast development of NAPP in the last years [5–10] has benefited from the advent of 3rd generation synchrotron radiation sources, with the brilliant and focused beams of which electron scattering losses in the gas phase could be counteracted, resulting in NAPP measurements with an improved signal-to-noise ratio.

The possibility to bridge, at least partially, the so-called ‘‘pressure-gap’’ between ultra-high vacuum (UHV) and catalytic operating conditions [11] has extended the range of applicability of XPS characterization to solid/liquid and solid/vapor interfaces. This has opened the door to a broader scientific audience, especially in electrochemistry [12], environmental chemistry [13] and heterogeneous catalysis [10]. In particular, environmental science is one of the disciplines that has seen some of the early applications of NAPP [14] and still offers tremendous further opportunities. Indeed, not only chemical reactions in the atmosphere take place under humid conditions, but water vapor is frequently one of the main reactants, e.g., in hydrolysis reactions. Water is present on solid surfaces at ambient conditions, forming several molecular layers at room temperature [15, 16]. Water in the form of ice is also a predominant material in some parts of the Earth, as snowpack or sea-ice, and in the atmosphere, in the form of ice particles. Chemical reactions at air–ice interfaces of snow or sea–ice, where the exchange of major and trace gases occurs, drive large-scale environmental effects such as ozone depletion events in Polar areas, and modify the cycling of halogen gases, and of nitrogen oxides on a global scale [17–23]. These examples show how heterogeneous chemistry affects the oxidative capacity of the atmosphere. The latter can be affected also by photochemical processes, such as the photochemistry of nitrogen oxides on mineral oxide particles contained in atmospheric mineral dust plumes uplifted from arid

areas, which represents another important playground for atmospheric chemistry and climate science. So far, only few experiments have attempted to probe surface species on, e.g., ice [24] or mineral oxides [25, 26] under atmospheric conditions. Indeed, the high water vapor pressure at environmentally relevant temperature (0.01–1 mbar) makes it difficult to use surface sensitive probes, thus pointing out the importance and potential of near ambient pressure XPS for environmental research.

Here we present a new chamber for the NAPP endstation [27] at the Swiss Light Source (SLS) designed for in situ XPS and electron yield near edge X-ray absorption fine structure spectroscopy (NEXAFS) at solid/vapor interfaces under environmentally relevant conditions of temperature and pressure. Compared to many NAPP systems, which consist of (relatively large) UHV chambers that are filled with vapors or gases up to the desired pressure in a nearly static regime, our chamber is designed as a compact flow tube cell surrounded by an external UHV environment. This layout enables to quickly shift between measurements at near ambient pressure and UHV conditions while at the same time reducing the exposed volume and surface area of the cell. In addition, it features a direct access from a gas dosing system down to the sample to allow admission of sticky gases. Following the concept originally conceived for the NAPP endstation of custom designed chambers dedicated to specific applications, the new chamber for solid samples can be exchanged with that dedicated to liquid microjet experiments described in Ref. [27]. The NAPP endstation, which covers an electron kinetic energy range of 2–7000 eV, can be operated at the SIM [28] and PHOENIX [29] beamlines at the Swiss Light Source (SLS) at the Paul Scherrer Institute (PSI) for experiments with soft and hard X-rays, respectively. The accessible photon energy range can be further extended by connecting a He discharge lamp, allowing for off-line ultraviolet photoelectron spectroscopy(UPS) measurements.

2.1.3 Experimental set-up

Figure 1 a shows a picture of the NAPP endstation with the new chamber for the investigation of solid/vapor interfaces. The schematic drawing of the whole assembly reported in Fig. 1 b illustrates the modular design of the NAPP endstation, which can accommodate either the chamber for solid samples (1) or the liquid microjet module [27] and enables flexible switching between these two operation

modes. The endstation is equipped with a Scienta R4000 HiPP-2 electron energy analyzer (200 mm mean radius) with variable entrance slit, coupled to a multi-channel plate (MCP) detector and a charge-coupled device (CCD) camera (2); the performance and design of this instrument are similar to those described in Ref. [7, 30]. The analyzer is mounted on a mobile frame allowing for movement in the x,y plane and in the z direction (3). In addition, the analyzer can rotate along the yaw, pitch and roll axes for fine alignment. All the movements are realized via commercially available stepper motors, with a resolution of 10 µm and 0.01 mrad for linear and rotational movements, respectively. These features ensure the flexibility required to operate the endstation at both SIM and PHOENIX beamlines at the SLS. The differential pumping on the electron lens and pre-lens (4), each fitted with three elements, allows XPS and electron yield NEXAFS measurements up to 20 mbar within an electron kinetic energy range from 2 to 7000 eV.

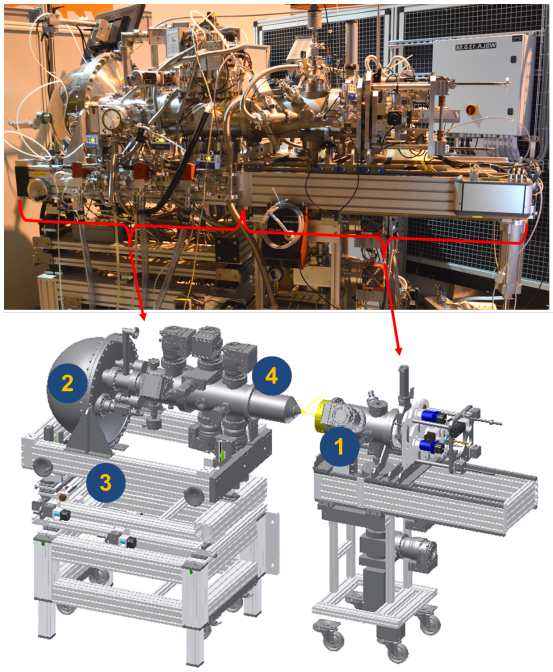

Figure 2.1: Picture of the new chamber for solid samples connected to the NAPP endstation. The endstation is mounted on a moveable frame to be attached to the SIM or to the PHOENIX beamline at PSI/SLS.
Schematic layout of the NAPP endstation with the R4000 HiPP-2 electron energy analyzer (left hand side) together with the new chamber (right hand side). See text for details

Shown in Figure 2 a is the schematic of the in situ cell together with the flow tube, which is 3 cm in diameter and has a length of 15 cm. In order to minimize the effect of external magnetic fields, a µ-metal shield covers the flow tube, the in situ cell and part of the sample manipulator. The flow tube and the in situ cell, which is pushed directly onto the analyzer nozzle, are surrounded by an external UHV environment (Fig. 2b), and the two are connected through a bypass: only the in situ cell is filled with vapors or gases, with the ultimate pressure limit depending on the diameter of the analyzer entrance cone (see below). After opening the bypass valve, a pressure drop from 1 mbar O_2 to below $5 \cdot 10^{-7}$ mbar in the sample region is achieved usually within less than 30 min. The possibility to quickly vary the pressure at the sample allows performing UHV and high pressure measurements one after the other in the same analysis cell. Compared to a standard XPS set-up, where the dosing of reactive gases is very difficult due to their interaction with the large surface of the analysis chamber and any other part associated with it (bellows, manipulators, etc.), our flow tube approach minimizes the internal surface and permits dosing sticky gases with reduced wall effects. This is possible thanks to the minimized surface area of only 140 cm^2 of the flow tube section between the exit of the gas dosing line (described below) and the sample. This feature distinguishes our chamber from all other set-ups dedicated to near ambient pressure XPS, even from those featuring smaller reaction chambers but longer gas admission lines through manipulator arms [8, 31]. At the present stage, the in situ cell and the flow tube are made of aluminum, but an upgrade to titanium is in order.

As shown in Fig. 2a, the X-ray beam enters the analysis chamber through a 1.5 mm x 1.5 mm x 100 nm thick Si_3N_4 window, which ensures vacuum protection to the beamline when working at high pressures (mbar range). Furthermore, physical separation between chamber and beamline also allows for using particularly corrosive gases. The impinging beam, the sample surface normal, and the analyzer axis lie in the same horizontal plane. The photon incident (Θ_{ph}) and the electron emission (Θ_e) angles are 60° and 30° from the sample surface normal, respectively, with the angle between the photon beam and the analyzer fixed at 90° (see the schematic illustration in Fig. 2a). The angle between the linear polarization vector and the electron emission axis can be varied between 0° and 90° both at SIM and PHOENIX beamlines. The distance between the Si_3N_4 window and the sample is 15 mm. The in situ cell is equipped with two viewports (Fig. 2b) on which a high-resolution endoscope and a wide-angle camera can be mounted. This allows for looking at the sample for alignment purposes, and for monitoring whether or

not its surface changes appearance with time during the experiment.

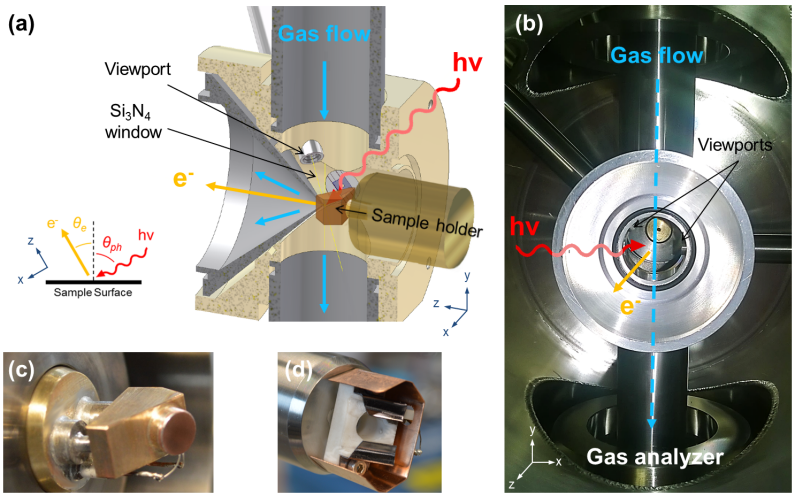

Figure 2.2: NAPP in situ cell set-up.
(a) Section view of the in situ cell together with the flow tube: the sample is in measurement position and the inlet and outlet tubes are shown together with the entrance cone of the electron spectrometer. A schematic of the measurement geometry is reported on the left side (see text for details).
(b) Picture of a view into the in situ cell, the flow tube and surrounding UHV chamber as seen from the electron analyzer.
(c) Liquid nitrogen cooled and
(d) IR-heated manipulators

The top part of the flow tube holds the dosing line. Gases and vapors, such as water, are mixed together before entering the flow tube. While gas flow is commonly controlled via leak valves, here, in addition, the vapor flow from volatile liquids is regulated by controlling the temperature of the liquid itself (and hence its vapor pressure) with a Peltier cell. More precisely, the flow rate is determined by the pressure difference along a capillary tube: one end is connected to the temperature-controlled reservoir of the liquid, while the other end is connected to the flow tube of the analysis cell. The reservoirs hold the liquid and its vapor, and are made of glass to minimize chemical reactions with, e.g., acidic liquids, or leaching promoted by these. The capillaries that transport the vapors to the flow tube with a diameter of 0.3–2.0 mm are made of stainless steel, while those with a diameter of 0.1–0.2 mm to dose acidic traces or other sticky gases are made of fused

silica. A typical length of the capillaries is 1 m. With such a dosing system attached to the flow tube, the surface area that the trace gas and vapors are exposed to increases to almost 600 cm^2, with a total volume of about 500 cm^3. Figure 3a highlights the flexibility of this approach for water and formic acid (HCOOH) dosing. For instance, by changing the water vapor pressure in the reservoir between 1 mbar and 15 mbar, reflecting temperatures of ice or water from 253 to 286 K, the pressure in the flow tube cell can be varied between 0.02 mbar and 1.4 mbar (blue dots). Partial pressures between 10^{-3} mbar and 10^{-1} mbar in the flow tube are realized with vapor pressures of formic acid in the dosing reservoir ranging from 8 to 50 mbar (pink dots). Figure 3 a further illustrates the high reproducibility of this dosing approach, as the individual data come from independent measurements. Figure 3b shows a selection of the formic acid dosing data. At time of 0 h the valve separating the formic acid reservoir at 265 K and the dosing capillary connecting with the analysis cell was opened. Then, in intervals of 30 to 60 min, the temperature of the formic acid in the reservoir was increased stepwise from 265 to 281 K to raise the vapor pressure at the inlet of the capillary (orange line). Whenever the temperature of the reservoir was changed, the valve connecting the reservoir and the capillary (the latter connected to the analysis cell) was closed and reopened once the pressure in the reservoir had stabilized. This explains the pressure drops in between the stepwise increases of the formic acid partial pressure in Fig. 3b. Generally, the data set illustrates the fast response time of the pressure in the reservoir to changes of the temperature and the stable formic acid pressure in the reservoir over hours. Even more, the pressure in the analysis cell shows a fast response of ~10 min to reach ~90 % of the final pressure; the last 10 % steadily and slightly increase over timescales of about an hour. This is a significant improvement in the response time compared to the standard NAPP set-ups, where response times of several hours were reported at comparable partial pressures of acetic acid [32]. For these measurements formic acid (98 %, Fluka 56302, stored at 252 K) was used and cleaned by freeze–pump–thaw cycles immediately before the dosing experiment.

A molecular beam sampling mass spectrometer (Hiden HPR-60) is mounted directly at the lower exit of the flow tube for quantitative analysis of the reactive gas species. Additionally, a quadrupole mass spectrometer is mounted at the second stage of the analyzer pre-lenses. The high pressure in the inner chamber is monitored by baratron capacitance manometers (MKS 626), while in all the other vacuum sections the pressures are probed by full range gauge sensors (Pfeiffer HPT-100). The pressure in the in situ cell is given by the inlet gas flow via the

capillaries or the leak valve and by the gas flow being pumped by the electron analyzer and the Hiden mass spectrometer. The outlet flow depends on the diameters of both mass spectrometer and electron energy analyzer orifices. The mass spectrometer is usually operated with an orifice of 0.4 mm diameter, while the electron analyzer either with 0.3 or 0.5 mm. A back-of-the-envelope calculation of the viscous and molecular flows via either of the orifices indicates that the in situ cell is typically operated at total flows between 20 ml/min at 10 mbar and 0.1 ml/min at 0.1 mbar total pressure in the in situ cell (volumetric flows at standard temperature and pressure (STP)). These rough calculations have been confirmed by measurements of the flows using mass flow controllers.

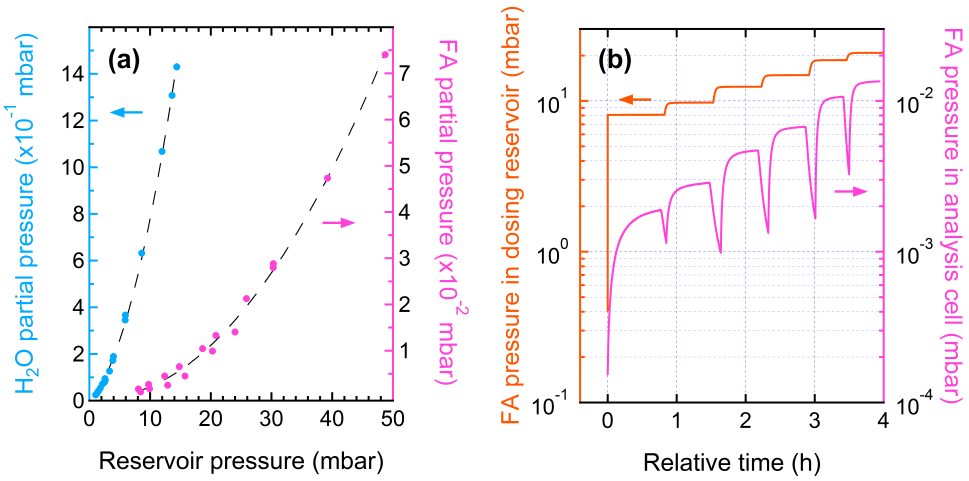

Figure 2.3: **(a)** Partial pressures of water (blue dots) and formic acid (pink dots) measured in the in situ cell as a function of the pressure measured in the reservoirs containing the corresponding liquid or frozen solid, respectively.
(b) Evolution of the formic acid pressure in the reservoir (orange line) and of the partial pressure of formic acid in the analysis cell (pink line) with time

Cooling and heating of samples are challenging task in a NAPP experiment. Indeed, when working with condensable gases, the manipulator sample surface has to be coldest point in the chamber, otherwise the gas will condense elsewhere. Also, traditional heating filaments, such as tungsten or platinum wires, cannot be used in oxidizing environments because they would either burn away or catalyze undesired reactions. To perform experiments with condensable gases a sample holder has been developed that is equipped with a liquid nitrogen cryostat (Fig. 2c). This

sample holder allows performing experiments at temperatures down to 160 K and, thus, to reach high relative humidity (RH) up to the water condensation point (100 % RH) at still reasonably low water partial pressure. This permits to address surface chemical composition at atmospherically relevant conditions. Thanks to the reduced temperature fluctuations below 0.2 K, ice samples can be grown on the cooled surface of this manipulator, as illustrated in the next section. In addition, this manipulator can also heat samples up to about 373 K by annealing the copper radiator serpentine with a heating plate. A second sample holder, equipped with an IR laser diode (Laser Components, 915 nm, 25 W), allows control of the sample temperature between 293 and 1270 K (Fig. 2d). The laser diode is connected to an optical fiber, which directs the IR beam on the backside of the sample mounting plate. This sample holder offers also a rotational movement along the z axis. As future prospective, this possibility to heat the sample will allow NAPP investigation of reactions on catalytic surfaces at elevated temperatures, which will further extend the versatility of this endstation.

Sample manipulation is another critical part of a NAPP system, as several technical issues arise when the sample has to be precisely positioned in a near ambient pressure environment that, at the same time, is sealed against UHV. Our new chamber features a load lock system allowing for a quick sample entry from ambient air to vacuum: the sample is first mounted on the manipulator and the whole stage is then connected to the gate valve. After evacuation of this volume, the gate valve opens and the sample is introduced in the flow-cell while the manipulator rod connects to the opening of the flow tube, thus assuring vacuum-tight sealing. The sample manipulator and its link to the translation stages are designed such that seals only exist between the analysis cell and the surrounding UHV volume on the one hand, and between the air side and the UHV chamber on the other hand. The sample load procedure is fully automated and requires short time, thus allowing for fast sample exchange. Sample positioning with a precision of ± µm along x, y, and z axes is achieved with linear stage drives controlled via a Lab-VIEW based software. This enables a precise control of the sample position, which is a critical parameter for high pressure measurements. Indeed, the effective pressure at the sample surface is reduced due to the perturbation of the entrance cone aperture. It is calculated that at a distance of 2 R (R being the radius of the cone aperture), the local pressure is about 95 % of the total pressure in the chamber [6, 16]. Remarkably, even small variations of the pressure field can lead to sizeable effects. For instance, we observed preferential evaporation of the ice surface close to the entrance cone at working distances below 2R, as previously reported in Ref. [16],

most probably due to a combination of local pressure reduction and radiative heating of the ice surface by the aperture cone. To avoid such issues during the investigation of ice samples, our analyzer can be fitted with customized entrance cones realized in such a way that the working distance, i.e., the distance between the orifice and the focus of the analyzer in the center of the analysis cell where the sample is positioned, corresponds to 4 R. Moreover, thanks to the high quality of the lens focusing system and the possibility to accurately align the chamber with respect to the photon beam, the working distance can be further optimized, thus permitting a precise tuning of the measurement geometry.

Figure 4 shows the layout of the vacuum system, which is almost identical to

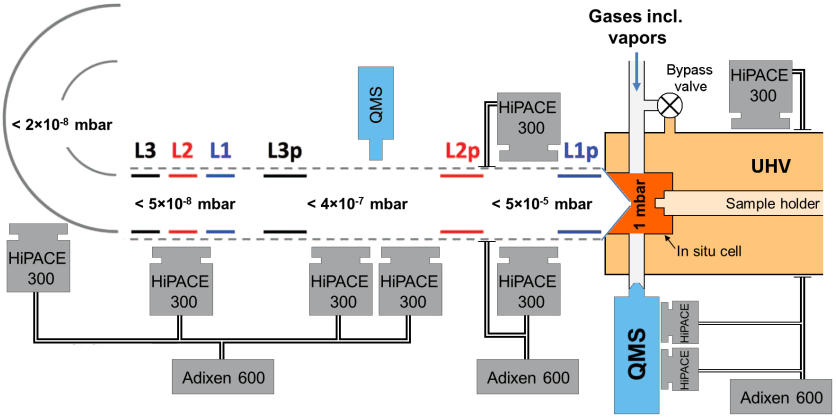

Figure 2.4: Schematic of the vacuum system: the typical pressures are measured with the 0.5 mm aperture cone (adapted from [27])

that shown in Ref. [27], except for the different experimental chamber. All the turbo pumps are from Pfeiffer (HiPace 300 l/s), while the root pumps of the pre-pumping stages are from Adixen (600 l/s). When the bypass is closed for high pressure measurements, the flow tube chamber is pumped through the orifices of the electron energy analyzer and mass spectrometer. Similar to a set-up we previously tested at the beamline 9.3.2 at ALS [25], a UV laser diode (Oxxius, 375 nm, 15 mW) is mounted on the viewport of the hemispherical electron energy analyzer and aligned to the measurement spot on the sample through the analyzer aperture by an adjustable mount. This experimental configuration allows the in situ investigation of photoactive materials under atmospherically relevant conditions and light while, compared to other set-ups [26], reducing the extent of gas phase photochemistry induced by UV irradiation.

2.1.4 Proof-of-Principle Measurements

In this section we provide selected examples that demonstrate the system capabilities. More precisely, we report on the preliminary study of three scientific cases of major impact in environmental and atmospheric chemistry, such as photochemistry of titania TiO_2 nanoparticles, interaction of trace gases with ice, and study of frozen NaCl-water mixtures.

Photocatalysis on TiO_2

Photocatalysis on TiO_2 is a major topic of research due to its straightforward implications for depolluting appliances [33, 34] and atmospheric chemistry [35]. For instance, TiO_2 is a component of natural mineral dust that represents an important reactive aerosol in the atmosphere affecting the ozone budget and the climate [36]. In this context, adsorption of water and hydroxylation of the surface, which are key aspects to understand TiO_2 photocatalysis in the environment, offer still major open questions. Earlier near ambient pressure XPS studies have provided important insight into the nucleation of water on this surface [37, 38]. In a recent study we have quantified the effect of humidity on ozone-induced band bending on the TiO_2 (110) surface [39], and found interesting changes in the partial electron yield oxygen K-edge absorption spectra indicative of changes in the hydrogen bonding structure in multilayers of water. Moreover, we have lately shown how the downward band bending induced by UV light [40] is likely to change the water adsorption properties on TiO_2(110) [25]. With the aim of improving the understanding of these issues, we have conducted first experiments using the NAPP set-up for a water adsorption experiment over a TiO_2 powder sample (Degussa P25) under UV-irradiation and relevant atmospheric conditions of humidity.
The TiO_2 samples were prepared according to the following procedure. A homogeneous solution of TiO_2 powder and ethanol was prepared and deposited on the gold- coated surface of the cooled manipulator. The sample was then dried to evaporate the ethanol and loaded into the analysis cell. The O 1s core level spectra shown below were measured at a photon energy of 730 eV and aligned with respect to the Fermi level, measured on the gold-coated surface of the manipulator in the same experimental conditions. The NEXAFS spectra were measured in Auger yield mode and are normalized to the beam intensity, recorded with a photodiode mounted instead of the sample before (and after) the experiments were

performed. The O K-edge NEXAFS spectra were measured at the ''magic angle'' of 54.7° between the (linear) polarization of the incident X-ray and the (k) vector of the electrons, using an electron kinetic energy window of 460–520 eV. These measurements were performed at the SIM beamline. The Ti K-edge NEXAFS measurements were performed at the PHOENIX beamline using a kinetic energy range of 3960–4020 eV. Oxygen was admitted to the chamber through a leak valve, while water was dosed using the capillary system described above.

Figure 5 shows the O 1s core level measured (a) in vacuum and (b) in humid

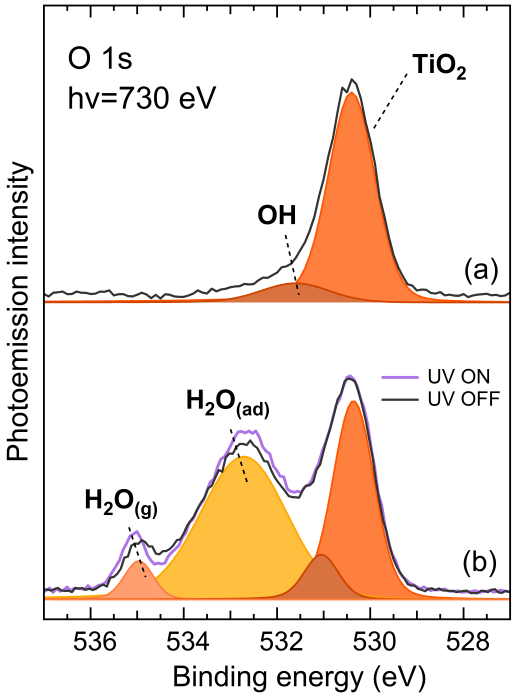

Figure 2.5: O 1s photoemission spectra of the TiO_2 powder sample measured **(a)** in vacuum and **(b)** at 0.06 mbar partial pressure of O_2 at 5 % RH (0.36 mbar partial pressure of H_2O at 272 K) together with the fitting components, which are slightly shifted downward for display. Overlapped in **(b)** is also the spectrum measured during UV exposure. The binding energy scale for the O 1s spectrum obtained on a clean surface in UHV conditions was constrained to the value of 530.4 eV for the oxide O 1s peak. All spectra are normalized to the oxide peak intensity after linear background subtraction. The measurements were performed at the SIM beamline

conditions (5 % RH) and 0.06 mbar partial pressure of O_2. As illustrated by the evolution of the O 1s core level region, several components appear upon water vapor exposure besides the main peak at 530.4 eV, which corresponds to oxygen

in the TiO_2 lattice. These components are associated to OH groups and molecular H_2O at about 531.1 and 532.8 eV, respectively [37]. Oxygen-containing carbon contaminants, desorbing from the chamber walls once it is exposed to high pressure or originating from the water source, might also contribute to the spectral intensity in the OH binding energy range. However, no increase of the C 1s intensity was observed during the experiment. The evolution of the spectral components as a function of RH is in line with previous experimental findings indicating a stepwise mechanism for water adsorption onTiO_2. More precisely, water molecules dissociatively adsorb on the oxygen vacancies of TiO_2 surfaces, leading to the formation of OH groups that act as nucleation centers for the adsorption of additional water molecules [37]. It can be observed that a small concentration of OH groups was found even before the admission of water into the chamber, most probably because the sample was not pretreated, e.g. annealed, before the measurements. The additional photoemission peak appearing at higher binding energy is associated with gas-phase water. It is noteworthy that the thickness of the water layer does not depend on the specific values of water vapor pressure and temperature, but only on their combination, i.e., on the RH value [6].

Figure 6 shows the comparison between O K-edge NEXAFS spectra measured in dark and under UV irradiation. The well-defined resonances A1 (531.3 eV) and A2 (534.0 eV) correspond to excitations to O 2p–Ti 3d mixed states [41]. The C1 (540.0 eV) and C2 (546.0 eV) peaks arise from electron transfer to mixed states derived from O 2p and Ti 4sp states [41]. The adsorption of water on TiO_2 causes an increase of the C1 and C2 resonances, as shown by the comparison between the NEXAFS spectra measured under dry (a) and humid (b) conditions. This is in accordance with the fact that these are the components most sensitive to oxygen–oxygen interactions, due to their prevailing oxygen p character [41]. The observation that these components further increase upon UV irradiation indicates that the concentration of water molecules on the surface further tends to increase under UV light. This is in line with the previous experimental observation that UV light irradiation led to an enhanced concentration of hydroxylgroups [25]. Furthermore, the comparison between O K-edge spectra in Fig. 6 a and b suggests that this photoinduced effect is sizeable only if a sufficiently large amount of H_2O molecules is provided, i.e., the effect is almost negligible under dry conditions. The outlined scenario is supported by the O 1s photoemission spectrum measured under humid conditions and during UV irradiation reported in Fig. 5b (purple

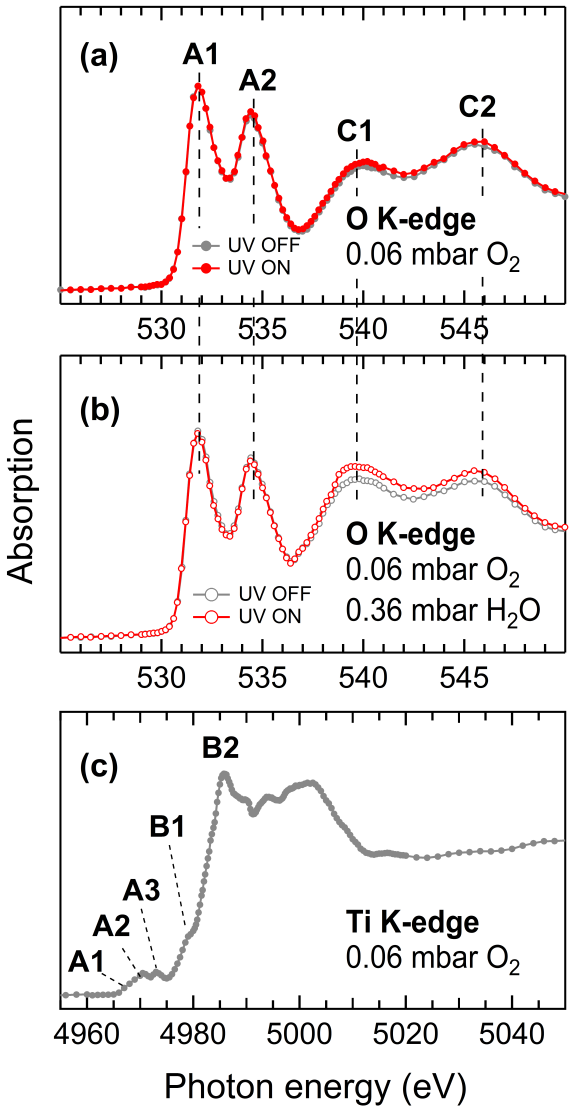

Figure 2.6: O K-edge NEXAFS spectra for a TiO_2 powder sample in presence of **(a)** 0.06 mbar O_2 and **(b)** with additional 0.36 mbar partial pressure of H_2O in dark conditions (*grey*) and under UV light irradiation (*red*). **(c)** Ti K-edge NEXAFS spectrum for TiO_2 powder sample at 0.06 mbar pressure of O_2. The measurements in **(a)** and **(b)** were performed at the SIM beamline, while those in **(c)** at the PHOENIX beamline

spectrum), which shows an increase of the H_2O (ad) component compared to the spectrum measured under dark conditions (grey spectrum). It is worth noting that the contribution of the gas phase to the NEXAFS spectra reported in Fig.6 a, b is negligible because of the low water vapor partial pressure used. Moreover, the absorption peaks of the water gas phase [42] do not overlap with the C1 and C2 resonances of the TiO_2 oxygen K-edge. Finally, Fig. 6 c illustrates the titanium K-edge NEXAFS of the sample measured under 0.06 mbar oxygen pressure. This spectrum shows three typical pre-edge features A1, A2, and A3 that are associated to a mixing of 4p and 3d titanium orbitals. The resonances B1 and B2, instead, are due excitations to Ti 4sp hybridized orbital with O 2p states [43]. It should be stressed that the capability to perform NEXAFS measurements with soft and hard X-rays brings about an enhanced depth selectivity. TiO_2 is a good example in this regard, because the O and Ti K-edge NEXAFS provide complementary information due to the different IMFP of the corresponding Auger electrons. Indeed, the electrons IMFP at 500 and 4000 eV in TiO_2 , corresponding approximately to the kinetic energy of the O and Ti KLL Auger lines, is ~13 and ~63Å, respectively. This makes the O K-edge NEXAFS a surface probe compared to the more bulk sensitive Ti K-edge NEXAFS.

Phase changes of NaCl-water binary systems

Sea salt, and in particular its major halide, chloride, is an important reactant in the atmosphere. Chloride in air-borne sea salt aerosol is–once chemically converted to a molecular halogen (Cl_2, BrCl) and released to the atmosphere–well known as important atmospheric reactant, driving large-scale changes to the atmospheric composition and in particular to ozone levels in remote areas, but also in coastal mega cities [17, 44]. Similar chemistry has been proposed for sea salt deposits in polar snow covers [45]. A crucial factor determining the overall reactivity is the local physical environment of the chloride ion. For example, the reactivity of liquid aerosols decreases significantly upon crystallization [17, 46, 47]. Surprisingly, the phases of NaCl-containing systems are still under debate [46, 48], partially due to the limited availability of in situ measurements directly probing the local environment at the surface of frozen NaCl-water binary systems. The top panel in Fig. 7 shows the phase diagram of NaCl-water at 200–300 K in the RH and temperature space as constructed by Koop [49]. Here, the RH parameterizes the concentration of NaCl in solution, which is used in the more commonly known phase diagrams;

the reference at each temperature is the vapor pressure of pure (supercooled) water. The corresponding solution composition can be roughly estimated through Raoult's Law, i.e., the mole fraction of water in the solution identical to RH, or precisely by applying detailed activity based thermodynamic equilibrium models [50], which is significant for the high ionic strength solutions below 80 % RH. The shaded area shows the region where the liquid aqueous solution is thermodynamically stable. The boundaries of this region define the regions at lower temperatures or lower RH where solids are thermodynamically stable. At the line indicating the ice-solution co-existence, the vapor pressures of ice and of the solution match. The point where the two boundary lines meet is the eutectic where solid ice, solid NaCl hydrohalite, and aqueous solution are stable and in thermodynamic equilibrium. Below the eutectic temperature of 252 K, the liquid solution of NaCl in water is thermodynamically not stable as macroscopic solution. It is evident how the water uptake to NaCl driven by changing RH dictates the phase of NaCl and its mixture with ice or water [49]. In particular, the occurrence of the NaCl hydrohalite has raised some uncertainty [51] as its formation is kinetically hindered. Further, micro-sized particles have been observed to deviate from this thermodynamic prediction and metastable liquid has been observed in the region indicated by the dashed line in Fig. 7 [49]. In the following, we show how NEXAFS spectroscopy at the Cl K-edge can be highly informative on the nature of the NaCl structure in NaCl-water binary systems. Using XPS and NEXAFS spectroscopies of the O 1s core level and O K-edge, respectively, we previously showed that these systems follow the phase rules at the air–ice interface [52]. This finding contrasts some earlier observations, where the presence of liquid-like Cl below the eutectic point of bulk solutions [53] was postulated (see Ref. [46] and references therein). In the present study, by probing the Cl K-edge, we are sensitive to small changes in the local environment of the chlorine atom and the spectra are not dominated by the excess water molecules as in the case of the O K-edge spectra reported in our previous investigation. The measurements reported in this section were performed at the PHOENIX beamline at SLS. Auger yield NEXAFS were measured at the Cl K-edge using a kinetic energy window of 2350–2400 eV.

The points at which XPS and Auger yield NEXAFS measurements have been performed are indicated by colored letters in the top panel in Fig. 7. After drying some droplets of NaCl solution on the sample holder at room temperature, and transferring it into the in situ cell, the solid NaCl sample was measured at 1.05

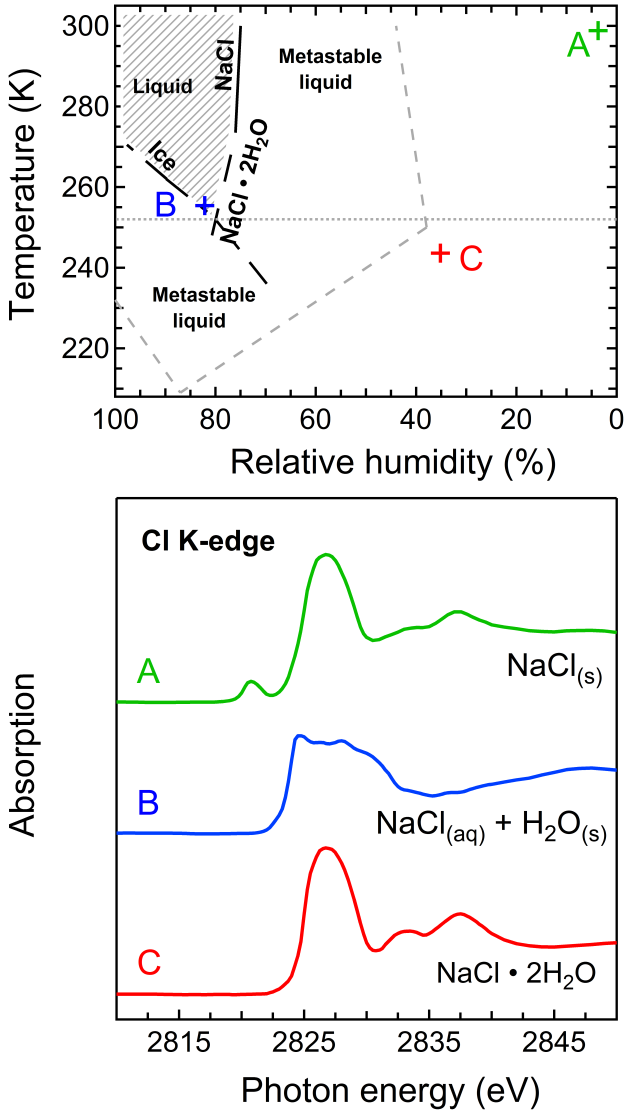

Figure 2.7: *Top* phase diagram of the NaCl-water system [45, 46]; indicated are the measured experimental points. *Bottom* Cl K-edge NEXAFS spectra of (A) solid NaCl at 299 K and 3 % RH, (B) a binary system of aqueous NaCl solution–-ice at 255 K and 82 % RH, and (C) NaCl dihydrate at 243 K and 35 % RH. The measurements were performed at the PHOENIX beamline

mbar water vapor pressure and 299 K (point (A), RH 3 %). Next, we increased the water vapor pressure to 2.01 mbar and lowered the temperature to 260 K (RH 107 %) to form a NaCl solution. At this point, after formation of the solution and its dilution by the excess water vapor pressure provided, we observed sudden nucleation of ice, both optically via the endoscope camera, as well as by a pressure drop in the in situ cell to 1.87 mbar, which is the vapor pressure of ice at the temperature of the frozen sample of 260 K. The formation of ice leads to the formation of a frozen NaCl solution, i.e. solid ice and liquid NaCl solution in a 2-phase system. We then equilibrated the system at 255 K (point (B), 1.17 mbar, RH ~82 %). Also this point is above the eutectic temperature of 252 K, meaning that the sample was expected to consist of a mixture of solid ice and of concentrated brine, the water activity of which was equal to the vapor pressure of ice at this temperature. We take advantage of this fundamental principle and derive surface temperatures of frozen aqueous samples based on the measured water vapor pressure in the in situ cell and the parameterization of water vapor pressure over ice by Ref. [54] when working with the cooled sample holder. In the final step, pressure and temperature were set to 0.18 mbar and 243 K, respectively, (point (C), RH ~35 %) in order to slowly evaporate the ice and allow the formation of NaCl dihydrate ($NaCl \cdot 2H_2O$). Note that $NaCl \cdot 2H_2O$ can only be formed in this way, and not by exposing NaCl to H_2O [45]. The bottom panel in Fig. 7 shows the chlorine K-edge spectra measured at the above described three points in the NaCl-water phase diagram. Dry NaCl, spectrum (A), shows a main absorption peak at 2825.0 eV, corresponding to the transition from 1s to 4p orbitals [55], and a typical post-edge feature [56] at 2836.0 eV. The pre-edge peak at 2820.8 eV can be attributed to C–Cl bonds [57] due to carbon contamination of the sample, as sizeable amounts of NaOCl, showing an absorption peak at a similar photon energy [58], can be excluded. The NEXAFS spectrum of the frozen NaCl solution (B) is quite different compared to that of the solid phase being characterized by a broader edge with two components. The overall shape of this spectrum is in agreement with that reported in Ref. [56] and [59] for aqueous Cl-. Finally, spectrum (C) from the presumed NaCl dihydrate is almost similar to that of the dry sample, but the carbon-related peak is absent. This can be related to a reduced carbon contamination, as also observed in the associated XPS spectra (not shown here). In summary, the Cl K-edge NEXAFS measurements indicate the formation of a solution above the eutectic, and formation of a solid salt phase below the eutectic and under dryer conditions. More detailed analysis is needed to unequivocally assign the Cl K-edge NEXAFS to the dihydrate phase of NaCl. These results rep-

resent the starting point for an improved understanding of the structure of eutectic and sub-eutectic frozen salt solutions in presence of ice (high relative humidity), and in the hydrate stability domain of the phase diagram (low relative humidity). Moreover, the Cl K-edge measurements complement and extend previously reported measurements at the O K-edge NEXAFS for the same system [52], which is sensitive to the hydrogen bonding environment of the water molecules. However, compared to the oxygen K-edge, the higher kinetic energy of the chlorine K-edge Auger electron corresponds to an increased probing depth of about 2–8 nm, and, therefore, to a much more bulk-sensitive measurement. This allows for better comparison with other bulk sensitive methods such as those described by Cho et al. [60], who used nuclear magnetic resonance to identify sub-eutectic liquid NaCl.

Uptake of trace gases to ice

In this last example we discuss the adsorption of trace gases to ice, a question of paramount importance in atmospheric and cryospheric environmental science. Another pioneering application of NAPP was the confirmation of the uptake of trace gases to ice, namely acetone [61] and acetic acid [32], which is a relevant process for environmental science, but directly linked also to catalytic research. Core level spectroscopy has successfully shown that strong acids are predominately ionized on amorphous solid water at 90 K leading to the suggestion of primal dissociation on ice at temperatures relevant to the Earth's environment [62, 63]. The only study that directly observed the degree of protonation and the structure of the hydrogen-bonding network at low dosage at the ice surface at temperatures of 240 K was recently published by our group [51]. The use of NAPP is particular appealing when targeting high environmental relevance, because this requires operation with temperatures of the ice sample above ~200–240 K. At colder temperatures, the ice structure might deviate from the hexagonal crystal structure typical for the Earth's cryosphere and those samples would thus not mimic environmental ices as ideally [64, 65].

In the following we describe the typical procedure that we followed to grow ice samples in our experiments on formic acid uptake. A constant water vapor pressure of 0.077 mbar was established in the analysis cell, which corresponds to an equilibrium vapor pressure of water over ice at 229 K. Then, the temperature of

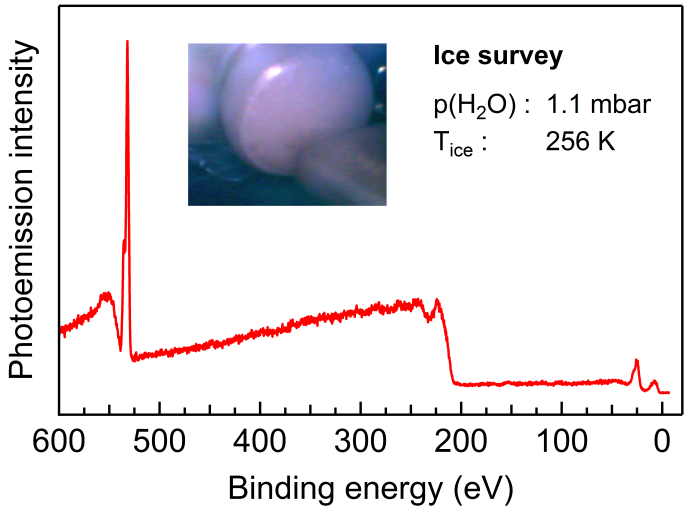

Figure 2.8: Survey spectrum of the ice surface taken at the SIM beamline of PSI/SLS with a photon energy of 730 eV. Note the absence of carbon, nitrogen, or other contamination traces. The *inset* shows a picture of the polycrystalline, crystal-clear ice film on the cooled sample holder and of the electron analyzer cone in measurement position taken during the measurement

the cooled sample holder was lowered to 218 K and ice started to grow directly on the copper surface. The water vapor pressure dropped to 0.022 mbar because, in presence of ice on the cold sample holder, the vapor pressure of the ice sample at the given temperature determines the water vapor pressure in the analysis cell. As long as this equilibrium vapor pressure was lower than the 0.077 mbar dosed to the analysis cell, the ice film grew. After 45 min the temperature of the cooled sample holder was raised to 229 K to stop the growth of the ice film and to maintain it stable at equilibrium. Based on calculated flows into the analysis cell and a surface area of the ice film of 0.8 cm^2, a thickness of the ice film of 500 µm can be estimated. The ice film was allowed to crystallize at a water partial pressure of 0.042 mbar (223 K) for 12 h prior to the formic acid dosing. This pressure is slightly lower than the vapor pressure of 0.077 mbar in absence of ice and corresponds to a slightly growing ice regime. Within this regime, the intensity of the O 1s XPS spectra did not change with time, thus indicating that the ice film at the measurement spot was stable. The slightly growing ice regime indicated by the macroscopic pressure measurements might be attributed to a heterogeneous temperature distribution at the sample holder, or might indicate that this growth

compensated the evaporation of ice caused either by heat transfer from the beam or by the pressure field gradient in the proximity of the aperture cone of the analyzer. Once a stable condition for the ice film was established, the formic acid was dosed into the chamber. Figure 8 shows an example of XPS survey spectrum of a clean ice surface showing the O 1s, 2s and 2p peaks at 533, 25 and about 7 eV, and the O Auger region. This spectrum was measured at the SIM beamline using a photon energy of 730 eV.

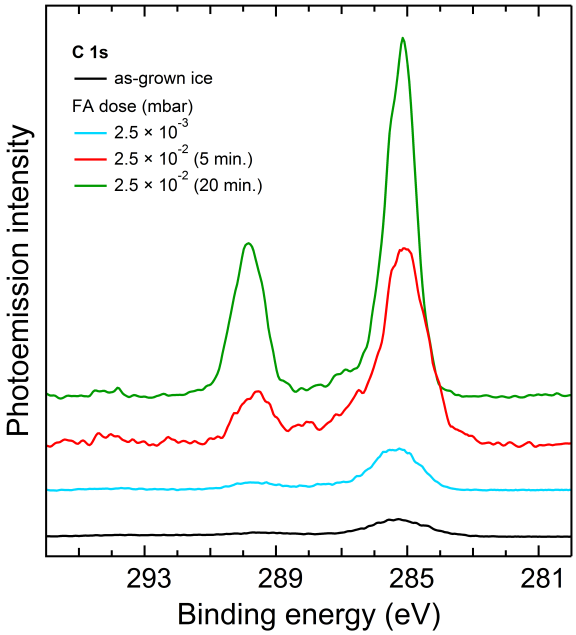

Figure 2.9: C 1s core level spectra measured during formic acid uptake on the ice surface at 223 K and $4.2 \cdot 10^{-2}$ mbar partial water vapor pressure in the analysis cell. The measurements were performed at the PHOENIX beamline of PSI/SLS with a photon energy of 2200 eV. The C 1s spectra are vertically shifted for display

Figure 9 shows the C 1s spectra measured during the formic acid uptake at the ice surface. C 1s and O 1s core levels (the latter not shown here) were measured in sequence during the uptake at the PHOENIX beamline using a photon energy of 2200 eV. The C 1s spectra are referenced to the binding energy of the O 1s core level peak at 533.4 eV [32], and displaced in the vertical direction for clarity. The C1s spectrum measured before the admission of formic acid into the analysis cell (black spectrum) shows a component at about 285 eV that is associated to adventitious

carbon contamination. Carbon impurities might desorb from the wall surfaces of the flow tube cell in the high pressure regime, for instance, during the ice growth. In addition, beam-induced photochemistry and/or contamination of the formic acid source may further contribute to this component, as its intensity increased during formic acid uptake. Once a formic acid partial pressure of 0.025 mbar was established in the analysis cell, the adventitious carbon peak slightly grew, and a broad feature appeared at about 290 eV, which is representative of carbon in a –C(O)OH (carboxyl) functional group. After increasing the partial pressure to 0.025 mbar, a direct response of the –C(O)OH intensity to the dosing of formic acid is evident. Within 5 min of dosing the –C(O)OH signal increased significantly (red spectrum) and after 20 min, when the uptake and pressure equilibrium at the sample was reached, a very intense and sharp peak had evolved (green spectrum). At this point, the visual inspection of the ice surface revealed a marked change of the sample, and its shiny look indicated the onset of melting. At this partial pressure range of about 0.025 mbar, the formic acid lowers the melting point of ice so that melting at 223 K might have occurred. This is based on a back-of-the envelope calculation of the ice melting point depression of formic acid [66] using Raoult's law. It is important to note that the response to changes in pressure illustrated in Figs. 9 and 3 represents a great improvement compared to the very long equilibration time, typically several hours, required for acid trace gases uptake with standard NAPP set-ups at comparable partial pressures [32]. Moreover, it is noteworthy that this is the first direct observation of formic acid on ice, as earlier studies were based on indirect observations of the gas-phase concentration of formic acid upon contact with ice samples [66, 67]. It is planned to continue the investigation of formic acid adsorbed to ice in the future.

2.1.5 Summary and Conclusions

A new chamber for near ambient pressure XPS and NEXAFS investigation of solid/vapor interfaces at the NAPP endstation has been presented. We have described first results on the photochemistry of TiO_2 that support previous experimental findings about increased concentration of water on TiO_2 under humid conditions and UV irradiation. Furthermore, we have characterized several distinct points in the NaCl-H_2O phase diagram via NEXAFS spectroscopy measurements at the Cl K-edge and correlated them with observed phase transitions. Finally, in the last example we have proved the feasibility of ice samples growth with the

new chamber and the possibility, precluded with other standard NAPP set-ups, to investigate the interaction of this and other surfaces with sticky acidic gases with reasonable equilibration times. These examples demonstrate the capability to study interfaces between solids and vapors as well as aqueous solutions, thus proving the potential of this new chamber at NAPP endstation for the investigation of many scientific cases of relevance to environmental and atmospheric chemistry.

2.1.6 Acknowledgements

Swiss National Science Foundation (SNF R'Equip, Grant No. 139139, SNF Grant Nos. 149492, 149629), PSI FoKo, SLS QV program, and the Center of Competence in Energy and Mobility (CCEM, NADiP project). Part of the work has been performed at the Surface/Interface: Microscopy (SIM) and PHOENIX beamlines at the Swiss Light Source.

2.2 Supplementary information about detailed set-up and experimental procedures relevant for ice – trace gas interaction experiments

2.2.1 Characterization of the NAPP ice set-up

S. Schneider did part of the experimental work during a summer internship under supervision of A. Waldner, T. Bartels-Rausch and M. Ammann.

One of the main challenges one faces in environmentally relevant in situ APXS ice – trace gas studies is appropriate dosing of H_2O and trace gases. Variable, but stable ratios of water/trace gas pressures over wide ranges for several hours are fundamental. Ensuring a stable, relatively high H_2O pressure (needed to investigate ice at temperatures close to the melting point) with low, environmentally relevant, trace gas partial pressures is a challenge. For measurements using common atmospheric trace gas partial pressures, the ability to dose stable trace gas concentrations in the ppt range, implying partial pressures of as little as 10^{-9} mbar, is required.
A dilution of the trace gas in any carrier gas as used for numerous other investigation techniques is limited since the absolute pressure in the *in situ* experimental cell should not exceed pressures of ~5 mbar. With increasing pressure in the *in situ* experimental cell the photoelectron signal intensity decreases dramatically due to inelastic scattering of the photoelectrons in the gas phase. Recent developments of graphene shielded experimental cells instead of a differentially pumped analyzer part might be an interesting option for future experiment. Nevertheless, the H_2O pressure should represent the main part of the overall pressure in the *in situ* experimental cell. A substantial change in the overall pressure in the *in situ* experimental cell during an experiment may, for example, lead to changes in thermal conductivity, perturbing the essential stability for meaningful and reproducible experiments. Therefore, I aim to maintain a total pressure of less than 2 mbar in the *in situ* experimental cell during all experiments.

As already emphasized, the ice stability is a point of concern. As shown in Figure 2.10, the actual thermodynamic conditions at the measurement spot can influence the ice stability. Radiative heating of the sample by the cone holding the electron sampling aperture in maximum 1.5 mm away and the surrounding cell walls about 2 cm away may lead to temperature gradients. Additionally, differential pumping

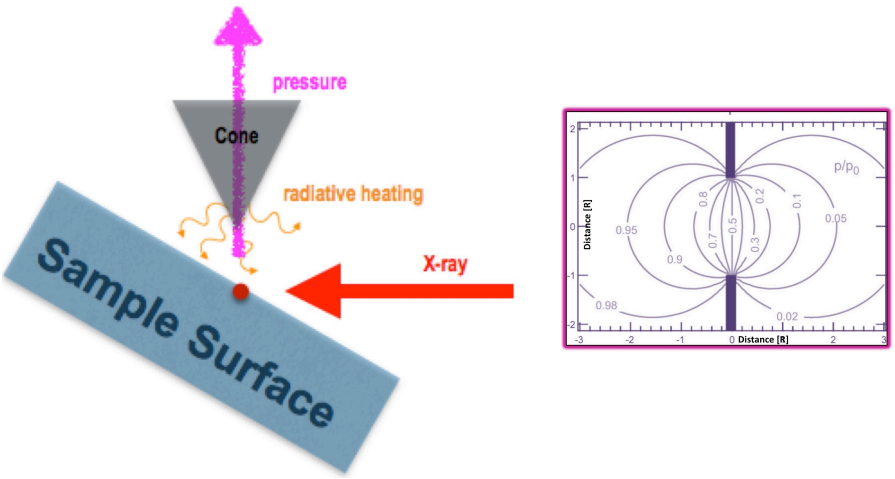

Figure 2.10: Influences on the ice stability in the NAPP set up. Showing the influence of radiation heating, pressure/gas fluxes and X-ray. On the right side the effect of the differential pumping is shown (Bluhm *et al.* 2010).

leads to a pressure gradient in the *in situ* experimental cell. Furthermore the X-ray itself may affect the ice at the measurement spot. Keeping the background H_2O partial pressure slightly above the equilibrium vapor pressure allows for reducing the perturbations adjusting a local equilibrium at the measurement spot. However, further actions and adaptations need to be taken to ensure that the ice–gas interaction experiments remain at stable conditions.

The X-ray affects the ice at the measurement spot through the deposition of energy by the absorption of photons resulting in thermodynamically and electron stimulated desorption. The effect of the X-ray on the ice stability depends on photon flux and photon energy. A reduction of perturbations by the X-ray can be achieved by reducing the intensity of the incident photon flux. However, even by detuning the photon flux by up to 80%, the beam still leaves an imprint on the sample, which is discussed in more detail in chapter 4. Further detuning would lead to unfavorable changes of the beam properties (e.g. photon distribution, spot size), thus limiting a reasonable reduction.

The adapted design of the NAPP experimental set-up at SLS addresses the challenges of stable ice – trace gas experiments, for example, with a very precise and promptly responding temperature control. A user designed sample holder with proportional–integral–derivative (PID) controller feedback by a platinum wire of 100 Ohm (PT 100) temperature sensor shows satisfying results. The temperature

stabilized substrate on which the ice sits is cooled using a regulated flow of liquid nitrogen cooled gas. As a result, the substrate can be maintained at temperatures between -100 and 90°C with stability better than 0.1 K.
To overcome pressure perturbations due the differential pumping, a customized aperture cone is used. As shown on the right side of Figure 2.10, the differential pumping leads to a pressure gradient in front of the orifice that can be illustrated by isobars of reduced pressure. By increasing the working distance (distance between sample and cone), and reducing the radius of the aperture of the cone, pressure perturbations can be reduced at the expense of photoemission signal, because the acceptance angle is reduced and the path length through the high pressure is longer. According to the observations and simulations of Bluhm (2010), the cones used during our experiments ensure perturbation of less than 2% at the sample spot.

The sketch of the adapted NAPP solid chamber set-up for ice–trace gas interaction experiments is shown in the upper part of Figure 2.11. It mainly consists of the analyzer with the differential pumping, the *in situ* experimental cell embedded in a bigger UHV chamber, and the dosing system. For a more detailed gas phase analysis, an additional mass spectrometer below the *in situ* experimental cell can be added. This, of course, modifies the fluxes trough the set-up.
The dosing system displayed in this scheme shows an exemplary set-up used for some ice–HCOOH interaction experiments. It enables the dosing of two different vapors, in this case, H_2O and HCOOH.
To ensure stable and reproducible dosing of different trace gases without cross contamination over a wide pressure range, I decided to use a capillary dosing approach. Vapors are admitted to the *in situ* experimental cell via different, and exchangeable capillaries. The pressure of the vapor in the temperature-stabilized reservoir in front of the capillary and the dimensions of the capillary determine the flow in the *in situ* experimental cell.
To ascertain an appropriate set-up, a characterization and estimation of the fluxes through the experimental set-up, displayed in Figure 2.11, was performed. This analysis is used to determine the flow rates through the whole set-up, including the dosing system, and allows an estimation of the respective flow regimes. With information on the flow regime I can estimate, for example, the probability of cross contamination. The flow regime can be assessed using the dimensionless Knudsen number, K_n. K_n is given by the ratio of the mean free path, λ, of the gas molecules and a representative physical length scale, L, of the set-up ($K_n = \lambda/L$).

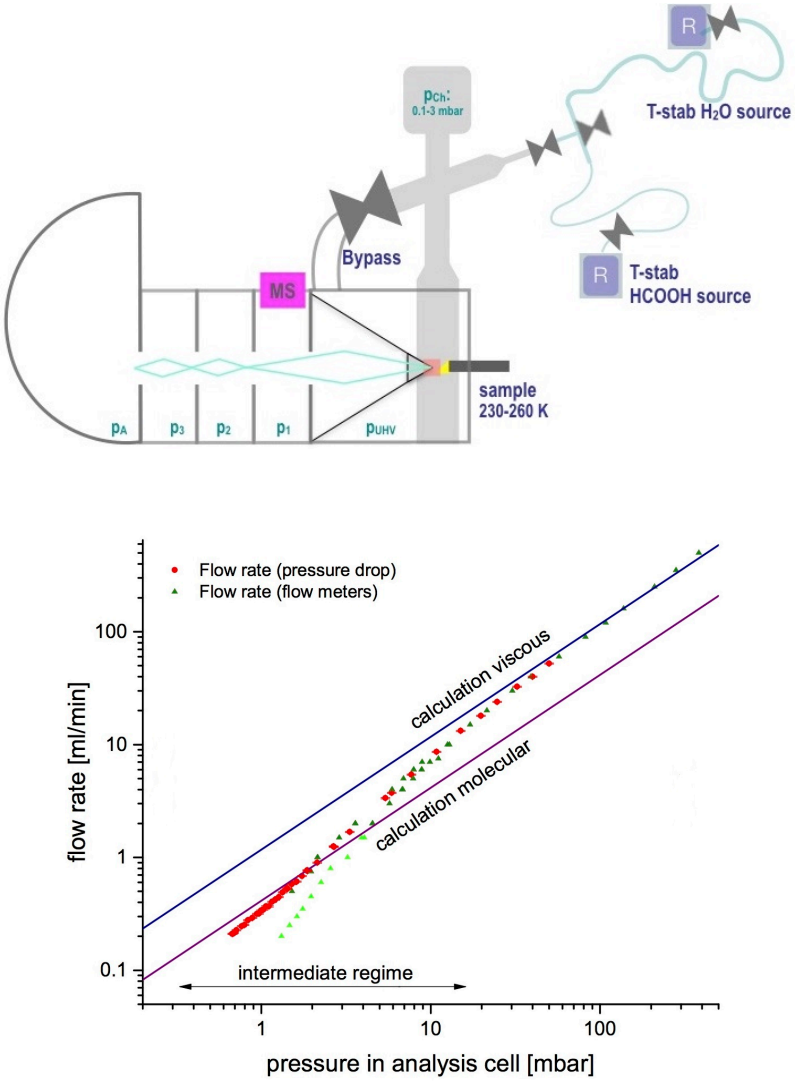

Figure 2.11: Overview of dosing in NAPP solid chamber.
Top: Scheme of NAPP set-up with exemplary dosing system attached.
Bottom: Fluxes and estimation of the flow regime trough the NAPP set-up displayed above. The flow rate is displayed as function of pressure in the *in situ* experimental cell. Error bars were calculated on the basis of random errors. Data in light green are outliers.

Large K_n (>2) indicate molecular flow, whereas small K_n (<0.01) indicates viscous flow. For viscous flow, the Navier-Stokes equation gives a good estimation about the transport. Thus the flow is strongly governed by pressure gradients and diffusion. Molecular flow can be understood as individual particles moving from wall to wall without collision with each other [71].
Capillaries are long narrow tubes. The representative physical length L is given by $3l^2/4d$, where d is inner diameter and l is tube length. By ascertaining viscous flow, thus adapting these dimensions, cross contamination of the used dosents can be avoided because axial diffusion against the viscous flow is too small. For an exemplary tube length of one meter and an inner diameter of 0.001 m we get a characteristic physical length of 75 m. In the mbar pressure range, a typical pressure in the reservoir, the mean free path of gas molecules is around 10^{-4} meter. This results in a Knudsen number in the capillary in the 10^{-7} range, thus far below 0.01. This means that viscous flow in the dosing lines is assured.

In addition, the range of the achievable flow rates trough the capillary in the

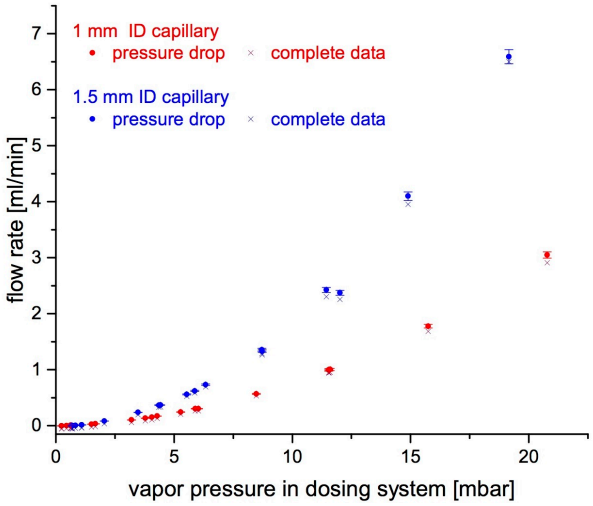

Figure 2.12: Response of the pressure *in situ* experimental cell on the capillary dosing. Dependence of the flow rate on the vapor pressure in the dosing system. Error bars were calculated on the basis of random errors.

in situ experimental cell needs to be considered. Here, the capillary dimensions and the vapor pressure in the reservoir need to be matched to achieve the favored pressure range in the *in situ* experimental cell and avoid cross contamination. Figure 2.12 shows the dependency of the flow rate in the *in situ* experimental cell

on the pressure in the dosing reservoir for two exemplary capillaries with different dimensions.
Using the analysis above, an appropriate selection of the respective capillaries for our experiments was achievable. Straightforward dosing of various compounds enabling reproducible and stable measurements could be attained. By varying material, diameter and length of the respective capillaries, very satisfactory dosing of different gases and partial pressures for various kinds of ice–trace gas interaction experiments can be achieved. One can exchange and add multiple dosing lines while dosing without harming the stability of the systems.
Capillaries allow an accurate adjusting of stable trace gas partial pressures over a great number and time of experiments and studies without cross contamination of the chemicals.

2.2.2 'Different types' of ice

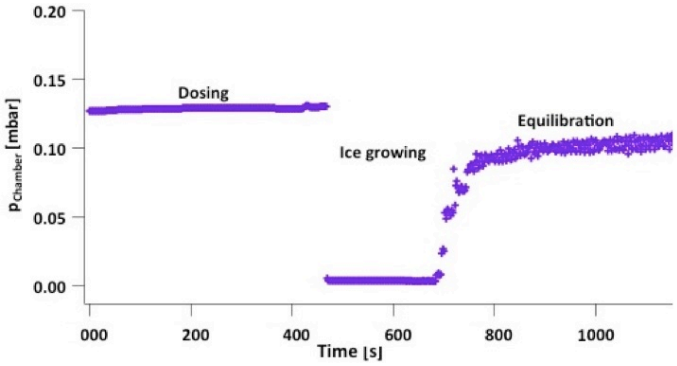

Figure 2.13: Pressure course in the *in situ* experimental cell during typical ice growing experiment resulting in different different ice samples.

In addition to the importance of stable conditions during an experiment, the production of 'different types' of ice is of interest for ice–trace gas interaction experiments.
There are a wide variety of complex shapes and habits of ice crystals common in the environment. As a function of temperature, ice supersaturation, and absolute pressure different 'types' of ice exist. The different crystals can be ascribed using two different regimes, columnar and plate-like. At temperatures higher than 230 K, thus the temperatures used during my studies, plate-like crystals are predomi-

nant (Bailey and Hallett (2009)). However, in the context of my investigations I was not interested in the detailed habit of the ice, but in the polycrystallinity of the ice sample. A single crystal ice sample does not have any grain boundaries, pores or veins. A more polycrystalline ice sample consists of more crystals, thus more grain boundaries, pores and pockets (see Figure 1.1).
As discussed in chapter 1.2.1, structure and compartments of ice may play an important role in ice – trace gas interactions. Depending on the amount of crystals in an ice sample, the ice properties and the interaction between trace gases and the ice may vary. Therefore, the demand for experiments of ice–trace gas interactions performed using and comparing different 'types' of ice is quite high.
Unfortunately, a sound detection and quantification of the actual amount of crystals and grain boundaries is not possible with the present set-up. Here, a modification of the *in situ* experimental cell would be necessary to enable the analysis of the respective polarizations of the different crystals. However, in general, the macroscopic appearance of an ice crystal reflects the symmetry of the underlying crystal structure (Furukawa and Wettlaufer (2007)). Thus optical observations allow a rough estimation of the polycrystallinity.
Depending on growing procedure, temperature, and supersaturation, I was able to produce 'different types' of ice, including really polycrystalline ice but also ice that looked like a single crystal.
Figure 2.13 shows the H_2O pressure in the *in situ* experimental cell of a typical ice growing procedure. After ascertaining stable water vapor pressure in the *in situ* experimental cell, I cool down the substrate of the cryo sample holder to trigger ice nucleation and growth. After a period of growth, thus thickening of the ice sample, I increase the temperature of the substrate until the ice sample is in equilibrium with the surrounding vapor pressure. By varying the speed of cooling and supersaturation during the growing process, I am able to influence and modify the 'type' of ice, meaning the presence and proportion of different compartments. Exemplary pictures of the different 'types' of ice I grew are presented in Figure 2.14.
In addition to the growing procedure, the material of the substrate as well as its roughness can influence the ice sample. For the final studies I used Au coated CuO_2 substrates of various roughness. A ceramic substrate did not show convincing nucleation and thermal properties (heat conductivity and distribution), hence, not used for further studies.
Figure 2.14 a and b presents photos of slowly grown ice using minor oversaturation on a smooth gold substrate. The ice reveals a single crystalline structure.

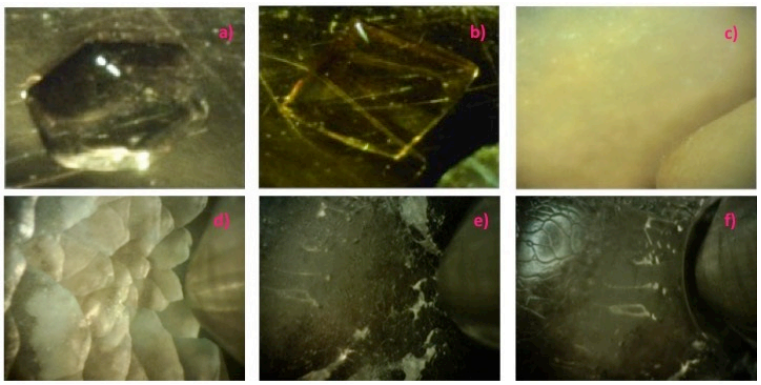

Figure 2.14: Different ice samples grown by slightly different growing procedures as described in the text. The pictures show an image section of about 0.45cm x 0.8 cm.
a) and b) showing single crystalline ice; c) whitish polycrystalline ice; d) polycrystalline ice with rough surface; e) polycrystalline ice with various inclusions; f) growing polycrystalline ice showing the effect of the pressure gradient close to the analyzer cone due to the differential pumping.

Rapid cooling together with high oversaturation leads to whitish, highly polycrystalline ice such as shown in c.
In d a slowly grown ice on a rough CuO_2 surface is presented. It has a rough surface indicating several ice crystals originating from various nucleation onset sites.
Ice regrown from molten ice on the substrate has an appearance as presented in e, exhibiting highly diverse pockets as pores and veins.
Figure 2.14 f displays a picture of ice for which nucleation onset was triggered quite quickly but slowly grown, and is still growing at the moment of the shot with slight oversaturation. The ice has a clear and shiny appearance with some structural features. Furthermore, the continuously growing ice clearly shows an imprint of the analyzer cone due to radiation heating and differential pumping. It nicely illustrates the effect of excessive oversaturation. A similar imprint on the ice can be observed in case of an improperly adjusted working distance of the sample.

In conclusion, I can state that the advanced and modified experimental set-up for ice–trace gas interactions at SLS (NAPP set-up with chamber for solid-vapor interfaces, cryo sample holder, and newly designed dosing system) enables us to perform various interesting ambient pressure X-ray spectroscopy studies of the interaction between ice and trace gases.

Bibliography

[1] Siegbahn, H., and Siegbahn, K.: ESCA applied to liquids. *Journal of Electron Spectroscopy and Related Phenomena,*, **2 (3)**, 319–325, 1973.

[2] Johner, R. W., Roberts, M. W., and Yates, K.: A "high-pressure" electron spectrometer for surface studies, *Surf. Sci.*, **87**, 501–509, 1979.

[3] Ruppender, H. J., Grunze, M, Kong, C. W., and Wilmers, M.: In situ X-ray photoelectron spectroscopy of surfaces at pressures up to 1 mbar, *Surf. Int. Anal.*, **15**, 245–253, 1990.

[4] Olgetree, D. F., Bluhm, H., Lebedev, G, Fadley, C. S., Hussain, Z. and Salmeron, M.: A differentially pumped electrostatic lens system for photoemission studies in the millibar range.*Rev. Sci. Inst.*, **73**, 3872, 2002.

[5] Bluhm, H., Hävecker, M., Knop-Gericke, A., Kleimenov, E., Schlbägl, R., Teschner, D., Bukhtiyarov, V. I, Ogletree, D. F., and Salmeron, M. : Methanol oxidation on a copper catalyst investigated using in situ X-ray photoelectron spectroscopy.*J. Phys. Chem. B*, **108**, 14340–14347, 2004.

[6] Olgetree, D. F., Bluhm, H., Hebenstreid, E. D. and Salmeron, M.: Photoelectron spectroscopy under ambient pressure and temper- ature conditions.*Nuc. Inst. and Met. in Phys. Res. Sec. A*, **601**, 151–160, 2009.

[7] Grass, M. E., Karlsson, P. G., Aksoy, F., Lundqvist, M., Wannberg, B., Mun, B. S., Hussain, Z. and Liu, Z.: New ambient pressure photoemission endstation at Advanced Light Source beamline 9.3.2. *Rev. Sci. Inst.*, **81**, 053106, 2010.

[8] Schnadt, J., Knudsen, J., Andersen, J. N, Siegbahn, H., Pietzsch, A., Hennies, F., Johansson, N., Martensson, N., Ohrwall, G., Bahr, S., Mahl, S., and Schaff, O.,: The new ambient-pressure X-ray photoelec- tron spectroscopy instrument at MAX-lab. *J. Synch. Rad.*, **19**, 701–704, 2012.

[9] Perez-Dieste, V., Aballe, L., Ferrer, S., Nicolas, J. Escudero, C., Milan, A. and Pellegrin, E.: Near ambient pressure XPS at ALBA. *J. Phys.*, **425**, 072023, 2013.

[10] Kaya, S., Ogasawara, H., Näslund, L-A., Forsell, J-O., Casalongue, H. S., Miller, D. J., and Nilsson, A.: Ambient-pressure photoelectron spectroscopy for heterogeneous catalysis and electrochemistry. *Catal. Tod.*, **205**, 101–105, 2013.

[11] Toyoshima, R. and Kondoh, H.: In-situ observations of catalytic surface reactions with soft X-rays under working conditions. *J. Phys. Con. Mat.*, **27**, 083003, 2015.

[12] Liu, X., Yang, W and Liu, Z.: Recent progree on synchrotron-based in situ soft X-ray spectroscopy for energy materials *Adv. Mat.*, **26**, 7710–7729, 2014.

[13] Samleron, M. and Schlögel, R.: Ambient pressure photoelectron spectroscopy: a new tool for surface science and nanotechnology. *Surf. Sci. Rep.*, **63**, 169–199, 2008.

[14] Ghosal, S., Hemminger, J. C., Bluhm, H., Mun, B. S., Hebenstreit, E. L. D., Ketteler, G, Ogletree, D. F., Requejo, F. G. and Salmeron, M.: Electron spectroscopy of aqueous solution interfaces reveals surface enhancement of halides. *Science*, **307**, 563–566, 2005.

[15] Carrasco, J., Hodgson, A. and Michaelides, A.: A molecular perspective of water at metal interfaces. *Nat Mater*, **11**, 667–674, 2012.

[16] Bluhm, H.: Photoelectron spectroscopy of surfaces under humid conditions. *J Electron Spectrosc Relat Phenom*, **177**, 71–84, 2010

[17] Abbatt, J. P. D., Thomas, J. L., Abrahamsson, K., Boxe, C., Granfors, A., Jones, A. E., King, M. D., Saiz-Lopez, A., Shepson, P. B., Sodeau, J., Toohey, D. W., Toubin, C., von Glasow, R., Wren, S. N. and Yang, X.: Halogen activation via interactions with environmental ice and snow in the polar lower troposphere and other regions. *Atmos Chem Phys*, **12**, 6237–6271, 2012.

[18] Bartels-Rausch, T., Jacobi, H-W., Kahan, T. F., Thomas, J. L., Thomson, E. S., Abbatt, J. P. D., Ammann, M., Blackford, J. R., Bluhm, H., Boxe, C., Domine, F., Frey, M. M., Gladich, I., Guzman, M. I., Heger, D., Huthwelker, T., Klan, P., Kuhs, W. F., Kuo, M. H., Maus, S., Moussa, S. G., McNeill, V. F., Newberg, J. T., Pettersson, J. B C., Roeselova, M.,and Sodeau, J. R.: A review of air–ice chemical and physical interactions (AICI): liquids, quasi-liquids, and solids in snow. *Atmos Chem Phys*, **14**, 1587–1633, 2014.

[19] McNeill, V. F., Domine, F., Grannas, A. M.,Abbatt, J. P. D., Ammann, M., Ariya, P. A., Bartels-Rausch, T., Donaldson, D. .J, Guzman, M. I., Heger, D., Kahan, T. F., Klan, P., Masclin, S., Toubin, C. and Voisin, D.: Organics in environmental ices: sources, chemistry, and impacts. *Atmos Chem Phys*, **12**, 9653–9678, 2012.

[20] George, C., D'Anna, B., Herrmann, H., Weller, C., Vaida, V., Donaldson, D. J., Bartels-Rausch, T. and Ammann, M.: Emerging areas in atmospheric photochemistry. *Springer, Berlin*, **1**, 1–54, 2012.

[21] Grannas, A. M.,Jones, A. E., Dibb, J., Ammann, M., Anastasio, C., Beine, H. J., Bergin, M., Bottenheim, J., Boxe, C. S., Carver, G., Chen, G., Crawford, J. H., Domine, F., Frey, M. M., Guzman, M. I., Heard, D. E., Helmig, D., Hoffmann, M. R., Honrath, R. E., Huey, L. G., Hutterli, M., Jacobi, H. W., Klan, P., Lefer, B., McConnell, J., Plane, J., Sander, R., Savarino, J., Shepson, P. B., Simpson, W. R., Sodeau, J. R., von Glasow, R., Weller, R., Wolff, E. W. and Zhu, T.: An overview of snow photochemistry: evidence, mechanisms and impacts. *Atmos Chem Phys*, **7**, 4329–4373, 2007.

[22] Pratt, K. A., Custard, K. D., Shepson, P. B., Douglas, T. A., Poehler, D., General, S., Zielcke, J., Simpson, W. R., Platt, U., Tanner, D. J., Gregory Huey, L., Carlsen, M. and Stirm, B. H.: Photochemical production of molecular bromine in Arctic surface snowpacks. *Nat Geosci*, **6**, 351–356, 2013.

[23] Simpson, W., von Glasow, R., Anderson, P., Anderson, P., Ariya, P. A., Bottenheim, J. W., Burrows, J., Carpenter, L., Carpenter, L., Friess, U., Goodsite, M., Heard, D., Heard, D., Hutterli, M. A., Jacobi, H-W., Kaleschke, L., Plane, J., Platt, U., Richter, A., Roscoe, H., Sander, R., Shepson, P. B., Sodeau, J. R., Steffen, A. and Wolff, E. W.: Halogens and their role in polar boundary-layer ozone depletion. *Atmos Chem Phys*, **7**, 4375–4418, 2007.

[24] Bluhm, H., Ogletree, D. F., Fadley, C. S., Hussain, Z. and Salmeron, M.: The premelting of ice studied with photoelectron spectroscopy. *J Phys*, **14**, L227–L233, 2002.

[25] Lampimaeki, M., Schreiber, S., Zelenay, V., Krepelova, A., Birrer, M., Axnanda, S., Mao, B., Liu, Z., Bluhm, H. and Ammann, M.: Exploring the environmental photochemistry on the TiO_2 (110) surface in situ by near ambient pressure X-ray photoelectron spectroscopy. *J Phys Chem C*, **119**, 7076, 2015.

[26] Rosseler, O., Sleiman, M., Montesinos, V. N., Shavorskiy, A., Keller, V., Keller, N., Litter, M. I., Bluhm, H., Salmeron, M. and Destaillats, H.: Chemistry of NO_X on TiO_2 surfaces studied by ambient pressure XPS: products, effect of UV irradiation, water, and coadsorbed K+. *J Phys Chem Lett*, **4**, 536–541, 2013.

[27] Brown, M. A., Redondo, A. B., Jordan, I., Duyckaerts, N., Lee, M-T., Ammann, M., Nolting, F., Kleibert, A., Huthwelker, T., Maechler, J-P., Birrer, M., Honegger, J., Wetter, R., Woerner, H. J., van Bokhoven, J. A.: A new endstation at the Swiss Light Source for ultraviolet photoelectron spectroscopy, and X-ray photoelectron spectroscopy, and X-ray absorption spectroscopy measurements of liquid solutions. *Rev Sci Instrum*, **84**, 073904, 2013.

[28] Flechsig, U., Nolting, F., Fraile Rodriguez, A., Krempasky, J., Quitmann, C., Schmidt, T., Spielmann, S. and Zimoch, D.: Performance measurements at the SLS SIM beamline. *AIP Conf Proc*, **1234**, 319–322, 2010.

[29] Kato, .S, Ammann, M., Huthwelker, T., Paun, C., Lampimaki, M., Lee, M-T., Rothensteiner, M. and van Bokhoven, J. A.: Quantitative depth profiling of Ce_{3+} in Pt/CeO_2 by in situ high-energy XPS in a hydrogen atmosphere. *Phys Chem Chem Phys*, **17**, 5078–5083, 2015.

[30] Eriksson, S. K., Hahlin, M., Kahk, J. M., Villar-Garcia, I. J., Webb, M. J., Grennberg, H., Yakimova, R., Rensmo, H., Edstroem, K., Hagfeldt, A., Siegbahn, H., Edwards, M. O. M., Karlsson, P. G., Backlund, K., Ahlund, J. and Payne, D. J.: A versatile photoelectron spectrometer for pressures up to 30 mbar. *Rev Sci Instrum*, **85**, 075119, 2014.

[31] Tao, F. F.: Operando studies of catalyst surfaces during catalysis and under reaction conditions: ambient pressure X-ray photoelectron spectroscopy with a flow-cell reactor. *Chem-CatChem*, **4**, 583–590, 2012.

[32] Křepelová, A., Bartels-Rausch, T., Brown, M. A., Bluhm, H., Ammann, M.: Adsorption of acetic acid on ice studied by ambient pressure XPS and partial-electron-yield NEXAFS spectroscopy at 230–240 K. *J Phys Chem A*, **117**, 401-409, 2012.

[33] Salthammer, T., Fuhrmann, F.: Photocatalytic surface reactions on indoor wall paint. *Environ Sci Technol*, **41**, 6573–6578, 2007.

[34] Kwon, S., Fan, M., Cooper, A. T. and Yang, H.: Photocatalytic applications of micro- and nano-TiO_2 in environmental engineering. *Crit Rev Environ Sci Technol*, **38**, 197–226, 2008.

[35] Chen, H., Nanayakkara, C. E.and Grassian, V. H.: Titanium dioxide photocatalysis in atmospheric chemistry. *Chem Rev*, **112**, 5919–5948, 2012.

[36] Monge, M. E., George, C., D'Anna, B., Doussin, J. F., Jammoul, A., Wang, J., Eyglunent, G., Solignac, G., Daele, V. and Mellouki, A.: Ozone formation from illuminated titanium dioxide surfaces. *J Am Chem Soc*, **132**, 8234–8235, 2010.

[37] Ketteler, G., Yamamoto, S., Bluhm, H., Andersson, K., Starr, D. E., Ogletree, D. F., Ogasawara, H., Nilsson, A. and Salmeron, M.: The nature of water nucleation sites on TiO_2 (110) surfaces revealed by ambient pressure X-ray photoelectron spectroscopy. *J Phys Chem C*, **111**, 8278–8282, 2007.

[38] Yamamoto, S., Bluhm, H., Andersson, K., Ketteler, G., Ogasawara, H., Salmeron, M. and Nilsson, A.: In situ x-ray photoelectron spectroscopy studies of water on metals and oxides at ambient conditions. *J Phys*, **20**, 184025, 2008.

[39] Lampimaki, M., Zelenay, V., Krepelova, A., Liu, Z., Chang, R., Bluhm, H. and Ammann, M.: Ozone-induced band bending on metaloxide surfaces studied under environmental conditions. *Chem-PhysChem*, **14**, 2419–2425, 2013.

[40] Zhang, Z. and Yates, J. T.: Band bending in semiconductors: chemical and physical consequences at surfaces and interfaces. *Chem Rev*, **112**, 5520–5551, 2012.

[41] De Groot, F. M. F., Faber, J., Michiels, J. J. M., Czyyk, M. T., Abbate, M. and Fuggle, J. C.: Oxygen 1s x-ray absorption of tetravalent titanium oxides: a comparison with single-particle calculations. *Phys Rev B*, **48**, 2074–2080, 1993.

[42] Myneni, S., Luo, Y., Naeslund, L. A., Cavalleri, M., Ojamae, L., Ogasawara, H., Pelmenschikov, A., Wernet, P., Vaeterlein, P., Heske, C.,Hussain, Z., Pettersson, L. G. M. and Nilsson, A.: Spectroscopic probing of local hydrogen-bonding structures in liquid water. *J Phys*, **14**, L213, 2002.

[43] Wu, Z. Y., Ouvrard, G., Gressier, P. and Natoli, C. R.: Ti and O K-edges for titanium oxides by multiple scattering calculations: comparison to XAS and EELS spectra. *Phys Rev B*, **55**, 10382–10391, 1997.

[44] Osthoff, H. D., Roberts, J. M., Ravishankara, A. R., Williams, E. J., Lerner, B. M., Sommariva, R., Bates, T. S., Coffman, D., Quinn, P. K., Dibb, J. E., Stark, H., Burkholder, J. B., Talukdar, R. K., Meagher, J., Fehsenfeld, F. C. and Brown, S. S.:

High levels of nitryl chloride in the polluted subtropical marine boundary layer. *Nat Geosci*, **1**, 324–328, 2008.

[45] Koop, T., Kapilashrami, A., Molina, L. T. and Molina, M. J.: Phase transitions of sea-salt/water mixtures at low temperatures: implications for ozone chemistry in the polar marine boundary layer. *J Geophys Res*, **105**, 26393–26402, 2000.

[46] Bartels-Rausch, T., Jacobi, H. W., Kahan, T. F., Thomas, J. L., Thomson, E. S., Abbatt, J. P. D., Ammann, M., Blackford, J. R., Bluhm, H., Boxe, C., Domine, F., Frey, M. M., Gladich, I., Guzman, M. I., Heger, D., Huthwelker, T., Klan, P., Kuhs, W. F., Kuo, M. H., Maus, S., Moussa, S. G., McNeill, V. F., Newberg, J. T., Pettersson, J. B. C., Roeselova, M. and Sodeau, J. R.: A review of air-ice chemical and physical interactions (AICI): liquids, quasi-liquids, and solids in snow. *Atmos Chem Phys*, **14**, 1587–1633, 2014.

[47] Kolb, C. E., Cox, R. A., Abbatt, J. P. D., Ammann, M., Davis, E. J., Donaldson, D. J., Garrett, B. C., George, C., Griffiths, P. T., Hanson, D. R., Kulmala, M., McFiggans, G., Poeschl, U., Riipinen, I., Rossi, M. J., Rudich, Y., Wagner, P. E., Winkler, P. M., Worsnop, D. R. and O'Dowd, C. D.: An overview of current issues in the uptake of atmospheric trace gases by aerosols and clouds. *Atmos Chem Phys*, **10**, 10561–10605, 2010.

[48] Bruzewicz, D. A., Checco, A., Ocko, B. M., Lewis, E. R., McGraw, R. L., Schwartz, S. E.: Reversible uptake of water on NaCl nanoparticles at relative humidity below deliquescence point observed by noncontact environmental atomic force microscopy. *J Chem Phys*, **134**, 044702, 2011.

[49] Koop, T., Kapilashrami, A., Molina, L. T., Molina, M. J.: Phase transitions of sea-salt/water mixtures at low temperatures: implications for ozone chemistry in the polar marine boundary layer. *J Geophys Res*, **105**, 26393–26402, 2000.

[50] Clegg, S. L., Brimblecombe, P. and Wexler, A. S.: Thermodynamic model of the system H^+–NH_4^+–Na^+–SO_4^{2-}–NO^{3-}–Cl^-–H_2O at 298.15 K. *J Phys Chem A*, **102**, 2155–2171, 1998.

[51] Huthwelker, T., Ammann, M., Peter, T.: The uptake of acidic gases on ice. *Chem Rev*, **106**, 1375–1444, 2006.

[52] Křepelová, A., Huthwelker, T., Bluhm, H. and Ammann, M.: Surface chemical properties of eutectic and frozen NaCl solutions probed by XPS and NEXAFS. *ChemPhysChem*, **11**, 3859–3866, 2010.

[53] Cheng, Y., Su, H., Koop, T., Mikhailov, E. and Poeschl, U.: Size dependence of phase transitions in aerosol nanoparticles. *Nat Commun*, **6**, 5923, 2015.

[54] Marti, M. and Mauersberger, K.: A survey and new measurements of ice vapor pressure at temperatures between 170 and 250 K. *Geophys Res Lett*, **20**, 363–366, 1993.

[55] Evans, K. A., Mavrogenes, J. A., O'Neill, H. S., Keller, N. S., Jang, L. Y.: A preliminary investigation of chlorine XANES in silicate glasses. *Geochem Geophys Geosyst*, **9**, Q10003, 2008.

[56] Higgins, F. E. and Huffmann, G. P.: Chlorine in coal: an XAFS spectroscopic investigation. *Fuel*, **74**, 556–569, 1995.

[57] Fujomori, T., Takaoka, M. and Morisawa, S.: Chlorinated aromatic compounds in a thermal process promoted by oxychlorination of ferric chloride. *Environ Sci Technol*, **44**, 1974–1979, 2010.

[58] Vaudey, C. E., Gaillard, C., Toulhoat, N., Moncoffre, N., Schlegel, M. L. and Raimbault, L.: Chlorine speciation in nuclear graphite studied by X-ray absorption near edge structure. *J Nucl Mater*, **418**, 16–21, 2011.

[59] Leri, A. C., Marcus, M. A. and Myneni, S. C. B.: X-ray spectromicroscopic investigation of natural organochlorine distribution in weathering plant material. *Geochim Cosmochim Acta*, **71**, 5834–5846, 2007.

[60] Cho, H., Shepson, P. B., Barrie, L. A., Cowin, J. P and Zaveri, R.: NMR investigation of the quasi-brine layer in ice/brine mixtures. *J Phys Chem B*, **106**, 11226–11232, 2002.

[61] Starr, D. E., Pan, D., Newberg, J. T., Ammann, M., Wang, E. G., Michaelides, A. and Bluhm, H.: Acetone adsorption on ice investigated by X-ray spectroscopy and density functional theory. *Phys Chem Chem Phys*, **13**, 19988–19996, 2011.

[62] Marcotte, .G, Ayotte, P., Bendounan, A., Sirotti, F., Laffon, C. and Parent, P.: Dissociative adsorption of nitric acid at the surface of amorphous solid water revealed by X-ray absorption spectroscopy. *J Phys Chem Lett*, **4**, 2643–2648, 2013.

[63] Parent, P., Lasne, J., Marcotte, G. and Laffon, C.: HCl adsorption on ice at low temperature: a combined X-ray absorption, photoemission and infrared study. *Phys Chem Chem Phys*, **13**, 7142–7148, 2011.

[64] Bartels-Rausch, T., Bergeron, V., Cartwright, J., Escribano, R., Finney, J., Grothe, H., Gutierrez, P., Haapala, J., Kuhs, W. F., Pettersson, J., Price, S., Sainz-Diaz, C., Stokes, D., Strazzulla, G., Thomson, E. S., Trinks, H. and Uras-Aytemiz, N.: Ice structures, patterns, and processes: a view across the icefields. *Rev Mod Phys*, **84**, 885–944, 2012.

[65] Kuhs, W. F., Sippel, C., Falenty, A., Hansen, T. C.: Extent and relevance of stacking disorder in in ''ice I(c)''. *Proc Natl Acad Sci*, **109**, 21259–21264, 2012.

[66] Jedlovszky, P., Hantal, G., Neurohr, K., Picaud, S., Hoang, P. N. M., Von Hessberg, P. and Crowley, J. N.: Adsorption isotherm of formic acid on the surface of ice, as seen from experiments and grand canonical Monte Carlo simulation. *J Phys Chem C*, **112**, 8976–8987, 2008.

[67] Von Hessberg, P., Pouvesle, N., Winkler, A. K., Schuster, G. and Crowley, J. N.: Interaction of formic and acetic acid with ice surfaces between 187 and 227 K. Investigation of single species- and competitive adsorption. *Phys Chem Chem Phys*, **10**, 2345–2355, 2008.

[68] Bluhm, H.: Photoelectron spectroscopy of surfaces under humid conditions. *Journal of Electron Spectroscopy and Related Phenomena*, **177(2)**, 71–84, 2010.

[69] Bailey, M. P.: Bailey, M. P., Hallett, J.: A comprehensive habit diagram for atmospheric ice crystals: Confirmation from the laboratory, AIRS II, and other field studies. *Journal of the Atmospheric Sciences*, **66(9)**, 2888-2899, 2009.

[70] Furukawa, Y: Furukawa, Y., Wettlaufer, J. S.: Snow and ice crystals. *Physics Today*, **60(12)**, 70-71, 2007.

[71] Wutz, M., and Hermann, A.: Theorie und Praxis der Vakuumtechnik. *Springer-Verlag*, **64**, 2013.

CHAPTER 3

Ambient pressure X-ray spectroscopy experiments of ice – trace gas interactions at LBL

3.1 The interaction ice – propionaldehyde investigated using XPS & NEXAFS

To be submitted to *The Journal of Physical Chemistry* as Waldner, A., Newberg, J. T., Pletincx, S., Karslıoğlu, O., Head, A. L. R., Ammann, M., Bartels-Rausch, T. and Bluhm, H.: The Interaction of Propionaldehyde with Ice: A Combined Photoemission and Near Edge X-ray Absorption Study.

3.1.1 Abstract

The interaction of ice with trace gases influences bio- and geochemical cycles and thus strongly affects atmospheric processes and climate. To date there is still a

scarcity of information on the molecular level processes that underlie trace gas-ice surface interactions. Langmuir type surface adsorption is most commonly used to describe the interaction between ice and trace gases; however, in a number of cases it cannot explain these processes completely, as additional phenomena, such as diffusion into the ice and dissolution of the trace gas into the uppermost ice layers may play a role. Using ambient pressure X-ray photoelectron spectroscopy (APXPS) and near edge X-ray absorption fine structure (NEXAFS), we here directly examined the interaction between ice and propionaldehyde over a temperature range from 230-270 K. Small aldehydes such as propionaldehyde are the most abundant carbonyl compounds and strong factors in the oxidation capacity of the atmosphere. Our APXPS measurements reveal that the uptake of propionaldehyde on ice follows a Langmuir type adsorption model, with an adsorption enthalpy of -6.3 kcal/mol, indicating a relatively weak interaction compared to hydrogen bonds between water molecules. The oxygen K-edge NEXAFS experiments indicate that propionaldehyde does not affect the hydrogen-bonding network of the ice surface layers.

Keywords: Ice surface, APXPS, NEXAFS, propionaldehyde

3.1.2 Introduction

Ice is a widespread occurrence in the environment, in the atmosphere as, e.g., ice clouds, graupel, and snowflakes, and in terrestrial regions in the form of snow, glaciers, sea ice and ice sheets. Even though the interaction between ice and trace gases are known to influence and modify (bio)geochemical cycles, there are still many unresolved questions about the fundamental physical chemistry of the uptake, solvation and reaction of trace gases on ice surfaces (e.g. Dominé and Shepson (2002), Grannas et al. (2013), Douglass et al. (2014), Bartels-Rausch et al. (2014)). One reason for this is the uncertainty about many aspects of the ice-air interface, whose physical and chemical properties, together with its role for ice – trace gas interactions, are still largely unknown and controversially debated (Dash et al. (1995), Huthwelker et al. (2006), Bartels-Rausch et al. (2014)). In particular the properties of the liquid like layer, or disordered interface (DI) at the ice-air interface are controversially discussed. For example, while there is general agreement that the thickness of this layer increases with increasing temperature (Bartels-Rausch et al. (2014) and references therein), there are large discrepancies about its absolute thickness as a function of temperature. A deeper understanding

of the molecular level processes at ice – trace gas interactions will also facilitate the interpretation of ice core records, which are an important part of paleoclimatological analysis and central to the prediction of the impact of ice – trace gas interactions on atmospheric chemistry and climate models.
Here we investigate the interaction between propionaldehyde (C_2H_5COH), a short chain aldehyde, and ice surfaces in the temperature range from 230-270 K. Small aldehydes are some of the most abundant carbonyl compounds in the atmosphere (e.g. Tunsaringkarn et al. (2014)) and are well known for their adverse effect on human health (Hauptmann et al. (2010)). They are emitted directly to the atmosphere from combustion sources and are also generated in a secondary process through photo-oxidation of biogenic and anthropogenic volatile organic compounds (VOC's) (Lary and Shallcross (2000), Atkinson (2000), Moussa et al. (2006)). As a result of their prevalence and active nature, aldehydes play a central role in atmospheric chemistry (Lary and Shallcross (2000), Shepson et al. (1996), Seinfeld and Pandis (2006)). Aldehydes are known to undergo photolysis to produce OH, a primary atmospheric oxidant (Chen et al. (2007), Yang et al. (2002), Dominé and Shepson (2002)). The main daytime sink for aldehydes is photolysis, with nighttime scavenging through dry and/or wet deposition (dust and water droplets, respectively). In Polar Regions as well aldehydes contribute significantly to the OH budget and decrease the amount of ozone in polar spring, by reacting with bromine atoms, where aldehydes terminate ozone-depleting chain reactions through bromine scavenging (Barrie et al. (1988), Simpson et al. (2007)). What makes small chain aldehydes particular interesting for ice – trace gas interaction studies is that their concentration in the interstitial air of Arctic and Antarctic snow, is higher than in air (e.g. Thomas et al. (2012), Grannas et al. (2002), Jacobi et al. (2004), Houdier et al. (2002)), which was variously attributed to to physical and chemical processes as well as photochemical reactions (e.g. Houdier et al. (2002), Guimbaud et al. (2002), Grannas et al. (2002), McNeill et al. (2012)). Petitjean et al. (2009) measured the partitioning coefficients between ice and acetaldehyde (CH_3CHO) and observed that for interactions below 223 K the measured partitioning coefficients match the calculated ones, assuming Langmuir surface adsorption, whereas at higher temperatures no saturation but a linearly increasing uptake was observed. Dissolution of the trace gas into the DI with a concomitant increase in the DI thickness may contribute to the non-Langmuirian uptake behavior at elevated temperatures. Depending on the solubility of trace gases in liquid water and the thickness of the DI, both depending on temperature, aldehyde dissolution into the DI may change the capacity of the ice to sorb trace

gases. Using ellipsometry and coated wall flow tubes, Kuo (2013) investigated the interaction between ice and formaldehyde (CH_2O) and acetaldehyde (CH_3CHO) at different temperatures, in particular the role of the DI in this process. Kuo's studies revealed that the interaction between small aldehydes and ice are more complex than simple Langmuir-type surface adsorption, but the thickness of the natural DI, thus the temperature, and an induced enhancement of the DI plays a major role for the interactions.
The examples above show that there is strong evidence that the DI plays an important role for the interaction between short chain aldehydes and ice, and thus may also influence the interaction of ice with propionaldehyde. In the present study, we investigate the molecular level processes of the interaction between propionaldehyde and ice using ambient pressure X-ray spectroscopy (APXPS), which probes the elemental and chemical composition with high surface sensitivity under equilibrium thermodynamic conditions and relevant aldehyde partial pressures. We measured uptake isotherms of propionaldehyde on ice at temperatures between 230 K and 270 K, which closely follows a Langmuir-type behavior. From isotherms taken at different temperatures we determined the adsorption enthalpy of propionaldehyde on ice. In addition, synchrotron based partial electron (Auger) yield near-edge X-ray absorption fine structure (NEXAFS) spectroscopic measurements were performed, enabling us to analyzed if propionaldehyde affects the molecular structure of hydrogen- bonding network at the ice surface.

3.1.3 Experimental

The ice samples for isotherm analysis were prepared *in situ* by depositing water from the gas phase onto a custom-built sample holder in the analysis chamber of the laboratory based ambient pressure X-ray photoelectron spectroscopy (SPECS Phoibos 150 NAP) set-up shown in Figure 3.1.

The set-up consists of an X-ray source (Al K-alpha, monochromatized, SPECS MF 60), an analysis chamber and the differentially pumped analyzer. The suitability of the set-up for adsorption experiments was demonstrated previously (Pletincx et al. (2017)). The labels in Fig. 1 indicate the different components of the experimental set-up: (A) marks the X-ray source, (B) the experimental cell and (C) the analyzer with differential pumping. A schematic view of the sample holder, which is based on a thermoelectric (Peltier) element, together with exemplary pictures

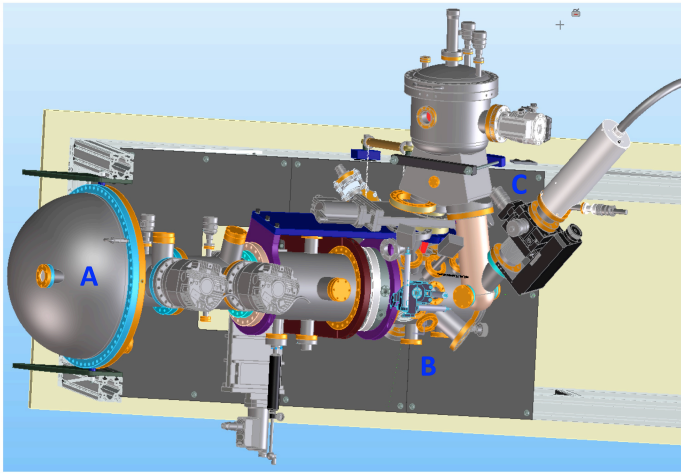

Figure 3.1: Schematic view of the laboratory based APXPS set-up at LBL. Numbers indicate the different components of the experimental set-up. (A) marks the X-ray source, (B) the experimental cell and (C) the analyzer with differential pumping.

of ice samples grown onto it is shown in Figure 3.2.

To grow the ice sample, water vapor was introduced through a precision leak

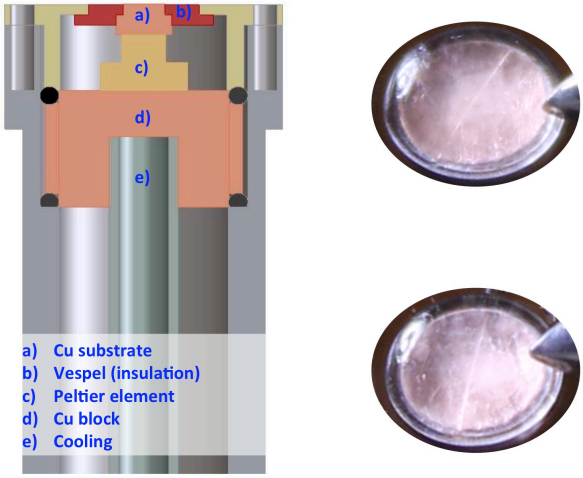

Figure 3.2: Ice experiments using the laboratory bases ambient pressure X-ray spectroscopy set-up.
Left: Cross section of the sample holder for solid/liquid-gas interfaces.
Right: Exemplary photos of ice samples.

valve from a temperature stabilized water source (MilliQ 18.2 MΩ cm). Before each experiment, the water was degassed by four consecutive freeze-pump-thaw cycles. During this study, ice samples were investigated at various temperatures. Water vapor was dosed into the analysis chamber at the equilibrium water vapor pressures for the desired ice temperature. The pressure in the analysis chamber was measured with a Baratron capacitance pressure gauge (10 Torr full range) with an accuracy of 1 mTorr. After establishing a stable water vapor pressure in the chamber, the sample holder was cooled until ice nucleation was observed. The ice grew slowly while an oversaturation of ~50% was maintained for about 0.5-1 hour, until an ice sample with a thickness of about 2 mm was formed. The ice appeared optically clear (see Figure 3.2). To stop the ice growth, the temperature was raised until the pressure in the camber, i.e. the vapor pressure of the ice sample, reached the initial pressure before nucleation onset. For the pure ice, the water vapor pressure in the analysis chamber corresponded to the literature value for the equilibrium water vapor pressure of ice at the respective temperature, confirming the correctness of the temperature and pressure measurements.
Once the clean ice sample was equilibrated, it was characterized by APXPS as is before introducing propionaldehyde to the analyzer chamber through a second precision leak valve. The propionaldehyde source was also degassed four consecutive freeze-pump-thaw cycles. Carbon 1s and Oxygen 1s core level spectra were acquired using a pass energy of 20 eV and an energy step of 0.1 eV. X-ray irradiated the sample under a grazing angle of 30°, with electron detected under grazing emission of 15-25° with respect to the sample surface. The X-ray source was set to an acceleration voltage of 12 kV and an irradiation power of 20 W. No X-ray beam-induced damage was observed. Typical acquisition times for C 1s spectra for low propionaldehyde concentrations were ~1 hour, requiring a high stability of the ice since even minor changes to the ice shape would lead to changes in working distance and irradiation of the sample, and thus signal intensity changes. In addition to the measurements with the laboratory X-ray source, some experiments at the Molecular Environmental Science beamline 11.0.2 at the Advanced Light Source in Berkeley, CA, were performed. Here, an experimental set-up and settings similar to previous work were used (e.g. Starr et al. (2011), Newberg and Bluhm (2015)).

3.1.4 Results and Discussion

Characterization as-grown ice

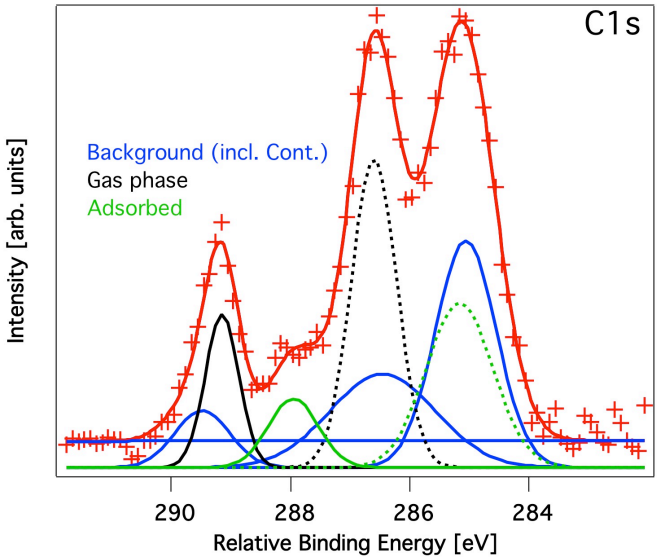

Figure 3.3: C1s spectrum of ice exposed to propionaldehyde. Dotted lines indicate peaks corresponding to methyl groups, solid lines the aldehyde group. In blue the fitted contamination of 'clean' ice, before exposure to propionaldehyde is displayed.

We first discuss the photoemission investigations of as-grown ice. In all of our measurements we observed some carbon contamination on the freshly grown ice, which was consistent in its amount throughout all experimental runs (see Figure 3). The origin of this carbon contamination could not be clearly identified; possible sources are gas-phase oxycarbon species present in the experimental set-up due to degassing chamber parts. Secondary electrons, but also the beam itself, can lead to splitting and decomposition of those compounds. The resulting fragments can then aggregate and form new, carbon contamination components. The presence of water vapor in a set-up is assumed to increase the observed amount of adventitious carbon condensing on surfaces (Piao and McIntyre (2002)). The carbon contamination showed three distinct peaks, which were quantified and for each fresh ice surface and later included in the analysis of ice in the presence of propionaldehyde. The assignment of the three chosen peaks was meaningless. For a proper assignment the use of more peaks would have been necessary. The patterns of the carbon contamination reveal the presence of mainly methyl (CH_X) groups,

but also oxygenated species as probably aldehydes (COH) and carboxyl (COOH). We can use the O 1s and C 1s XPS peak intensities for a rough estimate of the amount of contamination. From the measured O 1s and C 1s peak areas, corrected using sensitivity factors obtained from the gas phase peaks of propionaldehyde for the respective experiment, we determine C/O elemental ratios to be in the range from 0.01 to 0.07. The probed volume can be estimated using the IMFP of the photoelectrons in ice. In this study, the estimation of the IMFP of photoelectrons in ice is based on calculations from a theoretical model (NIST Standard Reference Database), using a band gap of 7.8 eV (Petrenko and Ryzhkin (1993)) and a mass density of 1g/cm^3 for ice. The probing depth, from which 95 % of the detected photoelectrons originate, is given by three times the IMFP multiplied by cos(θ). Theta is the set-up dependent take-off angle of the detected photoelectrons relative to the surface normal. In our set-up θ varies between 15-25°, depending on the volume and shape of the ice sample. This yields probing depths of ~2-6 nm (15 and 25°, respectively). Assuming that the sizes of the molecules of water and carbon contamination are similar, we can state that the average contamination makes less than one monolayer (0.3-0.7 for the minimum and maximum angle). Altogether the area of the contamination peaks compared to the acetone peaks is relatively small, of the order of in maximum ~50% for the final experiments. The amount of carbon contamination remained constant with increasing or decreasing propionaldehyde over the whole isotherm experiment, indicating that the presence of propionaldehyde in the experimental cell did not influence the carbon contamination.

Adsorption of propionaldehyde on ice

Representative C 1s spectra for the interaction between propionaldehyde and ice, together with the results of peak fitting, are shown in Figure 3.3. In Table 1, we give a summary of the different isothermal experiments, including fitting results of the isotherms, which are explained in more detail in the following sub-chapter. The two variables in the experiments were the ice temperature (~230 and 270 K) and propionaldehyde partial pressures (0.001 mbar to 0.76 mbar). To ensure saturation coverages in the adsorption isotherms the full range of propionaldehyde partial pressures was needed at the higher ice temperatures.

In addition to the three contamination-repeated peaks, four components due to propionaldehyde are observed, two each for adsorbed and gas phase propionalde-

Table 3.1: Description of isotherm experiments of propionaldehyde adsorbed on ice.

T [K]	pp_{low} [mbar]	pp_{high} [mbar]	K
270	0.06	0.39	2
265	0.003	0.253	2.5
264.5	0.03	0.1	3
264	0.003	0.39	3
263.5	0.074	0.61	2.35
263	0.017	0.381	6
261	0.03	0.76	5
260	0.01	0.32	3.75
259	0.075	0.68	10
255	0.11	0.48	10
253	0.005	0.585	8.5
248	0.04	0.54	16
247	0.03	0.265	22.75
243	0.008	0.345	26
235	0.02	0.31	60
230	0.001	0.029	100

hyde. Methyl (CH_x) groups adsorbed to surfaces are known to exhibit a peak at ~285 eV BE (Gelius et al. (1970)). The aldehyde (COH) peak of propionaldehyde is commonly shifted to higher binding energy (BE) by about ~2.5 eV (Gelius et al. (1970)) with respect to the methyl peak, which is clearly observed for the gas phase as well as the adsorbed peaks in our measurements. C 1s peaks due to adsorbed propionaldehyde are broadened by about 0.3 eV with respect to the gas phase peaks. This broadening may occur due to inhomogeneous charging of the ice, or due to electronic interactions between the ice surface and carbon species, which would include an averaging over many different adsorption geometries with slightly different core level binding energies, or due to ensemble effects (propionaldehyde in slightly different sample environments). The gas phase peaks are shifted by ~1.5 eV to higher BE compared to the adsorbed molecules, which is due to the reduced screening of core holes in the dilute gas environment and generally observed for gas phase compared to condensed phase species in APXPS (Hüfner (2013)). Even though contamination was present, a clear response of the propionaldehyde C 1s peaks to changes in propionaldehyde partial pressures, both increasing and decreasing, was observed, which reveals that the adsorption of propionaldehyde on ice under our experimental conditions is reversible. For the experiments performed at beamline 11.0.2 at the ALS, the C 1s PE spectra of clean ice showed the absence of carbon contamination. However, slight beam damage of propionaldehyde on ice

could be observed. The C K-edge NEXAFS (not shown here) of propionaldehyde interacting with ice indicates the presence of an additional oxidized species at the ice surface.

O K-edge NEXAFS – DI analysis

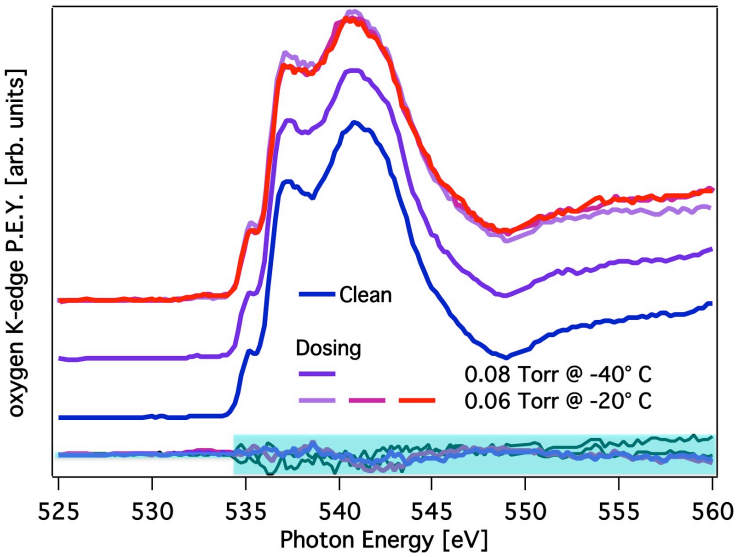

Figure 3.4: NEXAFS spectra of ice and ice exposed to propionaldehyde. In the lower part of the graph, differences between the clean ice spectra and the spectra of ice exposed to propionaldehyde are displayed. The blue shaded area represents the deviation between repeated measurements for clean ice, thus the experimental uncertainty.

Changes in the local hydrogen-bonding structure of the ice can be analyzed using O K-edge NEXAFS spectroscopy. The NEXAFS spectra obtained within the context of this study are in good agreement with those reported elsewhere (Bluhm et al. (2002), Nilsson et al. (2010)). In the range from 537 to 545 eV photon energy ice NEXAFS spectra show a double-peak structure, consisting of a main- edge peak followed by a more pronounced post-edge peak, as displayed in Figure 3.4 (Bluhm et al. (2002), Nilsson et al. (2010)). Upon transition to water this double peak structure broadens and the two peaks trade intensities. Furthermore both ice and water exhibits a characteristic pre-edge peak at 535 eV (e.g. Bluhm et al. (2002) , Nilsson et al. (2010)), which is present in all spectra

and indicates free hydrogen bonds, meaning weakly coordinated -OH in molecules with asymmetric donating H-bonds. With increasing disorder this peak increases. Additionally a dip, less pronounced for liquid water, at around 548 eV can be observed (e.g. Bluhm et al. (2002) , Nilsson et al. (2010)). Additional features in O K-edge spectra at 532.5 eV can be assigned to C=O or N=O bonds and indicate adsorbed species (e.g. Bluhm et al. (2002) , Nilsson et al. (2010)). Figure 3.4 shows that there is little or no change observed for spectra of neat ice and ice exposed to propionaldehyde, except for the peak at 532.5 eV, which indicates the presence of adsorbed propionaldehyde. In conclusion, O K-edge NEXAFS analyses reveal that propionaldehyde does not affect the hydrogen-bonding structure of the ice over the temperature range investigated here, pointing to a weak effect of propionaldehyde on the DI.

Analysis of propionaldehyde adsorption on ice

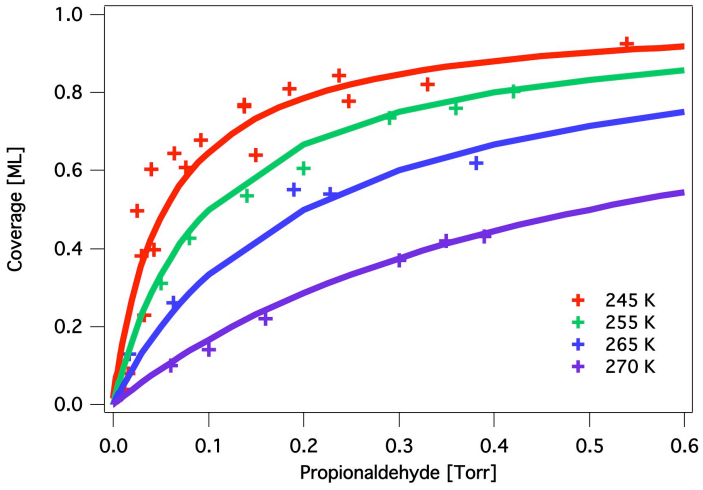

Figure 3.5: Exemplary isotherms for propionaldehyde interacting with ice at different temperatures. The fits are based on a Langmuir type surface adsorption isotherm.

Examples for isotherms of the adsorption of propionaldehyde on ice are shown in Figure 5. The smooth monotonic increase in the surface coverage followed by saturation is indicative of Langmuir adsorption-desorption kinetics. For Langmuir type surface adsorption, the surface coverage, C, is given by $C = K \cdot p/(1 + K \cdot p)$, with p as propionaldehyde partial pressure and K as Langmuir coefficient. The

larger K is, the greater is the partitioning of the gas molecules to the surface.
All of the 16 measured isotherms, including those measured at beamline 11.0.2, can be reproduced and fitted well using the Langmuir type adsorption isotherm. The Langmuir coefficients exhibit clear temperature dependence. The van't Hoff plot of the interaction between propionaldehyde and ice reveals a linear dependence of ln(K) on the 1000/T, as displayed in Figure 3.6.
From the slope of ln(K) over 1000/T the enthalpy of adsorption (ΔH) can be determined. From our measurements we determine the enthalpy of propionaldehyde adsorption onto ice as -6.3 kcal/mole (- 26 kJ/mol). This low adsorption enthalpy indicates a relatively weak interaction between ice and propionaldehyde. According to the binding energies of hydrogen-bonds discussed by Jeffrey (1997), the interaction can be interpreted as, at maximum, two weak hydrogen-bonds.
As far as we know, there are no other studies of the adsorption of propionaldehyde

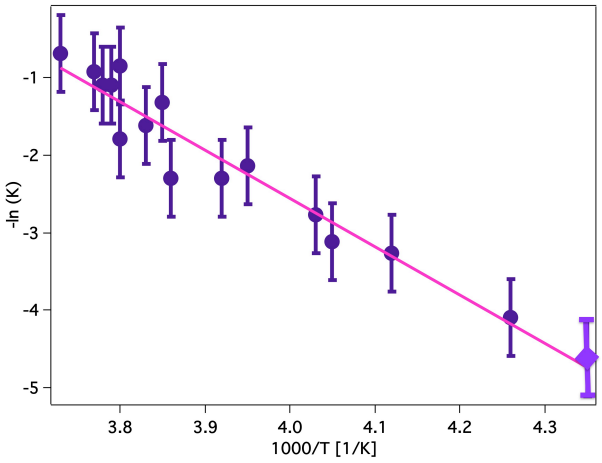

Figure 3.6: Van't Hoff plot of the interaction between propionaldehyde and ice. The used Ks were determined fitting the isotherms listed in Table 1 using Langmuir type surface adsorption theorem. The bright purple square indicates the experiment performed at ALS. In pink a linear fit to the data is added. The corresponding equation is: y = (-6.3 $\pm$ 0.4)x + (22.4 $\pm$ 1.6)

on ice, which afford a direct comparison with our results, but we can compare our results to other studies of the adsorption of small organic molecules on ice. Sokolov and Abbatt (2002) showed that at ~230 K the uptake of polar organic molecules on ice are adequately described by Langmuir type surface adsorption. Using van't Hoff analysis they derived adsorption enthalpies to be ~ -17.1 kcal/mol for 1-pentanol, decreasing with decreasing chain-length to ~ -14.8 kcal/mol for ethanol.

For aldehydes they found lower adsorption enthalpies compared to alkohols, for example ~ -15.5 kcal/mol for hexanal. Altogether, the observations by Sokolov and Abbatt (2002) showed that with increasing chain length the adsorption enthalpy increases. Petitjean et al. (2009) investigated the interaction between acetaldehyde and ice between 203 and 233 K and found Langmuir type surface adsorption with a temperature dependent adsorption enthalpy between $-$ 16 3 kJ/mol (-3.2 to -4.6 kcal/mol) describes the uptake quite well. These observations lead us to the conclusion that the adsorption enthalpy of propionaldehyde to ice of - 6.3 kcal/-mol is comparable to that of other small organic molecules on ice reported in the literature.

Some of the previous studies have observed pronounced deviations from the Langmuirian uptake behavior. For example, Sokolov and Abbatt (2002) observed a pronounced deviation of the uptake of acetic acid on ice at 245 K. Using MD simulations, Collignon and Picaud (2004) found that at 250 K methanol and formaldehyde penetrates into the ice. In addition, the interaction between some trace gases and ice are known to enhance the DI, what in turn may influence the capacity of the partitioning (e.g. McNeill et al. (2006)). Winkler et al. (2002) observed a discontinuity of the partitioning trend of formaldehyde to ice at around 223 K, which may be explained by an enhancement of the thickness of the DI due to the interaction between ice and formaldehyde.

During our analysis we could not detect any change of the uptake behavior over the whole investigated temperature range from 230-270 K. Since a pronounced increase of the natural DI is expected at ~250 K we assume that the DI may not play a role for the interaction between ice and propionaldehyde. Assuming Henry-like dissolution into the liquid-like DI, we can estimate the partitioning of propionaldehyde to ice. At 255 K the Henry's law constant of propionaldehyde is 3.5 mol/m^3 Pa; thus, even for the highest propionaldehyde partial pressure of 0.45 mbar at this temperature, the concentration of propionaldehyde in the DI would be less than 2 mol/cm^3, resulting in a molar ratio propionaldehyde-to-water of less than 0.03, where dissolution into the DI is only of minor importance.

To summarize, Langmuir-type surface adsorption seems to be the dominant process of the relative weak interaction between ice and propionaldehyde. The hydrogen-bonding structure of the DI, as well as its thickness, is not influenced by the interaction between ice and propionaldehyde. However, we cannot exclude minor dissolution of propionaldehyde in the DI following Henry's law.

3.1.5 Conclusion

Using the surface sensitive ambient pressure X-ray spectroscopy methods XPS and NEXAFS, we directly studied the molecular interaction between ice and propionaldehyde under conditions relevant for environmental discussions. In the context of this analysis we measured isotherms from 230 K to 270 K and at propionaldehyde partial pressures from ~10^{-3} mbar to 0.76 mbar, i.e. under conditions for which the DI is expected to undergo a strong change in thickness, even in the absence of the adsorption of other species. Our measurements showed weak propionaldehyde adsorption in ice, with an adsorption enthalpy of 6.5 kJ/mol. We also did not observe and signs of decomposition of propionaldehyde upon adsorption, which could be conclusively deduced from a comparison of the photoelectron spectrum of the adsorbed molecules with that of gas phase propionaldehyde.

3.1.6 Acknowledgements

We acknowledge support by the Director, Office of Science, Office of Basic Energy Sciences, and by the Division of Chemical Sciences, Geosciences and Biosciences of the U.S. Department of Energy at LBNL under Contract No. DE-AC02-05CH11231. The Advanced Light Source is supported by the Director, Office of Science, Office of Basic Energy Sciences of the U.S. Department of Energy at LBNL under Contract No. DE- AC02-05CH11231. The work was performed within the context of the PhD study of A. Waldner (Swiss National Science Foundation grant # 149629). We acknowledge the experiments and work performed by J. T. Newberg and S. Pletincx.

Bibliography

Atkinson, R.: Atmospheric chemistry of VOCs and NO_x. *Atmospheric environment*, **34(12)**, 2063-2101, 2000.

Barr, T. L., Seal, S.: Nature of the use of adventitious carbon as a binding energy standard. *Journal of Vacuum Science & Technology A: Vacuum, Surfaces, and Films*, **13(3)**, 1239-1246, 1995.

Barrie, L. A., Bottenheim, J. W., Schnell, R. C., Crutzen, P. J., Rasmussen, R. A.: Ozone destruction and photochemical reactions at polar sunrise in the lower Arctic atmosphere, *Nature*, **334**, 138–141, 1988.

Bartels-Rausch, T., Jacobi, H. W., Kahan, T. F., Thomas, J. L., Thomson, E. S., Abbatt, J. P. D., Ammann, M., Blackford, J. R., Bluhm, H., Boxe, C., Domine, F., Frey, M. M., Gladich, I., Guzmán, M. I., Heger, D., Huthwelker, Th., Klán, P., Kuhs, W. F., Kuo, M. H., Maus, S., Moussa, S. G., McNeill, V. F., Newberg, J. T., Pettersson, J. B. C., Roeselová, M., Sodeau, J. R.: A review of air-ice chemical and physical interactions (AICI): liquids, quasi-liquids, and solids in snow, *Atmos. Chem. Phys.*, **14**, 1587–1633, 2014.

Bluhm, H., Ogletree, D. F., Fadley, C. S., Hussain, Z., Salmeron, M.: The premelting of ice studied with photoelectron spectroscopy. *Journal of Physics: Condensed Matter*, **14(8)**, L227, 2002.

Chen, G., Huey, L. G., Crawford, J. H., Olson, J. R., Hutterli, M. A., Sjostedt, S., Tanner, D., Dibb, J., Lefer, B., Blake, N., Stohl, A., Davis, D.: An assessment of the polar HOx photochemical budget based on 2003 Summit Greenland field observations. *Atmospheric Environment*, **41(36)**, 7806-7820.

Collignon, B., Picaud, S.: Comparison between methanol and formaldehyde adsorption on ice: a molecular dynamics study. *Chemical physics letters*, **393.4**, 457-463, 2004.

Dash, J. G., Fu, H., Wettlaufer, J. S.: The premelting of ice and its environmental consequences. *Reports on Progress in Physics*, **58(1)**, 115, 1995.

Dominé, F., Shepson, P. B.: Air-snow interactions and atmospheric chemistry. *Science*, **297(5586)**, 1506-1510, 2002.

Douglass, A. R., Newman, P. A., Solomon, S.: The Antarctic ozone hole: An update. *Physics Today*, **67(7)**, 42-48, 2014.

Gelius, U., Heden, P. F., Hedman, J., Lindberg, B. J., Manne, R., Nordberg, R., Nordling, C., Siegbahn, K.: Molecular spectroscopy by means of ESCA III. Carbon compounds. *Physica Scripta*, **2(1-2)**, 70, 1970.

Grannas, A. M., Shepson, P. B., Guimbaud, C., Sumner, A. L., Albert, M., Simpson, W., Dominé, F., Boudries, H., Bottenheim, J., Beine, H. J., Honrath, R. (2002): A study of photochemical and physical processes affecting carbonyl compounds in the Arctic atmospheric boundary layer. *Atmospheric Environment*, **36(15)**, 2733-2742, 2002.

Grannas, A. M., Bogdal, C., Hageman, K. J., Halsall, C., Harner, T., Hung, H., Kallenborn, R., Klán, P., Klánová, J., Macdonald, R. W., Meyer, T., Wanian, F.: The role of the global cryosphere in the fate of organic contaminants. *Atmospheric Chemistry and Physics*, **13(6)**, 3271-3305, 2013.

Guimbaud, C., Grannas, A. M., Shepson, P. B., Fuentes, J. D., Boudries, H., Bottenheim, J. W., Dominé, F., Houdier, S., Perrier, S., Biesnenthal, B., Splawn, B. G.: Snowpack processing of acetaldehyde and acetone in the Arctic atmospheric boundary layer. *Atmospheric Environment*, **36(15)**, 2743-2752, 2002.

Hauptmann, M., Lubin, J. H., Stewart, P. A., Hayes, R. B., Blair, A.: Mortality from solid cancers among workers in formaldehyde industries. Environ Monit Assess (2010), *American Journal of Epidemiology*, **159**, 1117–1130, 2010.

Houdier, S., Perrier, S., Dominé, F., Cabanes, A., Legagneux, L., Grannas, A. M., Guimbaud, C., Shepson, P. B., Boudries, H.,Bottenheim, J. W.: Acetaldehyde and acetone in the Arctic snowpack during the ALERT2000 campaign. Snowpack composition,

incorporation processes and atmospheric impact. *Atmospheric Environment*, **36(15)**, 2609-2618, 2002.

Hüfner, S.: Photoelectron spectroscopy: principles and applications. *Springer Science & Business Media*, **3**, 2013.

Huthwelker, T., Ammann, M., Peter, T.: The uptake of acidic gases on ice. *Chem. Rev.*, **106**, 1375-1444, 2006.

Jacobi, H. W., Kwakye-Awuah, B., Schrems, O.: Photochemical decomposition of hydrogen peroxide (H2O2) and formaldehyde (HCHO) in artificial snow. *Annals of glaciology*, **39(1)**, 29-33, 2004.

Jeffrey, G. A: An introduction to hydrogen bonding. *New York: Oxford university press*, **32**, 1997.

Kuo, M. H.: Trace Gas-Induced Brine and Disordered Interfacial Layers on Ice *Doctoral dissertation, Columbia University*, 2013

Lary, D. J., Shallcross, D. E.: Central role of carbonyl compounds in atmospheric chemistry. *Journal of Geophysical Research: Atmospheres*, **105(D15)**, 19771-19778, 2000.

McNeill, V. F., Loerting, T., Geiger, F. M., Trout, B. L., Molina, M. J.: Hydrogen chloride-induced surface disordering on ice. *Proceedings of the National Academy of Sciences*, **103(25)**, 9422-9427, 2006.

McNeill, V. F., Geiger, F. M., Loerting, T., Trout, B. L., Molina, L. T., Molina, M. J.: Interaction of hydrogen chloride with ice surfaces: The effects of grain size, surface roughness, and surface disorder. *The Journal of Physical Chemistry A*, **111(28)**, 6274-6284, 2007.

McNeill, V. F., Grannas, A. M., Abbatt, J. P. D., Ammann, M., Ariya, P., Bartels-Rausch, T., Domine, F., Donaldsin, D. J., Guzman, M. I., Heger, D., Kahan, T. F., Klan, P., Masclin, S., Toubin, C., Voisin, D.: Organics in environmental ices: sources, chemistry, and impacts. *Atmospheric Chemistry and Physics*, **12(20)**, 9653-9678, 2012.

Moussa, S. G., El-Fadel, M., Saliba, N. A.: Seasonal, diurnal and nocturnal behaviors of lower carbonyl compounds in the urban environment of Beirut, Lebanon. *Atmospheric Environment*, **40(14)**, 2459-2468, 2006.

Newberg, J. T., Bluhm, H.: Adsorption of 2-propanol on ice probed by ambient pressure X-ray photoelectron spectroscopy. *Physical Chemistry Chemical Physics*, **17(36)**,

23554-23558, 2015.

Nilsson, A., Nordlund, D., Waluyo, I., Huang, N., Ogasawara, H., Kaya, S., Bergmann, U.,Näslund, L. Å., Öström, H., Wernet, Ph., Andersson, K. J., Schiros, T., Petterson, L. G. M.: X-ray absorption spectroscopy and X-ray Raman scattering of water and ice; an experimental view. *Journal of Electron Spectroscopy and Related Phenomena*, **177(2)**, 99-129, 2010.

Petitjean, M., Mirabel, P., Calvé, S. L.: Uptake measurements of acetaldehyde on solid ice surfaces and on solid/liquid supercooled mixtures doped with HNO3 in the temperature range 203−253 K. *The Journal of Physical Chemistry A*, **113(17)**, 5091-5098, 2009.

Petrenko, V. F., Ryzhkin, I. A.: Electron energy spectrum of ice. *Physical review letters*, **71(16)**, 2626, 1993.

Piao, H., McIntyre, N. S.: Adventitious carbon growth on aluminium and gold–aluminium alloy surfaces. *Surface and interface analysis*, **33(7)**, 591-594, 2002.

S. Pletincx, L. Trotochaud, L. Fockaert, J. M. C. Mol, H. Bluhm, H. Terryn, T. Hauffman: In Situ Characterization of the Initial Effect of Water on Molecular Interactions at the Interface of Organic/Inorganic Hybrid Systems *ACS letters*, under review, 2017.

Seinfeld, J. H., Pandis, S. N.: Atmospheric chemistry and physics: from air pollution to climate change.", *2nd ed. Wiley-Intersicience*, Hoboken, 1232, 2006.

Shepson, P. B., Sirju, A. P., Hopper, J. R., Barrie, L. A., Young, V., Niki, H., Dryfhout, H.: Sources and sinks of carbonyl compounds in the Arctic Ocean boundary layer: Polar Ice Floe Experiment. *Journal of Geophysical Research: Atmospheres*, **101(D15)**, 21081-21089, 1996.

Simpson, W. R., Glasow, R. V., Riedel, K., Anderson, P., Ariya, P., Bottenheim, J., Burrows, J., Burrows, J., Carpenter, L. J., Frieß, U., Goodsite, M. E., Heard, D., Hutterli, M., Jacobi, H.-W., Kaleschke, L., Neff, B., Plane, J., Platt, U., Richter, A., Roscoe, H., Sander, R., Shepson, P., Sodeau, J., Steffen, A., Wagner, T., Wolff, E.: Halogens and their role in polar boundary-layer ozone depletion. *Atmospheric Chemistry and Physics*, **7(16)**, 4375-4418, 2007.

Sokolov, O., Abbatt, J. P. D.: Adsorption to ice of n-alcohols (ethanol to 1-hexanol), acetic acid, and hexanal. *The Journal of Physical Chemistry A*, **106(5)**, 775-782, 2002.

Starr, D. E., Pan, D., Newberg, J. T., Ammann, M., Wang, E. G., Michaelides, A., Bluhm, H.: Acetone adsorption on ice investigated by X-ray spectroscopy and density

functional theory. *Physical Chemistry Chemical Physics*, **13(44)**, 19988-19996, 2011.

Thomas, J. L., Dibb, J. E., Huey, L. G., Liao, J., Tanner, D., Lefer, B., von Galsow, R., Stutz, J.: Modeling chemistry in and above snow at Summit, Greenland–Part 2: Impact of snowpack chemistry on the oxidation capacity of the boundary layer. *Atmospheric Chemistry and Physics*, **12(14)**, 6537-6554, 2012.

Tunsaringkarn, T., Tassanee, P., Morknoy, D., Siriwong, W., Kanjanasiranont, N., Semathong, S., Rungsiyothin, A., Zapaung, K. *International Journal of Research in Chemistry and Environment*, **4(2)**, 2248-9649, 2014.

Winkler, A. K., Holmes, N. S., Crowley, J. N.: Interaction of methanol, acetone and formaldehyde with ice surfaces between 198 and 223 K. *Physical Chemistry Chemical Physics*, **4(21)**, 5270-5275, 2002.

Yang, J., Honrath, R. E., Peterson, M. C., Dibb, J. E., Sumner, A. L., Shepson, P. B., Frey, M., Jacobi, H.-W., Blake, N.: Impacts of snowpack emissions on deduced levels of OH and peroxy radicals at Summit, Greenland. *Atmospheric Environment*, **36(15)**, 2523-2534, 2002.

CHAPTER 4

The interaction ice – HCOOH

4.1 The interaction ice – HCOOH investigated using XPS & NEXAFS

To be submitted to *The Journal of Physical Chemistry C* as: Waldner, A., Kong, X., Ammann, M., Orlando, F., Artiglia, L., Huthwelker, T., Kleibert, A., Birrer, M. and Bartels-Rausch, T.: The interaction ice – HCOOH investigated using XPS & NEXAFS.

4.1.1 Abstract

Ice is ubiquitous in the environment in the form of atmospheric ice and as cryosphere. Interactions between trace gases and ice are important for environmental chemistry and climate, as they, for example, may modify the composition and oxidation capacity of the atmosphere. Here, partitioning of trace gases to ice plays a prominent role. The interaction between some trace gases and ice has been shown to

exhibit a not fully understood partitioning. This may be linked to changes of the ice and its properties, especially in the topmost ice layers, often called the disordered interface (DI).
This study looks directly at the interaction between one of the strongest organic acids common in the atmosphere, HCOOH, and ice at 233 K and 253 K. It makes use of ambient pressure X-ray photoelectron spectroscopy (XPS) and partial electron (Auger) yield near edge X-ray absorption fine structure (NEXAFS) spectroscopy. The combination of these two surface sensitive techniques allows us to locate HCOOH in the ice and to determine if the interaction between HCOOH and ice leads to a modification of the DI.
Oxygen K-edge NEXAFS analyses show that the interaction ice–HCOOH does not lead to changes of the DI. Electron kinetic energy dependent C1s photoemission spectra indicate that HCOOH does not only adsorb to the ice surface but penetrates several nm into the pure ice. This can be interpreted as dissolution into the liquid like DI thus indicates the importance of the DI for exchange processes.

4.1.2 Introduction

Atmospheric and terrestrial ice, including cirrus clouds, sea-ice and snow, is omnipresent in the environment and has the capability to heavily influence environment and climate (Grannas et al. (2013), Bartels-Rausch et al. (2014)). The interactions of trace gases with ice influence the fate of the trace gases through uptake and release, as well as (photo)chemical reactions. Ice – trace gas interactions impact a number of biogeochemical and atmospheric cycles (e.g. Poole and McCormick (1988), Douglass et al. (2014)). For example, Solomon et al. (1997) showed that the presence of ice clouds locally decreases ozone concentration. Heterogeneous reactions at the ice surfaces involving HCl play a role.
The partitioning of trace gases between atmosphere and ice varies strongly between individual trace gases and is generally related to their tendency to form hydrogen-bonds at the ice surface (Pouvesle et al. (2010)). However, some trace gases show an uptake of the gas to the ice revealing two regimes: fast and reversible adsorption via hydrogen-bonding, and a long-term, partly irreversible uptake (Kerbrat et al. (2010), Abbatt (2003), Huthwelker et al. (2006) and references therein). The initial, fast and reversible adsorption can be reasonably well-described by Langmuir-type adsorption (Abbatt (2003), Huthwelker et al. (2006) and references therein). The long-term uptake can exceed this adsorptive uptake by several orders of magni-

tude (Kerbrat et al. (2010)) thus can be of major importance. Currently, the long-term uptake is not well understood. Processes, such as diffusion into the ice, dissociation, formation of hydrates and/or a modification of the ice structure may play a role. For example, McNeill et al. (2006) and McNeill et al. (2007) showed that the uptake of strong acids may modify the structure of the ice surface layers. Such a modifying interface may represent a reservoir in which gases could dissolve, leading to a long-term uptake via a positive feedback mechanism (McNeill et al. (2006)). Hereby, the acidity of a trace gas may play an important role due to dissociation and ion hydration capability (Bartels-Rausch et al. (2014), Huthwelker et al. (2006))
Already in 1840, Faraday demonstrated the importance of the ice surface layers and postulated that they are different from the bulk of the ice. Due to missing outer bonds, the crystal structure is modified forming an inherent interfacial layer. In the case of ice this layer is called DI, pre-melting, or quasi-liquid layer. It is characterized by changes of the average orientation and order of the water (H_2O) molecules at the ice–air interface. The thickness of this layer increases with increasing temperature, especially at temperatures higher than ~255 K, close to the melting point of ice (Henson and Robinson (2004)). Furthermore, impurities may enhance the disorder of the H_2O-molecules and increase the thickness of the DI (Bluhm et al. (2002), Nilsson et al. (2010), Bartels-Rausch et al. (2014)). However, the literature is full of unresolved inconsistencies about the DI. For example the lateral and vertical homogeneity, as well as the phase state of the interface is controversially discussed.

Until now, only few direct measurements at environmentally relevant conditions (i.e., temperatures from 210 K to the melting point of ice (273 K), and low surface concentrations within/close to the monolayer-range) looking at the importance of the DI for ice – trace gas interactions are available. The limited knowledge of molecular level processes of ice – trace gas interactions, especially in the DI, hampers an appropriate inclusion of ice as a substrate in models of various scales such as global chemistry climate models (GCMs) (Bartels-Rausch et al. (2014)). Particularly short chain organics deserve further study. They are present in boundary layer air above ice, and only limited studies of their interactions with ice are available (Millet et al. (2015) and references therein). Formic acid (HCOOH), one of the strongest organic short chain acids abundant in the atmosphere has mixing ratios of around ~2 parts per billion in boundary layer air (e.g. Liu et al. (2012)). HCOOH's primary sources are photochemical oxidation of volatile

organic compounds and biogenic sources such as direct forest emissions (Paulot et al. (2009), Neeb et al. (1997), Millet et al. (2015), Stavrakou et al. (2012) and references herein). Main HCOOH sinks include slowly proceeding photochemical oxidation (~25 days, Jacob and Wofsy (1988)) as well as dry and wet deposition. Since HCOOH is soluble in water with an effective Henry's law constant of ~100 M atm^{-1} at pH 7 (Sander (2016)), it is efficiently removed from the atmospheric boundary layer (e.g. Chameides and Davis (1983); Andrea et al. (1988), Millet et al. (2015), Stavrakou et al. (2012) and references herein). Considering the aforementioned sinks, the atmospheric lifetime of HCOOH in the atmosphere is 2-4 days (Paulot et al. (2011), Stavrakou et al. (2012)). Within that time HCOOH represents a significant sink for in-cloud OH (Jacob (1986)) and has significant impact on key chemical budgets such as NO_x. This makes HCOOH important for atmospheric chemistry (Millet et al. (2015) and references therein). In summary, partitioning of HCOOH to ice has the ability to influence the OH budget, thus the oxidation capacity of the atmosphere.
In this study, we used XPS and NEXAFS to investigate the molecular level picture of the interaction between HCOOH and ice. The investigations cover different ice temperatures, 233 and 253 K, and a broad range of HCOOH partial pressures.
XPS is a surface sensitive method to probe elemental composition with chemical specificity. By changing the energy of the used X-ray, depth profiles of dopants in/on the ice can be measured (e.g. Hofmann (1980), Křepelová et al. (2013)). During our experiments, we analyzed the HCOOH signal originating from at maximum the uppermost 120 ice bilayers.
Electron yield NEXAFS has become an established tool to look at changes of the hydrogen-bonding structure of water and ice of the uppermost ice layers (e.g. Bluhm et al. (2002), Nilsson et al. (2010)). It enables us to analyze changes in the molecular structure of the H_2O-molecules in the ice thus allows investigating changes to the DI.
The combination of XPS and NEXAFS enables us to directly probe the ice surface and changes to the DI, as well as analyze the concentration depth profile and chemical state of the dosed HCOOH. The suitability of using this combination was demonstrated in previous studies (e.g. Křepelová et al. (2010) and Křepelová et al. (2013) and Orlando et al. (2016)).

4.1.3 Methods

The X-ray electron spectroscopy experiments of the interaction between ice and HCOOH were performed at the Swiss Light Source (SLS) of the Paul Scherrer Institute using the Near Ambient Pressure Photoemission endstation (NAPP) at the beamlines PHOENIX X07MA/B and SIM X11MA. NAPP allows us to perform measurements at pressures up to several mbar (Orlando et al. (2016)), thus to maintain ice samples in equilibrium with their vapor pressure at temperatures close to the melting point. The set-up is presented in Figure 4.1. It consists of a small *in situ* experimental cell (grey shaded area), a surrounding UHV chamber, the analyzer with differential pumping stages, and the dosing system.

Using the photon energy range of SIM (100 to 2000 eV), oxygen (O) 1s and carbon

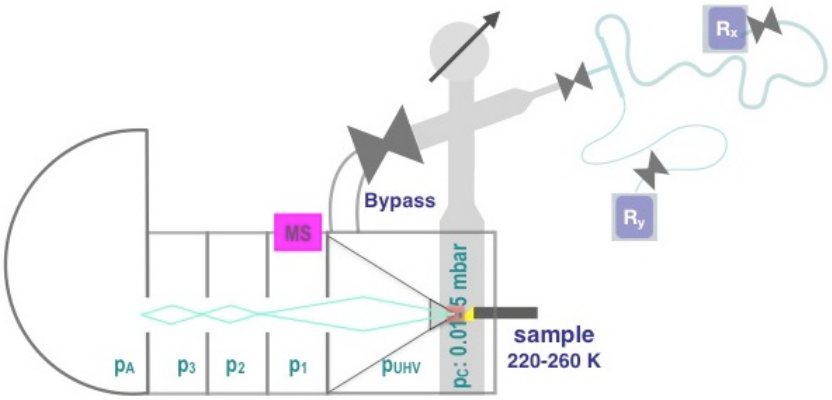

Figure 4.1: Schematic view of NAPP: The grey shaded area indicates the *in situ* experimental cell in which ice samples (shown in Figure 2) are analyzed. On the right-hand side of the sketch a detailed scheme of one of the dosing systems used for the HCOOH-ice experiments is presented. R_x and R_y refer to the temperature-stabilized sources for water and formic acid vapors, respectively.

(C) 1s photoemission, and O and C K-edge absorption spectra were recorded. The low photon energy ($\mathbf{h\nu}$), thus inelastic mean free path (IMFP) of the photoelectrons enables surface sensitive analyses. The IMFP describes the characteristic length over which electrons at a given kinetic energy (E_{kin}) can travel without inelastic scattering losses. For kinetic energies relevant for our experiment, the IMFP increases with increasing E_{kin}. We estimated the IMFP of photoelectrons in ice based on calculations from a theoretical model (NIST Standard Reference Database), using a band gap of 7.8 eV (Petrenko and Ryzhkin (1993)) and a mass density of 1 g/cm^{-3} for ice. Since the model allows only a calculation of the IMFP

up to 2000 eV $\mathbf{h\nu}$, two different extrapolations (polynomial and linear) were used for the estimation of the IMFP at higher E_{kin}. The probing depth of elastically scattered electron spectroscopy is given by three times the IMFP multiplied by $\cos(\boldsymbol{\theta})$. $\boldsymbol{\theta}$ is the set-up dependent take-off angle of detected electrons relative to the surface normal, in our set-up 30°. 95 % of the detected photoelectrons originate from molecules found in a layer ranging from the surface to the probing depth.
The maximum probing depth at SIM beamline is 12 nm. The higher photon energies at PHOENIX (2200 to 8000 eV), allow us to acquire O1s and C1s spectra with higher kinetic energies, therefore probe deeper and investigate the uppermost ~60 nm of the sample.
The ice samples were prepared in situ by depositing water (H_2O) from the gas phase onto a cooled sample holder in the *in situ* experimental cell.
For the dosing from a temperature stabilized source, either high precision leak valves, or a capillary dosing approach were used. For this, ~15 ml liquid water (Fluka TraceSelect Ultra; Water ACS reagent, for ultratrace analysis) and ~2.5 ml liquid formic acid (LC-MS ultra by Sigma-Aldrich) was filled into a reservoir. Depending on the temperature of the reservoir, different vapor pressures can be set in the reservoir. These and the capillaries' dimensions, or the adjustment of the leak valves, determine the flux into, thus the pressure in the *in situ* experimental cell. We used stainless steel capillaries of about ~1 m length and inner diameters from 0.8 to 1.0 mm to dose H_2O, and an ~1 m long fused silica capillary (postnova analytics) with an inner diameter of 0.1 or 0.2 mm for HCOOH. The Knudsen numbers for our experimental conditions are far below 0.01 for all capillaries at the high-pressure side, thus cross contamination by diffusion is negligible. Before dosing, the HCOOH as well as the H_2O was degassed by at least 4 freeze-pump-thaw cycles. The purity of HCOOH vapor dosed to the *in situ* experimental cell was confirmed by proton transfer reaction mass spectrometry (PTRMS) and ion chromatography (IC). Neither PTRMS nor IC showed the presence of any other carbon species than HCOOH and HCOOH dimers (detection limit: lower ppb range).
During this study, ice samples were investigated at two temperatures: 233 K and 253 K. The temperature of the ice sample was derived based on measurements of its vapor pressure. To grow ice at those temperatures, water was dosed in the *in situ* experimental cell at about 0.1 mbar and 1 mbar, respectively. The pressure was measured with mks Baratron capacitance manometers (0.1 Torr, 1 mbar, and/or 10 Torr) with an accuracy of 10^{-4} times the measurement range. The pressure of water in the *in situ* experimental cell determines the temperature

at which the ice is in equilibrium with its gas phase, meaning the ice is neither growing nor evaporating. Minimal variations in the ice temperature (< 0.1 K) led to fluctuations in the gas phase pressure, so that the actual achieved accuracy of the pressure measurement was ~2 $\cdot 10^{-3}$ mbar, at best.
After ascertaining a stable pressure in the *in situ* experimental cell, the sample holder was cooled until ice nucleation was detected either by a pressure decrease or by visual observation. For the warmer ice, onset of ice nucleation was observed at ~250 K and the ice crystalized only on few spots (1-10 spots) on the sample holder. The ice grew slowly while keeping the oversaturation for about half an hour leading to an ice sample composed of very few (< 10) crystals. The ice was about 0.5-2 mm thick and appeared optically crystal clear. For colder ice, growth was triggered at 200 K. The ice samples were generally whiter than the ice at 253 K, and individual crystals could not be identified.
To stop the ice growth, the temperature was raised until the pressure in the *in situ* cell, given by the vapor pressure of the ice sample, reached approximately the initial pressure before the onset of nucleation. This led to equilibration and subsequent restructuring of the ice samples.
To minimize perturbations due to radiative heating, heating by X-ray beam energy deposition, and the impact of the electron sampling aperture on the pressure field (gradient) near the ice surface, we kept a slight oversaturation (~5 %) in the *in situ* experimental cell. To reduce damage by the beam, the incident photon flux of ~10^{12} photons/sec was reduced by up to 80 %.
Once the clean ice was equilibrated, it was characterized by measuring photoemission (PE) and NEXAFS spectra. For all PE measurements, dwell time and pass energy were between 0.5 -2 milliseconds and 10-50 eV. PE led to charging of the ice samples, which was observed as shifts of 0-15 eV to lower E_{kin}. Therefore, all C1s PE spectra are, similar as in Křepelová et al. (2010) and Křepelová et al. (2013), referenced to the O1s peak at an E_{Bind} of 533.4 eV of the corresponding measurement.
In addition, we measured partial-electron-yield NEXAFS spectra at the C and O K-edges using E_{kin} windows at the background of the Auger lines of C (190-210 eV) and of O (450-470 eV). Due to the detection of the background of the Auger lines, including inelastically scattered Auger electrons, the probing depth of the O K-edge NEXAFS analysis can be estimated to be more than ~ 6 nm (based on the IMFP of the elastically scattered Auger electrons of ~2.5 nm). This means that a significant, non-negligible amount of the detected electrons may originate from substantially higher depths but surface sensitivity is still ensured. For these NEX-

AFS measurements, a pass energy of 20 eV and dwell times of 0.5-2 milliseconds were used. Polarization was set to 54.7° to ensure a signal intensity invariant to the angular orientation of the molecules. In the O K-edge regions of most interest, 529 to 542 eV $\mathbf{h\nu}$, we used a photon energy step size of 0.2 eV instead of 1 eV. For C K-edge analysis we chose a step size of 0.5 eV over the whole measurement range. All NEXAFS spectra were corrected for the incident photon flux varying with time and $\mathbf{h\nu}$. For that the measurements were corrected for photon energy dependent background absorption (I_0). For the O K-edge, I_0 was measured on a diode in the *in situ* experimental cell at the same measurement position and water vapor pressure used for the ice NEXAFS, whereas the C K-edge spectrum of the clean ice surface was used for the C K-edge correction. To compensate for variations in photon flux with time and between different beam times, all spectra were normalized to the photon current measured during the reference and data acquisition using beamline mirrors before the NAPP endstation. The reference O K-edge NEXAFS of water displayed in Figure 4.3 was obtained independently in earlier measurements at beamline 11.0.2 at the Advanced Light Source, California (ALS). A detailed description of the O K-edge measurements performed at ALS was published previously (e.g. Bluhm et al. (2002)). We normalized all O K-edge spectra to their integrated area between 534 and 555 eV, for reason of comparison. To obtain depth profiles of the chemical composition, the $\mathbf{h\nu}$ of the incoming X-rays was varied. The ratios of the respective HCOOH C1s peak areas to the O1s peak areas from spectra measured at the same photoelectron E_{kin} were calculated. An exception to this procedure is experiment 5 (see Table 1). Here, C1s and O1s measured at the same photon energy were used for the analysis. The calibration of the intensity ratios, $I_{carboxyl}/I_{oxygen}$, was performed by measuring gas-phase CO_2. CO_2 of around 0.1-0.5 mbar was admitted into the chamber and C 1s and O 1s PE spectra (in the absence of a sample in front of the analyzer sampling orifice) at the same photon energies used for the ice-experiments were recorded. In addition, reference spectra at a certain photon energy were measured for stability analysis of the HCOOH concentration. The C1s spectra were normalized to the area of O1s spectra measured alternatingly. Only measurements recorded between stable reference C/O ratios, meaning deviations of less than 20%, were used for depth profile analysis.

4.1.4 Results and discussion

Characterization of clean crystalline ice

An exemplary PE survey spectrum of clean ice measured at 740 eV $\mathbf{h\nu}$, covering a binding energy (E_{Bind}) range from 100-630 eV, is shown in Figure 4.2. The O 1s PE peak at 533.4 eV, together with its tail of inelastic scattered photoelectrons around 540 eV, and the O K-edge Auger peak at 250 eV (meaning 540 eV E_{kin}) are the only noticeable features. A zoom-in on the C1s region shows minor carbon contamination of less than 1 %. A slight change in the optical appearance of the ice surfaces at the sample spot emerged after about half an hour (Inlet in Figure 4.2). The imprint remained even after changing the sampling position. We interpret this as surface roughening in response to the thermal perturbation under the effect of the X-ray beam or as defect created by the radiation. Nevertheless, our spectra of clean ice did not change with time or vary with the presence or absence of this feature.

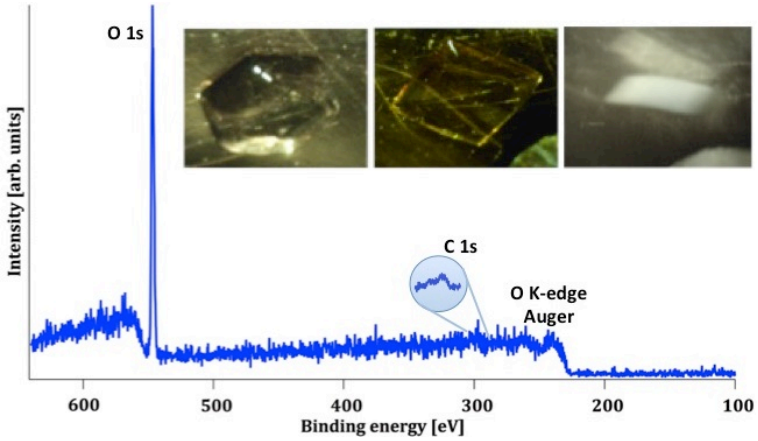

Figure 4.2: Clean ice in NAPP: PE survey spectrum of clean ice at 253 K acquired at beamline SIM X11MA at SLS. The inlet shows typical ice samples. The structure indicates single crystal ice. The PE spectrum displays minor contamination of the clean ice.

The local hydrogen-bonding structure of the ice surface layers can be analyzed using O K-edge NEXAFS spectra. In the range from 537 to 545 eV, the ice O K-edge NEXAFS spectra show a two-peak feature (main- and post-edge, C and D respectively), typical for ice. The post-edge peak results from strongly H-bonded

OH. In tetrahedral ice both OH groups are coordinated with neighboring H_2O molecules, thus the post-edge peak is well pronounced. The weakly coordinated OH molecules dominating in liquid water lead to different peak ratios compared to ice. As displayed in Figure 4.3, the water O K-edge NEXAFS spectrum exhibits a different main- to post-edge peak ratio with a maximum around 538 eV (e.g. Nilsson et al. (2010)).
In addition, ice and water O K-edge NEXAFS spectra exhibit an additional characteristic peak at 535 eV (B). The intensity of this pre-edge peak increases with increasing disorder of the H_2O molecules. It corresponds to a transition to empty states similar to the $4a_1$ lowest unoccupied molecular orbital of gas-phase H_2O molecules. Because of the dipole selection rule, the intensity of this transition depends on the degree of s or p character of the molecular energy state. In ice, oxygen is tetrahedrally coordinated thus symmetry arguments indicate predominant s-symmetry. With increasing disorder this symmetry starts to break, thus p-character is more probable and the peak intensity increases (e.g. Bluhm et al. (2002)).
Features at 532.5 eV (A), could be assigned to C=O or N=O bonds that would indicate contamination of the clean ice.
The absence of a peak in region B in our spectra indicate only marginal carbon-oxygen contamination species on the clean ice prior to exposure to HCOOH.
In general we are able to state that the shape of the O K-edge NEXAFS spectra of clean ice obtained within the context of this study, shown in Figure 4.3, are in good agreement with those reported elsewhere (e.g. Křepelová et al. (2013) dashed, Bluhm et al. (2002) in black) and were reproducible between different measurements although we measured at a different temperature.

According to Bluhm et al. (2002) analyzing the DI using Auger yield NEXAFS spectroscopy, pronounced changes of the DI are not expected to occur until ice temperatures are around 253 K. Nevertheless, we observe a distinct difference between our spectra and those obtained by Bluhm et al. (2002) and Křepelová et al. (2013) at a similar temperature. Compared to their spectra, ours indicate less disorder. These differences may originate from small systematic errors, as for example properties of the X-ray at the measurement spot due to the use of different beamlines and set-ups (Nilsson et al. (2010)), but also pressure and temperature off-sets at the sample spot of the different experimental set-ups. However, also different crystalline properties of ice, which are indicated due to the macroscopic appearance, may explain such a difference. Less polycrystalline ice, featuring

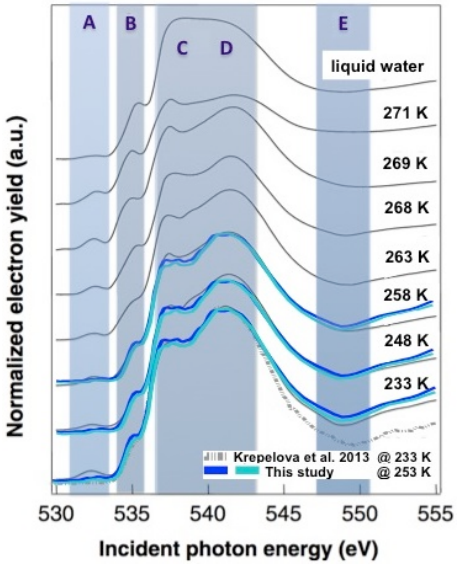

Figure 4.3: Characterization of clean ice: Oxygen K-edge NEXAFS spectra of clean ice acquired at beamline SIM X11MA at SLS for ice at a temperature of 253 K. For reasons of comparison O K-edge NEXAFS acquired at Advanced Light Source (black and grey) are added (Bluhm et al. (2002)).

less grain boundaries, may exhibit a more ordered structure at the sample spot compared to the polycrystalline ice films used in Křepelová et al. (2013) and Bluhm et al. (2002). The effects of enhanced disorder due to the higher temperature and the enhanced order due to less polycrystalline ice may cancel out, and result in O K-edge NEXAFS spectra at 253 K showing similar (dis)order to the those at 233 K, but more polycrystalline ice by Křepelová et al. (2013) and Bluhm et al. (2002).
In addition to the discussed difference in disorder, a distinct difference between all spectra could be observed for photon energies higher than 545 eV. This difference may be explained by a drifting sensitivity due to slightly unstable ice, which may also have affected measurements by Bluhm et al. (2002) and Křepelová et al. (2013) (personal communication).

HCOOH on ice

In Table 4.1 and Figure 4.4, we give a summary of the different experiments. Figure 4.4 shows the iso-solubility curves of HCOOH in mole fraction as a function of

Table 4.1: Experimental conditions and summary of results. Roman numerals indicate oxygen K-edge NEXAFS measurements, whereas Arabic numerals represent XPS experiments.

Exp.	T [K]	p_{FA} [mbar]	n_{CFA}/n_{O2}	n_{FA}/n_{H2O}	d [nm]	b[nm]	N_{FA} [10^{15}/cm^2]
1	233	0.005	0.18	0.28	3	5	1.5
2-3	233	0.015	0.25	0.51	2.5-3	5	3
4	233	0.035	0.45	4.5	4	8	9
I	253	0.005					
II	253	0.010					
5-6	253	0.015	0.17	0.26	2.5	4	2
III	253	0.020					
IV,7	253	0.050					
V	253	0.060					
8	253	0.106	0.29	0.68	3	8.5	5.5

HCOOH partial pressure (p(HCOOH)) and temperature, based on Henry's Law constants (Sander (2016)). The estimated phase boundary between the HCOOH-solution and ice is displayed as a solid curves. They are calculated according to freezing point depression (Lide (2003)) and Henry's law constants (Jacob (1986) and Sander et al. (2011)). The gray shaded area indicates the deviation of the phase boundary resulting from the two different Henry's Law estimations.
For high p(HCOOH) experiments, indicated in green, we realized an optically observable change of the ice. We interpret this as a melt layer on top of the ice. According to the phase diagram (Fig. 4.4), a phase change may not necessarily be favored during those measurements. In view of the uncertainties related to the exact position of the phase transition on the phase diagram, displayed in grey, as well as the uncertainty in temperature and pressure measurements at the sample spot, we assume that we actually observed a thermodynamic phase change.

Figure 4.5 shows representative C 1s spectra from the ice surface during exposure to different HCOOH pressures. In general, one can say that increasing the p(HCOOH) leads to an increasing overall C1s intensity.
The PE measurements indicate that we could not always ensure negligible carbon contamination of the ice before admission of HCOOH. The extent of contamination varied strongly between the different experiments and appears dependent on the handling history of the chamber. We characterized the observed adventitious carbon contamination of the clean ice and took it into account for the analysis (e.g. blue markers in Figure 4.8).

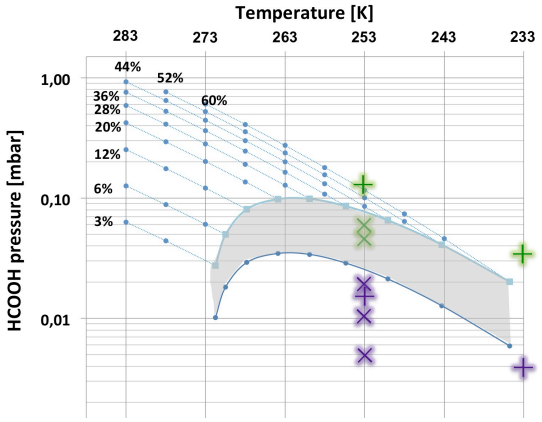

Figure 4.4: Phase diagram HCOOH—ice: Isosolubility curves of formic acid in mole fraction as a function of formic acid partial pressure (y-axis) and temperature (x-axis). Phase boundary between formic acid solution and ice is drawn as a solid curve. The uncertainty of the phase boundary displayed in grey originates from the uncertainty in the Henry constant (dark blue line using estimations by Jacob (1986), light blue by Sander et al. (2011)). The markers indicate the respective XPS depth profiles (+) and oxygen K-edge NEXAFS disorder (x) experiments. Green colored markers indicate high HCOOH partial pressures, whereas purple stands for low HCOOH partial pressure experiments.

Adventitious carbon is a ubiquitous carbon component, which seems to exhibit an instantaneous presence especially on air exposed surfaces (Barr and Sudipta (1995)). A possible source is gas-phase trace amounts of carbon species. Secondary electrons but also the beam itself can lead to decomposition of those species. The resulting fragments can then aggregate to form new, unintended carbon contaminants of variable volatility. The presence of water vapor in a set-up is assumed to increase the observed amount of adventitious carbon condensing on surfaces likely due to displacement effects of organic trace gases from the walls of the chamber and gas dosing lines. (Piao and McIntyre (2002)). Similar radiation chemistry acts on HCOOH leading to increased adventitious carbon patterns in the C1s spectra, increasing and decreasing with increasing and decreasing HCOOH pressures.

At least three Gaussians needed to be used for appropriate representation of the adventitious carbon in the C1s spectrum. The three peaks have E_{Bind} of 285, 286.5, and 288 eV. The adventitious carbon peaks at 285 and 286.5 eV may be assigned to aliphatic carbon and alcohol/ether, respectively. The peak at ~288 eV may be assigned to deprotonated carboxyl (Brown et al. (2012)), as well as

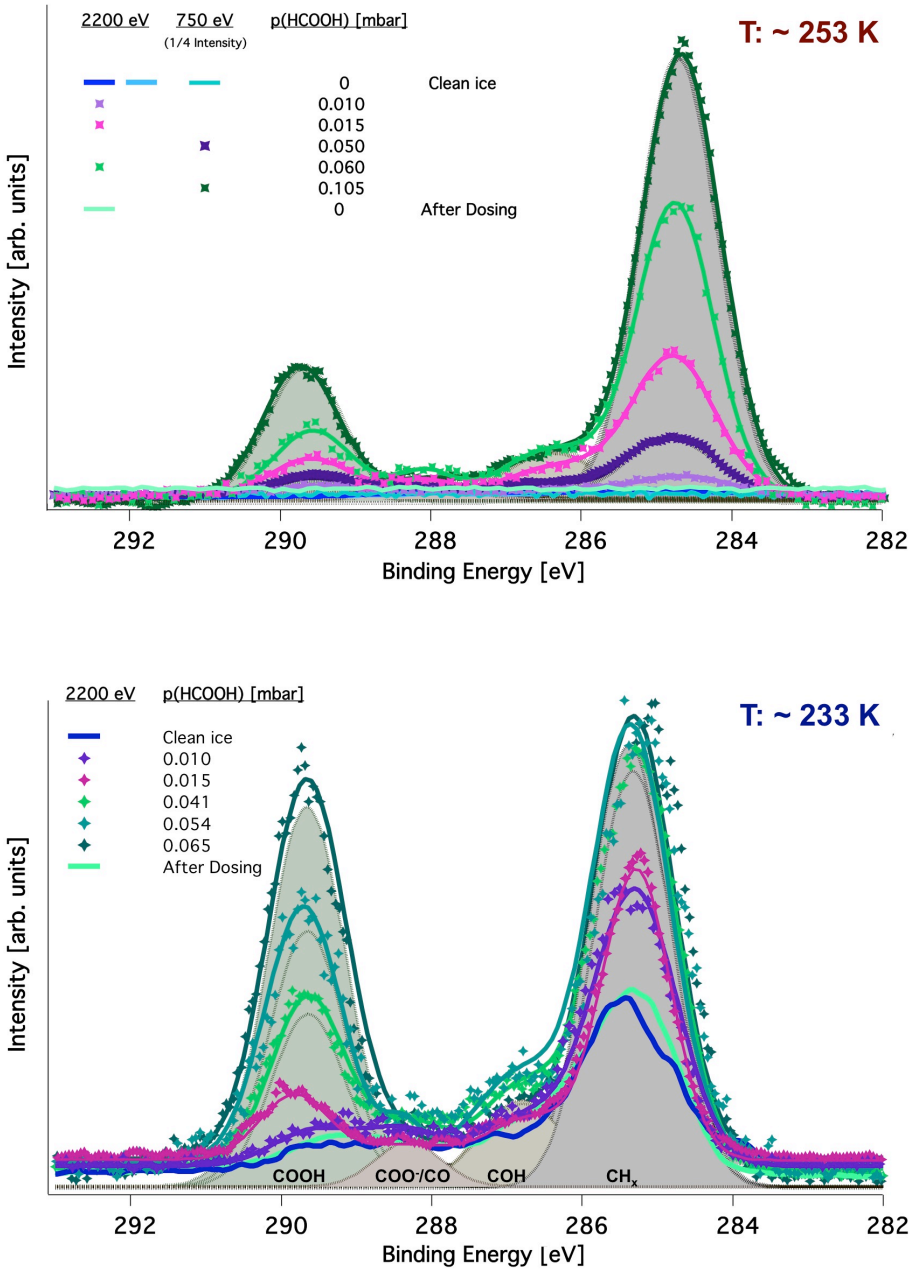

Figure 4.5: Exemplary C1s PE spectrum at 253 K (top) and 233 K (bottom) normalized to the corresponding O1s intensity. Blue spectra show the carbon contamination of clean ice, purple spectra of the interaction ice—HCOOH at low HCOOH partial pressures, green spectra of ice interacting with HCOOH at high HCOOH partial pressures. The error of the partial pressure is 0.005 mbar. Fit and respective peaks are highlighted in various grey shades. Spectra were acquired using beamline PHOENIX X07MA/B (2200 eV hv) and at SIM X11MA (750 eV hv). Spectra measured at 750 eV $\mathbf{h\nu}$ are multiplied by 0.25.

carbonyl.
To differentiate between these two options, Figure 4.6 shows the C K-edge NEXAFS with several identifiable features including the HCOOH and the adventitious carbon features. The C K-edge NEXAFS of HCOOH interacting with ice is dominated by a strong resonance feature at 288.6 eV which can be assigned to the **C1s-π^*** transition of the carboxyl carbon (e. g. Křepelová et al. (2013), Zelenay et al. (2011)). Depronated carboxyl carbon also exhibits a resonance at that energy (Brown et al. (2012)). In addition, at 287 eV a shoulder can be identified, which can be assigned to (aromatic) carbonyl contamination. Also, the feature at 290.5 eV, may represent carbonyl transitions. A small peak at 285 eV indicates the presence of unsaturated carbon (e.g. Zelenay et al. (2011)). The dip at 284 eV as well as the decreasing trend at lower photon energies is likely due to slightly incorrect I_0 normalization. Overall, the features of the C K-edge NEXAFS are consistent with the PE spectra.
Using the C K-edge NEXAFS analysis we can ascertain that carbonyl contamination is present, indicating that the peak at ~288 eV E_{Bind} in the C1s PE spectrum is at least partly due to carbonyl contamination. Since the C K-edge NEXAFS is not sensitive to HCOOH being dissociated or not, due to the overlap of the peaks, neither C K-edge NEXAFS analysis nor XPS analysis, can be used to determine the degree of dissociation.

Most of the spectra displayed in Figure 4.5 were obtained at a photon energy of 2200 eV, therefore providing information about the uppermost 15 nm of the sample. Some spectra, obtained at 750 eV **hν**, are more surface sensitive, displaying information about the topmost 7.5 nm of the ice. The changed ratio of adventitious carbon to carboxylic carbon of the spectra measured at 2200 eV **hν** compared to those at 750 eV **hν** indicated, that adventitious carbon, including the carbon species exhibiting a peak at 288 eV E_{Bind}, is limited to fewer layers at the ice surface.

Even though adventitious carbon was present, there was an observable response of the carboxylic peak to changes in p(HCOOH) at both temperatures as visible in Figure 4.6. However, the signal intensity of the adventitious features is not proportional to p(HCOOH) over the whole pressure range, but appears to level off at high p(HCOOH) indicating saturation effects in detection or in the chemical cycles causing and destroying them. The area of the peak assigned to HCOOH

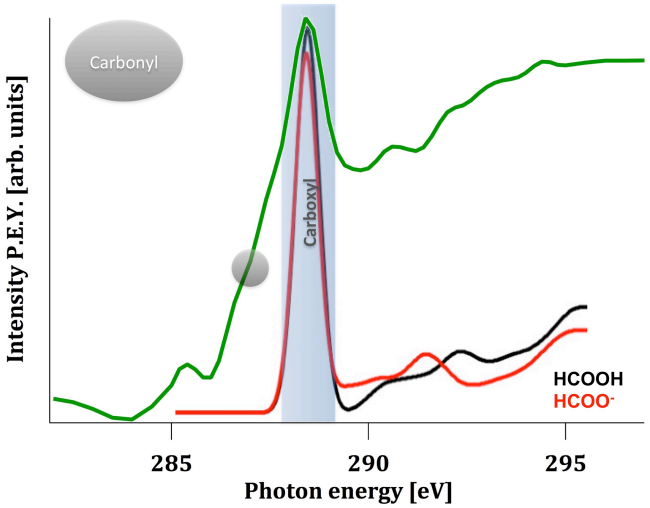

Figure 4.6: C K-edge NEXAFS of HCOOH on ice: The NEXAFS spectrum of HCOOH on ice indicates the primacy and significance of HCOOH interacting with ice in regard to any other functional carbon groups. In red and black calculated spectra are added (Brown et al. (2012)).

increased with higher gas-phase concentrations and returned fully to the initial values after the gas-phase dosing was stopped. The uptake of HCOOH to the ice are fully reversible for all measurements. For the experiments performed at the highest p(HCOOH), for which a melting of the ice surface was thermodynamically induced, also the phase change was reversible. This reversible uptake-behavior of HCOOH to ice is consistent with the adsorption-desorption equilibrium of HCOOH to ice presented by Jedlovszky et al. (2008). Using a combination of coated-wall flow tube (CWFT) experiments and computer simulation (grand canonical Monte Carlo), Jedlovszky et al. (2008) investigated the molecular picture of the interaction between ice and HCOOH. They showed that for ice at 187-221 K and low HCOOH pressures (10^{-5} mbar range), the ice – HCOOH interaction could be well explained using non-dissociative Langmuir-type adsorption. Also Compoint et al. (2002) investigated the interaction of ice and HCOOH, neglecting dissociation in their molecular dynamics simulations. However, dissociation of trace gases on or in ice is postulated to alter the interaction between trace gas and ice, influencing the capacity of ice for the uptake of the trace gas. Due to the presence of carbonyl during our experiments, no detailed analysis of the degree of dissociation of HCOOH in the ice was possible. If one assumes that no carbonyl is present,

the degree of dissociation of HCOOH on ice would be less than 35 %. In conjunction with the corresponding depth profiles of the peak at ~288 eV binding energy, which is similar to the other adventitious carbon compounds (not shown here), we can therefore conclude that dissociation is not a dominant uptake process for ice – HCOOH interactions. This provides justifications of the investigations of Jedlovszky et al. (2008) and Compoint et al. (2002) neglecting dissociation of HCOOH.

We can use the C1s PE data displayed in Figure 4.5 for a first rough estimation of the surface elemental composition. From the measured O1s and C1s peak areas divided by the measured I_0 and the photoelectrons cross sections (e.g. Yeh (1993)), we determine the carbon to oxygen ratios. The elemental ratios of the total carbon to oxygen vary between 0.1-2. Due to the unknown chemical composition of the adventitious carbon, we are unable to estimate the number of adventitious carbon molecules on top of the ice sample.

A first rough estimation of the carboxyl coverage on the ice due to the interaction between ice and HCOOH is possible using the carboxylic carbon to oxygen ratios. The $I_{Carboxyl}/I_O$ elemental ratios are 0.01–0.09 for experiments at 253 K, and 0.01–0.2 for experiments at 233 K. Taking into account that each HCOOH contains two oxygen atoms, the $I_{Carboxyl}/I_{Oxygen}$ ratio translates to $HCOOH/H_2O$ mole ratios of 0.01–0.21 at 253 K and 0.01–0.52 at 233 K.

Using a surface density of water molecules of about 1×10^{15} cm^{-2}, and the respective probe volume, we can roughly estimate the amount of HCOOH at the surface. The probed volume itself can be estimated using the E_{kin} of the photoelectrons in ice, yielding probing depths of ~7.5 nm and ~15 nm. With that, one could state that for the low dosing experiments the HCOOH coverages were close to the monolayer range of 5×10^{14} molec./cm^2 at maximum (Jedlovszky et al. (2008)). For the highest dosing at 233 K, we would get a layer of pure HCOOH solution spanning over the whole probing depth, featuring a HCOOH to water mole ratio of 250. The relative high surface coverages even for the lowest p(HCOOH) and the unrealistic high mole ratio of 250 for the HCOOH solution on top of the ice indicate an overestimation of the roughly estimated ratios and coverages. For an appropriate estimation the vertical distribution of the HCOOH in the sample and attenuation of the O signal need to be taken into account, as demonstrated in the following paragraph.

Depth profile analysis of HCOOH in ice

To obtain information about the distribution of HCOOH in the ice, we analyzed depth profiles of $I_{Carboxyl}/I_{Oxygen}$ intensity ratios. The obtained ratios are displayed in Figure 4.7. Measurements in the soft X-ray regime are not included. Error bars include errors of the correction factors used for quantification, as well as fitting errors of the C1s and O1s spectra. Due to adventitious carbon contamination prior to dosing of HCOOH, the concentration profiles of the corresponding 'clean' ice before exposure to HCOOH were analyzed and included as blue symbols in Figure 4.7. Turquoise symbols represent measurements after stopping the admission of HCOOH. The upper graph of Figure 4.7 presents experiments looking at the interaction of HCOOH with 'warm' ice (253 K) while the lower graph shows experiments using 'cold' ice (233 K).
Figure 4.7 shows that the exposure of ice to higher p(HCOOH) leads to higher $I_{Carboxyl}/I_{Oxygen}$ than the exposure to lower p(HCOOH) and indicates the reversible nature of the interaction. In addition, one can observe a decreasing $I_{Carboxyl}/I_{Oxygen}$ trend with increasing E_{kin}, for all experiments. This indicates that the HCOOH does not penetrate over the whole measurement range (~60 nm), into the ice. However, the relatively weakly decreasing slope indicates that HCOOH may not necessarily remain on the surface only.

For more in depth analysis of the concentration depth profiles and coverages, a 3-layer model, shown as inset in Figure 4.8, was used for fitting the profiles. The model used is similar to that presented in Křepelová et al. (2013), but to account for the adventitious carbon an additional surface layer, as well as carboxyl contamination was introduced. The carboxylic acid contamination, which was already present in the 'clean' ice before exposure to HCOOH is homogeneously distributed over the whole sample depth, as indicated by the blue profiles in Figure 4.7.
The presence of a surface layer containing adventitious carbon was justified on the basis of the $I_{Ctot}/ I_{Carboxyl}$ profiles displayed in Figure 4.8 and the I_{Ctot}/ I_{Oxygen} profiles not shown here. The strong decrease of the $I_{Ctot}/ I_{Carboxyl}$ ratios with sampling depth displays the presence of adventitious carbon exclusively in this surface layer. The lateral distribution of the adventitious carbon in this layer is unknown, either a homogeneous layer but also formation of islands on top of the ice is possible.
For the model analysis we assume a homogeneous surface layer of thickness d. This layer contains carbon atoms in the form of carboxylic acid (n_{FA1}), adventitious carbon (n_{Adv}), and contamination carboxylic acid (n_{ContCA}), together with

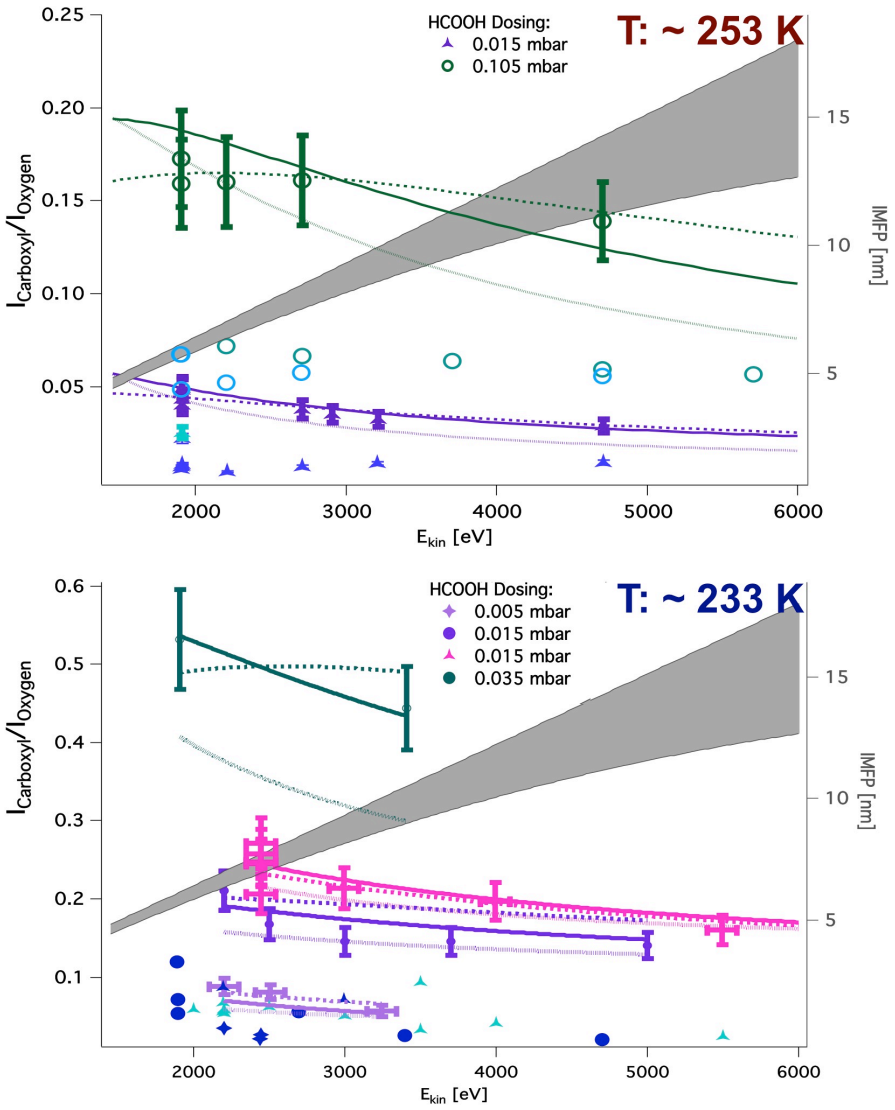

Figure 4.7: $I_{Carboxyl}/I_{Oxygen}$ depth profile together with 3-layer model fits of various experiments for cold (233 K) and warm (253 K) ice admitted to distinct HCOOH partial pressures. Different symbols, indicate different measurement sets. In some case the same ice was used for several, consecutive experiments. Solid lines represent the best fit, shaded lines optimised fits using half the thickness of the ice – HCOOH layer obtained from the best fit, and dotted line optimised fits using double the thickness of the ice – HCOOH layer.
The grey shaded areas represent the estimated IMFP displayed on the right axis. (For more details of the estimation see text).

n_{O1} oxygen atoms. This layer sits on top of a homogeneous 2nd layer with thickness b containing carboxylic acid (n_{FA2}), n_{ContCA} and n_{O2} oxygen atoms. This 2nd layer sits on top of an infinitely thick layer of 'clean' ice consisting of oxygen (n_{O2}) and carbon contamination (n_{ContCA}).
Since one of the aims of this study is to analyze the distribution of HCOOH in the ice, no a priori assumption that HCOOH stays at the surface was made.

Since the density of a HCOOH solution is similar to that of pure water, we assume carbon and oxygen contribute equally to the volume of each layer. Due to assumed similar density, we suppose that the IMFP is also similar. One should note that this analysis may carry systematic errors, since neither variations of the IMFP due to concentration changes or phase changes, nor the orientation of the HCOOH molecules is taken into account.

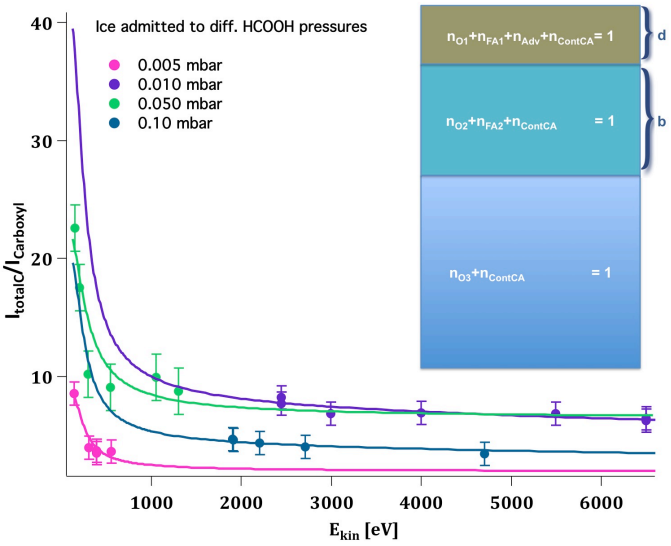

Figure 4.8: Depth profile of $I_{Ctot}/ I_{Carboxyl}$ together with fitted $I_{Ctot}/ I_{Carboxyl}$ ratios and sketch of the used 3-layer model: The continuously decreasing $I_{Ctot}/ I_{Carboxyl}$ ratio reveals the presence of an adventitious carbon layer on top of ice and HCOOH as shown in the inlet of the 3-layer model.

Assuming three layers with structure and composition as described above, the mea-

sured $I_{Carboxyl}/I_{Oxygen}$ can be modeled as follows (see supporting text for derivation):

$$\frac{I_{Carboxyl}}{I_{Oxygen}} = \frac{\frac{n_{FA1}}{n_{O_2}}(1-e^{-d/\lambda\cos\theta}) + \frac{n_{FA2}}{n_{O2}} \cdot (e^{-d/\lambda\cos\theta} - e^{-b/\lambda\cos\theta}) + \frac{n_{ContCA}}{n_{O2}}}{1 + (\frac{n_{FA2}}{n_{O2}} - \frac{n_{FA1}}{n_{O2}} - \frac{n_{Adv}}{n_{O2}})(1-e^{-d/\lambda\cos\theta}) + \frac{n_{FA2}}{n_{O2}} \cdot e^{-b/\lambda\cos\theta}}$$

Fits to the data applying the 3-layer model presented above are displayed in Figure 4.7. The best fits result from iterative optimization of the $I_{Carboxyl}/I_{Oxygen}$ and $I_{Ctot}/I_{Carboxyl}$ depth profiles. The fit results for layer thickness and concentrations are included in Table 4.1. The large number of unknowns (9) compared to data points leads to a high uncertainty of the fitting results (~35%). Therefore the fits using half and double the layer thickness of the best fit are added to the graph (dashed and dotted lines) to indicate the significance of the optimized fitting parameters. The iterative fitting of both $I_{Carboxyl}/I_{Oxygen}$ and $I_{Ctot}/I_{Carboxyl}$ depth profiles applied to enhance the significance of the fitting parameters, may lead to the fact that the best fit may not necessarily represent $I_{Carboxyl}/I_{Oxygen}$ best. Since the model includes attenuation, the calculated concentrations are reasonably lower, compared to the rough estimation demonstrated before and may represent the actual concentrations reasonably well as discussed in the following paragraphs.
For experiments at low p(HCOOH) displayed in purple, we find that the measurements are best represented by using a layer thickness of 5 nm of the 2nd, ice – HCOOH, layer. Altogether, HCOOH penetrates the uppermost 5 nanometers of the pure ice and ~8 nm of the whole sample including the contamination layer on top of the ice. At high p(HCOOH), the HCOOH penetrates deeper into the ice. Here, we get an HCOOH–ice layer with a thickness of about 10 nm.
The modeled layer thicknesses of experiments performed in a similar range of the phase diagram but different temperatures (Figure 4.4 and Table 4.1) reveal similar penetration of the HCOOH.
The thickness of the adventitious carbon layer shows minor influence by p(HCOOH). However, a phase change may lead to distinct changes (e.g. in IMFP), so that the assumptions used for the model development, thus the model, may no longer be valid for the experiments for which a liquid layer on top was visually observed.

Using the fit results we can estimate the amount of HCOOH in the ice sample. The

n_{FA2}/n_{O_2} ratios obtained from the fits can be converted to n_{HCOOH}/n_{H_2O} molar ratios using the following expression:

$$\frac{n_{HCOOH}}{n_{H_2O}} = \frac{\frac{n_{FA2}}{n_{O2}}}{1 - 2\frac{n_{FA2}}{n_{O2}}}$$

The resulting ratios are shown in Table 4.1.
As described in Křepelová et al. (2013), we can convert the molar ratios to the total number density of HCOOH molecules in the HCOOH-ice layer per unit surface area, also shown in Table 4.1. The obtained values are in the 10^{14}-10^{15} molecules/cm^2 range for low p(HCOOH). For high p(HCOOH) higher values could be observed. Using the 3-layer model, which takes attenuation of the oxygen into account, we get lower surface coverages than for the rough estimation presented in the first part of 4.1.4. In general we can state that the HCOOH concentrations in the uppermost ice layers obtained from the 3-layer model within the context of this study (e.g. ~0.014 mol/cm^3 at p(HCOOH) of 0.005 mbar and T_{ice}: 253 K), are comparable to the concentrations of a hypothetical aqueous solution exposed to similar p(HCOOH), calculated using Henry's law (~0.018 mol/cm^3). Nevertheless, the surface coverages observed in the context of this study are slightly higher than those of Jedlovszky et al. (2008) at colder temperatures. However, since we observed a penetration of the HCOOH of ~5 nm into the ice these values may not be directly comparable. The ice sample used for the simulations by Jedlovszky et al. (2008) was thinner than the penetration depth observed within the context of this studies. Assuming a penetration of HCOOH into the ice over a similar depth as observed in our study we find that the surface coverage extrapolated using Jedlovszky et al. (2008) data and those obtained within the context of this studies are similar. Our surface coverages are even a bit lower than the linearly extrapolated one of Jedlovszky et al. (2008). However, also the measurements performed within the study of Jedlovszky et al. (2008) indicate lower surface coverages than observed within our experiments. This might be explained by a smaller penetration depth of the HCOOH into the ice at the colder temperatures investigated by Jedlovszky et al. (2008). If we assume that the penetration depth depends on temperature this is a reasonable explanation.
To summarize, we observed reasonable concentrations of HCOOH, which penetrates into the uppermost ice layers. The observation of the penetration of HCOOH in ice concurs with results published by Compoint et al. (2002). They found a spreading of the HCOOH within the whole simulated DI. According to these re-

sults we may estimate the natural DI of crystalline ice at 253 K to be ~5 nm thick. However, using NEXAFS spectroscopy, Bluhm et al. (2002) estimated the DI to be less than 1 nm at temperatures lower than 255 K. They used changes in the free-hydrogen peak (A) to determine the thickness of the DI and assumed that the peak measured at 233 K corresponds to pure ice without any DI. The used estimation is debated. For example, Tse et al. (2008) claimed that the pre-edge feature used by Bluhm et al. (2002) lacks structural sensitivity since it is a core exciton. Overall the estimation of the thickness of the natural DI spread widely between different studies and techniques, from 0.2 – 20 nm (Bartels-Rausch et al. (2014)). Thus a penetration depth of the HCOOH of ~5 nm may indicate a spreading within a reasonably thick natural DI. However, an additional layer containing adventitious carbon was present on top of the HCOOH–ice layer. This layer may influence the absolute thickness of the DI.
We observed similar penetration of HCOOH for experiments performed in a similar range of the phase diagram but different temperatures. However, major changes of the DI are not expected within that temperature range. And since we used more polycrystalline ice for the experiments at lower temperature a similar thickness of the DI may be assumed.

Surface disordering of ice

In Figure 4.9, O K-edge NEXAFS spectra of ice at 253 K exposed to various p(HCOOH) are shown to discuss the extent to which the presence of HCOOH leads to a modification of the hydrogen-bonding structure of the ice surface region.
As discussed in Chapter 4.4.1, changes of the molecular structure of the hydrogen-bonding network of the ice surface layers indicating changes of the DI are reflected in spectral changes at 535, 538 eV and 542 eV (Fig. 4.3).
A distinct increase in intensity at ~532.5 eV photon energy, present in all spectra, can be assigned to the contribution of the oxygen-carbon or oxygen-nitrogen double bonds from adsorbed species, in this case due to oxygen of the carboxylate group of HCOOH.
At low p(HCOOH) (I-III), only minor further changes, within the uncertainty of repeated experiments, could be observed.
Distinct differences between neat ice and ice exposed to higher HCOOH partial

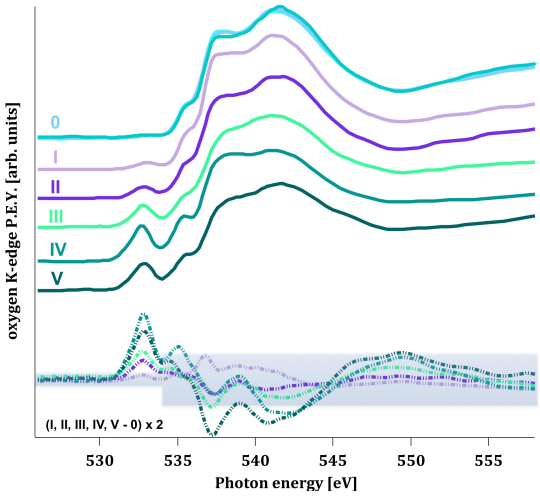

Figure 4.9: Oxygen K-edge Auger yield NEXAFS spectra of ice at ~253 K admitted to different HCOOH partial pressures (0: clean ice; I: 0.005 mbar; II: 0.010 mbar; III: 0.020 mbar; IV: 0.050 mbar; V: 0.060 mbar).
In the lower part the difference spectra between the neat ice and ice exposed to HCOOH is illustrated. The grey shaded region illustrates experimental uncertainties.

pressures (> 0.02 mbar) could be observed (Figure 4.9, IV and V). As mentioned above, the corresponding ice surfaces showed a visually changed appearance, which we interpret as presence of a melt on top of the ice. Taking a combination of water and ice O K-edge NEXAFS, we can state that about 50% of the H_2O molecules are H-bonded in a way similar to liquid water.
As visible in Figure 4.9, distinct differences between the NEXAFS spectra at 0.05 and 0.06 mbar are evident. Both show a liquid layer on the ice sample, but the spectrum obtained at 0.05 mbar p(HCOOH), measured within the first 1.5 hours of exposure to HCOOH, indicates a higher contribution by liquid like structure than that at 0.06 mbar, which was measured 2.5 hours after admission of HCOOH. The formation of a slowly spreading and therefore thinning liquid layer could be an explanation of the observed difference. In addition, a gradient (thermodynamic or gravitational) slowly reducing the amount of HCOOH solution at the sample spot, may lead to a lower contribution of liquid-like water to the latter NEXAFS spectrum. Also, an inhomogeneous surface (i.e., patches with ice and liquid HCOOH solution) may lead to the observed differences in the spectra. Comparing the two peaks at 532.5 eV photon energy (slightly more pronounced for the dosing at 0.05 mbar HCOOH), a heterogeneous distribution of the HCOOH on the ice surface

seems likely. For a homogeneous distributed layer we would expect that at higher HCOOH pressure the C=O peak would be higher as well, since it should scale with the concentration of carboxyl-oxygen near the sample surface. A slightly different morphology of the ice could play a role. However, for a clear differentiation, a more detailed analysis of the ice surface properties including thickness and homogeneity would be needed. The application of other analysis methods such as small angle X-ray scattering, or XRD might be advantageous.

From the O K-edge NEXAFS, we can state that at low p(HCOOH) changes of the hydrogen-bonding network at the ice surface are not significant (spectra I-III). Thus we can conclude that at p(HCOOH) as present in the environment no perturbations of the hydrogen-bonding network of the ice surface should occur. This result is similar to that by Křepelová et al. (2013) who showed for CH_3COOH at environmentally relevant conditions (< monolayer coverage, ice between 230 and 240 K), that the DI remained unchanged.
To summarize, despite the presence of adventitious carbon contamination and beam damage we are able to state that HCOOH does not disturb the hydrogen-bonding network of the ice surface, but penetrates several nm in the ice.

4.1.5 Conclusion

Using the surface sensitive ambient pressure X-ray electron spectroscopic methods XPS and NEXAFS we directly studied the molecular interaction between ice and HCOOH. In the context of this study, we looked at the ice – HCOOH interactions at two different temperatures (233 and 253 K) and varied p(HCOOH) from 0.005-0.040 mbar at 233 K and 0.005-0.1 mbar at 253 K, respectively. By doing so, we covered conditions resulting in both, low coverages and close to the thermodynamically induced phase change.
For low p(HCOOH) thus under conditions relevant for the environment, O K-edge NEXAFS analyses reveal no distinct change in the hydrogen-bonding structure near the ice surface. For high p(HCOOH), O K-edge NEXAFS spectra indicate a clear change of the hydrogen-bonding network of the ice surface due to the formation of a liquid HCOOH solution
At low p(HCOOH), the depth profile indicate that HCOOH does not accumulate at the outermost surface only, but actually distributes within the uppermost 5

nanometers, thus within 15 ice bilayers.
The observation of the penetration of HCOOH into ice concurs with results published by Compoint et al. (2002), observing a penetration of HCOOH into the ice over the whole natural DI. The estimation of the thickness of the natural DI spread widely between different studies and techniques, from 0.2 – 20 nm (Bartels-Rausch et al. (2014)). Thus the observed penetration depth of ~5 nm of HCOOH into the ice can be interpreted in a reasonable way as penetration into the natural DI. Using these analysis, we may estimate the natural DI of crystalline ice at 253 K to be ~5 nm thick.
In summary we can state that though the ice penetrates the uppermost 15 ice bilayers, HCOOH does not influence the hydrogen-bonding structure in the DI. The adsorption-desorption equilibrium analyses indicate a basically reversible uptake of HCOOH. However, the interaction between ice and HCOOH is different from Langmuir type surface adsorption. These investigations, give rise to a modified molecular level picture of the interaction between ice and trace gases. Rather than pure surface adsorption, the interaction between ice and trace gases can be understood as a composite process in which dissolution of trace gases into the uppermost ice layers may occur.

4.1.6 Acknowledgements

Swiss National Science Foundation (grant # 149629). Part of this work has been performed at the Surface/Interface beamlines Microscopy (SIM) and PHOENIX, at the Swiss Light Source. The work was conducted within the PhD studies of Astrid Waldner (main supervisor: Thomas Peter). Thanks to Marrio Birrer for his excellent engineering work.

4.2 Supplementary

4.2.1 Assessment and selection of data used for ice – HCOOH interaction analysis

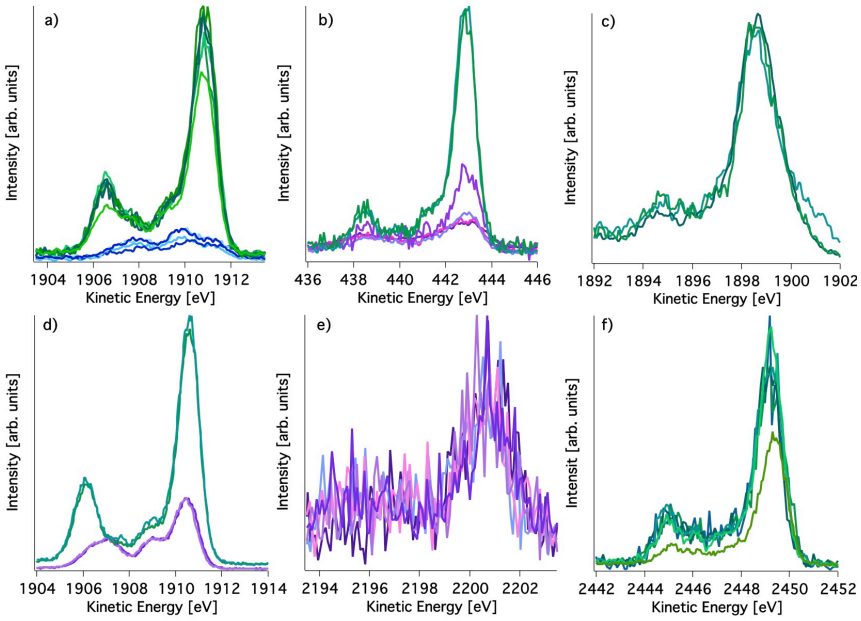

Figure 4.10: Exemplary C1s spectra, normalized to the respective O1s spectrum, of reference measurements taken during ice – HCOOH interaction experiments. The reference measurements were obtained during various beamtimes (a) April 2016, b) December 2015, c) November 2015, d) March 2015, e) December 2014 and f) August 2014). Purple colour indicate low p(HCOOH), whereas green colour indicates high p(HCOOH).

As noted in Chapter 4.1.4, not all measurements could be used for the analysis of the interaction between ice and HCOOH. For example, it is important to ensure the stability of the HCOOH concentration at constant p(HCOOH). To achieve that, O1s and C1s reference measurements were repeated several times during the experiments. The C1s spectra were normalized to the respective O1s intensities to correct for changes in the absolute measured intensity. Differences in the normalized reference C1s spectra reveal changes, thus unstable conditions, within an experiment. In cases where I observed unintended changes in the reference spectra, I excluded the data points obtained between the respective reference spectra from

concentration depth profile analysis.
Figure 4.10 shows the normalized C1s reference spectra used for stability analysis of the HCOOH concentrations. For the experiments performed in April 2016, December 2015, and August 2014, I observed distinct changes in the reference spectra, thus excluded some data points from further analysis. Especially in December 2015 (Fig. 4.10 (b)), changes of more than 100 % for the low p(HCOOH) experiment, displayed in purple, were observed.
Beyond the stability of the reference spectra, the effect of different correction factors on the data was used for an assessment of the quality of the data points. Different correction factors are obtained from HCOOH gas-phase peak ratios, and various I_0 measurements. In case of discrepancies and inconsistencies of the values of the corrected data point due to the different correction factors, the respective data point was not included in further analysis.
After such aforementioned assessment, I was able to conclude that most of the experiments showed satisfactory stability and reproducibility. However, I fully excluded some measurement sets, since a reasonable depth profile analysis of the HCOOH concentration in the ice was not possible with the remaining data points.

4.2.2 Proof of HCOOH purity

In Chapter 4.1.4, I discussed the presence of carbon contamination during our measurements. I observed a pronounced increase in the carbon contamination signal during exposure of ice to HCOOH. Either contamination of the dosed HCOOH vapor, or beam induced decomposition may cause such increases in contamination. To ensure the purity of the used HCOOH, we performed proton-transfer-reaction mass spectrometric (PTRMS) and ion chromatographic (IC) measurements. To ensure that neither the HCOOH nor the preparation nor the set-up of the dosing system introduced carbon contamination, we analyzed HCOOH samples during all the different steps of the procedure, including the Freeze-Pump-Thaw cycles. As visible in Figures 4.11 and 4.12 both PTRMS and IC revealed the absence of carbon contamination. This clearly indicates that the carbon contamination originates from the X-ray photoemission method itself. The adventitious carbon compounds are produced in-situ by decomposition products of the HCOOH due to the exposure to X-rays or secondary electrons.

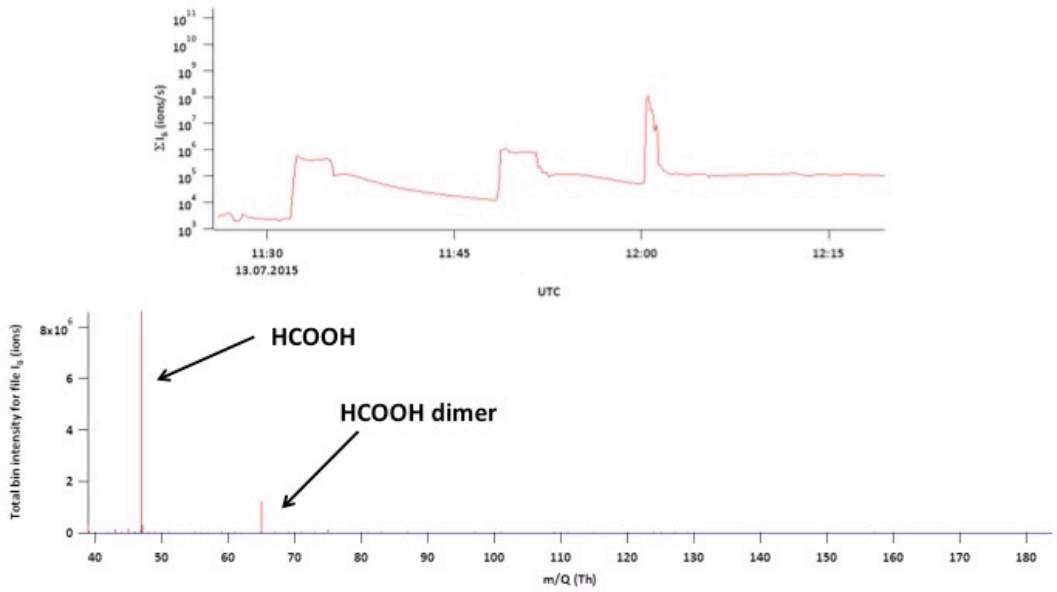

Figure 4.11: Analysis of HCOOH purity using PTRMS. Top: Signal intensity history of the different dosing tests for the HCOOH purity analysis. Bottom: Exemplary mass spectrogram of dosed HCOOH measured during maximum dosing of intensity history displayed above.

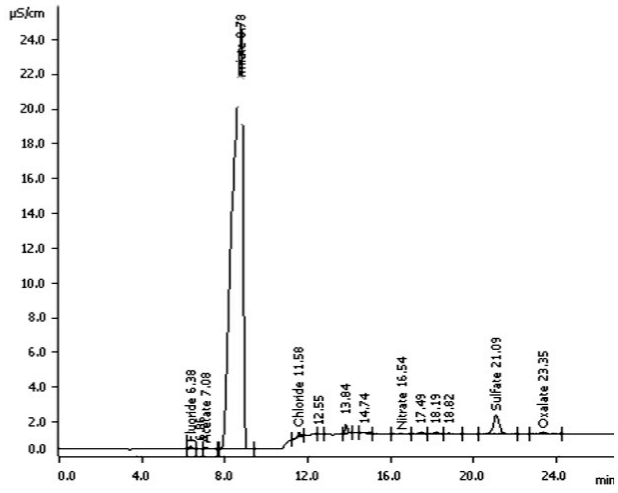

Figure 4.12: Analysis of HCOOH purity using IC.

4.2.3 3-layer model

To get a better understanding of the 3-layer model used for the concentration depth profile analysis presented in Chapter 4.1.4, a derivation of the equations used is given in the following paragraphs.
All fitted ratios are calculated on the basis of the corresponding compounds. For example, $I_{Carboxyl}/I_{Oxygen}$ are calculated by the division of the measured carboxyl intensity, $I_{Carboxyl}$, by the oxygen intensity, I_{Oxygen}. The respective intensities are given by the summed measurable intensity of the signal of all compounds with a certain functional group present in the sample. To get the measurable intensity, the actual intensity of the photoemission signal, depending on the probing depth, needs to be considered.
In general, the measurable photoemission intensity I(x) contributed by an atom at depth x can be described as:

$$I(x) = I_0 \cdot e^{-x/t}$$

where, t is the escape depth (1/3 of the probing depth), x is depth, and I_0 is the initial intensity, thus the actual amount of molecules of the respective compound. Integrating the contributions over the respective depths, we get the equations below.
For the uppermost layer containing adventitious carbon and spanning from 0-d the intensity, I_1, is given by:

$$I_1 = t \cdot I_0 \cdot e^{-0/t} - t \cdot I_0 \cdot e^{-d/t}$$

$$= t \cdot I_0 \cdot (1 - e^{-d/t})$$

For the ice–HCOOH layer spanning from d-b, I_2, can be calculated by:

$$I_2 = t \cdot I_0 \cdot e^{-d/t} - t \cdot I_0 \cdot e^{-b/t}$$

$$= t \cdot I_0 \cdot (e^{-d/t} - e^{-b/t})$$

For the 'pure' ice spanning from b to infinity the measurable intensity, I_3, is given by:

$$I_3 = t \cdot I_0 \cdot e^{-b/t} - t \cdot I_0 \cdot e^{-\infty/t}$$

$$= t \cdot I_0 \cdot e^{-b/t}$$

Going back to our analysis, we can determine the measurable $I_{Carboxyl}$, which is given by the summed intensity signal of all carboxylic compounds present in the

sample. Using the assignment and balance of all compounds used for the 3-layer model analysis of the ice sample, presented in Figure 4.8, we find that carboxylic compounds are present as carboxyl contamination and HCOOH. The carboxylic carbon contamination n_{ContCA} is distributed homogeneously over the whole sample, whereas HCOOH is present in the two upper layers with different concentrations (n_{FA1}, n_{FA2}).
Altogether, the detected $I_{Carboxyl}$ signal thus comprises of:

$$I_{Carboxyl} = n_{FA1}(I_1) + n_{FA2}(I_2) + n_{ContCA}(I_1 + I_2 + I_3)$$

Combining the calculations presented above, we get for $I_{carboxyl}$:

$$I_{Carboxyl} = n_{FA1} \cdot t \cdot (1 - e^{-d/t}) + n_{FA2} \cdot t \cdot (e^{-d/t} - e^{-b/t}) + n_{ContCA} \cdot t \cdot 1$$

Oxygen is present in the whole sample. It can be assumed to be n_{O1} in the first, n_{O2} in the second and n_{O3} in the 3rd layer. Therefore, for oxygen we can calculate I_{Oxygen} using:

$$I_{Oxygen} = n_{O1}(I_1) + n_{O2}(I_2) + n_{O3}(I_3)$$

thus,

$$I_{oxygen} = n_{O1} \cdot t \cdot (1 - e^{-d/t}) + n_{O2} \cdot t \cdot (e^{-d/t} - e^{-b/t}) + n_{O3} \cdot t \cdot e^{-b/t}$$

To get the ratios presented in Figure 4.7, I divide $I_{Carboxyl}$ by I_{Oxygen} and multiply, as well as factorize the nominator and the denominator by n_{O2}. Thus $I_{Carboxyl}/I_{Oxygen}$ can be written as:

$$\frac{I_{Carboxyl}}{I_{Oxygen}} = \frac{\frac{n_{FA1}}{n_{O2}}(1 - e^{-d/\lambda\cos\theta}) + \frac{n_{FA2}}{n_{O2}} \cdot (e^{-d/\lambda\cos\theta} - e^{-b/\lambda\cos\theta}) + \frac{n_{ContCA}}{n_{O2}}}{1 + (\frac{n_{FA2}}{n_{O2}} - \frac{n_{FA1}}{n_{O2}} - \frac{n_{Adv}}{n_{O2}})(1 - e^{-d/\lambda\cos\theta}) + \frac{n_{FA2}}{n_{O2}} \cdot e^{-b/\lambda\cos\theta}}$$

In addition, I used the mass balance equations displayed in the inset of Figure 4.8. I also substituted t with the escape depth, which is 1/3 of the probing depth, given by $t = \lambda\cos\theta$, where λ is the IMFP.
I compute the total carbon to HCOOH intensity profiles, $I_{totalC}/I_{Carboxyl}$, using similar calculations as for $I_{Carboxyl}/I_{Oxygen}$. For $I_{totalC}/I_{Carboxyl}$, we get:

$$\frac{I_{totalC}}{I_{Carboxyl}} = \frac{(\frac{n_{FA1}}{n_{O2}} + \frac{n_{Adv}}{n_{O2}}) \cdot (1 - e^{-b/\lambda\cos\theta}) + \frac{n_{FA2}}{n_{O2}} \cdot (e^{-b/\lambda\cos\theta} - e^{-d/\lambda\cos\theta}) + \frac{n_{ContCA}}{n_{O2}}}{\frac{n_{FA1}}{n_{O2}} \cdot (1 - e^{-d/\lambda\cos\theta}) + \frac{n_{FA2}}{n_{O2}} \cdot (e^{-b/\lambda\cos\theta} - e^{-d/\lambda\cos\theta}) + \frac{n_{ContCA}}{n_{O2}}}$$

Using the 3-layer model and the equations of the respective intensity ratios presented above concentration depth profiles can be fitted and estimated. Attenuation of the oxygen and compounds present in the second layer is considered. Depending

on the concentrations of the various compounds in the respective layers, together with the thickness of the different layers, I can get various depth profiles, as displayed in Figure 4.13.

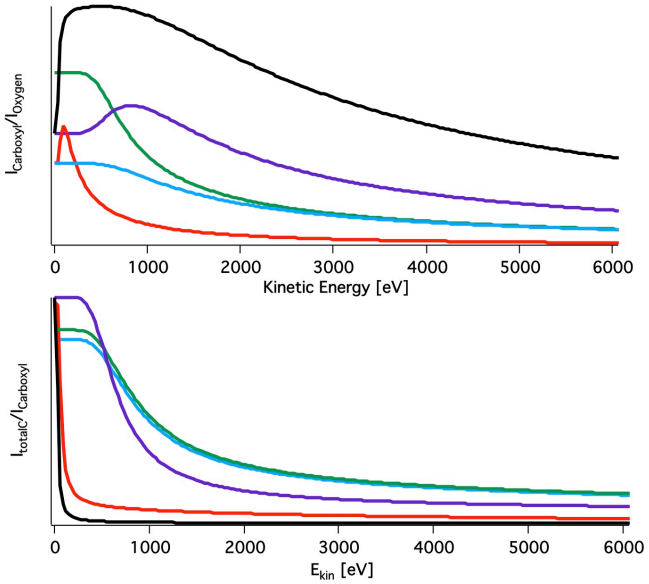

Figure 4.13: Exemplary runs of fitting using the 3-layer model.

red: small b and d; black: extended b, small d; green: extended b and d; blue: similar to green but higher n_{Adv}/n_{O2};purple: similar to green but higher n_{FA2}/n_{O2} and n_{Adv}/n_{O2}

I was able to reproduce the measured $I_{Carboxyl}/I_{Oxygen}$ and $I_{totalC}/I_{Carboxyl}$ profiles displayed in Figure 4.7 and 4.8, using the calculations described above. To optimize the fitting parameters, I iteratively fitted $I_{Carboxyl}/I_{Oxygen}$ and $I_{totalC}/I_{Carboxyl}$, alternately. The profiles nicely display that HCOOH does not stay at the ice surface but penetrates some nanometers into the ice.

Bibliography

Abbatt, J. P. D.:Interactions of atmospheric trace gases with ice surfaces: Adsorption and reaction. *Chemical reviews*, **103(12)**, 4783-4800, 2003.

Andreae, M. O., Talbot, R. W., Andrea, T. W., Harris, R. C.: Formic and acetic acid over the central Amazon region, Brazil: 1. Dry season. *Journal of Geophysical Research: Atmospheres*, **93(D2)**, 1616-1624, 1988.

Barr, T. L., Sudipta, S., Nature of the use of adventitious carbon as a binding energy standard. *Journal of Vacuum Science & Technology A*, **13(3)**, 1239-1246, 1995.

Bartels-Rausch, T., Jacobi, H.-W., Kahan, T. F., Thomas, J. L., Thomson, E. S., Abbatt, J. P. D., Ammann, M., Blackford, J. R., Bluhm, H., Boxe, C., Domine, F., Frey, M. M., Gladich, I., Guzmán, M., I., Heger, D., Huthwelker, Th., Klán, P., Kuhs, W. F., Kuo, M. H., Maus, S., Moussa, S. G., McNeill, V. F., Newberg, J. T., Petterson, J. B. C., Roselová, M., Sodeau, J. R.: A review of air–ice chemical and physical interactions (AICI): liquids, quasi-liquids, and solids in snow. *Atmospheric Chemistry and Physics*, **14(3)**, 1587-1633, 2014.

Bluhm, H., Ogletree, D. F., Fadley, C. S., Hussain, Z., Salmeron, M.: The premelting of ice studied with photoelectron spectroscopy. *Journal of Physics: Condensed Matter*, **14(8)**, L227, 2002.

Brown, M. A., Vila, F., Sterrer, M., Thürmer, S., Winter, B., Ammann, M., Rehr, J. J., van Bokhoven, J. A.: Electronic Structures of Formic Acid (HCOOH) and Formate (HCOO–) in Aqueous Solutions. *The journal of physical chemistry letters*, **3(13)**, 1754-1759, 2012.

Chameides, W. L., Davis, D. D.: Aqueous-phase source of formic acid in clouds. *Nature*, **304**, 427–429, 1983.

Compoint, M., Toubin, C., Picaud, S., Hoang, P. N. M., Girardet, C.: Geometry and dynamics of formic and acetic acids adsorbed on ice. *Chemical physics letters*, **365(1)**, 1-7, 2002.

Dominé, F., and Shepson, P. B.: Air-snow interactions and atmospheric chemistry." *Science*, **297(5586)**, 1506-1510, 2002.

Douglass, A. R., Newman, P. A., Solomon, S.: The Antarctic ozone hole: An update. *Physics Today*, **67(7)**, 42-48, 2014.

Grannas, A. M., Bogdal, C., Hageman, K. J., Halsall, C., Harner, T., Hung, H., Kallenborn, R., Klán, P., Klánová, J., Macdonald, R. W., Meyer, T., Wanian, F.: The role of the global cryosphere in the fate of organic contaminants. *Atmospheric Chemistry and Physics*, **13(6)**, 3271-3305, 2013.

Henson, B. F., Robinson, J. M.: Dependence of quasiliquid thickness on the liquid activity: A bulk thermodynamic theory of the interface. *Phys. Rev. Lett.*, **92(24)**, 246107, 2004.

Hofmann, S.: Quantitative depth profiling in surface analysis: A review. *Surf. Interface Anal.*, **2**, 148–160, doi:10.1002/sia.740020406, 1980.

Huthwelker, Th., Ammann, M., Peter, T.: The uptake of acidic gases on ice. *Chemical reviews*, **106(4)**, 1375-1444, 2006.

Hüfner, S.: Photoelectron spectroscopy: principles and applications. *Springer Science & Business Media*, **3**, 2013.

Jacob, D. J.: Chemistry of OH in remote clouds and its role in the production of formic acid and peroxymonosulfate. *Journal of Geophysical Research: Atmospheres*, **91(D9)**, 9807-9826, 1986.

Jacob, D. J., and Wofsy, S. C.: Photochemistry of biogenic emissions over the Amazon forest *Journal of Geophysical Research: Atmospheres*, **93(D2)**, 1477-1486, 1988.

Jedlovszky, P., Hantal, G., Neuróhr, K., Picaud, S., Hoang, P. N., Von Hessberg, P., Crowley, J. N.: Adsorption isotherm of formic acid on the surface of ice, as seen from experiments and grand canonical Monte Carlo simulation. *The Journal of Physical Chemistry C*, **112(24)**, 8976-8987, 2008.

Kerbrat, M., Huthwelker, Th., Gäggeler, H. W., Ammann, M.: Interaction of nitrous acid with polycrystalline ice: Adsorption on the surface and diffusion into the bulk. *The Journal of Physical Chemistry C*, **114(5)**, 2208-2219, 2010.

Křepelová, A., Newberg, J., Huthwelker, T., Bluhm, H., Ammann, M.: The nature of nitrate at the ice surface studied by XPS and NEXAFS. *Physical Chemistry Chemical Physics*, **12(31)**, 8870-8880, 2010.

Křepelová, A., Bartels-Rausch, T., Brown, M. A., Bluhm, H., Ammann, M.: Adsorption of acetic acid on ice studied by ambient-pressure XPS and partial-electron-yield NEXAFS spectroscopy at 230–240 K. *The Journal of Physical Chemistry A*, **117(2)**, 401-409, 2013.

Lide, D. R., CRC *Handbook of Chemistry and Physics*, **95th Ed.**; CRC Press: Boca Raton, FL, Section 5, 23, 2003.

Liu, J., Zhang, X., Parker, E. T., Veres, P. R., Roberts, J. M., Gouw, J. A. D., Hayes, P. L., Jimenez, J. L., Murphy, J. G., Ellis, R. A., Huey, L. G., Weber, R. J.: On the gas-particle partitioning of soluble organic aerosol in two urban atmospheres with contrast- ing emissions: 2. Gas and particle phase formic acid, *J. Geophys. Res.*, **117**, D00V21, 2012.

McNeill, V. F., Loerting, T., Geiger, F. M., Trout, B. L., Molina, M. J.: Hydrogen chloride-induced surface disordering on ice. *Proceedings of the National Academy of Sciences*, **103(25)**, 9422-9427, 2006.

McNeill, V. F., Geiger, F. M., Loerting, T., Trout, B. L., Molina, L. T., Molina, M. J.: Interaction of hydrogen chloride with ice surfaces: The effects of grain size, surface roughness, and surface disorder. *The Journal of Physical Chemistry A*, **111(28)**, 6274-6284, 2007.

Millet, D. B., Baasandorj, M., Farmer, D. K., Thornton, K J. A., Baumann, K., Brophy, P., Chaliyakunnel, S., de Gouw, J. A., Graus, M., Hu, L., Koss, A., Lee, B. H., Lopez-Hilfiker, F. D., Neuman, J. A., Paulot, F., Peischl, J., Pollack, I. B., Ryerson, T. B., Warneke, C., Williams, B. J., Xu, J.: A large and ubiquitous source of atmospheric formic acid. *Atmospheric Chemistry and Physics*, **15(11)**, 6283-6304, 2015.

Myneni, S., Luo, Y., Näslund, L. Å., Calalleri, M., Ojamäe, L., Ogasawara, H., Pelmenschikov, A., Wernet, Ph., Väterlein, P., Heske, C.: Spectroscopic probing of local hydrogen-bonding structures in liquid water. *Journal of Physics: Condensed Matter*, **14(8)**, L213, 2002.

Neeb, P., Sauer, F., Horie, O., Moortgat, G. R.: Formation of hydroxymethyl hydroperoxide and formic acid in alkene ozonolysis in the presence of water vapor. *Atmos. Environ.*, **31**, 1417–1423, 1997.

Nilsson, A., Nordlund, D., Waluyo, I., Huang, N., Ogasawara, H., Kaya, S., Bergmann, U.,Näslund, L. Å., Öström, H., Wernet, Ph., Andersson, K. J., Schiros, T., Petterson, L. G. M.: X-ray absorption spectroscopy and X-ray Raman scattering of water and ice; an experimental view. *Journal of Electron Spectroscopy and Related Phenomena*, **177(2)**, 99-129, 2010.

Powell, C. J., Jablonski, A.: NIST Electron Inelastic-Mean-Free-Path. *Database*, **Version 1.2**, Standard Reference Data Program Database 71, US Department of Commerce, National Institute of Standards and Technology, Gaithersburg, MD, 2010.

Orlando, F., Waldner, A., Bartels-Rausch, T., Birrer, M., Kato, S., Lee, M.-T., Proff, C., Huthwelker, Th., Kleibert, A., van Bokhoven, J., Ammann, M.: The Environmental Photochemistry of Oxide Surfaces and the Nature of Frozen Salt Solutions: A New in Situ XPS Approach.

Topics in Catalysis, **59(591)**, 1-14, 2016.

Paulot, F., Crounse, J. D., Kjaergaard, H. G., Kroll, J. H., Seinfeld, J. H., Wennberg, P. O.: Isoprene photooxidation: new insights into the production of acids and organic nitrates, *Atmos. Chem. Phys.*, **9**, 1479–1501, 2009.

Paulot, F., Wunsch, D., Crounse, J. D., Toon, G. C., Millet, D. B., DeCarlo, P. F., Vigouroux, C., Deutscher, N. M., González Abad, G., Notholt, J., Warneke, T., Hannigan, J. W., Warneke, C., de Gouw, J. A., Dunlea, E. J., De Mazière, M., Griffith, D. W. T., Bernath, P., Jimenez, J. L., Wennberg, P. O.: Importance of secondary sources in the atmospheric budgets of formic and acetic acids. *Atmospheric Chemistry and Physics*, **11(5)**, 1989-2013, 2011.

Petrenko, V. F., Ryzhkin, I. A.. "Electron energy spectrum of ice. *Physical review letters*, **71(16)**, 2626, 1993.

Piao, H., McIntyre, N. S.: Adventitious carbon growth on aluminium and gold–aluminium alloy surfaces. *Surface and interface analysis*, **33(7)**, 591-594, 2002.

Poole, L. R., McCormick, M. P.:Polar stratospheric clouds and the Antarctic ozone hole. *Journal of Geophysical Research: Atmospheres*, **93(D7)**, 8423-8430, 1988.

Pouvesle, N., Kippenberger, M., Schuster, G., Crowley, J. N.: The interaction of H 2 O 2 with ice surfaces between 203 and 233 K. *Physical Chemistry Chemical Physics*, **12(47)**, 15544-15550, 2010.

Sander, S. P., Abbatt, J., Barker, J. R., Burkholder, J. B., Friedl, R. R., Golden, D. M., Huie, R. E., Kolb, C. E., Kurylo, M. J., Moortgat, G. K., Orkin, V. L., Wine, P. H.: Chemical Kinetics and Photochemical Data for Use in Atmospheric Studies, Evaluation No. 17, *JPL*, **10-6**, Jet Propulsion Laboratory, Pasadena, available at: http://jpldataeval.jpl.nasa.gov, 2011.

Sander, R., "Henry's Law Constants" in NIST Chemistry WebBook, NIST Standard Reference Database Number 69, Eds. P.J. Linstrom and W.G. Mallard, National Institute of Standards and Technology, Gaithersburg MD, 20899, http://webbook.nist.gov, (retrieved September 5, 2016).

Solomon, S., Borrmann, S., Garcia, R. R., Portmann, R., Thomason, L., Poole, L. R., Winker, D., McCormick, M. P.: Heterogeneous chlorine chemistry in the tropopause region." *Journal of Geophysical Research: Atmospheres*, **102(D17)**, 21411-21429, 1997.

Starr, D. E., Pan, D., Newberg, J. T., Ammann, M., Wang, E. G., Michaelides, A., Bluhm, H.: Acetone adsorption on ice investigated by X-ray spectroscopy and density functional theory. *Physical Chemistry Chemical Physics*, **13(44)**, 19988-19996, 2011.

Stavrakou, T., Müller, J.-F., Peeters, J., Razavi, A., Clarisse, L., Clerbaux, C., Coheur, P.-F., Hurtmans, D., De Mazière, M., Vigouroux, C., Deutscher, N. M., Griffith, D. W. T., Jones, N., Paton-Walsh, C.: Satellite evidence for a large source of formic acid from boreal and tropical

forests. *Nature Geoscience*, **5(1)**, 26-30, 2012.

Tse, J. S. Shaw, D. M., Klug, D. D., Patchkovskii, S., Vankó, G. and Monaco, G. and Krisch, M.: X-Ray Raman Spectroscopic Study of Water in the Condensed Phases, *Phys. Rev. Lett.*, **100(9)**, 095502-099506,

Yeh, J. J.: Atomic Calculation of Photoionization Cross-Sections and Asymmetry Parameters, Gordon and Breach Science Publishers, Langhorne, PE (USA), 1993.

Zelenay, V., Huthwelker, T., Křepelová, A., Rudich, Y., Ammann, M.: Humidity driven nanoscale chemical separation in complex organic matter. *Environmental Chemistry*, **8(4)**, 450-460, 2011.

CHAPTER 5

The interaction ice – HCl

Chapter 5.2 is submitted to *Science* as: Adsorption, hydration and dissociation of HCl on warm ice;
X. Kong, A. Waldner, F. Orlando, L. Artiglia, T. Huthwelker, M. Ammann, and T. Bartels-Rausch (Version of 18th Mai 2017)

I participated actively in all the measurements described below. Furthermore I did the preparatory work and initiated the ice – HCl interaction experiments presented in Chapter 5.1.

5.1 First approach to ice – HCl ambient pressure X-ray spectroscopy experiments

5.1.1 Background and Preparation

As demonstrated in Chapter 1, the interaction between ice and HCl is of importance for atmospheric chemistry for more than one reason. HCl is a reactive

halogen species which can facilitate catalytic ozone depletion in the atmosphere (e.g. Platt and Hönninger (2003)). Furthermore, partitioning of HCl to ice influences the oxidation capacity of the atmosphere. Reason for that is that the rate coefficients of Cl atoms for hydrocarbon oxidation are about 10^3 times higher than those of OH. Hereby Cl atoms are produced for example by reaction of HCl with OH under relatively low humidities preventing wet deposition. The higher rate coefficients of Cl indicate that already low amounts of chlorine compounds have the ability to influence the degradation of volatile organic compounds, thus hydrocarbon oxidation capacity in the atmosphere (e.g. Monks (2005)). In addition to these processes, the interaction between ice and HCl is also of exemplary importance for atmospheric chemistry. By using the highly acidic HCl, we expand the range of acidities of trace gases used for direct ice – trace gas interaction experiments, thus enable more in depth investigation of the effect of the acidity.
Under environmentally relevant conditions, the investigation of the interaction between ice and HCl is challenging. Until now, the interaction between ice and HCl was never directly examined. One reason for that is the low HCl/H_2O pressure ratios required for experiments performed under environmentally relevant conditions. HCl partial pressures (p(HCl)) prevalent in the environment are in maximum 10^{-9} mbar therefore a stable dosing of the resulting HCl/H_2O pressure ratios may be difficult. For example, the stickiness of HCl, leading to adsorption of HCl to the experimental set-up instead of the ice, is a major challenge. Depending on the experimental set-up, this stickiness may result in unrealistic equilibration times. In addition, the interaction between ice and HCl under environmentally relevant conditions results in very low HCl concentrations on the ice. This makes a direct investigation of the interaction between ice and HCl difficult.
I extensively tested and characterized the newly developed NAPP set-up presented in Chapter 2.2. As a result of these investigations, together with the gained knowledge, I am able to conclude that the HCl-ice interaction studies are feasible. Low p(HCl) is achieved by admitting dilute HCl to the *in situ* experimental cell using a high precision leak valve connected to Teflon tubing.
Indeed, using the NAPP set-up I was able to directly analyze the interaction between HCl and ice. Already after about one hour of equilibration time, I detected HCl on the ice sample. Unfortunately, the actual HCl concentration in the gas phase, thus partial pressure of HCl in the in situ experimental cell, could not be determined during the performed experiments. Mass spectrometric analysis was not possible due to technical difficulties. Using the mixing ratio of HCl in N2 we can roughly estimate the upper limit of HCl pressure in the *in situ* experimental

cell by measuring the absolute pressure change. As discussed, for example, in chapter 4, the determination of the actual HCl pressure at the sample spot was accompanied with difficulties. In addition, the absolute pressure changes for the low dosing experiments of HCl, was below or close to the detection limit of changes in the pressure reading. Thus the investigation of the HCl partial pressure was only possible in a really limited way.

5.1.2 1st results

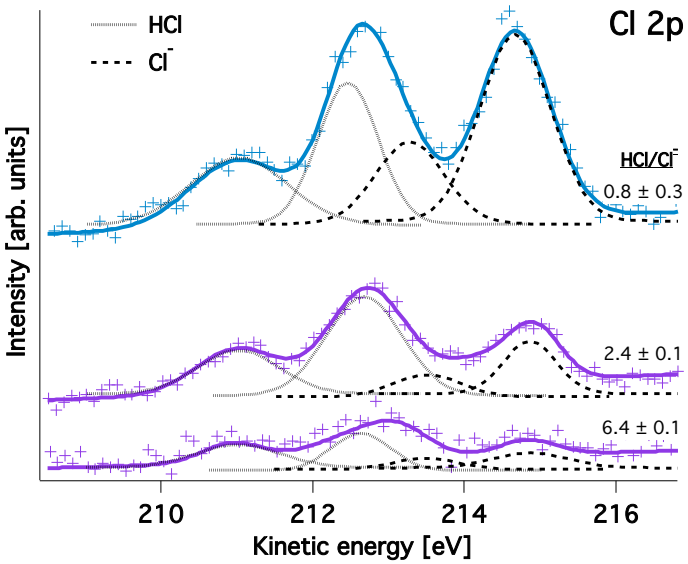

Figure 5.1: Cl 2p PE spectra of the interaction ice – HCl normalised to the respective O1s PE spectrum. Purple colour indicates measurements for which no induced DI was observed. The spectra were acquired at SIM X11MA using a photon energy of ~600 eV. The ice temperature was ~250 K.

As visible in the Cl 2p PE spectra displayed in Figure 5.1, the interaction of HCl with ice leads to several chloride features on the ice surface. The Cl 2p PE spectrum of HCl interacting with ice consists of two doublets. Those two doublets can be interpreted as one representing molecular HCl and one dissociated HCl (e.g. Parent and Laffon (2005)). For the lower p(HCl) dosing, most of the HCl is present as molecular HCl on the ice surface. For the highest dosing, dissociated HCl is clearly the dominant species. Due to the low amount of Cl molecules on the ice, the acquisition time of the spectra was between 0.5 for the two upper spectra and 0.75-1 hour for the lower ones.

At the highest p(HCl), also a clear change of the DI can be observed as displayed in Figure 5.2. The O K-edge NEXAFS indicates the formation of a liquid (like) layer at the ice surface. More precisely, a strengthening of those features in the spectrum that represent water in liquid water, or in aqueous solution could be observed. However, whether actually a liquid layer emerges, the DI actually thickens, or the H_2O molecules simply reorder in a way similar to an aqueous solution, remains open. For a more detailed discussion about the use and interpretation of O K-edge NEXAFS analysis of changes in the hydrogen-bonding network of the ice surface see Chapter 4.1.4. In general, I interpret the observation in a way that the increased mobility of the H_2O molecules in the enhanced DI seems to facilitate dissociation. However, since chloride ions may also compete with ice for H_2O molecules to establish a sufficient hydration shell, it might also be that more H_2O molecules aggregate in structures as in an aqueous HCl solution.
Directly analyzing the interaction between HCl and ice, we discovered a hitherto not observed interplay between concentration of HCl, dissociation and change of the DI. One can only observe a change of the molecular structure of the ice surface layer and dominant dissociation close to the phase transition. For lower p(HCl), no effect on the natural DI can be observed and molecular HCl is the dominant species.
The detection of molecular HCl on the ice surface is a major finding which contradicts previous results and assumptions. For example, Th. Huthwelker postulated that molecular HCl is only present on ice surfaces in case of carbon contamination of the ice (personal communication). However, for the lowest p(HCl), thus the most intense molecular HCl signal, I observed only minor carbon contamination. For higher p(HCl)s, thus less intense molecular HCl signals, the carbon contamination was more pronounced but still magnitudes lower than the HCl concentration. These observations support the presence of molecular HCl on the ice. A more in depth discussion on the observation of molecular HCl can be found in Chapter 5.2.

As with many X-ray studies, there is a possibility of beam damage during measurements. In our case, a decrease of the chlorine signal intensity with increasing exposure to the beam was observed. We attribute this to beam damage, more precisely radiolysis and oxidation of chloride, followed by desorption of atomic or molecular chlorine to the gas phase. Such effect was most pronounced on the signal of dissociated HCl, which decreased tremendously with increasing exposure. However, the general picture of the observed change of the molecular HCl-to-dissociated HCl-ratio does not change due to beam damage, since the exposure of the sample

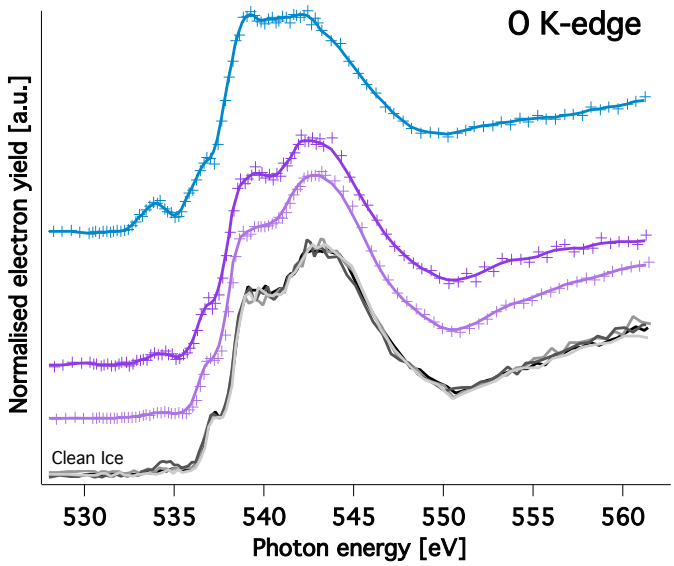

Figure 5.2: Auger yield O K-edge NEXAFS measurements of the interaction between HCl and ice. Purple colour indicates measurements for which no induced DI was observed. The spectra were acquired at SIM X11MA.

to the beam are similar for the upper spectra presented in Figure 5.2.
However, due to the observed beam damage, and the fact that low HCl partial pressures were below the detection limit of the MS, no closer and quantitative analyses were conducted for the case of low p(HCl). In the following sections, we describe further analyses of higher p(HCl) cases, inducing an enhanced DI.

5.2 Adsorption, hydration and dissociation of HCl on warm ice

Submitted to *Science* as: Adsorption, hydration and dissociation of HCl on warm ice;

5.2.1 Abstract

Since long, the dissociation of the strong acid HCl on ice has been studied intensively at low temperatures and was found to occur spontaneously and completely at temperatures approaching 140 K. At 253 K, we observe that adsorbed HCl retains its molecular state at the ice surface using surface-sensitive ambient-pressure core level X-ray photoelectron spectroscopy. Depth profiles of both molecular HCl and ionic Cl^- further show the presence of Cl^- within the uppermost ice layers and indicate that complete dissociation occurs upon hydration in the near surface region. Complementary X-ray absorption measurements suggest that the presence of Cl^- ions induces significant changes to the hydrogen bonding network in the surface region.

One Sentence Summary Sorption of the acidic trace gas HCl to ice at 253 K shows a *Janus*-like behavior with two distinct chemical identities, a molecular state on the ice surface and the dissociated state within the uppermost bulk ice layers, that were simultaneously observed and that go along with significant changes of the hydrogen bonding network.

5.2.2 Main Text

The interaction of strong acids with ice had since long attracted scientific interest, most notably as acidic gases play a pivotal role in forming the stratospheric ozone hole (Molina et al. (1987)) and in tropospheric ozone depletion events (Abbatt et al. (2012)). Experimental studies achieved consistency that HCl fully dissociates on ice below 140 K (Devlin et al. (2002), Kang et al. (2000), Parent et al. (2011), Park and Kang (2005)). Bolton and Pettersson (2001) performed

ab initio (8) calculations and showed that HCl ionization on ice is a barrierless process, agreeing with quantum mechanics/molecular mechanics (Svanberg et al. (2000)), density function theory (Calatayud et al. (2003)) and molecular dynamics (Gertner and Hynes (1996), Mantz et al. (2001))work. However, extrapolation to warmer temperatures is hampered as the aforementioned experimental studies refer to conditions where HCl-H_2O hydrates are the thermodynamic stable phase (Thibert and Dominé (1997), Huthwelker et al. (2006))but not hexagonal water ice as prevalent in Earth's troposphere. Furthermore, at temperatures approaching the melting point of ice, surface pre-melting becomes relevant (Dash et al. (2006)). The chemical properties of this disordered interface (also called quasi-liquid layer, QLL), in particular the impact on the adsorption of acidic gases is still under considerable debate (Bartels-Rausch et al. (2014)). For example, *ab initio* molecular dynamics works showed efficient acid dissociation (Riikonen et al. (2014))in the QLL, whereas recent experimental evidence indicates that the dissociation of HCl is restrained at the surface of both warm ice (Wren and Donaldson (2012)) and aqueous surfaces (Morris et al. (2012), Brastad and Nathanson (2011)). As acid-base equilibria of acids govern the availability of protons, the dissociation is key to chemical reactions that are accelerated by H^+. Hence, it is crucial to provide direct experimental evidence of the fate of strong acids on warm ice. Therefore, we aim to answer the following key questions in this study: 1) Can molecular HCl *survive*on warm ice within chemical equilibria? 2) *Where* does the dissociation most likely occur? 3) Does the presence of HCl/Cl^- *change* the crystalline ice structure?

We performed core level electron X-ray photoelectron spectroscopy (XPS) and partial electron yield near edge X-ray absorption fine structure (NEXAFS) spectroscopy experiments at the near ambient pressure photoelectron (NAPP) end station (fig. S1) at the Swiss Light Source (SLS) (Orlando et al. (2016)). XPS experiments allows evaluating the dissociation degree of HCl and depth profiles of the acid in the gas-ice interface region (Brastad and Nathanson (2011)). The NEXAFS spectroscopy at the oxygen K-edge directly reveals information about the local H-bond arrangement of water molecules in the condense phases (Orlando et al. (2016)). The XPS experiments allow evaluating the degree of dissociation of HCl and deriving depth profiles of the acid in the gas-ice interface region (Krepelova et al. (2013)). NEXAFS spectroscopy at the oxygen K-edge reflects the local H-bonding arrangement around the probed oxygen atom (Nilsson et al. (2010)), and hence the extent of disorder at the ice surface. Therefore NEXAFS spectra, taken on ice in presence of acidic dopants (Krepelova et al. (2013), Krepelova et

al. (2010)) provide a direct probe of the dopants impact on local order at the ice surface. The ice samples were prepared in-situ by depositing water vapor on a gold coated sample holder kept at 253 K (movie S1). Crystal-clear, hexagonal shaped features formed during ice preparation though their orientation differed from case to case, as shown in Fig. 1A and B for the initial phase of ice growth. Such features are comparable to the single crystals of ice reported in previous variable pressure scanning electron microscopy studies (Pfalzgraff et al. (2011)). The absence of gas pores in this vapor deposited ice and the minimization of grain boundaries is of great advantage as both features significantly impact the interaction of acidic gases with the ice sample (Huthwelker et al. (2006), Zimmermann et al. (2016)). Fig. 1C illustrates an XPS survey spectrum of a clean ice sample before HCl adsorption, showing the O 1s and O 2s peaks of water at ca. 534 eV and 26 eV, respectively, and very level adventitious carbon contamination as shown in the inset. During the XPS experiments, the carbon intensity remained lower than that of chlorine by at least one order of magnitude.

During HCl exposure, both the dissociated and the covalent state on warm ice were directly detected by XPS. Fig. 1D and E show examples of the Cl 1s and Cl 2p XPS spectra, respectively at the ice surface region in presence of HCl in the gas phase. The Cl 1s spectrum associated with HCl on ice has two main features that we assign to covalent HCl (green) and to ionic chloride (blue). The Cl 2p XPS spectrum well reproduced by two spin-orbit split doublets representing HCl and Cl^-. As a comparison, ionic Cl^- was the only chloride state observed in a NaCl solution, as shown in Fig. 1F, which rationalizes the assignment of the features at lower binding energy (BE) as ionic Cl^-. The chemical shift in BE of 2.2 eV between the covalent HCl and the ionic Cl^- features, observed both in the Cl 1s singlets and Cl 2p doublets, is in good agreement to previous XPS measurements of HCl on ice (Parent et al. (2011)) aThe chemical shift can be most likely interpreted in terms of a gain of negative charge upon dissociation, as observed for other acids, like formic (Brown et al. (2012)), acetic (Krepelova et al. (2013)) and nitric (Lewis et al. (2011)) acid. A possible attribution of the high BE feature to carbon-Cl compounds appears unlikely due to the low molar ratio of carbon to chlorine as detected by XPS. Consequently, these measurements provide direct spectroscopic evidence of the presence of molecular HCl and ionic Cl^- upon adsorption with an average ratio of about 1:1 within the upper few nanometers of the ice sample. The apparent HCl/Cl^- ratio was invariant in two repeated experiments after a few hours of exposure to HCl in the gas phase indicating that a steady-state was reached. Higher apparent molar ratios of HCl/Cl^- were observed with lower HCl

partial pressures in separate experiments, as shown in fig. S2.

To analyze the distribution and speciation of HCl in the ice surface region in

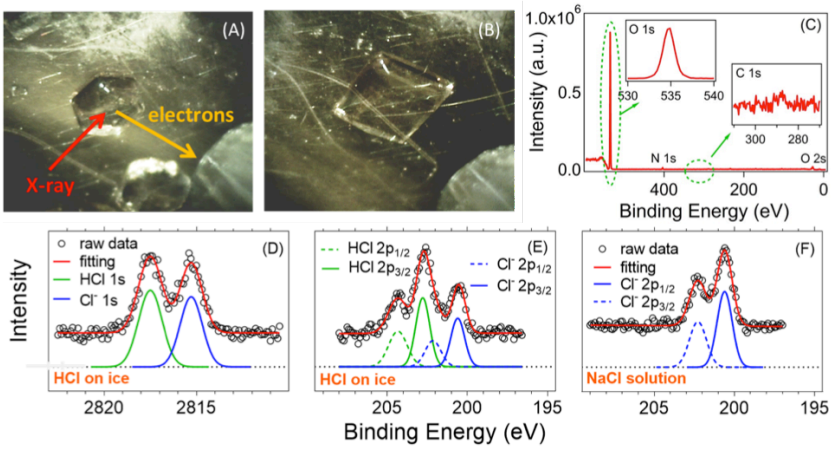

Figure 5.3: (A, B) Single crystal ice during growth of the samples on the gold coated sample holder at 253 K. (C) Photoelectron survey spectrum of the ice acquired at the PHOENIX beamline with 2200 eV photon energy. The insets show the oxygen 1s peak and carbon 1s region. (D) Chloride 1s and (E) chloride 2p core level spectra during adsorption of HCl taken at the PHOENIX beamline with 3090 eV photon energy and the SIM beamline with 420 eV photon energy, respectively. (F) Chloride 2p spectra of a NaCl solution at 263 K acquired at PHOENIX beamline with a photon energy of 2200 eV. The red lines are the sum of symmetric Gaussians representing molecular HCl (green) and ionic Cl^- (blue).

greater detail, depth profiles (DP) of the Cl 1s XPS intensities with increasing photon energy and, therefore, probing depth (top axis) or photoelectron kinetic energy (bottom axis), were derived. The depth information is based on the dependence of the electron inelastic free mean path on the electron kinetic energy (N. S. R. Database (2016)). Fig. 2A shows a sharp decrease of the apparent HCl/Cl^- intensity ratio in individual XPS spectra with increasing probing depth, indicating that the presence of molecular HCl relative to Cl^- is strongly favored at the outermost surface of ice. In Fig. 2B normalized XPS signal intensities of HCl and of Cl^- reflecting the trend in signal intensity relative to the probing depth are shown (text S3& S4). While the XPS signal intensity of HCl shows a steep decrease with kinetic energy, the ionic Cl^- XPS intensity profile shows a depletion at the uppermost surface compared to the deeper region followed by a slower intensity decay with depth than that of HCl. This gives clear experimental indication that indeed HCl is only found at the uppermost surface, while Cl^- resides deeper in the ice surface region. To quantitatively interpret the depth profiles and to derive the concentration of the chlorine species in the surface region, a 3-layer model was

developed (text S5).

In short, a 1st layer is set to have a thickness of d nm, with the flexibility of

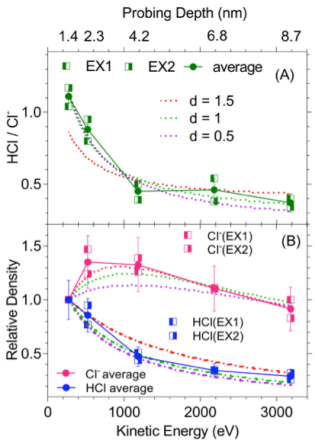

Figure 5.4: Depth profiles of (A) HCl/Cl^- molar ratio and (B) HCl and Cl^- signal intensities relative to the probing depth as given by the photoelectron kinetic energy (dots), based on two repeated experiments (half-filled squares). The initial HCl partial pressure did not exceed $7.5 \cdot 10^{-5}$ mbar in either experiment. Data are normalized to the data point at KE = 274 eV. The solid lines are guide to the eye. The discontinuous lines represent fits based on a 3-layer model for different thicknesses of the first layer (d). Probing depth is indicated on the top axis (text S1). The data fitting, measurement strategy, data processing and sensitivity analysis are detailed in the supporting material (text S2-S4, fig. S3-S6). The error bars in panel (A) originate from the uncertainties of fitting the XPS spectra, and in panel (B) the error bars reflect uncertainties in data processing and in fitting the XPS spectra.

containing HCl molecules and Cl^- ions at any molar ratio. The 2nd layer, ranging from Because of the unlikelihood that molecular HCl exists below the ice surface, the second layer, ranging from d to D contains Cl^- but no HCl. This choice is justified by separate fits to the HCl depth profile (eq. 10 in SI) suggesting that molecular HCl is confined to an upper layer with sub-nm thickness. The relative amount of chlorine species in the 2nd layer is set as R R times of that in the 1st layer. The resulting fits to the averages are plotted in Fig. 2 with the thickness d of 0.5, 1.0, or 1.5 nm. Considering the overall fit quality and the fact that the HCl/Cl^- ratios give the most robust information because less data processing was needed, the case with $d = 1$ nm reproduces the data best. For these fits, the model indicates the presence of molecular HCl restrained to a sub-monolayer surface layer which is low in Cl^-. The second layer holding Cl^- ends at $D = 9$ nm with $R = 0.65$

The observed locally distinct presence of either HCl or of Cl^- can be interpreted as adsorption of HCl at the outermost ice surface and spatially separated dissociation occurring within the ice-gas interfacial region as illustrated in Fig 3. For energetic reasons, HCl can dissociate only if it forms a sufficient number of hydrogen bonds (Devlin et al. (2002), Bolton and Pettersson (2001)). Molecular beam studies provide evidence for the presence of weakly bound, molecular adsorbed HCl on the surface of aqueous solutions (Morris et al. (2012), Brastad and Nathanson (2011)). Apparently, the water molecules within the interfacial region are mobile or flexible enough to accommodate the need of Cl^- to stabilize by forming hydration shells and it therefore seems unlikely that HCl survives un-dissociated during diffusion into the ice-gas interfacial layers. The low amount of Cl^- that was found at the topmost surface is consistent with the classic electrostatic picture of ion repulsion from the interface to a dielectric medium (Winter and Faubel (2006)). This picture also fits to the observed increase of HCl/Cl^- with decreasing exposure to HCl in the gas phase, taken that the equilibrium coverage at the surface and the equilibrium concentration within the surface region have different dependencies on HCl pressure, with the surface coverage likely being in saturation. The complex behavior of HCl observed here explains that the partitioning of HCl to ice exceeds predictions based on parameterization of other atmospherically relevant species by orders of magnitude (Zimmermann et al. (2016)). In striking contrast to HCl, a simple surface mechanism where trace gases form hydrogen bonds explains the adsorption behavior of non- and weakly acidic trace gases (Pouvesle et al. (2010)). The Cl^- in the surface region increases the total amount of adsorbed hydrochloric acid beyond the saturated surface coverage, though the model results indicate that the contribution of the second layer to the total amount of chlorine in the ice is relatively small ($R = 0.65$) at these specific experimental settings. Interestingly, earlier experimental work (Hynes et al. (2002)) indicated that in presence of HNO_3, the adsorption of HCl can be described by a surface mechanism alone and it was concluded that the presence of HNO_3 suppresses the dissociation of adsorbed HCl. It appears now that HNO_3 acidifies the sub-surface region preventing HCl to dissociate and solvate there, restricting the interaction to the surface adsorbed state. As HCl is a sticky gas, it is difficult to directly measure the precise local pressure right at the sample spot. Here we estimate the upper and lower limits for the local pressure to constrain the region in the HCl/water phase diagram (Molina et al. (1994)). The possibly maximum pressure is $7.5 \cdot 10^{-5}$ mbarwhich is based on the mixing ratio of the incoming gas (500 ppm HCl in N_2), the total pressure in the system and the assumption that there were no HCl losses during transport.

The lower limit can be estimated from the molar ratio of HCl to H_2O of the ice ($\sim 4.2 \cdot 10^{-3}$: 1 for 1st layer and $\sim 3.4 \cdot 10^{-4}$: 1 for 2nd layer), as discussed in text S6. By extrapolating the recently reported apparent Langmuir constant measured between 190 K and 220 K (Zimmermann et al. (2016)) to 253 K, such a ratio of total Cl corresponds to an apparent surface coverage of ~ 8% at 253 K. In equilibrium, an HCl partial pressure of 10^{-8} mbar establishes such a surface coverage. However, this back-of-the-envelope calculation is highly uncertain due to the crude extrapolations required. Further, beam induced depletion at the sample spot might contribute to a reduced Cl/O ratio compared to other regions of the ice sample. According to the E-AIM aerosol thermodynamics model (Massucci et al. (1999), Carslaw et al. (1995)), the Cl^- to H_2O ratio of a solution on the liquid/solid phase boundary at 253 K is about $6.0 \cdot 10^{-2}$: 1, with an HCl partial pressure of $1.4 \cdot 10^{-4}$ mbar (text S7). As here the molar ratios of Cl/O in the two layers are lower than that of the saturated solution by 1-2 orders of magnitudes, a local pressure in the range of 10^{-5} to 10^{-6} mbar seems reasonable, ensuring that the experimental conditions are well within the ice stability domain (Molina et al. (1994)). Moreover, based on the estimated partial pressure and surface coverage a binding energy of ca. 50 kJ/mol between undissociated HCl and water can be derived indicating that the HCl molecules form about slightly more than 2 hydrogen bonds with water molecules on ice surface (text S9).

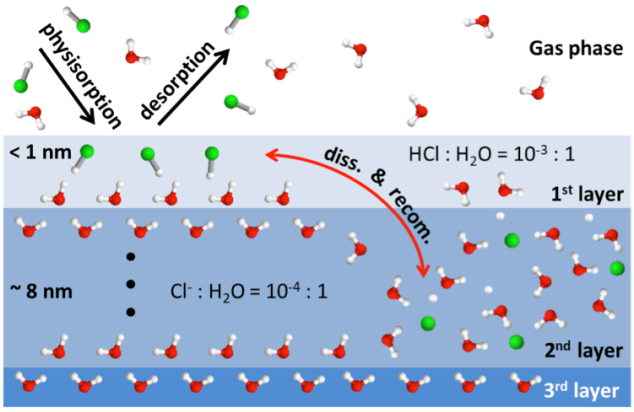

Figure 5.5: Schematic view of the three-layer model with the fitted parameters and indicative processes. The red arrows indicate dissociation (diss.) and recombination (recom.).

To shed light on the question to which extent the solvation of Cl^- in the surface region results in notable changes to the hydrogen bonding network, we performed partial electron yield NEXAFS measurements at the oxygen K-edge. Fig. 4 shows

the spectra of (A) liquid water, (B) clean ice, ice exposed to HCl with partial pressures of (C) $7.5 \cdot 10^{-5}$ mbar and (D) $6 \cdot 10^{-6}$ mbar, and a series of linear combinations of liquid water and clean ice spectra (1-3). The first peak (a) located at ca. 533 eV is assigned to a carbon-oxygen double bond, due to a slight sample contamination which occurred during this measurement (text S8). The second peak (b) is termed pre-peak or free-hydrogen peak (Myneni et al. (2002)), which was used to quantify the level of surface disorder of pure ice (Bluhm et al. (2002)). For the HCl doped ice, the peaks (b) seem to become broader compared to that of pure ice at each partial pressure. The most evident change in the NEXAFS of ice with increasing presence of HCl is the ratio between the main-edge peak (c) and the post-edge peak (d) where the line shape of the NEXAFS transits from that of solid ice towards that of liquid water. Among the linear combinations, the 25% ice and 75% water combination best captures the shape of the spectrum (D) indicating that majority significant fraction of water molecules are engaged in solvating Cl- and forming hydrogen bonds similar to those in aqueous solution. Main-edge to post-edge peak ratios increase only slightly in concentrated HCl solutions compared to pure water (Cappa et al. (2006)), so that the NEXAFS of water serves as a good proxy for HCl-solutions in this study. The NEXAFS probes the upper few nm of the ice surface, which includes the first layer and parts of the second layer shown in Fig. 3. Thus, in spite of the caveats in terms of the precise location of the experimental conditions in the phase diagram, we present clear experimental evidence that the presence of Cl^- perturbs the hydrogen bonding network of water ice presumably by binding water molecules into hydration shells. The substantial number of water molecules influenced by the solvation of Cl^- is in qualitative agreement to ellipsometry work by Zimmermann et al. (2016) and McNeill et al. (2007). The changes observed in the NEXAFS spectra at the low molar ratio of HCl in the ice point to significant long-range interactions within the hydrogen bonding structure at the air-ice interface, as recently suggested by molecular dynamics calculations (Irudayam and Hechman (2012)).

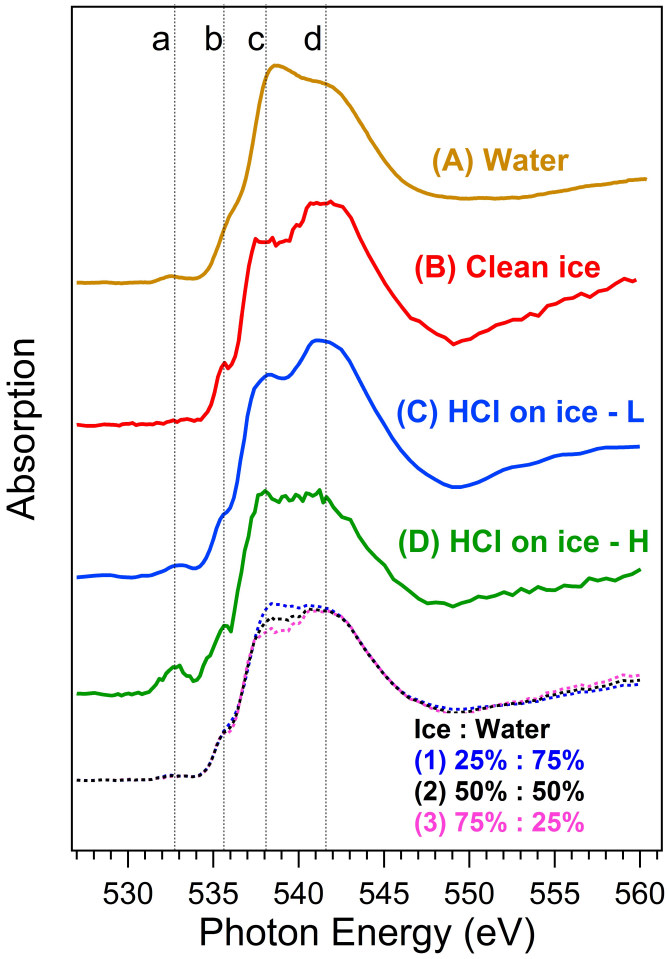

Figure 5.6: Partial electron-yield oxygen K-edge NEXAFS recorded at the SIM beamline. Normalizations were made to the areas from 532 eV to 553 eV. (A) Liquid water from Sellberg et al. (1); (B) Clean ice; (C, D) HCl doped ice, with low and high HCl partial pressures, respectively; and a series of linear combinations of water and ice: (1) 25% ice and 75% water, (2) 50% ice and 50% water and (3) 75% ice and 25% water.

5.2.3 Acknowledgements

We acknowledge the financial support from the Swiss National Science Foundation (Grant 149629). XK thanks the International Postdoc Fellowship from the Swedish Research Council (Grant 2014-6924). The technical support by Mario Birrer is greatly acknowledged. We thank Jan Pettersson for fruitful discussions. We are also very grateful to Armin Kleibert and the beamline staffs of SIM and PHOENIX at SLS. This research is part of AW doctoral thesis at ETH Zürich.

5.2.4 Supplementary Materials

Materials and Methods Text S1 to S8 Fig. S1 to S5 Movie S1

Materials and Methods

The experiments were performed at the SIM and PHOENIX beamlines of the Swiss Light Source (SLS) at Paul Scherrer Institute (PSI), using the near ambient pressure photoelectron (NAPP) spectroscopy end station (Orlando et al. (2016)). Fig. S1 shows the schematic view of (A) the in-situ cell connected with flow tubes, and (B) the sample holder. Before the experiments, the cell had been kept in ultra-high vacuum (UHV) condition. Water vapor is dosed via a stainless steel capillary of 800 µm inner diameter from a temperature controlled water reservoir. The water source (Fluka TraceSelect Ultra; Water ACS reagent, for ultra-trace analysis) was degassed by 3 freeze-pump-thaw cycles. The water reservoir was set at 258 K, which gave a pressure about 1 mbar in the cell, corresponding to the saturation pressure of ice at 253 K. To trigger the single crystal ice nucleation, the sample holder was cooled down, by cold nitrogen gas that went through liquid nitrogen bath, to obtain the critical supersaturation. Each step of lowering temperature is subtle, to avoid the formation of polycrystalline ice. At the onset of ice nucleation, the pressure in the cell was observed to decline because more gas molecules from the gas phase condense to grow the ice than are desorbed. The ice crystals were kept under this slight oversaturation to grow smoothly until covering the major part of the sample holder. Then, the sample holder was warmed up back to 253 K where the measured pressure matched the initial pressure before ice nucleation occurred. The HCl was from a gas bottle (Messer, 500 ppm HCl in N2 5.0) through

a calibrated leak valve. The total pressure of HCl/N_2 mixture was 0.15 mbar, corresponding to an HCl partial pressure of $7.5 \cdot 10^{-5}$ mbar . Measurements were started after introducing HCl vapor for a few hours, when both Cl 1s and O 1s intensities stabilized (fig. S4). The depth profile experiment was performed at the PHOENIX beamline. This beamline uses two undulators that provide photons in the range 2200 eV - 8000 eV. The beam size at the sample was about 0.1 mm × 0.1 mm. The XPS survey spectrum (Fig. 1C) was acquired with a photon energy of 2200 eV, and the Chloride 1s peak (Fig. 1D) was measured at PE = 3090 eV as one of the depth profile data points. For the depth profile, the Cl 1s spectrum was measured at the following photon energies: 3090 eV, 3340 eV, 4000 eV, 5000 eV, and 6000 eV. The NEXAFS and additional XPS measurements were carried out at the SIM beamline, which is capable of an energy range of 250 eV - 1500 eV, with a beam size of about 0.1 mm × 0.05 mm at the sample spot. The Cl 2p (Fig. 1E) was measured with a photon energy of 420 eV, and the Cl 2p for NaCl solution (Fig. 1F) was measured at PE = 2200 eV at the PHOENIX beamline as a parallel project. Partial electron yield NEXAFS spectra were acquired at the oxygen K-edge in partial electron yield mode using a kinetic energy window of 450 eV - 470 eV, corresponding to the background of the oxygen Auger line. All spectra were normalized to the incident beam flux determined from the electron current measured on the last mirror of the beamline before the endstation.

Text

Text S1: Probing depth

The probing depth (DP) is calculated as the product of inelastic free mean path (IMFP) (Devlin et al. (2002), Kang et al. (2000), Parent et al. (2011)) and the cosine of take-off angle (θ), i.e. DP = IMFP $\cdot$ cos (θ), where $\theta = 30$

Text S2: Ice stability and measurements strategy

The signal intensity in high-pressure XPS is a critical function of the distance between the sample and the inlet of the differential pumping stage of the analyzer (working distance). In order to minimize the variation in working distance between the individual sampling spots for each depth profile data point, we always took

reference measurements at fixed photon energy before and after each DP measurement. The reference is also used to monitor the stability of the working distance and thus to ensure that the ice sample was neither growing nor evaporating during each individual measurement. Fig. S4 shows the good stability of Cl 1s and O 1s before (solid line) and after (dotted line) each DP measurement. These reference measurements further demonstrate that the total amount of chlorine and the ratio of HCl to Cl^- did not change during the measurement time. To acquire a DP data point took about 5 minutes. The reference was measured at 3340 eV.
The DP measurements are based on 2 independent experiments with similar surface coverage but different dosing history. The first DP is with an initial HCl partial pressure of $7.5 \cdot 10^{-5}$ mbar, where the HCl-N_2 mixture were dosed into a clean chamber that was free of HCl. The second DP is with an HCl partial pressure of $2.5 \cdot 10^{-5}$ mbar, where the chamber had been exposed to higher HCl pressure. Due to the memory effects in the system, the ice in the two DPs seems to have similar HCl surface coverages, as the HCl/Cl^- ratio seems to be a function of local HCl partial pressure/surface coverage. The actual orders of the two measurements were: 1) DP4-DP2-DP3-DP5-DP1; 2) DP3-DP4-DP5-DP1-DP2 to avoid artefacts that may arise from time-dependent trends.
The NEXAFS measurements were optimized for shortest possible measurement time of not more than 30 min to minimize potential changes during beam exposure. Spectra were recorded in the photon energy range of 525 eV to 560 eV. In Fig.4, the measurement of spectrum (B) started from 525 eV, and the spectra (C) and (D) were recorded from the 560 eV.

Text S3: XPS data processing

Before plotting the depth profile data, normalization were performed so that the photoelectron intensities obtained at different kinetic energy can be compared. The normalization process includes (N. S. R. Database (2016)) photoionization cross section (Trzhaskovskaya et al. (2001)), to account for the ionization efficiency at different photon energy; (Ottosson et al. (2010)) inelastic free mean path (IMFP) in ice (Krepelova et al. (2013), Nikjoo et al. (2008), Tanuma et al. (2005)), to normalize the different probing depths at different kinetic energies; (Orlando et al. (2016)) X-ray photon flux, to account for beam intensity fluctuations; (Krepelova et al. (2013)) transmission of the electron analyser, to account for detection efficiency at different electron kinetic energies. The spectra were fitted with Gaus-

sians functions and a linear background. The binding energy scale was referenced to the O 1s core level peak at 535 eV. Such core level XPS spectra were recorded for this purpose for each Cl 1s spectrum at the same photon energy.

Text S4: Sensitivity analysis of depth profiles on IMFPs

The IMFP values used in the DP normalization are from previous studies of ice and water(Krepelova et al. (2013), Nikjoo et al. (2008), Tanuma et al. (2005)). Due to the considerable uncertainty of IMFP (Ottosson et al. (2010), Nikjoo et al. (2008), Suzuki et al. (2014), Thürmer et al. (2013)), we performed sensitivity analysis of IMFP impacting on the DP data. Assuming the IMFPs are linearly correlated to kinetic energy, the slope of the IMFP was increased by 20 %, 40 %, 60 %, 80 % (fig. S5), which were between the values from previous studies (Krepelova et al. (2013), Ottosson et al. (2010)). Fig. S5 generally shows a strong decrease of the measured cumulative Cl^- and HCl normalized concentration with KE as the slope of IMFP increases. The ratio of HCl/Cl^- is not shown because it is not shown because it is not affected by IMFP. When approaching the IMPF in water, the HCl depth profile becomes significantly steeper, while the one of Cl^- mainly levels off in the initial part. The fitting results from the sensitivity test are shown in fig. S6. In each panel, three cases of d were compared: 1) $d = 0.5$; 2) $d = 1$; 3) freely fitted d, where d always locates between 1.5 nm and 2 nm. The free d case gives the minimum overall residue of three DP, but due to the worse fitting to the HCl/Cl^- ratio (the most certain data set, no normalization was needed) it is regarded as the worst fitting compared to the other two cases. No significant differences of the fitting outcome were seen. The border of the second layer is always around 10 nm, and the first layer depth was 0.5 - 1.5 nm. An interesting point is that in higher IMFP cases, the first layer was assigned with some Cl-fraction. Thus, a minor amount of Cl^- might be present in the first layer, regarding the uncertainty of IMFP.

Text S5: Three layer model

The intensity of the photo-emitted electrons for a homogeneous sample is described as,

$$I(x) = I_0 e^{-x/\lambda \cdot \cos\theta} \tag{5.1}$$

where λ is the inelastic mean free path, x is the depth, θ is the take-off angle at which electrons are detected, I_0 is the photoemission signal intensity in absence of attenuation ($\theta = 30$ degree in our experiments). Three components are allowed to be in the first layer, which are molecular HCl, ionic Cl^-, and H_2O of ice. Only taking account of chloride containing species and normalizing the sum of them to unity we have,

$$n(HCl) + n(Cl^-_{1st}) = 1 \tag{5.2}$$

where and are the fractions of HCl and Cl^- in a unit volume, respectively. In the second layer, Cl^- is the only Cl containing species. A parameter R is used to represent the relative amount of chlorine species between the two layers,

$$\frac{n(Cl^-_{2nd})}{n(HCl) + n(Cl^-_{1st})} = n(Cl^-_{2nd}) = R \tag{5.3}$$

No Cl^- containing species diffuse into the third layer (bulk), thus it is pure ice. The total photoemission signal is given by integrating the contributions over the sample thickness,

$$\begin{aligned} I(x)dx &= I_0 \cdot e^{-x/\lambda\cos\theta} dx \\ &= \lambda \cdot \cos\theta \cdot I_0 \cdot e^{-x/\lambda\cos\theta} \end{aligned} \tag{5.4}$$

Applying equation (5.4) to integrate the signals from the first layer (from depth 0 to d), we have

$$\begin{aligned} I_{1st} &= \lambda \cdot \cos\theta \cdot I_0 \cdot e^{-0/\lambda\cos\theta} - \lambda \cdot \cos\theta \cdot I_0 \cdot e^{-d/\lambda\cos\theta} \\ &= \lambda \cdot \cos\theta \cdot I_0 \cdot (1 - e^{-d/\lambda\cos\theta}) \end{aligned} \tag{5.5}$$

Integration of the second layer is from depth x from d to D,

$$\begin{aligned} I_{1st} &= \lambda \cdot \cos\theta \cdot I_0 \cdot e^{-d/\lambda\cos\theta} - \lambda \cdot \cos\theta \cdot I_0 \cdot e^{-D/\lambda\cos\theta} \\ &= \lambda \cdot \cos\theta \cdot I_0 \cdot (e^{-d/\lambda\cos\theta} - e^{-D/\lambda\cos\theta}) \end{aligned} \tag{5.6}$$

We now look at HCl and Cl^-, respectively. As HCl only exists in the first layer, the HCl signal is

$$\begin{aligned} I_{HCl} &= n(HCl) \cdot I_{1st} \\ &= n(HCl) \cdot \lambda \cdot \cos\theta \cdot I_0 \cdot (1 - e^{-d/\lambda\cos\theta}) \end{aligned} \tag{5.7}$$

The ionic Cl^- signals are from both of the first and second layer,

$$\begin{aligned} I_{Cl^-} &= n(Cl^-_{1st}) \cdot I_{1st} + n(Cl^-_{2nd}) \cdot I_{2nd} \\ &= n(Cl^-_{1st}) \cdot \lambda \cdot \cos\theta \cdot I_0 \cdot (1 - e^{-d/\lambda\cos\theta}) + n(Cl^-_{2nd}) \cdot \lambda \cdot \cos\theta \cdot I_0 \cdot (e^{-d/\lambda\cos\theta} - e^{-D/\lambda\cos\theta}) \end{aligned} \tag{5.8}$$

Combining equations (5.7) and (5.8), the ratio of HCl and Cl^- at a same KE will be

$$\begin{aligned}\frac{I_{HCl}}{I_{Cl^-}} &= \frac{n(HCl)\cdot\lambda\cdot\cos\theta\cdot I_0\cdot(1-e^{-d/\lambda\cos\theta})}{n(Cl^-_{lst})\cdot\lambda\cdot\cos\theta\cdot I_0\cdot(1-e^{-d/\lambda\cos\theta})+n(Cl^-_{2nd})\cdot\lambda\cdot\cos\theta\cdot I_0\cdot(e^{-d/\lambda\cos\theta}-e^{-D/\lambda\cos\theta})} \\ &= \frac{n(HCl)\cdot(1-e^{-d/\lambda\cos\theta}}{n(Cl^-_{lst})\cdot(1-e^{-d/\lambda\cos\theta})+R\cdot(e^{-d/\lambda\cos\theta}-e^{-D/\lambda\cos\theta})} \\ &= \frac{n(HCl)\cdot(1-e^{-d/\lambda\cos\theta}}{n(Cl^-_{lst})+(R-n(Cl^-_{lst}))\cdot e^{-d/\lambda\cos\theta}-R\cdot e^{-D/\lambda\cos\theta}}\end{aligned} \tag{5.9}$$

According to equation (5.7), relative HCl intensities measured at different photon energies can be written as

$$\begin{aligned}\frac{I_{HCl}(KE)}{I_{HCl\_ref}} &= \frac{n(HCl)\cdot\lambda(KE)\cdot\cos\theta\cdot I_0\cdot(1-e^{-d/\lambda(KE)\cos\theta})}{n(HCl)\cdot\lambda_{ref}\cdot\cos\theta\cdot I_0\cdot(1-e^{-d/\lambda_{ref}\cos\theta})} \\ &= \frac{\lambda(KE)\cdot(1-e^{-d/\lambda(KE)\cos\theta})}{\lambda_{ref}\cdot(1-e^{-d/\lambda_{ref}\cos\theta})}\end{aligned} \tag{5.10}$$

where KE is the kinetic energy yielded from different photon energy, $\lambda(KE)$ is a function of KE, $I(HCl_{ref})$ refers to the HCl intensity measured by a reference photon energy, and λ_{ref} is the IMFP corresponding to the reference kinetic energy. Similarly, from equation (5.8) relative Cl^- intensities measured at different photon energies can be written as

$$\begin{aligned}\frac{I_{Cl^-}(KE)}{I_{Cl^-ref}} = &\frac{n(Cl^-_{lst})\cdot\lambda(KE)\cdot\cos\theta\cdot I_0\cdot(1-e^{-d/\lambda(KE)\cos\theta})+n(Cl^-_{2nd})\cdot\lambda(KE)\cdot\cos\theta\cdot I_0\cdot(e^{-d/\lambda(KE)\cos\theta}-e^{-D/\lambda(KE)\cos\theta})}{n(Cl^-_{lst})\cdot\lambda_{ref}\cdot\cos\theta\cdot I_0\cdot(1-e^{-d/\lambda_{ref}\cos\theta})+n(Cl^-_{2nd})\cdot\lambda_{ref}\cdot\cos\theta\cdot I_0\cdot(e^{-d/\lambda_{ref}\cos\theta}-e^{-D/\lambda_{ref}\cos\theta})} \\ &\frac{n(Cl^-_{lst})+(R-n(Cl^-_{lst}))\cdot e^{-d/\lambda(KE)\cos\theta}-R\cdot e^{-D/\lambda(KE)\cos\theta}}{n(Cl^-_{lst})+(R-n(Cl^-_{lst}))\cdot e^{-d/\lambda_{ref}\cos\theta}-R\cdot e^{-D/\lambda_{ref}\cos\theta}}\end{aligned} \tag{5.11}$$

The fitting was done in a non-linear least square fashion to minimize global residual of three depth profiles by using equations (5.9), (5.10) and (5.11). Note that the depth profiles of HCl and Cl^- are normalized to the first point, thus the reference IMFP (λ_{ref}) in equations (5.10) and (5.11) corresponds to that of the first data point (Photon Energy = 3090 eV, Kinetic Energy = 274 eV). The HCl/Cl^- ratio does not need any correction procedure to account for the experimental set-up, because it is calculated directly from the ratio between the XPS areas of molecular and ionic peaks in the Cl 1s spectra. Regarding this last point, we have to specify that we applied an internal normalization to the reference as we always measured a reference and the DP points at the same sample spot.

Text S6: Estimation of the Cl/O ratio

According to measurements where Cl and O have same kinetic energy (3184 eV, IMFPs were thus identical, 10 nm), the Cl/O ratio is about $5 \cdot 10^{-4}$: 1. From equation (1), it is clear that about 97% of the total photoemission intensity comes from the surface region of thickness 3λ, i.e. from the top 30 nm (at the kinetic energy considered). This value is however much larger than the calculated 9 nm effective thickness where all Cl species are distributed Because the fraction of Cl species compared to H_2O is very small, we can assume that H_2O is homogeneously distributed, which means that the top 9 nm of ice contributes with a factor of $(e^{(-9(10\cos\theta))}$= 65% to the total O 1s signal. Thus, within the top 9 nm, the Cl/O ratio is $5 \cdot 10^{-4}$: 0.65 = $7.7 \cdot 10^{-4}$: 1.
The distribution of O is proportional to the thickness of the two layers, i.e. the 1st layer has d/9 = 1/9 = 0.11 and the 2nd layer has (9–1)/9 = 0.89 of total O in 9 nm.
Also, according to the fitted parameters, in the first layer (0 nm to 1 nm) there are [1 / (1 + R)] · 100% = [1 / (1 + 0.65)] · 100% 60% of total Cl, so (corresponding to $7.7 \cdot 10^{-4}$· 60% = $4.6 \cdot 10^{-4}$), and the other 40% is stored in the 2nd layer (corresponding to $7.7 \cdot 10^{-4}$· 40% = $3.1 \cdot 10^{-4}$).
The HCl/H2O ratio in the first layer is thereby $4.6 \cdot 10^{-4}$: 0.11 = $4.2 \cdot 10^{-3}$: 1. Similarly, the ionic Cl^- being the only chlorine species in the second layer, the Cl^-/O ratio in the second layer is $3.1 \cdot 10^{-4} : 0.89 = 3.4 \cdot 10^{-4}$: 1. In the gas phase, we know that the ice vapor pressure at 253 K is about 1 mbar, and the partial pressure of HCl that we dosed is $7.5 \cdot 10^{-5}$ mbar, which gives the HCl/H_2O ratio in the gas phase is $7.5 \cdot 10^{-5}$: 1.

Text S7: Parameters for the E-AIM model

The vapor pressure of the second layer is calculated by using the E-AIM model (Model I). The input parameters are:
T = 253 K;
RH = 1 (for ice);
Result: HCl partial pressure is about $1.4 \cdot 10^{-4}$ mbar, and the molar ratio of Cl and H_2O is 0.57 / (0.57 + 8.9) = $6 \cdot 10^{-2}$: 1.

Text S8: Estimation of binding energy between molecular HCl and ice

Impingement rate (F) is written as

$$\mathrm{F} = \frac{\mathrm{P}}{\sqrt{2\pi \cdot \mathrm{m} \cdot \mathrm{k_b} \cdot \mathrm{T}}} \tag{5.12}$$

where P is partial pressure, m is atomic mass unit, k_b is Boltzmann constant, T is temperature.
The residence time of HCl on ice is

$$\tau = \frac{\mathrm{S} \cdot \mathrm{C}}{\mathrm{F}} = \frac{\mathrm{S} \cdot \mathrm{C} \cdot \sqrt{2\pi \cdot \mathrm{m} \cdot \mathrm{k_b} \cdot \mathrm{T}}}{\mathrm{P}} \tag{5.13}$$

where S is saturated surface density, C is HCl surface coverage.
$S \approx 10^{15}$ molecules $\cdot\, \mathrm{cm}^{-2}$
$C \approx 4 \cdot 10^{-3}$
As discussed in the main text, P may be about 10^{-6} to 10^{-5} mbar, where the residence time is corresponding to 8.2 ms to 0.82 ms.
From the Arrhenius equation,

$$\mathrm{k} = \mathrm{A} \cdot \mathrm{e}^{\frac{-\mathrm{E}}{\mathrm{R} \cdot \mathrm{T}}} \tag{5.14}$$

where k is desorption rate constant ($1/\tau$), A is pre-exponential factor, E is activation energy of desorption, R is ideal gas constant. By assuming a pre-exponential factor A as 10^{13} for an ordinary desorption process (Kong et al. (2014)), the binding energy of non-dissociated HCl on ice can be determined in the range from 48.0 kJ/mol to 52.9 kJ/mol. By allowing A changes by ±50% as uncertainty range, the binding energy is ranged from 51.4 kJ/mol to 56.2 kJ/mol (+50%) and 46.6 kJ/mol to 51.4 kJ/mol. Such binding energy indicates that HCl forms slightly more than 2 hydrogen bonds with ice surface.

Text S9: Carbon contamination in NEXAFS

The oxygen K-edge NEXAFS was taken in the SIM beamline because of the applicable X-ray photon energy range. Carbon signal was visible during the measurement, but no consequences or changes to the system were observed compared to other carbon-free measurements in this beamline or the other beamline, i.e. PHOENIX. Kong et al. (2014), discussed the carbon contamination and suggested that such

a trace level carbon does not have visible influence on the ice surface disorder. Further, to our knowledge, in order to cause phase change of ice at -20°C, the strongest carbocyclic acid, formic acid, needs a partial pressure in the range of 10^{-2} mbar (N. S. R. Database (2016), Bluhm et al. (2002)), which is higher than needed for HCl ($1.4 \cdot 10^{-4}$ mbar) by more than 2 orders of magnitudes. Thus, the effects of carbon contamination on surface disorder can be excluded.

Figures

Figure S1

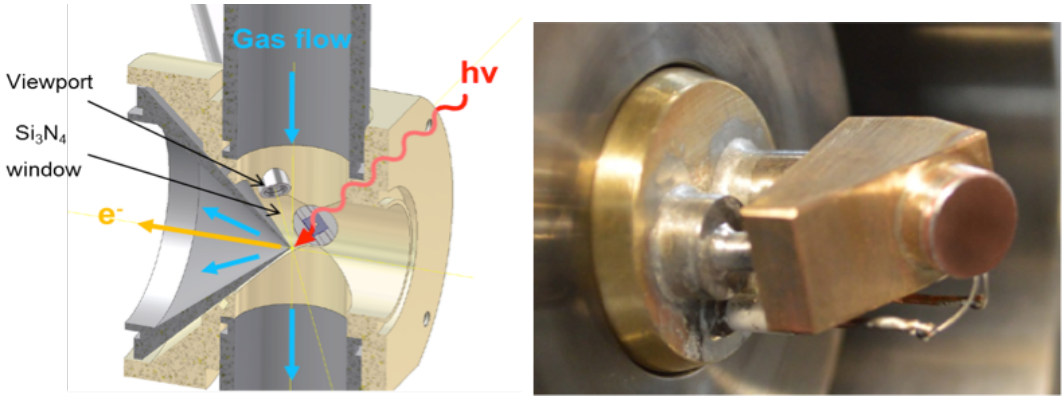

Figure 5.7: Schematic view of (A) the in-situ cell, and (B) the sample holder. In (A), the X-ray is directed through the Si_3N_4 window and pointed on the sample holder that is shown in (B). The emitted photoelectrons and Auger electrons went through the cone which interfaces the vacuum and the high pressure sides. The gas flow is indicated. A viewport is located in front of the sample holder, from where the pictures shown in Fig.1 and the movie S1 were taken.

Figure S2

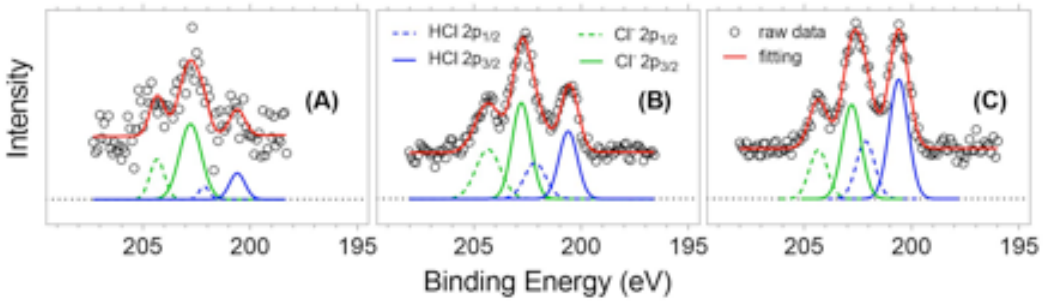

Figure 5.8: Chloride 2p core level spectra along with increasing HCl partial pressureat the SIM beamline with 420 eV photon energy. The temperature of the ice was 253 K. The measured HCl partial pressures were: (A) $1 \cdot 10^{-5}$ mbar; (B) $2 \cdot 10^{-5}$ mbar; (C) $8 \cdot 10^{-5}$ mbar, respectively. Note that the uncertainty of the absolute HCl partial pressure is discussed in the main text. The HCl/Cl^- ratios were: (A) 4 : 1; (B) 1.7 : 1; (C) 0.8 : 1.

Figure S3

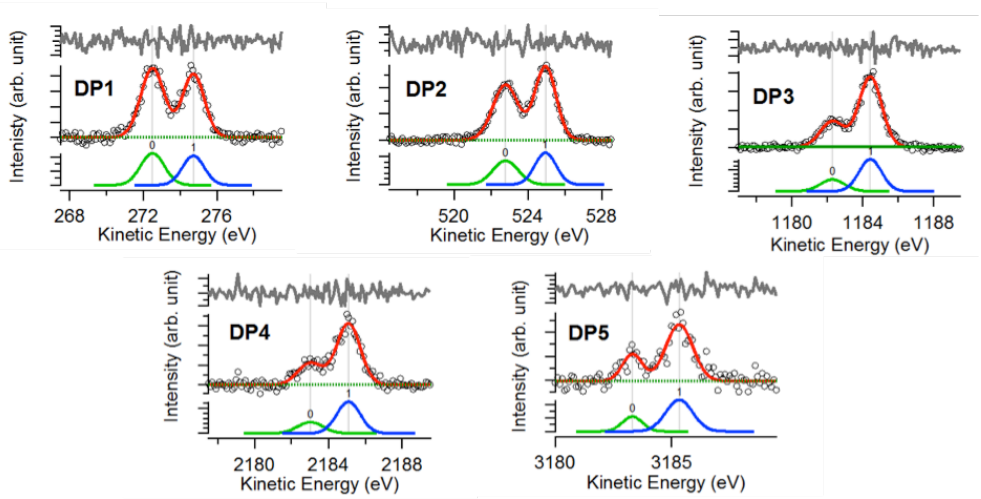

Figure 5.9: Illustration of the fittings of Cl 1s used in the depth profile. Note that the normalized process (text S3) was performed after this fitting process. The circles are raw data; the red curves are the overall fitting; the grey curves are the residue between fitting and raw data; the blue distributions are corresponding to ionic Cl^- and the green ones are for molecular HCl.

Figure S4

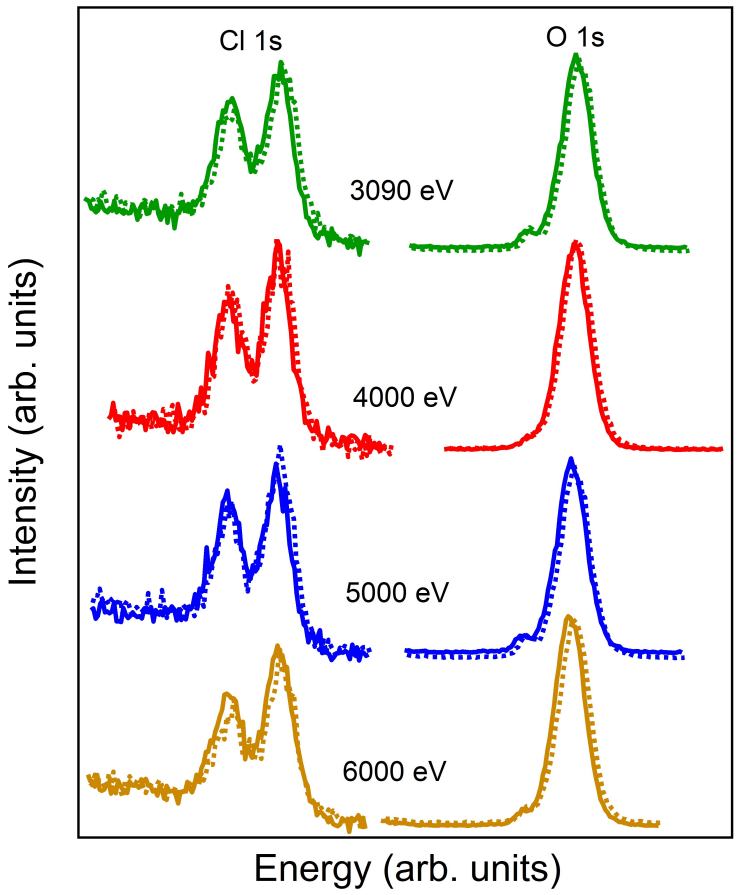

Figure 5.10: Reference Cl 1s and O 1s measured at 3340 eV photon energy before (solid line) and after (dotted) depth profile measurements at marked photon energy. Both Cl and O were stable during the measurements.

Figure S5

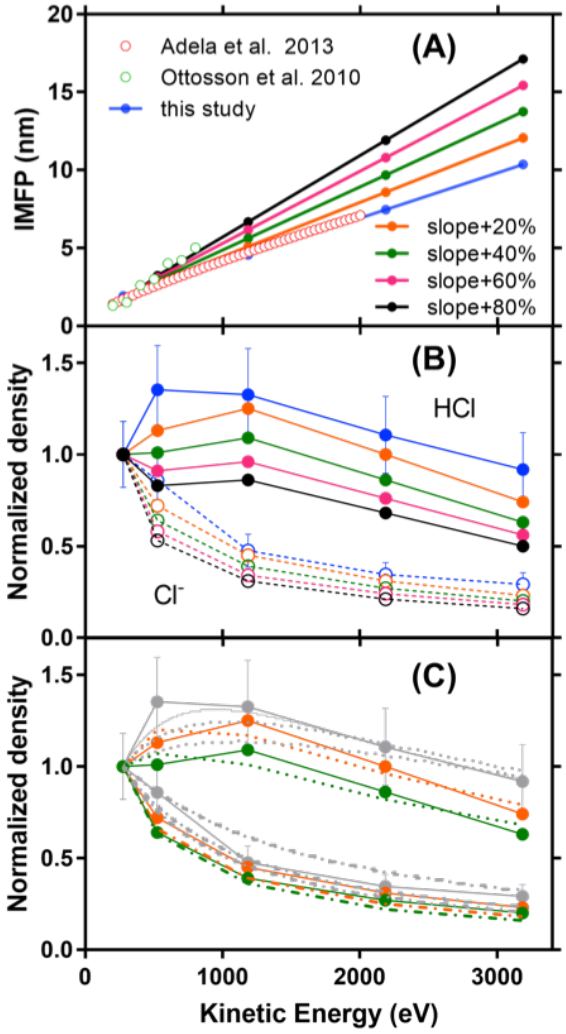

Figure 5.11: Sensitivity analysis of the depth profiles for different IMFPs. Panel (A) shows the currently used IMFP in blue, same as NIST Chemistry WebBook in red empty circles (1); green empty circles show that from Ottosson et al. (2010) (2); adjusted slopes were indicated in respective colors. Panel (B) shows the depth profiles of HCl and Cl^- with different IMFP, indicated by the same colors. Panel (C) shows the fittings results from the layer model, where the grey curves are those shown in the main text (Fig. 2) for comparison, and the orange and green ones correspond to +20% and +40% slope cases.

Figure S6

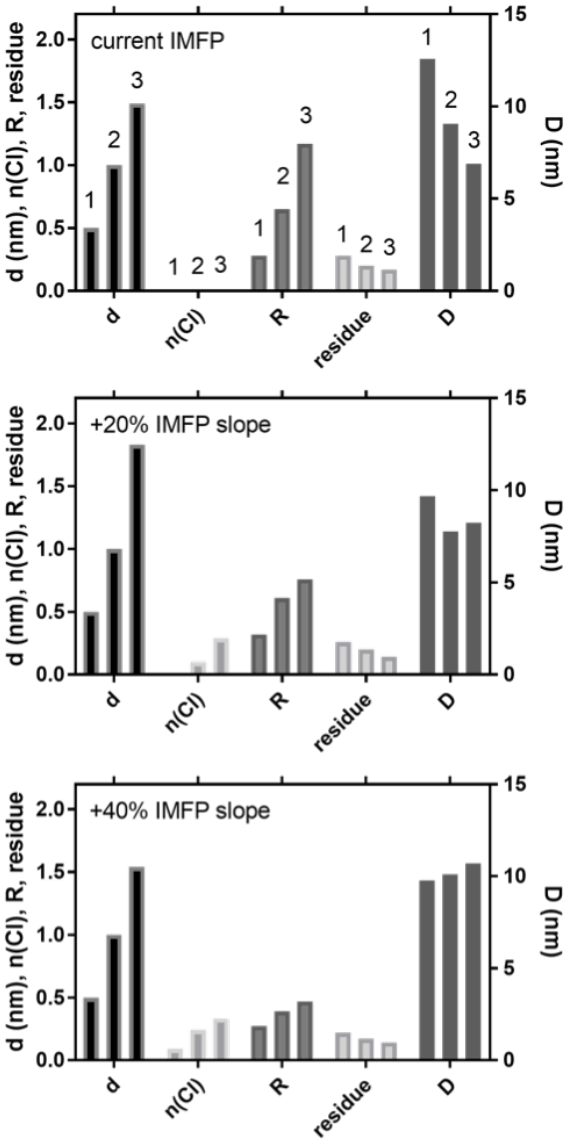

Figure 5.12: Fitted parameters from different d values and IMFPs. d is the thickness of the first layer; n(Cl) is the fraction of $Cl^-/(HCl+Cl^-)$ in the first layer; R is the molecular ratio of Cl between the second layer and the first layer; residue is the difference between fitting and actual values; D is the depth where the border of the second layer locates.

Movie
Movie S1 Single crystal ice growth in NAPP

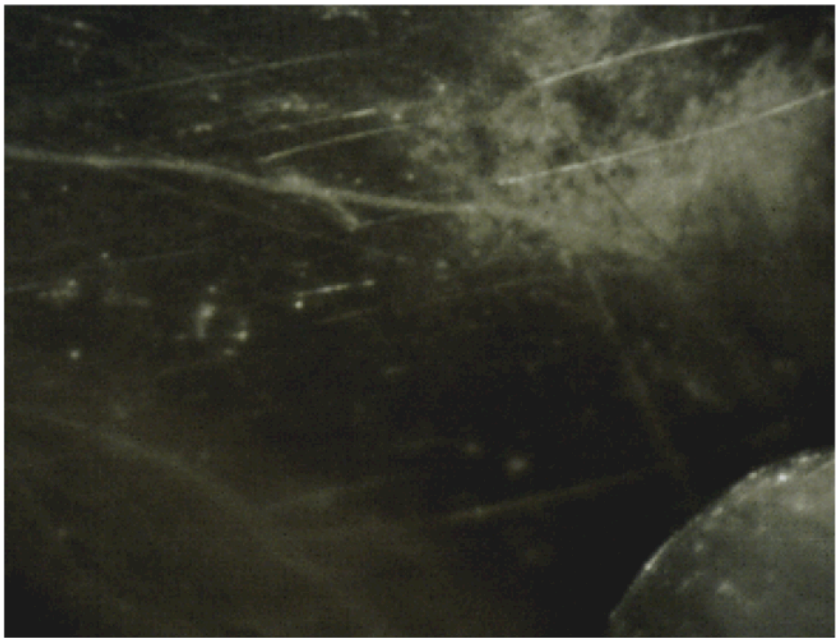

Bibliography

Monks, P. S.: Gas-phase radical chemistry in the troposphere. *Chemical Society Reviews*, **34(5)**, 376-395, 2005.

Parent, P., Laffon, C.:Adsorption of HCl on the water ice surface studied by x-ray absorption spectroscopy. *The Journal of Physical Chemistry B*, **109(4)**, 1547-1553, 2005.

Platt, U., Hönninger, G.: The role of halogen species in the troposphere. *Chemosphere*, **52(2)**, 325-338, 2003.

Molina, M. J. , T.-L. Tso, L. T. Molina, F. C.-Y. Wang,: Antarctic Stratospheric Chemistry of Chlorine Nitrate, Hydrogen Chloride, and Ice: Release of Active Chlorine. *Science*, **238**, 1253-1257 (1987).

Abbatt, J. P. D. et al.: Halogen activation via interactions with environmental ice and snow in the polar lower troposphere and other regions. *Atmos. Chem. Phys*, **12**, 6237-6271 (2012).

Devlin, J. P., N. Uras, J. Sadlej, V. Buch: Discrete stages in the solvation and ionization of hydrogen chloride adsorbed on ice particles. *Nature*, **417**, 269-271, 2002.

Kang, H., T. H. Shin, S. C. Park, I. K. Kim, S. J. Han: Acidity of Hydrogen Chloride on Ice. *Journal of the American Chemical Society*, **122**, 9842-9843, 2000.

Parent, P., J. Lasne, G. Marcotte, C. Laffon: HCl adsorption on ice at low temperature: a combined X-ray absorption, photoemission and infrared study. *Physical Chemistry Chemical Physics*, **13**, 7142-7148, 2011.

Ayotte, P., P. Marchand, J. L. Daschbach, R. S. Smith, B. D. Kay: HCl Adsorption and Ionization on Amorphous and Crystalline H2O Films below 50 K. *The Journal of Physical Chemistry A*, **115**, 6002-6014, 2011.

Bolton, K., J. B. C. Pettersson: Ice-catalyzed ionization of hydrochloric acid. *J. Am. Chem. Soc.*, **123**, 7360-7363, 2001.

Svanberg, M., J. B. C. Pettersson, K. Bolton: Coupled QM/MM Molecular Dynamics Simulations of HCl Interacting with Ice Surfaces and Water Clusters − Evidence of Rapid Ionization. *The Journal of Physical Chemistry A*, **104**, 5787-5798, 2000.

Calatayud M., D. Courmier, C. Minot: Ionization of HCl and HF in ice: a periodic DFT study. *Chem. Phys. Lett.*, **369**, 287-292, 2003.

Gertner, B. J., J. T. Hynes: Molecular dynamics simulation of hydrochloric acid ionization at the surface of stratospheric ice. *Science*, **271**, 1563-1566, 1996.

Mantz, Y. A., F. M. Geiger, L. T. Molina, M. J. Molina, B. L. Trout: The interaction of HCl with the (0001) face of hexagonal ice studied theoretically via Car-Parrinello molecular dynamics. *Chem. Phys. Lett.*, **348**, 285-292, 2001.

Thibert, E., F. Dominé: Thermodynamics and Kinetics of the Solid Solution of HCl in Ice. *The Journal of Physical Chemistry B*, **101**, 3554-3565, 1997.

Huthwelker, T., M. Ammann, T. Peter: The uptake of acidic gases on ice. *Chem Rev*, **106**, 1375-1444, 2006.

Dash, J. G., A. W. Rempel, J. S. Wettlaufer: The physics of premelted ice and its geophysical consequences. *Reviews of Modern Physics*, **78**, 695-741, 2006.

Bartels-Rausch, T., Jacobi, H. W., Kahan, T. F., Thomas, J. L., Thomson, E. S., Abbatt, J. P. D., Ammann, M., Blackford, J. R., Bluhm, H., Boxe, C., Domine, F., Frey, M. M., Gladich, I., Guzmán, M. I., Heger, D., Huthwelker, Th., Klán, P., Kuhs, W. F., Kuo, M. H., Maus, S., Moussa, S. G., McNeill, V. F., Newberg, J. T., Pettersson, J. B. C., Roeselová, M., Sodeau, J. R.: A review of air-ice chemical and physical interactions (AICI): liquids, quasi-liquids, and solids in snow, *Atmos. Chem. Phys.*, **14**, 1587–1633, 2014.

Riikonen, S., P. Parkkinen, L. Halonen, R. B. Gerber: Ionization of Acids on the Quasi-Liquid Layer of Ice. *The Journal of Physical Chemistry A*, **118**, 5029-5037, 2014.

Wren, S. N., D. J. Donaldson, Laboratory Study of pH at the Air-Ice Interface. *Journal of Physical Chemistry C*, **116**, 10171-10180, 2012.

Morris et al., Molecular beam scattering from supercooled sulfuric acid: Collisions of HCl, HBr,and HNO3 with 70 wt D2SO4 *The Journal of Physical Chemistry A*, **104**, 6738-6751, 2012.

Brastad, S. M., G. M. Nathanson,Molecular beam studies of HCl dissociation on cold salty water. *Physical Chemistry Chemical Physics*, **13**, 8284-8295, 2011.

Orlando, F. et al., The Environmental Photochemistry of Oxide Surfaces and the Nature of Frozen Salt Solutions: A New in Situ XPS Approach. *Top Catal*, **59**, 591-604, 2016.

Krepelova, A., T. Bartels-Rausch, M. A. Brown, H. Bluhm, M. Ammann, Adsorption of Acetic Acid on Ice Studied by Ambient-Pressure XPS and Partial-Electron-Yield NEXAFS Spectroscopy at 230-240 K. *J Phys Chem A*, **117**, 401-409, 2013.

Nilsson, A. et al., X-ray absorption spectroscopy and X-ray Raman scattering of water and ice; an experimental view. *J Electron Spectrosc*, **177**, 99-129, 2010.

Krepelova, A., J. T. Newberg, T. Huthwelker, H. Bluhm, M. Ammann, The nature of nitrate at the ice surface studied by XPS and NEXAFS. *Physical Chemistry Chemical Physics*, **12**, 8870-8880, 2010.

Pfalzgraff, W., S. Neshyba, M. Roeselova, Comparative Molecular Dynamics Study of Vapor-Exposed Basal, Prismatic, and Pyramidal Surfaces of Ice. *J Phys Chem A*, **115**, 6184-6193, 2011.

Zimmermann, S., M. Kippenberger, G. Schuster, J. N. Crowley, Adsorption isotherms for hydrogen chloride (HCl) on ice surfaces between 190 and 220 K. *Physical Chemistry Chemical Physics*, 2016.

Brown, M. A. et al., Electronic Structures of Formic Acid (HCOOH) and Formate (HCOO–) in Aqueous Solutions. *The Journal of Physical Chemistry Letters*, **3**, 1754-1759, 2012.

Lewis, T. et al., Does Nitric Acid Dissociate at the Aqueous Solution Surface? *Journal of Physical Chemistry C*, **115**, 21183-21190, 2011.

Database, N. S. R.: NIST Standard Reference Database. P. J. Linstrom, W. G. Mallard, Eds., *National Institute of Standards and Technology, Gaithersburg,* , **vol. 69**, 2016.

Winter, B., M. Faubel, Photoemission from liquid aqueous solutions. *Chem Rev*, **106**, 1176-1211, 2006.

Pouvesle, N., Kippenberger, M., Schuster, G., Crowley, J. N.: The interaction of H2O2 with ice surfaces between 203 and 233 K. *Physical Chemistry Chemical Physics*, **12**, 15544-15550 (2010).

Hynes, R. G., M. A. Fernandez, R. A. Cox, Uptake of HNO3 on water-ice and coadsorption of HNO3 and HCl in a temperature range 210-235 K. *J. Geophys. Res.-Atmos.*, **107**, 2002.

Molina, M. J., The Probable Role of Stratospheric 'Ice' Clouds: Heterogeneous Chemistry of the Ozone Hole. J. G. Calvert, Ed., Chemistry of the Atmosphere: The Impact of Global Change *Blackwell Scientific Publications, Oxford*, pp. 27-38, 1994.

Massucci, M., S. L. Clegg, P. Brimblecombe, Equilibrium Partial Pressures, Thermodynamic Properties of Aqueous and Solid Phases, and Cl2 Production from Aqueous HCl and HNO3 and Their Mixtures. *The Journal of Physical Chemistry A*, **103**, 4209-4226, 1999.

Carslaw, K. S., S. L. Clegg, P. Brimblecombe, A Thermodynamic Model of the System HCl-HNO3-H2SO4-H2O, Including Solubilities of HBr, from <200 to 328 K. *The Journal of Physical Chemistry*, **99**, 11557-11574, 1995.

Myneni, S. et al., Spectroscopic probing of local hydrogen-bonding structures in liquid water. *J Phys-Condens Mat*, **14**, L213-L219, 2002.

Bluhm, H., D. F. Ogletree, C. S. Fadley, Z. Hussain, M. Salmeron, The premelting of ice studied with photoelectron spectroscopy. *J Phys-Condens Mat*, **14**, L227-L233, 2002.

Cappa, C. D. et al., The electronic structure of the hydrated proton: A comparative X-ray absorption study of aqueous HCl and NaCl studies *The Journal of Physical Chemistry B*, **110**, 1166-1171, 2006.

McNeill, V. F. et al., Interaction of hydrogen chloride with ice surfaces: The effects of grain size, surface roughness, and surface disorder. *J Phys Chem A*, **111**, 6274-6284, 2007.

Irudayam, S. J., R. H. Hechman, Long-range hydrogen-bond structure in aqueous solutions ans the vapor-water interface *J Chem Phys*, **137**, 034508, 2012.

Database, N. S. R.: NIST Standard Reference Database. P. J. Linstrom, W. G. Mallard, Eds., *National Institute of Standards and Technology, Gaithersburg*, **vol. 69**, 2016.

Ottosson, N., M. Faubel, S. E. Bradforth, P. Jungwirth, B. Winter, Photoelectron spectroscopy of liquid water and aqueous solution: Electron effective attenuation lengths and emission-angle anisotropy. *J Electron Spectrosc*, **177**, 60-70, 2010.

Orlando, F. et al., The Environmental Photochemistry of Oxide Surfaces and the Nature of Frozen Salt Solutions: A New in Situ XPS Approach. *Top Catal*, **59**, 591-604, 2016.

Krepelova, A., T. Bartels-Rausch, M. A. Brown, H. Bluhm, M. Ammann, Adsorption of Acetic Acid on Ice Studied by Ambient-Pressure XPS and Partial-Electron-Yield NEXAFS Spectroscopy at 230-240 K. *J Phys Chem A*, **117**, 401-409, 2013.

Nikjoo, H., S. Uehara, D. Emfietzoglou, A. Brahme, Heavy charged particles in radiation biology and biophysics. *New J Phys*, **10**, 2008.

Tanuma, S., C. J. Powell, D. R. Penn, Calculations of electron inelastic mean free paths. VIII. Data for 15 elemental solids over the 50-2000 eV range. *Surf Interface Anal*, **37**, 1-14, 2005.

Trzhaskovskaya, M. B., V. I. Nefedov, V. G. Yarzhemsky, PHOTOELECTRON ANGULAR DISTRIBUTION PARAMETERS FOR ELEMENTS Z=1 TO Z=54 IN THE PHOTOELECTRON ENERGY RANGE 100–5000 eV. *Atomic Data and Nuclear Data Tables*, **77**, 97-159, 2001.

Suzuki, Y.-I., K. Nishizawa, N. Kurahashi, T. Suzuki, Effective attenuation length of an electron in liquid water between 10 and 600 eV. *Phys Rev E*, **90**, 010302, 2014.

Thürmer, S. et al., Photoelectron Angular Distributions from Liquid Water: Effects of Electron Scattering. *Physical Review Letters*, **111**, 173005, 2013.

Ottosson, N., M. Faubel, S. E. Bradforth, P. Jungwirth, B. Winter, Photoelectron spectroscopy of liquid water and aqueous solution: Electron effective attenuation lengths and emission-angle anisotropy. *J Electron Spectrosc*, **177**, 60-70, 2010.

Kong, X. R., P. Papagiannakopoulos, E. S. Thomson, N. Markovic, J. B. C. Pettersson, Photoelectron sWater Accommodation and Desorption Kinetics on Ice. *J Phys Chem A*, **118**, 3973-3979, 2014.

Bluhm, H., D. F. Ogletree, C. S. Fadley, Z. Hussain, M. Salmeron, The premelting of ice studied with photoelectron spectroscopy. *J Phys-Condens Mat*, **14**, L227-L233, 2002.

Lide, D. R.: CRC handbook of chemistry and physics: a ready-reference book of chemical and physical data. *CRC Press, Florida*, **ed. 85th**, 2004.

CHAPTER 6

Summary & Outlook

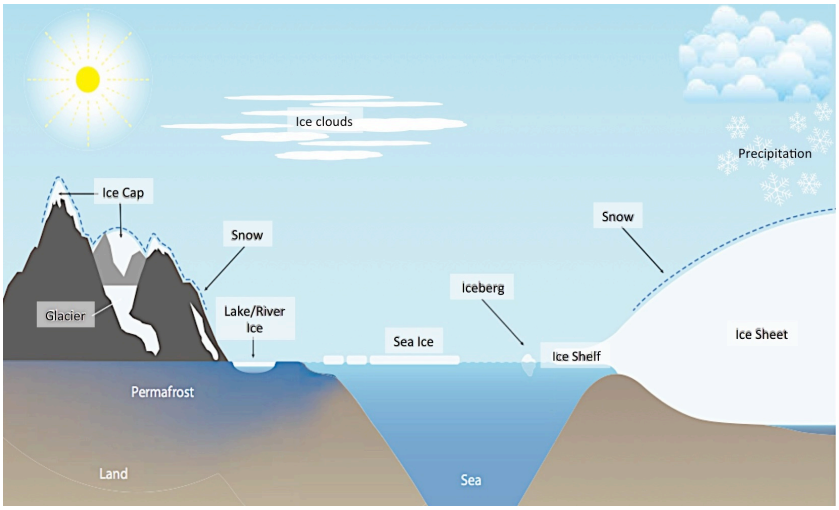

Figure 6.1: Overview about different types of ice present in the environment.

The compartments of the Earth system are tightly interconnected. A connection, which is worth receiving increased attention, is that between ice and air. As displayed in Figure 6.1, ice is present in many different forms, such as snow, glaciers, ice caps, and ice clouds. This ice can interact with (trace) gases present in the

atmosphere in many different ways, influencing the environment. For example, the polar cryosphere can have a major influence on trace gas concentrations in the overlying atmosphere. But not only the cryosphere, also ice present in the atmosphere can modify chemical processes and concentrations of trace gases in the atmosphere influencing the oxidation capacity and climate.

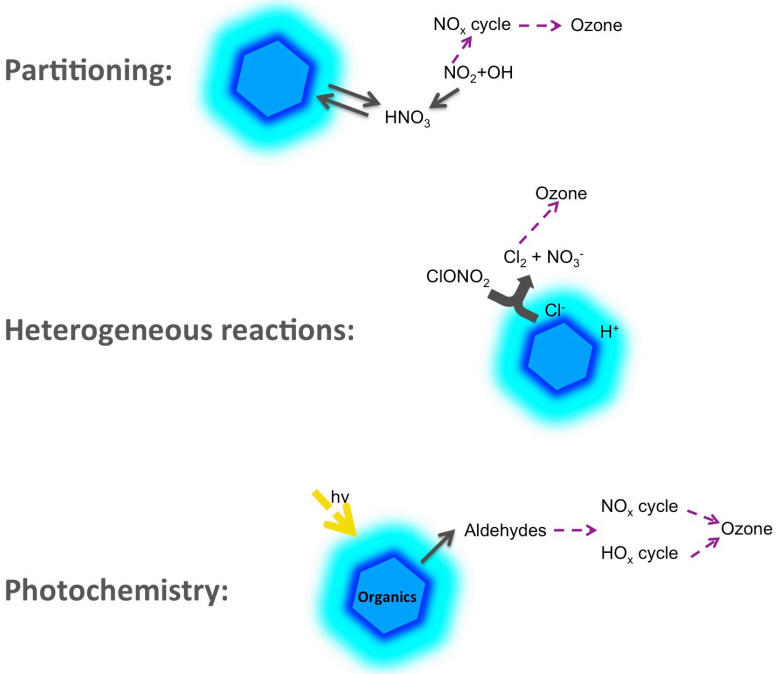

Figure 6.2: Overview about the three different kinds of ice – trace gas interactions important for atmospheric chemistry, environment and climate. Green arrows indicate the effect on important atmospheric cycles and species.

In general, one can differentiate three fundamental types of ice – trace gas interactions (Figure 6.2). One is the partitioning of gases to the ice leading to a (temporary) loss from the gas phase, as for example, the partitioning of HNO_3 to cirrus clouds (e.g. Abbatt et al. (1992)). Changes in HNO_3 concentration influence the NO_x cycle, which in turn modifies the O_3 concentration, resulting in changes of the radiation balance of the upper troposphere. (Photo)chemical processes of species in ice represent a further important kind of ice – trace gas interactions (Dominé and Shepson (2002)). The photolysis of organics in snow, resulting in emission of aldehydes from the cryosphere, influencing the oxidation capacity of the lowermost atmosphere, is a prominent example. In addition, heterogeneous

chemical reactions of gases, for example, of $ClONO_2$ with HCl at the ice surface, are important ice – trace gas interactions (Von Hobe et al. (2001)).
The presented interactions are only few of many interactions occurring between ice and trace gases, which emphasizes their relevance. But until now, little is known about the interplay of different molecular level processes involved in the interaction between ice and air. Commonly, the simple assumption of Langmuir type surface adsorption is used to describe ice – trace gas interactions. This may not necessarily be an appropriate description of ice – trace gas interactions, as for example shown by Orem and Adamson (1969), Abbatt et al. (1992), Tabazadeh et al. (1999), McNeill et al. (2006), Kuo (2013), Bartels-Rausch et al. (2014). Especially the uppermost ice layers called disordered interface (DI), liquid-like, or quasi-liquid layer, in which the hydrogen-bonding network is modified due to the outer layers missing bonds, may play an important role for ice – trace gas interactions. It is the direct interface between ice and gas phase. Its properties, such as phase state and thickness, but also its effect on ice – trace gas interactions are controversially debated.
The aim of this work has been to contribute and improve the common understanding of ice – trace gas interactions. In the context of this, I directly analyzed the molecular level interactions between ice and different trace gases, focusing on the following questions: Do different interaction processes dominate for the different trace gases? What do the depth profiles of trace gases in ice look like, and are they comparable for different trace gases? How does the acidity of a trace gas influence trace gas–ice interactions? Does dissociation play a role? Does the interaction between some trace gases and ice lead to changes of the hydrogen-bonding network in the interfacial region near the ice surface?

By comparing the interactions between ice and three different trace gases, I aimed to answer these questions. I chose to investigate the interaction between ice and propionaldehyde, a non-acidic short chain aldehyde, as well as formic acid, a relatively weak acid, but one of the strongest organic acids, and HCl, one of the strongest acids abundant in the atmosphere. To analyze these interactions, I used ambient pressure X-ray electron spectroscopy (APXES) (Figure 6.3).
APXES stands out for analyzing *in-situ* ice – trace gas interactions, due to its surface sensitivity, chemical selectivity, but also due to the fact that it is one of the few methods enabling non-destructive, direct analysis of the ice. The sample is irradiated with a X-ray of a specific photon energy and emitted electrons are detected. In XPS, the intensity of photoelectrons with a given kinetic energy give information about concentration and chemical state of atoms of the sample

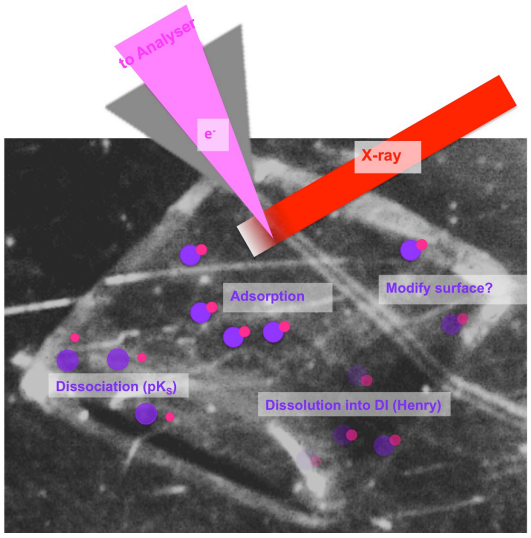

Figure 6.3: Scheme of ice – trace gas interaction analysis performed in the context of this thesis.

(Huefner (1995)). Using X-rays with different photon energies, as possible at synchrotron facilities, we can try to reconstruct concentration depth profiles from PE signals measured at different kinetic energies, thus probing depth. Depending on the energy of the X-ray, which in turn depends on the chosen synchrotron and beamline, I can analyze the composition of the uppermost ~50 nm of the ice sample.

Using partial electron (Auger) yield NEXAFS analysis, we can additionally examine if the interaction between ice and a trace gas leads to changes of the hydrogen-bonding network of the ice surface layers. Unlike most other methods, I do not need precise *a priori* knowledge about the phase and specific properties of the DI for the analysis of changes of the hydrogen-bonding network of the uppermost ice layers, which represents a further advantage of ambient pressure X-ray electron spectroscopy.

Since inelastic scatterings of electrons in the gas phase occur, the use of an ambient pressure electron emission spectroscopy set-up with a differentially pumped electrostatic lens system into the analyzer is indispensable.

To enable the analyses described above, I further developed and commissioned a dedicated chamber for the NAPP endstation at the SLS and the laboratory based droplet/solid-vapor set-up at LBL. Main challenges were the stable dosing of various ice – trace gas ratios and the ice stability. Despite initial troubles, I was able to successfully investigate the envisaged interactions.

I analyzed the effect of the ice – trace gas interaction on the hydrogen-bonding network of the uppermost ice layers for all three trace gases. For the interaction between ice and HCOOH, as well as HCl, I was able to analyze concentration depth profiles of the trace gases in/on the ice, but not for propionaldehyde. However, for propionaldehyde I could analyze isotherms and the temperature dependence of the partitioning. Experimental difficulties, such as the precision of the temperature and pressure measurements, limited the possibility of these investigations for HCOOH and HCl. In addition, I could not determine the degree of dissociation of HCOOH due to beam damage limiting the interpretation of the PE spectra of the HCOOH-ice experiments. However, I was able to estimate an upper limit of dissociation, as discussed in Chapter 4.1.4. Due to these constraints, the direct comparison of the molecular level interactions remains incomplete.

As demonstrated in Chapter 3, we were able to show that propionaldehyde does not influence the hydrogen-bonding network of the ice surface layers. The measured isotherms of the partitioning of propionaldehyde to ice can be fitted using Langmuir type surface adsorption isotherms over the whole investigated temperature range from 230-270 K. The natural logarithm of the partitioning coefficients obtained from the Langmuir fitting increases continuously and linearly with the inverse temperature, indicating that Langmuir type surface adsorption is the dominant interaction process.

For HCOOH, discussed in Chapter 4, we observed that formic acid, similar to propionaldehyde, does not influence the hydrogen-bonding network of the ice surface layers. In spite of that, we observed that a significant amount of HCOOH penetrates into the ice surface layers.

For the interaction ice-HCl discussed in Chapter 5, we also detected a penetration of the trace gas into the ice. In addition to molecular HCl, we observed dissociation of HCl in the uppermost ice layers. The ratio between molecular and dissociated HCl changes with HCl partial pressure. In case of the highest HCl partial pressure, close to the expected phase transition to a liquid solution, dissociated HCl is the overall dominant species in the ice sample. The observation of the presence of molecular HCl contradicts several previous studies which mainly investigated the interaction at lower ice temperatures (Barone et al. (1999), Abbatt et al. (2012), Devlin et al. (2002), Kang et al. (2000), Parent et al. (2011), Park and Kang (2005)) but corroborates relatively recent studies by e.g. Brastad and Nathanson (2011). NEXAFS analyses show that at this partial pressure a modification of the hydrogen-bonding network of the ice surface layers occurs.

These observations reveal that the picture of pure Langmuir surface adsorption does not match my observations of the interactions between trace gases and ice at the molecular level. As for example proposed by e.g. Tabazadeh et al. (1999), the interaction process between ice and trace gases may be a composite process. Instead of assuming simple surface adsorption of trace gases onto the ice surface, the interaction between gases and ice may be understood as a combination of adsorption and dissolution of the trace gas into the DI of the ice, as displayed in Figure 6.4. The importance of dissolution of trace gases into the ice was previously discussed (e.g. Abbatt et al. (1992), Diehl et al. (1998), Mmereki et al. (2000), McNeill et al. (2006) and Pártay et al. (2007)).
Such a proposed dissolution into the natural DI, which has a confined thickness, can explain finite penetration of trace gases into the uppermost nanometers of the ice. Due to the quasi liquid properties of the DI a dissolution comparable to dissolution into the liquid phase, for example following Henry's law, may be expected. Since the thickness of the DI increases (Bluhm et al. (2002), Bartels-Rausch et al. (2014) and references therein) and the solubility decreases (Sander (2016)), with increasing temperature, different partitioning trends of trace gases to the liquid like surface layer of ice can be explained. Here the absolute solubility of a trace gas determines the strength of the trend. At around 255 K the thickness of the natural DI increases strongly (Bluhm et al. (2002), Bartels-Rausch et al. (2014)), thus I would expect a changing trend of the equilibrium partitioning coefficient. In conclusion, due to the temperature dependence of the thickness of the DI and the solubility of a trace gas, dissolution into the DI has the ability to explain changes of the temperature trend of the equilibrium partitioning coefficients (Kong et al. (2014)) as observed for several trace gases (Orem and Adamson (1969), Kuo (2013)). These partitioning coefficients should be referred to as apparent Langmuir constants, since common experiments, such as CWFT and laboratory based XPS, are not able to distinguish between true surface adsorption (physisorption) and uptake (dissolution) into the DI.
Comparing the Henry constants [$mol/m^3 \cdot Pa$] of propionaldehyde, HCOOH and HCl at 255 K (~3.55, ~3000 and ~13, respectively (Sander (2016))), I can state, that dissolution into the DI, thus finite penetration into the uppermost nanometres of the ice, is only of minor importance for propionaldehyde, whereas for HCOOH and HCl it is more important, even though the case of HCl requires further attention, as discussed below. This is in good agreement with my observations.
In the following I present an exemplary estimation of the dissolution of HCl into ice showing that the interaction between ice and HCl can actually be explained by

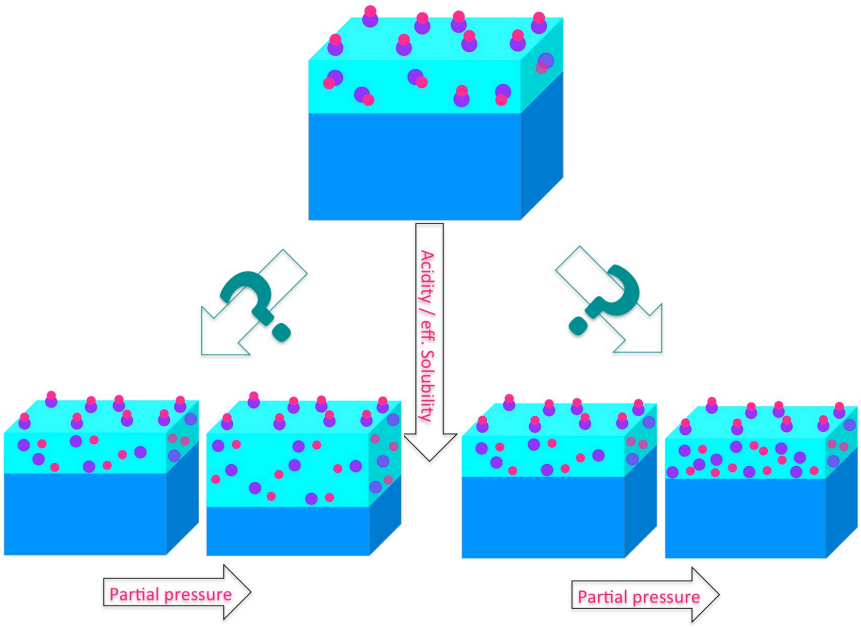

Figure 6.4: Scheme of the interaction behavior of ice–trace gas interactions depending on the acidity, thus effective solubility of the trace gas.

surface adsorption and dissolution into a liquid DI with finite thickness. Assuming a penetration of HCl into pure single crystal ice of about 10 nm, the amount of dissolved HCl molecules in the ice (e.g Thibert and Dominé (1997), Thibert and Dominé (1998)) is about six orders of magnitude lower (~10^5 molecules/cm^2) than observed within the context of this thesis (~10^{11} molecules/cm^2). However, when considering the DI as liquid (like) reservoir, the solubility of HCl in this layer, following Henry's law, is far higher than that in ice (Huthwelker et al. (2006), Sander (2016)). Nevertheless, the capacity of the partitioning is still relatively low (~10^8 molecules/cm^2) and cannot fully explain the observations discussed in Chapter 5. Reason for that is that dissociation is not considered, but especially for the experiment discussed in 5.2 a distinct amount of HCl was present as deprotonated HCl. Using the effective solubility to describe the interaction between ice and HCl, including dissociations, is more appropriate.
For strong acids the effective solubility is given by the product of the Henry constant and the acidity constant (Sander (2016)). For HCl, the effective solubility at 250 K is ~$5 \cdot 10^6$ mol/m^3 Pa, thus the effective solubility is several orders of magnitude higher than pure Henry solubility. Assuming dissolution of HCl in a liquid like DI with a thickness of 10 nm we can explain the uptake of HCl

to ice in our observations (Experiment: $\sim 10^{11}$ molecules/cm^2 <-> calculations: $\sim 7 \cdot 10^{10}$ molecules/cm^2).
For low trace gas concentrations, dissociation does not necessarily play the major role for the interaction between acidic trace gases and ice. For the interaction between ice and HCl, molecular, non-dissociated HCl seems to represent a significant fraction in the uppermost ice layers. Merely, at higher HCl pressures, Cl^- seems to be the dominant species. The observation of molecular HCl within the uppermost ice layers kind of matches the observations by Brastad and Nathanson (2011). They investigated HCl dissolution and dissociation in cold salt water using molecular beam studies. According to their observations HCl does not necessarily dissociate immediately upon interaction with cold salt water. HCl seems to be trapped at the surface in a state in which dissociation does not occur. Only when overcoming a barrier towards dissolution may dissociation and proton exchange occur, this means that fast proton exchange, thus dissociation, at the interface is suppressed. Using this knowledge, I interpret the interaction between ice and HCl as adsorption of molecular HCl to the ice followed by dissolution into the DI. The dissolved HCl then dissociates. Corresponding to the gas phase HCl less HCl dissolves and dissociates at lower p(HCl), whereas at higher pressures more HCl dissolves in the DI and dissociates, leading to more Cl^- in the DI. Since the isotherm for adsorption into the weakly bound molecular HCl state may be in saturation at already low HCl partial pressure, the fraction of molecular HCl may be higher at low HCl pressure, whereas at high HCl pressure the dissociated chloride in the DI dominates. In conclusion, the interaction between ice and HCl can be qualitatively explained by adsorption, followed by effective dissolution into the DI.
HCOOH and especially propionaldehyde are less acidic than HCl. Considering auto dissociation of water; we can estimate the acid dissociation constant for a hypothetical aqueous solution similar to calculations for acetic acid presented in Křepelová et al. (2012). In conclusion I can state that dissociation is of minor importance for the interaction between ice and these trace gases.
The investigation of the interaction between HCOOH clearly indicates, that non-dissociated HCOOH is the dominant species in/on the ice. Even though HCOOH is one of the strongest organic acids prevalent in the atmosphere, it is still a relatively weak acid ($K_A << 1$). Assuming dissolution following Henry's law, a distinct amount of HCOOH dissolves into the DI. This is what I observe. Dissolution of HCOOH into the DI can also explain observations by Jedlovszky et al. (2008), revealing a discontinuity in the partitioning of HCOOH to ice for higher tempera-

tures.
For propionaldehyde the picture of the interactions and the interpretations of the observations is a bit different. As discussed we were not able to directly measure concentration depth profiles which might indicate dissolution of propionaldehyde into the DI, but I would expect a discontinuity of the Langmuir coefficients at around 255 K if dissolution of propionaldehyde into the DI is a dominant process of the interaction. I do not observe such a discontinuity. However, I cannot exclude that minor amounts of propionaldehyde, consistent with calculations using Henry's law, penetrate the uppermost ice layers. Based on Henry's law we would expect in maximum about 10^9 molecules/cm^2 to dissolve into the DI, thus less than 0.1%. Using the presented measurements we can neither exclude nor confirm such a dissolution, since the high amount of adsorbed propionaldehyde at the interface leads to masking of the propionaldehyde dissolved in the DI and adsorbed and dissolved propionaldehyde cannot be distinguished spectroscopically.
Summarizing, I emphasize an adapted picture of the interaction between ice and trace gases as displayed in Figure 6.4. These observations indicate that the interaction between ice acetic acid can also not be explained by pure surface adsorption. Thus the interaction between ice and trace gases seems to be a composite process of Langmuir type surface adsorption followed by dissolution into the liquid like DI with a finite thickness. Depending on the solubility of a trace gas, dissolution of the trace gas into the DI can be of major importance for the interaction between ice and trace gas. The effective solubility enables a reasonable estimation of the importance of the dissolution into the DI for ice – trace gas interactions.
In addition, I analyzed the effect of the interaction between trace gases and ice on the hydrogen-bonding network in the DI using NEXAFS spectroscopy. For propionaldehyde and HCOOH I did not observe any change of the hydrogen-bonding network in the DI. At the highest examined HCl pressure, close to the thermodynamic phase transition, the concentration of Cl^- in the DI is relatively high. Here, NEXAFS analysis reveals a change of the hydrogen-bonding network in the uppermost ice layers. A pronounced amount of the H_2O molecules are ordered in a way similar to aqueous solution. However using the presented analyses, I cannot distinguish, whether a thermodynamic phase transition occurs, the DI thickens, or the high concentration of Cl^- in the DI leads to a modification of the mean hydrogen-bonding structure, merely because a significant amount of H_2O molecules may be tied up in the hydration shell of chloride. This is also illustrated in the lower part of Figure 6.4. In the case of a trace gas induced increase of the thickness of the DI, a long-term uptake trend as observed and discussed by e.g. Huthwelker et al.

(2006), could be explained (McNeill et al. (2006)). Nevertheless, dissolution and diffusion into other compartments, such as grain boundaries and veins, may also lead to a similar trend as discussed by e.g. Huthwelker et al. (2006) and Bartels-Rausch et al. (2014). To distinguish between these cases, further investigations would be necessary.

For that I propose performing additional experiments looking at the interaction between ice and a non-acidic trace gas, as well as a slightly more acidic trace gas than HCOOH. If possible these experiments should be performed in absence of beam damage and carbon contamination. To reduce contamination, plasma cleaning of the experimental set-up and electron sputtering of the sample holder may be used. In addition, the investigation of interactions between ice and trace gases in which an atom other than carbon can be used as an XPS tag, such as HONO, might be a chance to reduce the influence of adventitious carbon on the PE spectra relevant to study the interaction. The use of trace gases, which are known to show negligible fragmentation in electron impact ionization mass spectrometry, indicative of the ease with which molecules may fragment under the effect of secondary electrons in a photoemission experiment, may reduce the probability of beam damage.

I propose to measure concentration depth profiles, and isotherm over a temperature range from 180 K to 270 K and compare the observations with simulations. In addition to those experiments, I suggest to perform in depth studies on the effect of the DI on ice – trace gas interactions but also the effect of ice – trace interactions on the DI. Here, I suggest experimental investigations as for example NEXAFS, but to include also theoretical studies based on thermodynamics. Here I would suggest using a theoretic and modeling approach comparable to investigations by Wettlaufer (1999), who analyzed the effect of impurities on interfacial and surface melting by calculating van der Waals and Coulombic interactions with emphasize on the solid phase of the phase diagram.

To get a better understanding of the effects of the different compartments of ice for ice – trace gas interactions, I suggest studies using different 'types' of ice. As presented above and discussed in more detail in 1.2.2, the 'type' of the ice may play an important role in ice – trace gas interactions. APXES investigations using ice with various macroscopic appearances seem feasible. The observation of the detailed ice 'composition' during an experiment, meaning an investigation of the different compartments of ice parallel to APXES analysis would be an even more interesting achievement. Using for example the APXES imaging mode, or scanning transmission microscopy (STXM) measurements enable the analysis of the spatial distribution of the trace gas in the ice. Investigating the ice sample

using polarization microscopic methods would additionally allow a mapping of the compartments. However, to perform those experiments, a modification and adaptation of the recent set-ups would be required.
In principle, all those investigations seem feasible and may help to establish an improved, commonly accepted understanding of the molecular level interaction between trace gases and ice. Such a generally accepted picture may facilitate interpretation and application of ice – trace gas interaction observations.
To summarize, in the context of this thesis I was able to improve the understanding of the molecular level interactions between trace gases and ice, indicating that it is worth to revisit common assumptions. In conclusion I state, that the interaction between ice and trace gases is of composite nature. Adsorption and dissolution into the liquid like DI, depending on the effective solubility, describes the molecular level interaction between trace gases and ice reasonably well. Considering the dissolution of trace gases into the DI, especially the partitioning of trace gases to ice is more strongly and in a different manner influenced by temperature, than if only surface adsorption is considered. Due to climate change the global temperature, thus the ice temperature, increases as for example presented and discussed in the Fourth Assessment Report by the Intergovernmental Panel on Climate Change (IPPC). As emphasized, this influences the partitioning of trace gases to ice, which in turn influences atmospheric chemistry and climate (Neu and Prather (2012), Kuo (2013)). Following my suggestions for future research presented above, we can further develop our understanding about ice – trace gas interactions, and hopefully facilitating improved atmospheric chemistry and climate models. So far, there is no model simulating changes over time, in which the physical and chemical processes in ice are represented. To simulate the fate of trace gases in ice, the structural and chemical environment, thus the understanding of the dominant physical and chemical processes crucial for the ice – trace gas interactions, needs to be considered. The investigations performed in the context of this thesis, as well as the proposed further research, may be a big step towards this.
In this last paragraph of my thesis, I would like to suggest and emphasize one further ice related research topic which is, in my opinion, worth growing attention and should be considered in atmospheric and climate models, namely direct investigations of photochemistry in ice. The science of ice photochemistry is relatively unexplored since interest arose only recently. Since the initial discoveries of CH_2O and NO_x production within polar ice evidence for the photochemical production and release of a range of trace gases has been found (e.g. Grannas et al. (2007)). The significance of those processes varies depending on the local background con-

centrations of pollutants. However, in remote areas, emissions from the snow can dominate boundary layer chemistry. On the Antarctic plateau, some oxidants are as abundant as in the tropical troposphere.
For example, photochemical ozone production during polar day has been observed at South Pole due to enhanced OH and NO levels (e.g Dibb et al. (2002)). Reason is the NO_x flux out of the ice due to the photochemistry of nitrate in the ice (e.g Dibb et al. (2002), Dominé and Shepson (2002)). It was also shown that a variety of low molecular weight organic compounds are emitted from sunlit ice (e.g Grannas et al. (2007)). However, details of the underlying mechanism have not been elucidated. But also for photochemistry in ice the liquid like DI seems to play a key role, as for example emphasized by Klanova et al. (2003).
Due to the chemical selectivity, APXES is a nice approach to get deeper insights on the processes going on near the ice-air interface. Surface chemical evolution analysis can be performed. Using APXES, the electronic structure and the local environment of chromophores can be assessed, in comparison to gas phase or bulk aqueous phase environments. Furthermore, it is possible to examine the effect of UV radiation on the concentration and chemical composition at the ice surface. The surface chemical evolution under UV irradiation gives information on the processes in the ice caused by photochemical process, thus knowledge about photochemistry in/on ice can be created.

Bibliography

Abbatt, J. P. D., Beyer, K. D., Fucaloro, A. F., McMahon, J. R., Wooldridge, P. J., Zhang, R., Molina, M. J.: Interaction of HCl vapor with water-ice: Implications for the stratosphere. *Journal of Geophysical Research: Atmospheres*, **97(D14)**, 15819-15826, 1992.

Abbatt, J. P.: Interaction of HNO3 with water-ice surfaces at temperatures of the free troposphere. *Geophysical Research Letters*, **24(12)**, 1479-1482, 1997.
bibitem[Ayotte et al.(2011)]3HCl Ayotte, P., P. Marchand, J. L. Daschbach, R. S. Smith, B. D. Kay: HCl Adsorption and Ionization on Amorphous and Crystalline H2O Films below 50 K. *The Journal of Physical Chemistry A*, **115**, 6002-6014, 2011.

Barone, S. B., Zondlo, M. A., Tolbert, M. A.: Investigation of the heterogeneous reactivity of HCl, HBr, and HI on ice surfaces. *The Journal of Physical Chemistry A*, **103(48)**, 9717-9730, 1999.

Bartels-Rausch, T., Jacobi, H. W., Kahan, T. F., Thomas, J. L., Thomson, E. S., Abbatt, J. P. D., Ammann, M., Blackford, J. R., Bluhm, H., Boxe, C., Domine, F., Frey, M. M., Gladich, I., Guzmán, M. I., Heger, D., Huthwelker, Th., Klán, P., Kuhs, W. F., Kuo, M. H., Maus, S., Moussa, S. G., McNeill, V. F., Newberg, J. T., Pettersson, J. B. C., Roeselová, M., Sodeau, J. R.: A review of air-ice chemical and physical interactions (AICI): liquids, quasi-liquids, and solids in snow, *Atmos. Chem. Phys.*, **14**, 1587–1633, 2014.

Bluhm, H., Ogletree, D. F., Fadley, C. S., Hussain, Z., Salmeron, M.:The premelting of ice studied with photoelectron spectroscopy. *Journal of Physics: Condensed Matter*, **14(8)**, L227, 2002.

Brastad, S. M., Nathanson, G. M.: Molecular beam studies of HCl dissolution and dissociation in cold salty water. *Physical Chemistry Chemical Physics*, **13(18)**, 8284-8295, 2011.

Devlin, J. P., N. Uras, J. Sadlej, V. Buch: Discrete stages in the solvation and ionization of hydrogen chloride adsorbed on ice particles. *Nature*, **417**, 269-271, 2002.

Dibb, J. E., Arsenault, M., Peterson, M. C., Honrath, R. E.: Fast nitrogen oxide photochemistry in Summit, Greenland snow. *Atmospheric Environment*, **36(15)**, 2501-2511, 2002.

Diehl, K., Mitra, S. K., Pruppacher, H. R.: A laboratory study on the uptake of HCl, HNO 3, and SO 2 gas by ice crystals and the effect of these gases on the evaporation rate of the crystals. *Atmospheric research*, **47**, 235-244, 1998.

Dominé, F., Shepson, P. B.: Air-snow interactions and atmospheric chemistry. *Science*, **297(5586)**, 1506-1510, 2002.

Grannas, A. M., Shepson, P. B., Filley, T. R.: Photochemistry and nature of organic matter in Arctic and Antarctic snow. *Global Biogeochemical Cycles*, **18(1)**, 2004.

Grannas, A. M., Jones, A. E., Dibb, J., Ammann, M., Anastasio, C., Beine, H. J., Bergin, M., Bottenheim, J., Boxe, C. S., Carver, G., Crawford, J. H., Dominé, F., Frey, M. M., Guzmán, M. I., Heard, D. E., Helmig, D., Hoffmann, M. R., Honrath, R. E., Huey, L. G., Hutterli, M., Jacobi, H. W., Klán, P., Lefer, B., McConnell, J., Plane, J., Sander, R., Savarino, J., Shepson, P. B., Simpson, W. R., Sodeau, J. R., von Glasow, R., Weller, R., Wolff, E. W., Zhu, T., Chen, G.: An overview of snow photochemistry: evidence, mechanisms and impacts. *Atmospheric chemistry and physics*, **7(16)**, 4329-4373, 2007.

Huefner, J: Photoelectron Spectroscopy. *Chemical Physics Letters*, **315(1)**, 7-11, 1999.

Huthwelker, T., Ammann, M., Peter, T.: The uptake of acidic gases on ice. *Chem. Rev.*, **106**, 1375-1444, 2006.

Jedlovszky, P., Hantal, G., Neuróhr, K., Picaud, S., Hoang, P. N., Hessberg, P. V., Crowley, J. N.: Adsorption isotherm of formic acid on the surface of ice, as seen from experiments and grand canonical Monte Carlo simulation. *The Journal of Physical Chemistry C*, **112(24)**, 8976-8987, 2008.

Kang, H., T. H. Shin, S. C. Park, I. K. Kim, S. J. Han: Acidity of Hydrogen Chloride on Ice. *Journal of the American Chemical Society*, **122**, 9842-9843, 2000.

Klanova, J., Klan, P., Nosek, J., Holoubek, I.: Environmental ice photochemistry: monochlorophenols. *Environmental science & technology*, **37(8)**, 1568-1574, 2003.

Kong, X., Papagiannakopoulos, P., Thomson, E. S., Markovic, N., Pettersson, J. B.: Water accommodation and desorption kinetics on ice. *The Journal of Physical Chemistry A*, **118(22)**, 3973-3979, 2014.

Křepelová, A., Bartels-Rausch, T., Brown, M. A., Bluhm, H., Ammann, M.: Adsorption of acetic acid on ice studied by ambient pressure XPS and partial-electron-yield NEXAFS spectroscopy at 230–240 K. *J Phys Chem A*, **117**, 401-409, 2012.

Kuo, M.-H.: Trace Gas-Induced Brine and Disordered Interfacial Layers on Ice. *PhD Thesis*, Columbia University, 2013.

McNeill, V. F., Loerting, T., Geiger, F. M., Trout, B. L., Molina, M. J.: Hydrogen chloride-induced surface disordering on ice. *Proceedings of the National Academy of Sciences*, **103(25)**, 9422-9427, 2006.

Mmereki, B. T., Hicks, J. M., Donaldson, D. J. (2000). Adsorption of Atmospheric Gases at the Air− Water Interface. 3: Methylamines. The Journal of Physical Chemistry A, 104(46), 10789-10793.

Neu, J. L., Prather, M. J.: Toward a more physical representation of precipitation scavenging in global chemistry models: cloud overlap and ice physics and their impact on tropospheric ozone. *Atmospheric Chemistry and Physics*, **12(7)**, 3289-3310, 2012.

Orem, M. W., Adamson, A. W. (1969):Physical adsorption of vapor on ice: II. n-alkanes. *Journal of Colloid and Interface Science*, **31(2)**, 278-286, 1969.

Parent, P., J. Lasne, G. Marcotte, C. Laffon: HCl adsorption on ice at low temperature: a combined X-ray absorption, photoemission and infrared study. *Physical Chemistry Chemical Physics*, **13**, 7142-7148, 2011.

Park, S.-C., H. Kang: Adsorption, Ionization, and Migration of Hydrogen Chloride on Ice Films at Temperatures between 100 and 140 K. *The Journal of Physical Chemistry B*, **109**, 5124-5132, 2005.

Pártay, L. B., Jedlovszky, P., Hoang, P. N., Picaud, S., Mezei, M.: Free-Energy Profile of Small Solute Molecules at the Free Surfaces of Water and Ice, as Determined by Cavity Insertion Widom Calculations. *Journal of Physical Chemistry C*, **111(26)**, 9407-9416, 2007.

Sander, R., "Henry's Law Constants" in NIST Chemistry WebBook, NIST Standard Reference Database Number 69, Eds. P.J. Linstrom and W.G. Mallard, National Institute of Standards and Technology, Gaithersburg MD, 20899, http://webbook.nist.gov, (retrieved September 5, 2016).

Tabazadeh, A., Toon, O. B., Jensen, E. J.: A surface chemistry model for nonreactive trace gas adsorption on ice: Implications for nitric acid scavenging by cirrus. *Geophysical research letters*, **26(14)**, 2211-2214, 1999.

Thibert, E., Dominé, F.: Thermodynamics and kinetics of the solid solution of HCl in ice. *The Journal of Physical Chemistry B*, **101(18)**, 3554-3565, 1997.

Thibert, E., Dominé, F.: Thermodynamics and kinetics of the solid solution of HNO3 in ice. *The Journal of Physical Chemistry B*, **102(22)**, 4432-4439, 1998.

Von Hobe, M. , Grooß, J-U., Günther, G., Konopka, P., Gensch, I., Krämer, M., Spelten, N., Afchine, A., Schiller, C., Ulanovsky, A., Sitnikov, N., Shur, G., Yushkov, V., Ravegnani, F.,

Cairo, F., Roiger, A., Voigt, C., Schlager, H., Weigel, R., Frey, W., Borrmann, S., Müller, R., Stroh, F.: Evidence for heterogeneous chlorine activation in the tropical UTLS. *Atmospheric Chemistry and Physics*, **11(1)**, 241-256, 2011.

Wettlaufer, J. S.: Impurity effects in the premelting of ice. *Physical Review Letters*, **82(12)**, 2516, 1999.

CHAPTER 7

Appendix

7.1 Ambient pressure X-ray spectroscopy measurements of ice – trace gas interactions performed within the context of this study

7.1.1 August 2014

- First beamtime investigating the interaction between ice and HCOOH at PHOENIX.
- Adsorption-desorption equilibrium over a wide p(HCOOH) range, as well as a depth profile of ice exposed to 0.01 mbar HCOOH, were measured. For the depth profile analysis C1s and O1s spectra were acquired over a kinetic energy range from 2000-6500 eV.
- For the dosing of H_2O and HCOOH high precision leak valves were used.
- The polycrystalline ice remained stable at a temperature of ~233 K over more than 24 hours.

- A pronounced carbon contamination of the 'clean' ice before exposure to HCOOH was observed.
- Both MS were used for gas phase analysis.

7.1.2 December 2014

- Beamtime investigating the interaction between ice and HCOOH at PHOENIX.
- A depth profile of ice exposed to ~0.01 mbar HCOOH, were measured. For the depth profile analysis C1s and O1s spectra were acquired over a kinetic energy range from ~2000-4500 eV.
- For the dosing of H_2O a capillary approach and for HCOOH a high precision leak valve were used.
- The polycrystalline ice remained stable at a temperature of ~233 K over about 24 hours.
- A pronounced (but slightly lower than in August 2014) carbon contamination of the 'clean' ice before exposure to HCOOH was observed.
- Both MS were used for gas phase analysis.

7.1.3 February 2015

- Beamtime investigating the interaction between ice and HCOOH at SIM.
- During the beamtime sudden problems with the experimental set-up occurred. Furthermore a stabilization of the ice under the beam was not possible. No valuable analysis was possible.
- Only the MS of the differential pumping stage was used for gas phase analysis. The MS below the *in-situ* experimental cell was detached due to technical difficulties before the beam time. Thus the flux through the system was reduced compared to former beam times.

7.1.4 March 2015

- Beamtime investigating the interaction between ice and HCOOH at PHOENIX.
- Depth profile of ice exposed to ~0.015 mbar and 0.040 mbar HCOOH, were measured. For the depth profile analysis C1s and O1s spectra were acquired over a kinetic energy range from ~2000-5500 eV.
- For the dosing of H_2O and HCOOH a capillary approach was used.
- The polycrystalline ice remained relatively stable at a temperature of ~233 K over about 24 hours. However, changes in peak intensity due to evaporating ice could be observed making a detuning of the beam intensity and an increase of the H_2O oversaturation necessary.
- A pronounced (peak patterns modified compared to former beamtimes) carbon contamination of the 'clean' ice before exposure to HCOOH was observed.
- Only the MS of the differential pumping stage was used for gas phase analysis.

7.1.5 November 2015

- Beamtime investigating the interaction between ice and HCOOH at PHOENIX.
- A depth profile of ice exposed to ~0.1 mbar HCOOH, were measured. For the depth profile analysis C1s and O1s spectra were acquired over a kinetic energy range from ~2000-5500 eV.
- For the dosing of H_2O and HCOOH a capillary approach was used.
- The ice consisting of few crystals remained relatively stable at a temperature of ~253 K over about 24 hours. The beam intensity was detuned.
- A pronounced carbon contamination of the 'clean' ice before exposure to HCOOH was observed.
- Only the MS of the differential pumping stage was used for gas phase analysis.

7.1.6 December 2015

- Beamtime investigating the interaction between ice and HCOOH at SIM.
- Depth profiles of ice exposed to ~0.005 and 0.05 mbar HCOOH, were measured. For the depth profile analysis C1s and O1s spectra were acquired over a kinetic energy range from ~150-1250 eV. Additionally C and O K-edge NEXAFS measurements were performed for each p(HCOOH).
- For the dosing of H_2O and HCOOH a capillary approach was used.
- The ice consisting of few crystals remained relatively stable at a temperature of ~253 K over about 24 hours. The beam intensity was detuned.
- Only a negligible carbon contamination of the clean ice before exposure to HCOOH was observed.
- During the low p(HCOOH) experiments an increase of the HCOOH concentration on the ice over 100% occurred.
- Only the MS of the differential pumping stage was used for gas phase analysis.

7.1.7 February 2016

- Beamtime at SIM investigating the interaction between ice and HCOOH, HCl and MeOH, respectively.
- Depth profiles of ice exposed to ~0.01, 0.015 and 0.07 mbar HCOOH, were measured. For the depth profile analysis C1s and O1s spectra were acquired over a kinetic energy range from ~150-1050 eV. Additionally C and O K-edge NEXAFS measurements were performed for each p(HCOOH).
- For HCl adsorption-desorption analysis, as well as O K-edge measurements were performed.
- C1s spectra of ice exposed to MeOH were used as a reference.
- For the dosing of H_2O and HCOOH a capillary approach was used. For the dosing of HCl (in N_2 carrier gas) a high precision leak valve was used.
- The ice consisting of few crystals remained relatively stable at a temperature of ~253 K over about 24 hours. The beam intensity was detuned.

- Measurements of clean ice at 233 K did not show convincing stability even though higher H_2O saturations were used.
- Only a negligible carbon contamination of the clean ice before exposure was observed.
- Only the MS of the differential pumping stage was used for gas phase analysis.

7.1.8 April 2016

- Beamtime investigating the interaction between ice and HCl at PHOENIX.
- Depth profiles of ice exposed to HCl, as well as adsorption-desorption equilibrium were measured.
- For the dosing of H_2O a capillary approach was used. For the dosing of HCl (in N_2 carrier gas) a high precision leak valve was used.
- The ice consisting of few crystals and remained relatively stable at a temperature of ~253 K over about 24 hours. The beam intensity was detuned.
- Only a negligible carbon contamination of the clean ice before exposure was observed.
- Only the MS of the differential pumping stage was used for gas phase analysis.

7.1.9 Fall 2016

- Laboratory bases investigation of the interaction between ice and propionaldehyde at LBL.
- Adsorption-desorption equilibrium and isotherms were measured. The ice temperature was varied from 230-270 K.
- For the dosing of H_2O and propionaldehye a high precision leak valves were used.
- The ice was crystal clear and remained stable over more than 12 hours.
- A pronounced carbon contamination of the 'clean' ice before exposure was observed.

- Gas phase analysis was not possible.

7.1.10 February 2017

- Beamtime at PHOENIX investigating the interaction between ice and HCl, as well as ice and HNO_3.
- Depth profiles of ice exposed to ~HCl, as well as adsorption-desorption equilibrium were measured.
- For the dosing of H_2O a capillary approach was used. For the dosing of HCl and HNO_3 high precision leak valves were used.
- The ice consisted of few crystals and remained relatively stable at a temperature of ~243 K over about 24 hours. The beam intensity was detuned and a pronounced H_2O oversaturation needed to be used to prevent evaporation at the measurement spot.
- A pronounced carbon contamination of the clean ice before exposure was observed.
- Only the MS of the differential pumping stage was used for gas phase analysis. To increase the flow through the set-up, a further vacuum pump was attached to the system. This increases the stability of the ice tremendously.

Acknowledgements

Many people have contributed to this work. Some more direct than others. I like to thank all of them. Most probably I won't name all of them. Not by purpose and not because I am not thankful, but I simply forgot them to mention. However, without any of you I would not have been able to finish the thesis in this way. I would therefore like to thank:

- Tom Peter for taking me on as a PhD student and for the support during this project.
- Thorsten Bartels-Rausch, for supervising my work, giving me feedback and sometimes even believing in my data when I didn't. We had many discussions about the preparation, realization and analysis of our experiments. I am also very thankful for the many opportunities to present my work at conferences and workshops.
- Markus Ammann, for helping me with my work, giving valuable scientific input and sometimes anchoring discussions.
- Hendrik Bluhm and his group for giving me the great opportunity to come to his lab and improve my knowledge about APXPS and science in general.
- Jan Petterson for agreeing to review this work.
- Mario Birrer for fixing the things which break and building really cool new ones. He almost never was upset about broken stuff but was always happy

to help. It was a pleasure working with him. This work would not have been possible without your amazing support.

- Fabrizio Orlando, for teaching me the basics of XPS.
- Xiangrui Kong for fruitful ice discussions.
- Jacinta Edebeli and Katharina Domnanich for their time they spent reading my writings.
- All my former and current colleagues from the surface chemistry group, and the former Laboratory of Radiochemistry and Environmental Chemistry.
- I especially thank the whole NAPP team; We spent endless hours during the nights, but never got bored.
- Angela Blattmann, Doris Buehler and Petra Forney for taking care of all things bureaucratic.
- My family and friends who supported me and cared to keep me distracted.

Thanks!